

THE UNIVERSITY of ADELAIDE

The effects of high temperature metamorphic and melting processes on granulite-facies rocks

Kiara L. Alessio

Earth Sciences
School of Physical Sciences
University of Adelaide

This thesis is submitted in fulfilment of the requirements
for the degree of Doctor of Philosophy

31st of July, 2019

Abstract 7

Declaration 9

Acknowledgements 10

Publications arising from this project 12

CHAPTER 1: INTRODUCTION AND THESIS OUTLINE 15

Introduction 16

Background 16

Thesis outline 21

References 22

CHAPTER 2: MELT REINTEGRATION MODELLING: TESTING AGAINST A SUBSOLIDUS REFERENCE ASSEMBLAGE 31

Abstract 34

Introduction 34

Geological setting 35

Materials and Methods 38

Results 41

Discussion 42

Conclusions 48

Acknowledgements 48

References 48

CHAPTER 3: CONSERVATION OF DEEP CRUSTAL HEAT PRODUCTION 55

Abstract 58

Introduction 58

Background 59

Results 60

Discussion 60

Conclusions 63

Acknowledgements 63

References 63

CHAPTER 4: THERMAL MODELLING OF VERY LONG-LIVED HIGH THERMAL GRADIENT METAMORPHISM 69

Abstract 72

Introduction 72

Geological background 73

Analytical methods 78

Results 80

Discussion 82

Conclusions 92

Acknowledgements 92

References 92

CHAPTER 5: CONTRASTING TEMPERATURE–TIME RECORDS IN INTERLAYERED GRANULITES 99

Abstract 102

Introduction 102

Geological background 104

Methods 107

Results 111

Discussion 117

Conclusions 125

Acknowledgements 126

References 126

CHAPTER 6: DISCUSSION AND CONCLUSIONS 133

Appendix 1 140

1A: Mineral compositions obtained on MicroProbe SXFive 140

1B: TX models 142

1C: Mineral mode TCI outputs 144

Appendix 2 147

2A: Detailed location and sample maps 148

2B: Comparison of GRS vs XRF data 149

2C: Methods 150

2D: GRS data 151

Appendix 3 205

3A: Microprobe analyses 206

3B: T–X and TCInvestigator plots 212

3C: Geochronology 221

3D: Rock Properties 222

3E: Thermal modelling code 223

Appendix 4 231

4A: Microprobe analyses 232

4B: Geochronology and REEs 236

4C: Garnet LA-ICP-MS maps 240

4D: Garnet LA-ICP-MS analyses 242

This thesis presents research on high-temperature metamorphic processes. A recent development in petrological modelling of granulite facies rocks is reintegration of melt generated and lost during metamorphism. The aim of melt reintegration is to create bulk compositions suitable for modelling prograde subsolidus evolution. Melt reintegration methodology was applied to a low-pressure granulite assemblage containing unambiguous textural evidence for subsolidus andalusite. Melt reintegration methodology resulted in a bulk composition that stabilised subsolidus and modally correct andalusite, providing validation of this petrological modelling technique.

Melting and melt loss modifies rock chemistry and a long-standing paradigm is that melting depletes rocks in heat producing elements (HPEs). However, comprehensive K–U–Th datasets taken from a number of terranes show that in metapelites, melting and melt loss does not deplete U–Th concentrations, with overall terrane averages suggesting bulk heat production partitioning between melt and residuum is essentially 1:1.

Modelling of HPE concentrations derived from terrane-scale elemental mapping in central Australia show that low-pressure (150–175 °C/kbar) granulite-facies metamorphism was driven by elevated crustal heat production. This energy source resulted in extremely long-lived (> 150 Ma) low-P–high-T metamorphism. High thermal gradient metamorphism driven by this energy source is characterised by contractional structures, kinematically late temperature maxima, and tight clockwise *P*–*T* loops.

Petrochronology (the nexus between the isotopic age of a mineral and its compositional controls) is being increasingly used to interrogate the thermobarometric record contained in metamorphic rocks. Combined zircon and monazite REE-isotopic U–Pb compositions from interlayered metapelite and metabasic granulites show essentially identical peak metamorphic assemblages were achieved by substantially different *P*–*T*–*t* paths. The metabasic rock composition reached peak conditions at least 30 Ma before the metapelite. While speculative, the thermal delay recorded by the metapelite may reflect thermal buffering associated with partial melting and persistent structurally focussed melt streaming.

I certify that this work contains no material which has been accepted for the award of any other degree or diploma in my name, in any university or other tertiary institution and, to the best of my knowledge and belief, contains no material previously published or written by another person, except where due reference has been made in the text. In addition, I certify that no part of this work will, in the future, be used in a submission in my name, for any other degree or diploma in any university or other tertiary institution without the prior approval of the University of Adelaide and where applicable, any partner institution responsible for the joint-award of this degree.

I acknowledge that copyright of published works contained within this thesis resides with the copyright holder(s) of those works.

I also give permission for the digital version of my thesis to be made available on the web, via the University's digital research repository, the Library Search and also through web search engines, unless permission has been granted by the University to restrict access for a period of time.

I acknowledge the support I have received for my research through the provision of an Australian Government Research Training Program Scholarship.

Kiara Louise Alessio
31st of July, 2019

To my husband Brandon, my greatest memory throughout my time at university will forever be marrying you. This has been a journey that I would not have been able to take without your love and support. If we were able to organise and have a wedding in the third year of our PhDs, I strongly believe that we can do anything and look forward to our many adventures together in the years to come.

To Charlie and Louie, my furbabies, you cannot read this so I will simply say that I love you to the moon and back. Your (somewhat forced) night-time cuddles and hilarious antics have brightened up the lives of not only myself and Brandon, but many other residents of the Mawson whom I have forced your photos and videos upon.

To my mum and dad, thank you so much for your never-ending love and support. I would have never been here in the first place if it wasn't for you and I will forever appreciate the sacrifices that you made to get me here.

To my brother Mitchell, I'm (mostly) glad that you also chose to study Geology and we wound up in the same office during our PhDs. Upon the submission of this thesis I bequeath to you MY porridge bowl, which you may now use without fear of me catching you.

To Carol, Lino and Donna, I am so happy that I now get to call you guys family. Your support has been invaluable to Brandon and me and we appreciate everything that you have done for us.

To my supervisors Martin, Dave and Laura, none of this would have been possible without your guidance. Martin, we may have had our ups and downs throughout the last few years, but I would never have picked another supervisor. You have played a significant role in me growing into the person I am today and for that I will always be grateful. Dave, your technical knowledge, numerous complex spreadsheets and Thermocalc expertise have been greatly appreciated throughout my PhD. I was sad to see you leave for WA, but I wish you all the best in your new role and I hope that our paths cross again in the future. Laura, even as a PhD student yourself you were someone I looked to for guidance, so it was fitting that you would become one my supervisors. Thank you for your patience and all of the time you spent cleaning up my Thermocalc mistakes!

To the current and previous residents of the CERG Tank, Jie, Brad, Dillon, Mitchell, Renee, Kam, Meg, Laura, Kieran, Naomi, Xiaofang and anyone else I may have missed, thank you for all of the times that we shared in our office. From parties to meetings and everything in between, you guys have made this a much more enjoyable experience and I couldn't have asked for a better group to share it with. Thank you also to the other members of CERG, Karin, Claire, Funny, Alicia and Alex, who have been there for these events.

To my bridesmaids, Kam, Briony and Renee, thank you for not only standing beside me on my special day, but also being there for me throughout my entire journey through university. I have many great memories of our times together and hope to keep making many more into the future.

To the Hot Choc Crew, Kam, Briony (again!) and Alicia, thank you for keeping my mental health in check by catching up and venting about our life problems over hot chocolates on a regular basis.

To Sarah, Ben, Dave and the rest of the crew at Adelaide Microscopy, thank you for your hours of assistance and patience while I was (trying) to use the analytical equipment.

JOURNAL ARTICLES

Alessio K., Hand M., Morrissey L., Kelsey D. & Payne J. 2017 Melt Reintegration Modelling: Testing against a Subsolidus Reference Assemblage, Geosciences, vol. 7, no. 3, p. 75.

Alessio K. L., Hand M., Kelsey D. E., Williams M. A., Morrissey L. J. & Barovich K. 2018 Conservation of deep crustal heat production, Geology.

Williams M. A., Kelsey D. E., Baggs T., Hand M. & **Alessio K. L.** 2018 Thorium distribution in the crust: Outcrop and grain-scale perspectives, Lithos, vol. 320, pp. 222-235.

Submitted: **Alessio K. L.**, Hand M., Hasterok D., Morrissey L. J., Kelsey D. E. & Raimondo T. 2019 Very long-lived high thermal gradient metamorphism in the Reynolds–Anmatjira Ranges, Lithos.

CONFERENCE PRESENTATIONS

Bockmann KL, Hand, M, Kelsey, DE, Morissey, LJ, Kemp, C., 2015, July. Metamorphic Controls on U-Th Distribution in the Crust. In Granulites and Granulites.; Windhoek, Namibia.

Bockmann KL, Payne, JL, Morrissey LJ., 2016, June. Age of Metamorphism in the Kanmantoo Sediments at Reedy Creek, South Australia. In Australian Earth Science Convention.; Adelaide, South Australia.

Bockmann KL, Hand, M, Morrissey, LJ, Kelsey, DE, Kemp, C., 2016, June. Metamorphic Controls on U-Th Distribution in the Crust. In Australian Earth Science Convention.; Adelaide, South Australia.

Bockmann, K., Hand, M., Morrissey, L., Kelsey, D., Williams, M., Barovich, K. and Kemp, C., 2017, April. Th-U redistribution during fluid-absent partial melting of the crust. In EGU General Assembly Conference Abstracts (Vol. 19, p. 622).

Hand, M., Barovich, K., Morrissey, L., **Bockmann, K**., Kelsey, D. and Williams, M., 2017, April. Voluminous low-T granite: fluid present partial melting of the crust?. In EGU General Assembly Conference Abstracts (Vol. 19, p. 10501).

Hand M., Barovich K., Morrissey L., **Bockmann, K**., Kelsey D. & Williams M. 2017 Voluminous low-T granite: fluid present partial melting of the crust? In EGU General Assembly Conference Abstracts. pp. 10501.

Hand M., **Alessio K**., Morrissey L. & Clark C. 2018 Heat production driven high-temperature metamorphism. In EGU General Assembly Conference Abstracts. pp. 5562.

Alessio K., Hand M., Kelsey D., Williams M., Morrissey L. & Barovich K. 2018 Conservation of deep crustal heat production. In Granulites and Granulites.; Ullapool, Scotland.

Alessio K., Hand M., Kelsey D., Williams M., Morrissey L. & Barovich K. 2018 Conservation of deep crustal heat production rates. In Australian Geoscience Council Convention.; Adelaide, South Australia.

CHAPTER 1

Introduction and thesis outline

INTRODUCTION

Metamorphic rocks hold vital information about the evolution of Earth's crust, and their study allows us to place important constraints on the physical, chemical and chronological properties of tectonic events that have shaped the character of the continents. Metamorphic petrologists use of a wide range of techniques, including petrography, bulk rock and mineral geochemistry, geochronological analysis and numerical modelling to explore the processes that have shaped the Earth. More specifically, these techniques allow us to constrain the timing and pressure–temperature (*P–T*) conditions of tectonic events, which can be applied to the reconstruction of tectonic models, and the identification of promising areas for mineral exploration. Without the field of metamorphic petrology there would be an enormous gap in our understanding of the processes that occur within the Earth. However, there is still a vast amount of information that we do not yet know and the techniques and models that we use are constantly evolving to incorporate new findings and produce more accurate outputs. One of the areas where these new techniques are being applied is in the understanding of how rocks attain and record high temperature (granulite-facies) metamorphic conditions. Granulite-facies rocks form at temperatures above 700 °C and at pressures of 2–15 kbars. They offer an important window into the high-temperature processes occurring deep in the Earth's crust. These rocks vary widely in character and occur in a range of tectonic environments, making the interpretation of their formation challenging. Therefore, the drivers of high temperature metamorphism, the role of melting and melt loss in the redistribution of some elements in the crust and the way in which different rocks record high temperature processes remain uncertain in many situations.

In a broad sense, this thesis aims to address some of these unknowns and expand our knowledge of high-temperature metamorphic processes. This goal can be broken down into three more specific aims:

1. To assess the validity of current modelling techniques to calculate protolith compositions for granulite-facies rocks.
2. To investigate how high-temperature metamorphism, and the partial melting and melt loss that accompanies it, redistributes heat producing elements (HPEs) and how these elements may contribute to high metamorphic temperatures.
3. To compare the way in which mineral growth and metamorphic events are recorded by granulite-facies rocks of differing composition.

Together, the chapters of this thesis build upon our knowledge of several important metamorphic processes, and provide validation and extra considerations for many of the methods that are currently used.

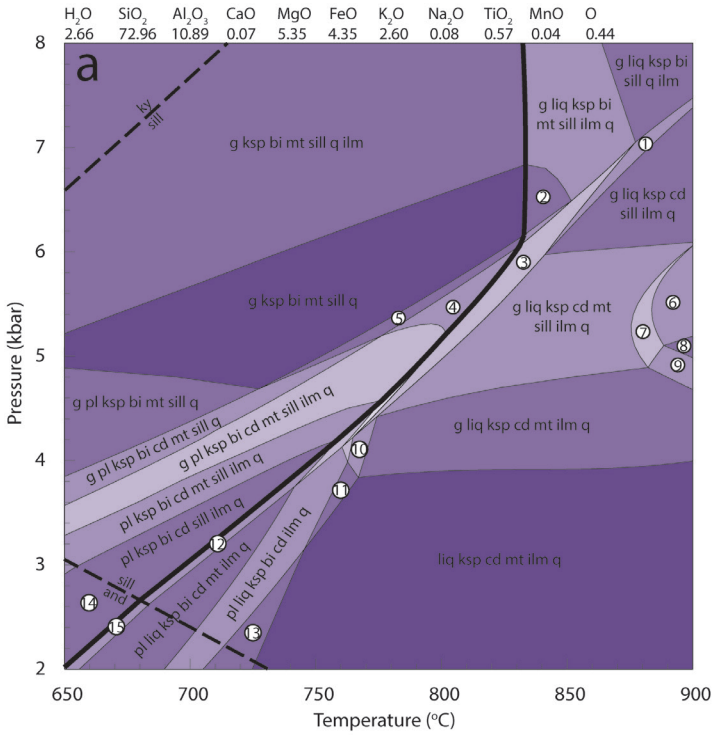
BACKGROUND

Regardless of the environment of formation, granulite facies rocks are generally regarded as restites, comprising residual material left-over after partial melting and melt loss has occurred. This model was initially proposed by Fyfe (1973) and was later built upon by a number of researchers who suggested that fluid-absent partial melting (i.e. melting of hydrous phases, such as biotite, muscovite and hornblende) was likely an important process in granulite-facies metamorphism (Thompson 1982, Powell 1983, Grant 1985). Fluid-absent partial melting was used to explain numerous natural examples, including Broken Hill, central Australia (Phillips 1981), New England (Tracy and Robinson 1983), and Namaqualand, South Africa (Waters and Whales 1984, Waters 1988). These early studies commonly assumed that extraction of large volumes of melt was needed to form the residual granulites. However, more recent studies on fluid-absent melting do not assume the extraction of such large volumes of melt, realising

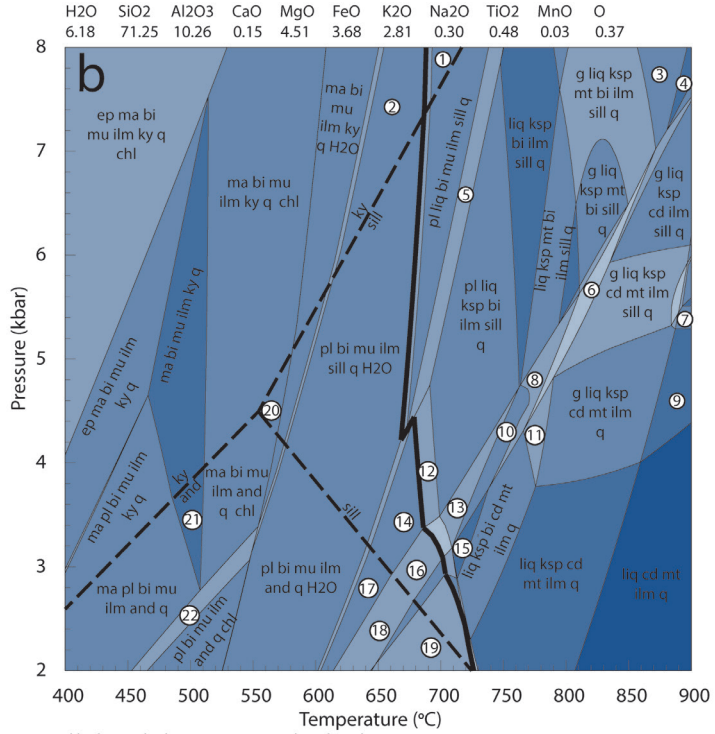
that residual granulite compositions may be achieved after only comparatively small volumes of incremental melt loss (e.g. Rosenberg and Handy 2005, but see also, Brown 2010). The process of melt extraction is no largely thought to be cyclic, where melt builds up until a critical threshold is reached and melt can buoyantly escape from the system (Laporte et al. 1997, Rosenberg and Handy 2005, Brown 2013, Yakymchuk and Brown 2014b). These processes result in modified rock compositions and generally destroy or obscure the rock's early metamorphic history. This makes granulites somewhat challenging to interpret, particularly when looking at timescales. However, predictive modelling techniques have significantly improved over time, and so too has our ability to model how rocks evolve in both *P–T* space and chemically.

Phase equilibria forward modelling has long been applied towards constraining the *P–T* conditions of metamorphic rocks (Connolly and Kerrick, 1987, Connolly, 1995, Holland and Powell 1998, White et al. 2007, Powell and Holland 2008, Brown 2014, White et al. 2014). This practice of quantitative predictive petrology has developed significantly over the last several decades, with the production of internally-consistent thermodynamic databases and literature describing the link between thermodynamic methods and principles of metamorphic petrology (Holland and Powell 1985, Powell and Holland 1985, Powell and Holland 1988, Holland and Powell 1990, Holland and Powell 2001, Pattison et al. 2002, Holland and Powell 2011, Powell et al. 2014, Connolly, 2017). This information, when incorporated into software capable of producing complex mineral assemblage stability models with some input from the user (e.g. Holland and Powell 1985, Connolly and Kerrick, 1987, Holland and Powell 2011), has become the backbone of modern metamorphic petrology. Phase equilibria models provide an accessible and robust way to investigate the peak pressure–temperature (*P–T*) conditions reached by a rock of particular bulk composition, the *P–T* path it evolved on, as well as to investigate processes such as melting or infiltration of fluid. The ability to determine a complete *P–T* path of a rock at granulite-facies conditions is particularly important in many cases, as it enables a better understanding of the tectonic environment and conditions under which it formed. However, this can be made extremely difficult in suprasolidus rocks, as the *P–T* models in their simplest implementation are only applicable to the final residual bulk rock composition after melt loss has occurred (Figure 1a). Subsolidus mineral stability in residual rock compositions commonly produce unrealistic mineral assemblages and cannot be reliably used to determine a prograde *P–T* path (Figure 1b). As such, several methods have been developed by which melt is reintegrated back into a residual bulk composition until a viable protolith composition is reached (Figure 1). These methods vary from a single-step approach, where a melt composition is calculated and reintegrated into the bulk composition in a single step (Indares et al. 2008, Guilmette et al. 2011, Hallett and Spear 2013, Zhang et al. 2017, Zou et al. 2017), a multi-step approach, where a melt composition is calculated at several different points and is added back at several stages (White et al. 2004, Korhonen et al. 2013), and a T–Mmelt section approach, where a T–X section is calculated between the residual rock composition and the melt composition and a point is chosen in between (Anderson et al. 2013). Each method has some limitations, but all approaches have the potential to recreate viable protolith compositions that can be used to make inferences about the prograde history (White et al. 2004, Bartoli 2017).

As well as reconstructing viable protolith compositions, it can also be a challenge to constrain the duration or even the number of events that a granulite facies rock may have experienced.



1. g liq ksp cd bi sill q ilm
2. g liq ksp bi mt sill q
3. g liq ksp bi cd mt sill ilm q
4. g ksp bi cd mt sill ilm q
5. g ksp bi cd mt sill q
6. g liq ksp cd sp sill ilm q
7. g liq ksp cd mt sp sill ilm q
8. g liq ksp cd sp ilm q
9. g liq ksp cd mt sp ilm q
10. g liq ksp bi cd mt ilm q
11. liq ksp bi cd mt ilm q
12. pl liq ksp bi cd sill ilm q
13. pl liq ksp cd ilm q
14. pl ksp bi cd and ilm q
15. pl liq ksp bi cd and ilm q



1. pl liq bi mu ilm ky q
2. pl bi mu ilm ky q H2O
3. g liq ksp bi ilm sill q
4. g liq bi ilm sill q
5. pl liq ksp bi mu ilm sill q
6. g liq ksp bi cd mt ilm sill q
7. g liq cd mt sp ilm q
8. liq ksp mt bi cd ilm sill q
9. g liq cd mt ilm q
10. liq ksp bi cd ilm sill q
11. g liq ksp bi cd mt ilm q
12. pl liq ksp bi ilm sill q H2O
13. pl liq ksp bi cd ilm sill q
14. pl ksp bi ilm sill q H2O
15. liq ksp bi cd ilm q
16. pl ksp bi cd ilm sill q H2O
17. pl ksp bi ilm and q H2O
18. pl ksp bi cd ilm and q H2O
19. pl ksp bi cd mt ilm q H2O
20. ma bi mu ilm sill q chl
21. ma bi mu ilm and q
22. ma pl bi mu ilm and q chl

Figure 1. (a) Phase equilibria model of an average granulite-facies sample from Reynolds Range, central Australia. (b) Phase equilibria model of the granulite composition from (a), with melt reintegrated to replicate an unmelted protolith composition. In both models the solid bold line represents the solidus and the bold dashed lines represent aluminosilicate boundaries. Alessio unpublished.

High-temperature processes generally overprint any information about earlier events, meaning that any events prior to high grade metamorphism may not be recorded. Similarly, high grade metamorphism and melt loss limits the ability of a rock to form new mineral assemblages or reset geochronometers, meaning that subsequent events may not be recorded. This has the effect that some outcrops or samples may appear to record a different metamorphic history to the rest of the terrane, depending on the reactivity of the rock prior to metamorphism (e.g. Morrissey et al. 2016). Therefore, to best understand the tectonic history of a granulite facies terrane it is necessary to sample multiple lithologies and, where possible, differing metamorphic grades. Previously, phase equilibria modelling of granulite facies rocks was limited to pelitic bulk compositions. However, the recent release of mafic melt thermodynamic models (Green et al. 2016) has, for the first time, allowed for more accurate *P–T* modelling of suprasolidus mafic rocks. These models have been utilised by a number of researchers to investigate high–temperature processes in mafic rocks (e.g. Agard et al. 2016, Jiang et al. 2016, Palin et al. 2016, Johnson et al. 2017, Tang et al. 2017, Yakymchuk et al. 2017). However, few studies have attempted to compare the accuracy of mafic *P–T* models with the more thoroughly refined pelitic models. One study that has made this comparison found that there was a significant difference in the T conditions recorded by rocks of differing compositions, which was primarily controlled by the energetics of variable melt generation of each rock (Schorn and Diener 2019). This highlights the need for studies to assess more than just one sample, or samples of only one type of composition, in order to best understand the events that occurred in a given area.

A further issue with phase equilibria modelling is that it is largely constrained to modelling major elements and phases. Although there have been numerous studies on accessory mineral chemistry (e.g. Bea 1996, Bea and Montero 1999, Rubatto et al. 2006, Rubatto et al. 2008, Kelsey and Powell 2011), and trace elements are now being directly and indirectly incorporated into phase equilibria models (e.g. Kelsey et al. 2008, Stepanov et al. 2012, Yakymchuk and Brown 2014a, Johnson et al. 2015), the changing distribution of accessory phases and trace elements during metamorphism and melting is still comparatively unexplored. Two key elements that are not presently considered directly by phase equilibria modelling are U and Th, which along with K, are the primary heat producing elements (HPEs) in the Earth's crust. Since the lower crust is generally thought to be relatively HPE-depleted with comparison to the upper crust (Heier and Adams 1965, Heier 1965, Hacker et al. 2011, Bea 2012, Jaupart et al. 2016) it has long been thought that the process of high-temperature metamorphism, and associated melting and melt loss, was the likely cause of this depletion. However, without the use of modelling software and large internally consistent thermodynamic datasets, this is difficult to test. Previous work has attempted to investigate the relationship between metamorphism and HPE distribution (e.g. Bea and Montero 1999, Kumar and Reddy 2004, Vilà et al. 2010), but many of these studies were limited by small datasets or differing lithologies. In recent years HPEs have been acknowledged as an important potential driver for metamorphism, particularly in high temperature, low pressure terranes (Sandiford et al. 1998, McLaren et al. 1999, Andreoli et al. 2006, Anderson et al. 2013, McLaren and Powell 2014, Morrissey et al. 2014, Horton et al. 2016). However, there have been few studies that have attempted to quantitatively model the temperature conditions that could be obtained by radiogenic heating in an HPE-rich terrane (c.f Horton et al. 2016), nor are there many constraints on the time that this type of heating may take.

Since granulite-facies metamorphism can be

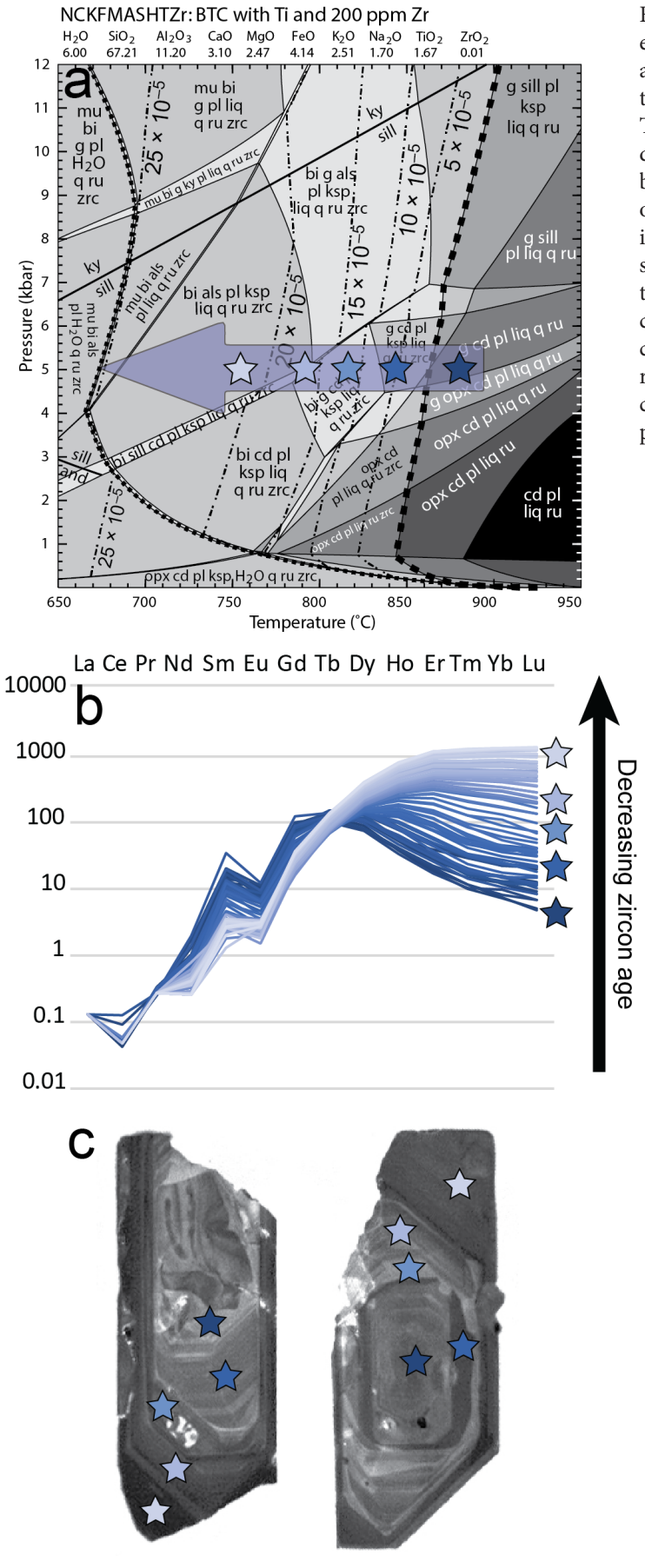


Figure 2. (a) *P–T* pseudosection with included model for zircon modified from Kelsey and Powell (2011). The small dashed line to the left of the diagram represents the solidus. The dashed and dotted lines throughout the diagram represent the zircon mode and the bold dashed line to the right is the zircon–out line. The blue arrow indicates a simple isobaric cooling path, with the stars representing changing zircon compositions along that path. (b) REE spider plot showing the changes that occur in REEs in zircon analyses corresponding to the stars in (a). (c) Theoretical locations of analyses from zoned zircon grains that could correspond to the REE patterns and ages shown in (a) and (b).

driven by a number of different heat sources, the timescales over which it occurs varies greatly and is still relatively poorly understood. High-grade metamorphic events have been recorded occurring over periods of <1 Myr (Ague and Baxter 2007, Viete et al. 2011), 10–50 Myr (Vry and Baker 2006, Baldwin and Brown 2008, Janots et al. 2009), and even up to 100 Myr (Buick et al. 2008, Smithies et al. 2011). Some of these longer-lived events may require the use of several different geochronometers to constrain their full length. Zircon and monazite are both vital tools for determining the ages of metamorphic rocks. They contain information necessary for understanding crustal processes and the timescales of high-temperature events (Watson 1996, Rubatto et al. 2001, Zeh et al. 2003). The conditions at which zircon and monazite grow, recrystallise and dissolve are dependent on a number of chemical and physical variables making their overall behaviour complex (Rubatto et al. 2001, Williams 2001, Pattison et al. 2002, Rubatto 2002, Pyle and Spear 2003, Clark et al. 2005, Buick et al. 2006, Hinchey et al. 2007, Rubatto and Hermann 2007, Tomkins and Pattison 2007, Kelsey et al. 2008, Stepanov et al. 2012). In migmatitic rocks, zircon commonly forms at suprasolidus conditions as Zr solubility decreases in the melt as temperatures decrease from their peak (Hacker et al. , Kelsey et al. 2008, Kelsey and Powell 2011, Yakymchuk and Brown 2014b, Kohn et al. 2015). Monazite generally forms at lower temperatures during melt crystallisation and so records younger ages than zircon in migmatitic rocks (Machado et al. 1989, Parrish 1990, Williams et al. 1996, Kelsey et al. 2008). However, unlike zircon, monazite also commonly grows during subsolidus prograde metamorphism (Kelsey et al. 2008), so if it can be preserved then monazite may feasibly also record older ages. It is now known that monazite and zircon grow at completely different points in *P–T* space (Hermann and Rubatto 2003, Rubatto and Hermann 2003, Baldwin et al. 2007, Gordon et al. 2013, Rubatto et al. 2013), and therefore zircon and monazite behaviour may vary significantly from sample to sample. The recently emerging field of petrochronology aims to address this, by combining geochronology, petrology, *P–T* calculations and REE analysis to gain a better understanding of the baric, thermal and chemical changes that occur in rocks and the rate at which they happen. An example of how this information is used together is shown in Figure 2, where a theoretical isobaric cooling *P–T* path results in zoned zircons, where the zones record different ages, *P–T* conditions and REE patterns. Understanding the timescales over which these changes occur is particularly important in the case of long-lived, high-geothermal gradient metamorphic terranes, as the heat sources required to generate high temperatures for prolonged periods remain relatively poorly understood.

THESIS AIMS AND OUTLINE

The central aims of this thesis are primarily to assess how certain elements are redistributed as a result of the partial melting and melt loss that occurs with high-grade metamorphism, and the duration of these events and how they may be recorded in metamorphic terranes. Branching off from this was also an investigation of the potential drivers for long-lived metamorphism and an assessment of how we are able to model protolith compositions in which to make petrographic interpretations. Each chapter focuses on specific processes that occur with high-grade metamorphism, and use specific terranes as natural laboratories in which to test hypotheses.

Chapter 2. This chapter focuses on assessing the validity of reproducing a protolith composition of a highly metamorphosed rock through melt reintegration modelling. This was done using a sample of Mg-rich granulite from the Delamerian Orogen, South Australia. This sample contains evidence for the former presence of andalusite porphyroblasts, providing a constraint on the

original precursor assemblage. An initial phase equilibria model of the sample was calculated and then used to calculate the theoretical composition of the melt at peak *P–T* conditions, which was reintegrated back into the rock until the model became water-saturated at the solidus. A protolith composition was formed that contained andalusite in modal abundances similar to those predicted from the petrographic textures in the residual rock, indicating that this method of melt reintegration modelling can be a valid way to create protolith compositions from which to draw information about a rock's prograde history.

Chapter 3. This chapter investigates the distribution of the HPEs K, U and Th in the continental crust, as a result of partial melting and melt loss that occurs during high-grade metamorphism. It is commonly assumed that granulite-facies rocks become depleted in HPEs as a result of melt loss(Heier and Adams, 1965; Jaupart et al., 2016). However, this chapter shows that the concentration of these elements in pelitic rocks remains relatively constant with increasing metamorphic grade, and instead suggests that the primary control on HPE distribution in the crust is the original bulk rock composition. Consequently, highly metamorphosed lower crust may retain more heat production than currently thought, and therefore be more thermomechanically responsive to younger tectonic events.

Chapter 4. The fourth chapter provides a case study from Reynolds Range, central Australia that explores the duration of high geothermal gradient metamorphism and the role that crustal heat production can play in driving metamorphism. A combination of monazite U–Pb geochronology and phase equilibria modelling from this study and several others from the Reynolds and neighbouring Anmatjira Ranges suggest that Paleo-Mesoproterozoic high geothermal gradient metamorphism may have lasted for >100 Myr, significantly longer than the previous estimates of *ca.* 30 Myr. The potential longevity of this event, as well as the fact that there are no obvious thermal drivers, suggest that high concentrations of HPEs are the likely cause of metamorphism in this area. Thermal modelling results confirm that HPE concentrations were high enough to produce the temperatures recorded in the Reynolds Range, but require that the crust was <25 km thick, to prevent excessive temperatures and catastrophic melting in the lower crust.

Chapter 5. This chapter assesses the petrochronological differences between granulite-facies mafic and pelitic bulk compositions from the Harts Range, central Australia. A combination of phase equilibria modelling, zircon and monazite U–Pb geochronology and REE analysis, and garnet REE mapping are used to determine the maximum *P–T* conditions reached by each of the samples, as well as their ages, timing of garnet growth and the duration of high-grade conditions. Both bulk compositions produce similar *P–T* results and zircon ages, but zircon–garnet REE analysis shows that garnet grows at different times in each sample. This chapter highlights that using two different bulk compositions and interrogating the zoning and trace element patterns in garnet, zircon and monazite provides more information on the duration of metamorphism than can be obtained by traditional metamorphic petrology on pelitic samples alone.

Chapter 6. The final chapter provides a summary of the work that has been done to produce this thesis and the direction of future work required to continue to progress our understanding and ability to apply this information.

REFERENCES

Agard P., Yamato P., Soret M., Prigent C., Guillot S., Plunder A., Dubacq B., Chauvet A. & Monié P. 2016 Plate interface rheological

switches during subduction infancy: Control on slab penetration and metamorphic sole formation, Earth and Planetary Science Letters, vol. 451, pp. 208-220.

Ague J. J. & Baxter E. F. 2007 Brief thermal pulses during mountain building recorded by Sr diffusion in apatite and multicomponent diffusion in garnet, Earth and Planetary Science Letters, vol. 261, no. 3-4, pp. 500-516.

Anderson J. R., Kelsey D. E., Hand M. & Collins W. J. 2013 Conductively driven, high-thermal gradient metamorphism in the Anmatjira Range, Arunta region, central Australia, Journal of Metamorphic Geology, vol. 31, no. 9, pp. 1003-1026.

Andreoli M. A., Hart R. J., Ashwal L. D. & Coetzee H. 2006 Correlations between U, Th content and metamorphic grade in the western Namaqualand Belt, South Africa, with implications for radioactive heating of the crust, Journal of Petrology, vol. 47, no. 6, pp. 1095-1118.

Baldwin J. & Brown M. 2008 Age and duration of ultrahigh-temperature metamorphism in the Anápolis–Itauçu Complex, Southern Brasília Belt, central Brazil–constraints from U–Pb geochronology, mineral rare earth element chemistry and trace-element thermometry, Journal of Metamorphic Geology, vol. 26, no. 2, pp. 213-233.

Baldwin J., Brown M. & Schmitz M. 2007 First application of titanium-in-zircon thermometry to ultrahigh-temperature metamorphism, Geology, vol. 35, no. 4, pp. 295-298.

Bartoli O. 2017 Phase equilibria modelling of residual migmatites and granulites: an evaluation of the melt-reintegration approach, Journal of Metamorphic Geology.

Bea F. 1996 Residence of REE, Y, Th and U in granites and crustal protoliths; implications for the chemistry of crustal melts, Journal of Petrology, vol. 37, pp. 521-552.

Bea F. 2012 The sources of energy for crustal melting and the geochemistry of heat-producing elements, Lithos, vol. 153, no. 0, pp. 278-291.

Bea F. & Montero P. 1999 Behavior of accessory phases and redistribution of Zr, REE, Y, Th and U during metamorphism and partial melting of metapelites in the lower crust: an example from the Kinzigite Formation of Ivrea-Verbano, NW Italy, Geochimica et Cosmochimica Acta, vol. 63, pp. 1133-1153.

Brown M. 2010 The spatial and temporal patterning of the deep crust and implications for the process of melt extraction, Philosophical Transactions of the Royal Society a-Mathematical Physical and Engineering Sciences, vol. 368, no. 1910, pp. 11-51.

Brown M. 2013 Granite: From genesis to emplacement, Geological Society of America Bulletin, vol. 125, no. 7-8, pp. 1079-1113.

Brown M. 2014 The contribution of metamorphic petrology to understanding lithosphere evolution and geodynamics, Geoscience Frontiers, vol. 5, no. 4, pp. 553-569.

Buick I., Storkey A. & Williams I. 2008 Timing relationships between pegmatite emplacement, metamorphism and deformation during the intra-plate Alice Springs Orogeny, central Australia, Journal of Metamorphic Geology, vol. 26, no. 9, pp. 915-936.

Buick I. S., Hermann J., Williams I. S., Gibson R. L. & Rubatto D. 2006 A SHRIMP U–Pb and LA-ICP-MS trace element study of the petrogenesis of garnet–cordierite–orthoamphibole gneisses from the Central Zone of the Limpopo Belt, South Africa, Lithos, vol. 88, no. 1-4, pp. 150-172.

Clark C., Mumm A. S. & Faure K. 2005 Timing and nature of fluid flow and alteration during Mesoproterozoic shear zone formation, Olary Domain, South Australia, Journal of Metamorphic Geology, vol. 23, no. 3, pp. 147-164.

Connolly J. A. 1995 Phase diagram methods for graphitic rocks and application to the system C– O– H– FeO– TiO 2– SiO 2. Contributions to Mineralogy and Petrology

119, 94-116.

Connolly J. A. & Kerrick, D., 1987 An algorithm and computer program for calculating composition phase diagrams. Calphad 11, 1-55.

Connolly J. A. 2017 A primer in gibbs energy minimization for geophysicists. Petrology 25, 526-534.

Fyfe W. S. 1973 A Discussion on the evolution of the Precambrian crust-The granulite facies, partial melting and the Archaean crust, Philosophical Transactions of the Royal Society of London. Series A, Mathematical and Physical Sciences, vol. 273, no. 1235, pp. 457-461.

Gordon S. M., Whitney D. L., Teyssier C. & Fossen H. 2013 U–Pb dates and trace-element geochemistry of zircon from migmatite, Western Gneiss Region, Norway: significance for history of partial melting in continental subduction, Lithos, vol. 170, pp. 35-53.

Grant J. A. 1985 Phase equilibria in partial melting of pelitic rocks. Migmatites. pp. 86-144. Springer.

Green E., White R., Diener J., Powell R., Holland T. & Palin R. 2016 Activity–composition relations for the calculation of partial melting equilibria in metabasic rocks, Journal of Metamorphic Geology, vol. 34, no. 9, pp. 845-869.

Guilmette C., Indares A. & Hébert R. 2011 High-pressure anatectic paragneisses from the Namche Barwa, Eastern Himalayan Syntaxis: Textural evidence for partial melting, phase equilibria modeling and tectonic implications, Lithos, vol. 124, no. 1, pp. 66-81.

Hacker B., Kylander-Clark A. & Holder R. REE Partitioning Between Monazite and Garnet: Implications for Petrochronology, Journal of Metamorphic Geology, vol. 0, no. ja.

Hacker B. R., Kelemen P. B. & Behn M. D. 2011 Differentiation of the continental crust by relamination, Earth and Planetary Science Letters, vol. 307, no. 3, pp. 501-516.

Hallett B. W. & Spear F. S. 2013 The *P–T* history of anatectic pelites of the Northern East Humboldt Range, Nevada: Evidence for tectonic loading, decompression, and anatexis, Journal of Petrology, vol. 55, no. 1, pp. 3-36.

Heier K. & Adams J. 1965 Concentration of radioactive elements in deep crustal material, Geochimica et Cosmochimica Acta, vol. 29, no. 1, pp. 53-61.

Heier K. S. 1965 Metamorphism and the chemical differentiation of the crust, GFF, vol. 87, no. 2, pp. 249-256.

Hermann J. & Rubatto D. 2003 Relating zircon and monazite domains to garnet growth zones: age and duration of granulite facies metamorphism in the Val Malenco lower crust, Journal of Metamorphic Geology, vol. 21, no. 9, pp. 833-852.

Hinchey A. M., Carr S. D. & Rayner N. 2007 Bulk compositional controls on the preservation of age domains within metamorphic monazite: a case study from quartzite and garnet–cordierite–gedrite gneiss of Thor-Odin dome, Monashee complex, Canadian Cordillera, Chemical Geology, vol. 240, no. 1-2, pp. 85-102.

Holland T. & Powell R. 1998 An internally consistent thermodynamic data set for phases of petrological interest, Journal of metamorphic Geology, vol. 16, no. 3, pp. 309-343.

Holland T. & Powell R. 2001 Calculation of phase relations involving haplogranitic melts using an internally consistent thermodynamic dataset, Journal of Petrology, vol. 42, no. 4, pp. 673-683.

Holland T. & Powell R. 2011 An improved and extended internally consistent thermodynamic dataset for phases of petrological interest, involving a new equation of state for solids, Journal of Metamorphic Geology, vol. 29, no. 3, pp. 333-383.

Holland T. J. B. & Powell R. 1985 An internally consistent thermodynamic dataset with un-

certainties and correlations: 2. Data and results, Journal of Metamorphic Geology, vol. 3, no. 4, pp. 343-370.

Holland T. J. B. & Powell R. 1990 An enlarged and updated internally consistent thermodynamic dataset with uncertainties and correlations: the system K2O–Na2O–CaO–MgO–MnO–FeO–Fe2O3–Al2O3–TiO2–SiO2–C–H2–O2, Journal of Metamorphic Geology, vol. 8, no. 1, pp. 89-124.

Horton F., Hacker B., Kylander-Clark A., Holder R. & Jöns N. 2016 Focused radiogenic heating of middle crust caused ultrahigh temperatures in southern Madagascar, Tectonics, vol. 35, no. 2, pp. 293-314.

Indares A., White R. & Powell R. 2008 Phase equilibria modelling of kyanite-bearing anatectic paragneisses from the central Grenville Province, Journal of Metamorphic Geology, vol. 26, no. 8, pp. 815-836.

Janots E., Engi M., Rubatto D., Berger A., Gregory C. & Rahn M. 2009 Metamorphic rates in collisional orogeny from in situ allanite and monazite dating, Geology, vol. 37, no. 1, pp. 11-14.

Jaupart C., Mareschal J.-C. & Iarotsky L. 2016 Radiogenic heat production in the continental crust, Lithos, vol. 262, no. Supplement C, pp. 398-427.

Jiang Y., Schulmann K., Sun M., Štípská P., Guy A., Janoušek V., Lexa O. & Yuan C. 2016 Anatexis of accretionary wedge, Pacific-type magmatism, and formation of vertically stratified continental crust in the Altai Orogenic Belt, Tectonics, vol. 35, no. 12, pp. 3095-3118.

Johnson T. E., Brown M., Gardiner N. J., Kirkland C. L. & Smithies R. H. 2017 Earth's first stable continents did not form by subduction, Nature, vol. 543, no. 7644, p. 239.

Johnson T. E., Clark C., Taylor R. J. M., Santosh M. & Collins A. S. 2015 Prograde and retrograde growth of monazite in migmatites: An example from the Nagercoil Block, southern India, Geoscience Frontiers, vol. 6, no. 3, pp. 373-387.

Kelsey D. & Powell R. 2011 Progress in linking accessory mineral growth and breakdown to major mineral evolution in metamorphic rocks: a thermodynamic approach in the Na2O-CaO-K2O-FeO-MgO-Al2O3-SiO2-H2O-TiO2-ZrO2 system, Journal of Metamorphic Geology, vol. 29, no. 1, pp. 151-166.

Kelsey D. E., Clark C. & Hand M. 2008 Thermobarometric modeling of zircon and monazite growth in melt-bearing systems: examples using model metapelitic and metapsammitic granulites, Journal of Metamophic Geology, vol. 26, pp. 199-212.

Kohn M. J., Corrie S. L. & Markley C. 2015 The fall and rise of metamorphic zircon, American Mineralogist, vol. 100, no. 4, pp. 897-908.

Korhonen F., Brown M., Clark C. & Bhattacharya S. 2013 Osumilite–melt interactions in ultrahigh temperature granulites: phase equilibria modelling and implications for the *P*–*T*–t evolution of the Eastern Ghats Province, India, Journal of Metamorphic Geology, vol. 31, no. 8, pp. 881-907.

Kumar P. S. & Reddy G. 2004 Radioelements and heat production of an exposed Archaean crustal cross-section, Dharwar craton, south India, Earth and Planetary Science Letters, vol. 224, no. 3, pp. 309-324.

Laporte D., Rapaille C. & Provost A. 1997 Wetting Angles, Equilibrium Melt Geometry, and the Permeability Threshold of Partially Molten Crustal Protoliths. In BOUCHEZ J. L., HUTTON D. H. W. & STEPHENS W. E. eds. Granite: From Segregation of Melt to Emplacement Fabrics. pp. 31-54. Dordrecht: Springer Netherlands.

Machado N., Goulet N. & Gariépy C. 1989 U–Pb geochronology of reactivated Archean basement and of Hudsonian metamorphism in the northern Labrador Trough, Canadian Journal of Earth Sciences, vol. 26, no. 1, pp. 1-15.

Mclaren S. & Powell R. 2014 Magmatism, orogeny and the origin of high-heat-producing

granites in Australian Proterozoic terranes, Journal of the Geological Society, vol. 171, no. 2, pp. 149-152.

Mclaren S., Sandiford M. & Hand M. 1999 High radiogenic heat–producing granites and metamorphism—An example from the western Mount Isa inlier, Australia, Geology, vol. 27, no. 8, pp. 679-682.

Morrissey L. J., Hand M., Kelsey D. E. & Wade B. P. 2016 Cambrian High-temperature Reworking of the Rayner–Eastern Ghats Terrane: Constraints from the Northern Prince Charles Mountains Region, East Antarctica, Journal of Petrology, vol. 57, no. 1, pp. 53-92.

Morrissey L. J., Hand M., Raimondo T. & Kelsey D. E. 2014 Long-lived high-T, low-P granulite facies metamorphism in the Arunta Region, central Australia, Journal of Metamorphic Geology, vol. 32, no. 1, pp. 25-47.

Palin R. M., White R. W., Green E. C., Diener J. F., Powell R. & Holland T. J. 2016 High-grade metamorphism and partial melting of basic and intermediate rocks, Journal of Metamorphic Geology, vol. 34, no. 9, pp. 871-892.

Parrish R. R. 1990 U–Pb dating of monazite and its application to geological problems, Canadian Journal of Earth Sciences, vol. 27, no. 11, pp. 1431-1450.

Pattison D., Spear F., Debuhr C., Cheney J. & Guidotti C. 2002 Thermodynamic modelling of the reaction muscovite+ cordierite→ Al2SiO5+ biotite+ quartz+ H2O: constraints from natural assemblages and implications for the metapelitic petrogenetic grid, Journal of Metamorphic Geology, vol. 20, no. 1, pp. 99-118.

Phillips G. N. 1981 Water activity changes across an amphibolite-granulite facies transition, Broken Hill, Australia, Contributions to Mineralogy and Petrology, vol. 75, no. 4, pp. 377-386.

Powell R. 1983 Processes in granulite-facies metamorphism, Migmatites, melting and metamorphism, pp. 127-139.

Powell R. & Holland T. 1985 An internally consistent thermodynamic dataset with uncertainties and correlations: 1. Methods and a worked example, Journal of Metamorphic Geology, vol. 3, no. 4, pp. 327-342.

Powell R. & Holland T. 1988 An internally consistent thermodynamic dataset with uncertainties and correlations: 3. Applications to geobarometry, worked examples and a computer program, J. Metamorphic Geol., vol. 6, pp. 173-204.

Powell R. & Holland T. 2008 On thermobarometry, Journal of Metamorphic Geology, vol. 26, no. 2, pp. 155-179.

Powell R., White R., Green E., Holland T. & Diener J. 2014 On parameterizing thermodynamic descriptions of minerals for petrological calculations, Journal of Metamorphic Geology, vol. 32, no. 3, pp. 245-260.

Pyle J. M. & Spear F. S. 2003 Four generations of accessory-phase growth in low-pressure migmatites from SW New Hampshire, American Mineralogist, vol. 88, no. 2-3, pp. 338-351.

Rosenberg C. L. & Handy M. R. 2005 Experimental deformation of partially melted granite revisited: implications for the continental crust, Journal of Metamorphic Geology, vol. 23, no. 1, pp. 19-28.

Rubatto D. 2002 Zircon trace element geochemistry: partitioning with garnet and the link between U–Pb ages and metamorphism, Chemical Geology, vol. 184, no. 1, pp. 123-138.

Rubatto D., Chakraborty S. & Dasgupta S. 2013 Timescales of crustal melting in the Higher Himalayan Crystallines (Sikkim, Eastern Himalaya) inferred from trace element-constrained monazite and zircon chronology, Contributions to Mineralogy and Petrology, vol. 165, no. 2, pp. 349-372.

Rubatto D. & Hermann J. 2003 Zircon formation during fluid circulation in eclogites (Monviso, Western Alps): implications for Zr and Hf budget in subduction zones, Ge-

ochimica et Cosmochimica Acta, vol. 67, no. 12, pp. 2173-2187.

Rubatto D. & Hermann J. 2007 Experimental zircon/melt and zircon/garnet trace element partitioning and implications for the geochronology of crustal rocks, Chemical Geology, vol. 241, no. 1-2, pp. 38-61.

Rubatto D., Hermann J. & Buick I. S. 2006 Temperature and bulk composition control on the growth of monazite and zircon during low-pressure anatexis (Mount Stafford, central Australia), Journal of Petrology, vol. 47, no. 10, pp. 1973-1996.

Rubatto D., MüNtener O., Barnhoorn A. & Gregory C. 2008 Dissolution-reprecipitation of zircon at low-temperature, high-pressure conditions (Lanzo Massif, Italy), American Mineralogist, vol. 93, no. 10, pp. 1519-1529.

Rubatto D., Williams I. S. & Buick I. S. 2001 Zircon and monazite response to prograde metamorphism in the Reynolds Range, central Australia, Contributions to Mineralogy and Petrology, vol. 140, no. 4, pp. 458-468.

Sandiford M., Hand M. & Mclaren S. 1998 High geothermal gradient metamorphism during thermal subsidence, Earth and Planetary Science Letters, vol. 163, no. 1–4, pp. 149-165.

Schorn S. & Diener J. F. A. 2019 Seemingly disparate temperatures recorded in coexisting granulite facies lithologies, Journal of Metamorphic Geology, vol. 0, no. ja.

Smithies R., Howard H., Evins P., Kirkland C., Kelsey D., Hand M., Wingate M., Collins A. & Belousova E. 2011 High-temperature granite magmatism, crust–mantle interaction and the Mesoproterozoic intracontinental evolution of the Musgrave Province, Central Australia, Journal of Petrology, vol. 52, no. 5, pp. 931-958.

Stepanov A. S., Hermann J., Rubatto D. & Rapp R. P. 2012 Experimental study of monazite/melt partitioning with implications for the REE, Th and U geochemistry of crustal rocks, Chemical Geology, vol. 300, pp. 200-220.

Tang L., Santosh M., Tsunogae T., Koizumi T., Hu X. K. & Teng X. M. 2017 Petrology, phase equilibria modelling and zircon U–Pb geochronology of Paleoproterozoic mafic granulites from the Fuping Complex, North China Craton, Journal of Metamorphic Geology, vol. 35, no. 5, pp. 517-540.

Thompson A. B. 1982 Dehydration melting of pelitic rocks and the generation of H 2 O-undersaturated granitic liquids, American Journal of Science, vol. 282, no. 10, pp. 1567-1595.

Tomkins H. & Pattison D. 2007 Accessory phase petrogenesis in relation to major phase assemblages in pelites from the Nelson contact aureole, southern British Columbia, Journal of Metamorphic Geology, vol. 25, no. 4, pp. 401-421.

Tracy R. & Robinson P. 1983 Acadian migmatite types in pelitic rocks of central Massachusetts, Migmatites, melting and metamorphism, pp. 163-173.

Viete D. R., Hermann J., Lister G. S. & Stenhouse I. R. 2011 The nature and origin of the Barrovian metamorphism, Scotland: diffusion length scales in garnet and inferred thermal time scales, Journal of the Geological Society, vol. 168, no. 1, pp. 115-132.

Vilà M., Fernández M. & Jiménez-Munt I. 2010 Radiogenic heat production variability of some common lithological groups and its significance to lithospheric thermal modeling, Tectonophysics, vol. 490, no. 3, pp. 152-164.

Vry J. K. & Baker J. A. 2006 LA-MC-ICPMS Pb–Pb dating of rutile from slowly cooled granulites: Confirmation of the high closure temperature for Pb diffusion in rutile, Geochimica Et Cosmochimica Acta, vol. 70, no. 7, pp. 1807-1820.

Waters D. & Whales C. 1984 Dehydration melting and the granulite transition in metapelites from southern Namaqualand, S. Africa, Contributions to Mineralogy and

Petrology, vol. 88, no. 3, pp. 269-275.
Waters D. J. 1988 Partial melting and the formation of granulite facies assemblages in Namaqualand, South Africa, Journal of Metamorphic Geology, vol. 6, no. 4, pp. 387-404.
Watson E. B. 1996 Dissolution, growth and survival of zircons during crustal fusion: kinetic principals, geological models and implications for isotopic inheritance, Earth and Environmental Science Transactions of the Royal Society of Edinburgh, vol. 87, no. 1-2, pp. 43-56.
White R., Powell R. & Halpin J. 2004 Spatially-focussed melt formation in aluminous metapelites from Broken Hill, Australia, Journal of Metamorphic Geology, vol. 22, no. 9, pp. 825-845.
White R., Powell R. & Holland T. 2007 Progress relating to calculation of partial melting equilibria for metapelites, Journal of metamorphic Geology, vol. 25, no. 5, pp. 511-527.
White R., Powell R., Holland T., Johnson T. & Green E. 2014 New mineral activity–composition relations for thermodynamic calculations in metapelitic systems, Journal of Metamorphic Geology, vol. 32, no. 3, pp. 261-286.
Williams I. 2001 Response of detrital zircon and monazite, and their U–Pb isotopic systems, to regional metamorphism and host-rock partial melting, Cooma Complex, southeastern Australia, Australian Journal of Earth Sciences, vol. 48, no. 4, pp. 557-580.
Williams I., Buick I. & Cartwright I. 1996 An extended episode of early Mesoproterozoic metamorphic fluid flow in the Reynolds Range, central Australia, Journal of Metamorphic Geology, vol. 14, no. 1, pp. 29-47.
Yakymchuk C. & Brown M. 2014a Behaviour of zircon and monazite during crustal melting, Journal of the Geological Society, vol. 171, no. 4, pp. 465-479.
Yakymchuk C. & Brown M. 2014b Consequences of open-system melting in tectonics, Journal of the Geological Society, vol. 171, no. 1, pp. 21-40.
Yakymchuk C., Clark C. & White R. W. 2017 Phase relations, reaction sequences and petrochronology, Reviews in Mineralogy and Geochemistry, vol. 83, no. 1, pp. 13-53.
Zeh A., Williams I. S., Brätz H. & Millar I. L. 2003 Different age response of zircon and monazite during the tectono-metamorphic evolution of a high grade paragneiss from the Ruhla Crystalline Complex, central Germany, Contributions to Mineralogy and Petrology, vol. 145, no. 6, pp. 691-706.
Zhang Z., Xiang H., Dong X., Li W., Ding H., Gou Z. & Tian Z. 2017 Oligocene HP metamorphism and anatexis of the Higher Himalayan Crystalline Sequence in Yadong region, east-central Himalaya, Gondwana Research, vol. 41, pp. 173-187.
Zou Y., Zhai M., Santosh M., Zhou L., Zhao L., Lu J. & Shan H. 2017 High-pressure pelitic granulites from the Jiao-Liao-Ji Belt, North China Craton: A complete PT path and its tectonic implications, Journal of Asian Earth Sciences, vol. 134, pp. 103-121.

CHAPTER 2

This chapter is published in *Geosciences* as:
Alessio K., Hand M., Morrissey L., Kelsey D. & Payne J. 2017 Melt Reintegration Modelling: Testing against a Subsolidus Reference Assemblage, Geosciences, vol. 7, no. 3, p. 75.

Statement of Authorship

Title of Paper	Melt Reintegration Modelling: Testing against a Subsolidus Reference Assemblage
Publication Status	☑ Published ☐ Accepted for Publication ☐ Submitted for Publication ☐ Unpublished and Unsubmitted w ork w ritten in manuscript style
Publication Details	Alessio, K., Hand, M., Morrissey, L., Kelsey, D., Payne, J., 2017. Melt Reintegration Modelling: Testing against a Subsolidus Reference Assemblage. Geosciences 7, 75.

Principal Author

Name of Principal Author (Candidate)	Kiara Alessio		
Contribution to the Paper	Fieldwork Data collection and modelling Manuscript writing		
Overall percentage (%)	70		
Certification:	This paper reports on original research I conducted during the period of my Higher Degree by Research candidature and is not subject to any obligations or contractual agreements with a third party that would constrain its inclusion in this thesis. I am the primary author of this paper.		
Signature		Date	30/07/2019

Co-Author Contributions

By signing the Statement of Authorship, each author certifies that:

i. the candidate's stated contribution to the publication is accurate (as detailed above);

ii. permission is granted for the candidate in include the publication in the thesis; and

iii. the sum of all co-author contributions is equal to 100% less the candidate's stated contribution.

Name of Co-Author	Martin Hand		
Contribution to the Paper	Manuscript editing Ideas for manuscript Fieldwork		
Signature		Date	30/07/2019

Name of Co-Author	Laura Morrissey		
Contribution to the Paper	Manuscript editing Ideas for manuscript Data modelling		
Signature		Date	30/07/2019

Name of Co-Author	David Kelsey		
Contribution to the Paper	Manuscript editing Data modelling Fieldwork		
Signature		Date	25/07/2019

Name of Co-Author	Justin Payne		
Contribution to the Paper	Manuscript editing Ideas for manuscript Fieldwork		
Signature		Date	26/07/2019

ABSTRACT

Phase equilibria modelling incorporating melt reintegration offers an inverse methodology to create hypothetical rock compositions that may have existed prior to melt loss, allowing the potential prograde evolution of rocks to be explored. However, melt reintegration modelling relies on assumptions concerning the volume of melt that was lost and is generally restricted by the absence of direct constraints on the pre-anatectic mineral assemblages. Mg-rich granulite in the 514–490 Ma Delamerian Orogen in southern Australia contains spinel–cordierite symplectic intergrowths that surround rare, coarse blocky domains of sillimanite. These sillimanite cores, as well as the widespread presence of andalusite in lower grade areas of the southern Delamerian Orogen, suggest the subsolidus precursor to the granulite contained andalusite. This provides the opportunity to test if melt reintegration modelling of the granulite predicts subsolidus andalusite. Stepwise down-temperature melt reintegration modelling produces a water-saturated solidus after the addition of 12 mol% melt. When modelled at subsolidus conditions, the resulting rock composition produces andalusite-bearing assemblages with andalusite modes similar to the abundance of the sillimanite-cored spinel–cordierite intergrowths. The modelling results from this case study suggest that melt reintegration modelling is a valid method to recreate prograde subsolidus bulk rock compositions.

INTRODUCTION

Melting and melt loss during granulite facies metamorphism is a fundamental process that differentiates the continental crust and causes chemical depletion in the residual material [1-3]. Advances in thermodynamic modelling of mineral assemblages have enabled quantitative phase equilibria modelling of the melting processes operating in partially molten siliciclastic rocks in increasingly complex chemical systems [4-11]. These models have been used to investigate the effects of melting and melt loss on crustal rheology, composition and the preservation of geochronometers [e.g. 1,5,12-15]. However, the application of these models has been limited to theoretical situations, as in almost all real cases there is little information about the composition of the rock prior to melting [cf. 11]. This lack of information about the likely protolith composition also means that it is essentially impossible to determine the prograde *pressure–temperature* (*P–T*) evolution of a granulite facies rock, because the composition of the rock in which prograde minerals developed has been irrevocably modified [16]. For this reason, quantitative petrological interpretation of mineral inclusions captured within prograde minerals is difficult and often impossible. In trying to reconstruct potential prograde bulk compositions, metamorphic petrologists approach the problem via melt reintegration modelling, in which theoretical compositions of melt are integrated into a rock composition in order to create a hypothetical 'protolith' bulk composition. A recent study by Bartoli [17] has shown that a number of methods of melt reintegration modelling, including the stepwise method used here, are able to produce plausible subsolidus bulk rock compositions. However, significant underestimations of melt productivity may still occur, as exact protolith compositions are unknown in most cases. While useful, this process relies on assumptions regarding the prograde metamorphic path and volume of melt that has been lost and is commonly done up to a point at which a water-saturated solidus is achieved [18,19]. The determination of a final composition is unconstrained, as the prograde compositions often no longer exist for comparison, except in some rare cases [e.g. 20,21]. However, one way to assess the viability of melt reintegration modelling as a means of determining a reasonable prograde rock composition is to choose a granulite facies sample where the prograde subsolidus mineralogy is relatively well constrained.

The aim of this study is to use melt reintegration to reproduce the original bulk composition of a residual granulite facies rock from the Delamerian Orogen in southern Australia. The existence of andalusite in the subsolidus assemblage provides a test to see whether melt reintegration *P–T* modelling of the reintegrated bulk composition stabilises the observed modal abundance of subsolidus andalusite, giving some constraints on the validity of model-generated subsolidus bulk compositions.

GEOLOGICAL SETTING

The footprint of the 514–490 Ma Delamerian Orogeny has a north-south extent from the Peake and Denison Inliers in the far north of South Australia, to the western tip of Kangaroo Island in the south (Figure 1). It extends to the east into western New South Wales, Victoria and Tasmania. The Antarctic continuation of the orogen is the Ross Orogen [22,23], which formed along the same paleo-continental margin but largely predates the Delamerian Orogeny. In South Australia, Victoria, western New South Wales and Tasmania, the Delamerian Orogen is primarily composed of Late Neoproterozoic and Early Cambrian sedimentary rocks that were deposited in a passive margin setting. In South Australia, the Early Cambrian sequences comprise the basal Normanville and overlying Kanmantoo Groups that were deposited in the Stansbury Basin [24-26].

The early compressional stages of the Delamerian Orogeny involved west-vergent thrusting (D1) and the development of a low-angle fabric (S1), which was overprinted by

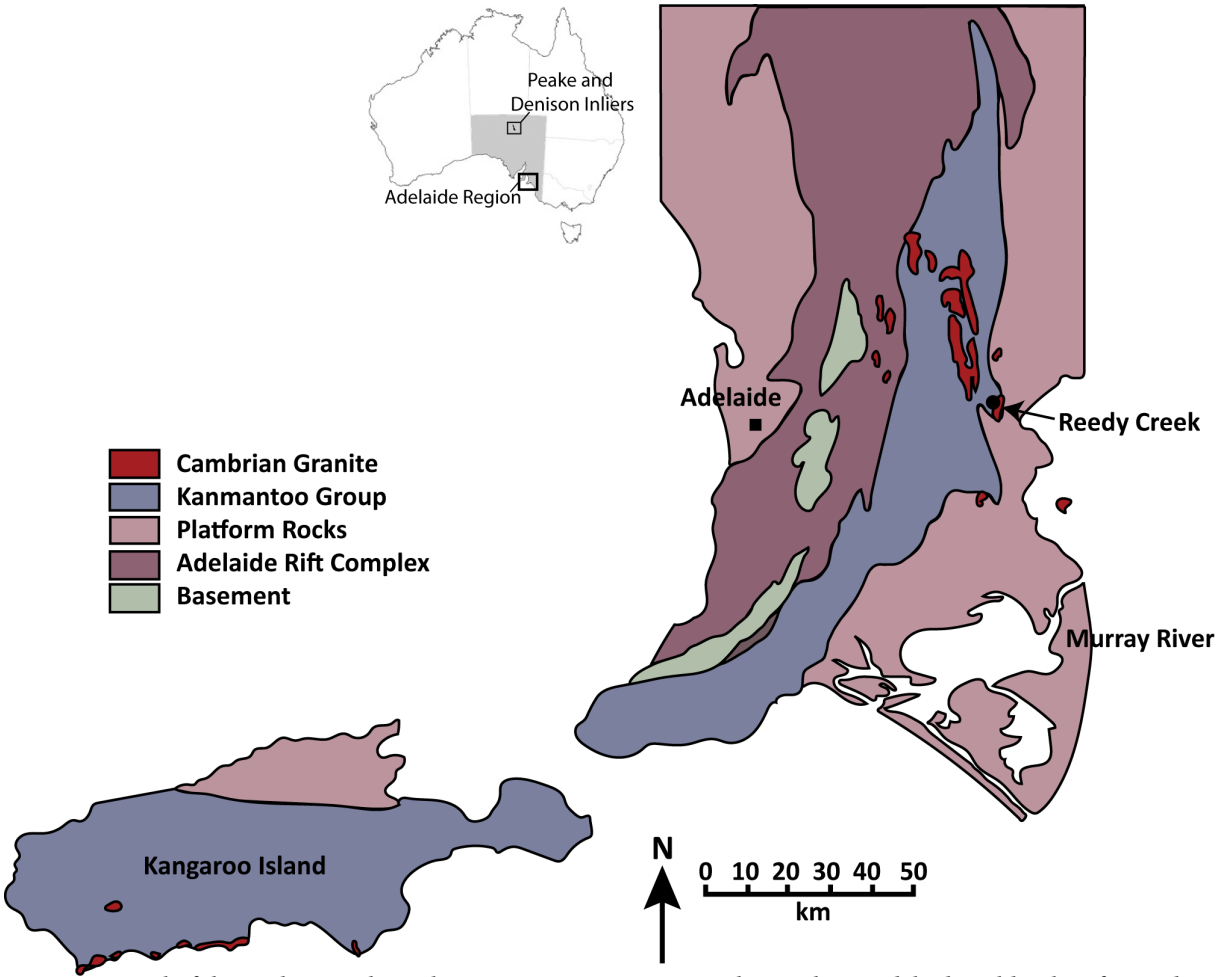


Figure 1. Detail of the geology in the Delamerian Orogen as seen in the southern Adelaide Fold Belt. After Foden, et al. [27].

two phases of tight to open upright folds during D2 and D3 [28-30]. The early stages of the event were synchronous with granitic magmatism throughout the region, with the earliest syntectonic granite intruded during the onset of orogenic crustal shortening at 514 ± 4 Ma [31]. Increasingly mantle-derived magmatism marked the end of the orogenic event (c. 490 Ma) and continued into the Early Ordovician [32-34]. Following the Delamerian Orogeny, an extensional setting was re-established and post-orogenic magmatism resulted in the intrusion of rhyolite and diorite dikes [27]. Within the Kanmantoo Group, Delamerian-aged metamorphism is characterised by mostly amphibolite facies low-pressure–high-temperature metamorphism resulting in the formation of andalusite- to sillimanite-bearing assemblages in aluminous rocks [31,35]. Metamorphic grade increases in proximity to the late-tectonic granitic intrusives, culminating in extensive partial melting [27,36,37].

The Kanmantoo Group metasedimentary rocks at Reedy Creek consist primarily of extensively migmatised metapsammitic lithologies interlayered with thin discontinuous layers of metapelite. The hosting metapsammitic lithologies are primarily composed of quartz–plagioclase–cordierite–biotite±sillimanite. The sequence contains a pervasive biotite-bearing foliation that is parallel to and cross-cut by migmatitic segregations. Abundant partial melting has resulted in the segregation of leucosome and melanosome. Thin leucosomes (<2 cm wide) have been folded with the original foliation, suggesting that some melting occurred in the early stages of the Delamerian Orogeny. However, some leucosomes are only slightly deformed and others cross-cut the original foliation, suggesting that melting continued throughout the whole event. The migmatitic rocks were intruded by the Reedy Creek Granodiorite and associated diorites at 492.6 ± 1.1 Ma [27]. The granodiorite is weakly foliated parallel to the fabric in the migmatitic metasediments. Within the metasediments, decimetre-scale bodies of diorite have been converted to hornblende-bearing migmatites that contain K–feldspar-bearing melts.

Although the bulk of the metasedimentary sequence consists of metapsammitic lithologies with thermodynamically insensitive bulk compositions, thin discontinuous layers of cordierite-dominated Mg-rich (MgO/(MgO+FeO) = 0.66) metapelite—that were likely to have been mud layers in the original sequence—form sensitive mineral assemblages that can be used to investigate the *P–T* evolution of the sequence. The discontinuous metapelite layers contain domains that are dominantly composed of orthopyroxene–biotite–cordierite–plagioclase (Figure 2a, b). Locally these domains contain cordierite–spinel symplectites that rarely surround coarse/blocky aggregates of sillimanite (Figure 2c). In adjacent psammitic layers cordierite occurs as porphyroblasts within felsic segregations and veins. We interpret the orthopyroxene and cordierite-bearing metapelitic layers to represent residual domains that have lost melt. These layers do not contain assemblages or chemistry typical of granitic compositions that would form leucosomes, due to their high Mg content and abundant orthopyroxene and cordierite. The peritectic mineral assemblages preserved in these layers are very fresh and relatively unretrogressed, indicating that melt has been drained from these layers [38]. Blocky, porphyroblastic aggregates of sillimanite surrounded by cordierite–spinel symplectites (up to 3 cm by 1 cm) (Figure 2c) in the pelite layers are interpreted to reflect the former presence of andalusite, based on the extensive presence of andalusite in lower grade areas of the Kanmantoo Group (Figure 2d) [29,30,39]. Therefore, we infer the prograde sequence to have contained andalusite. Despite the intensity of the deformation, there is no evidence for distributed sillimanite within the foliation, suggesting that the proportion of blocky silli-

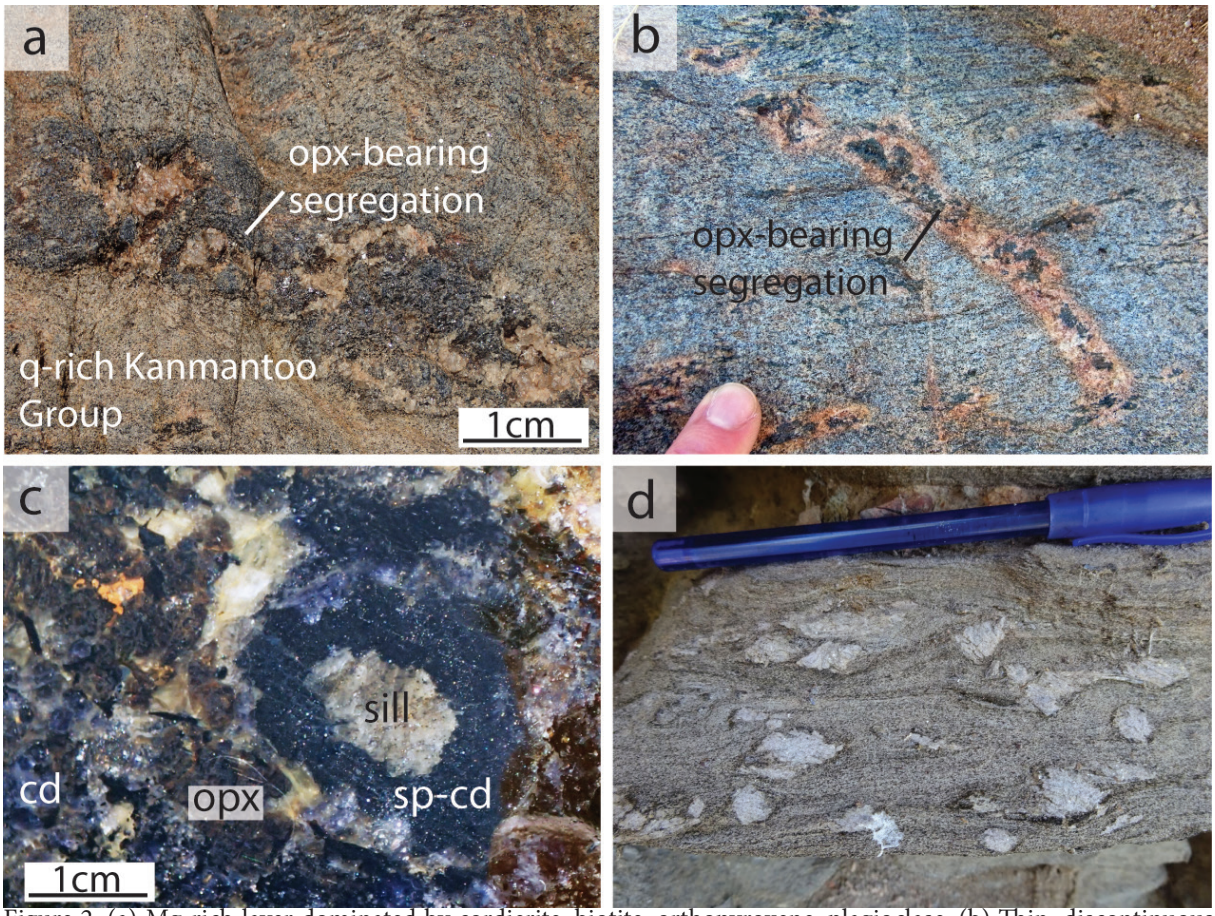


Figure 2. (a) Mg-rich layer dominated by cordierite–biotite–orthopyroxene–plagioclase. (b) Thin, discontinuous orthopyroxene-bearing domain. (c) Rock sample of the thin layer that was sampled showing cordierite-spinel symplectites, amongst orthopyroxene and plagioclase. (d) Andalusite porphyroblasts enclosed within metapelite from a lower grade area of the Delamerian (54K 0316690 E, 6122806 S, datum WGS84).

manite aggregates represents the approximate proportion of andalusite in the protolith. Layers containing these sillimanite aggregates are relatively rare in the Kanmantoo Group sequence, but in the cordierite-dominated Mg-rich layers they comprise around 5% of the current rock volume.

Samples and Petrography

The sample used in this study (sample 14-RDC-04) was taken from a thin metapelitic layer (>10 cm in width), within thick metapsammitic layers in Reedy Creek (Figure 1, 2a, b). Sample 14-RDC-04 contains orthopyroxene, biotite, cordierite, spinel, plagioclase, magnetite, ilmenite and minor sillimanite. Coarse-grained (1–6 mm) euhedral grains of orthopyroxene are common throughout the leucosomes and contain inclusions of biotite, ilmenite and magnetite. Coarse-grained, poikiloblastic cordierite (1–6 mm) contains inclusions of biotite, plagioclase, magnetite and ilmenite. Symplectites of spinel and cordierite (in patches 4–10 mm in diameter) are common (Figure 3a). In rare instances these cordierite–spinel symplectites surround aggregates of sillimanite grains (3–6 mm; Figure 3b and c). Orthopyroxene grains occur in direct contact with biotite and are surrounded by cordierite and plagioclase (Figure 3d). There are two morphologies of biotite. Some biotite grains are aligned and define a weak foliation, whereas other biotite is randomly oriented. Biotite adjacent to cordierite occurs as ragged anhedral grains. No biotite is present in the areas immediately adjacent to the cordierite–spinel symplectites (Figure 3a and c). Cordierite¬–spinel symplectites and sillimanite grains do not show any orientation and no foliation is observed in the biotite-absent regions. We

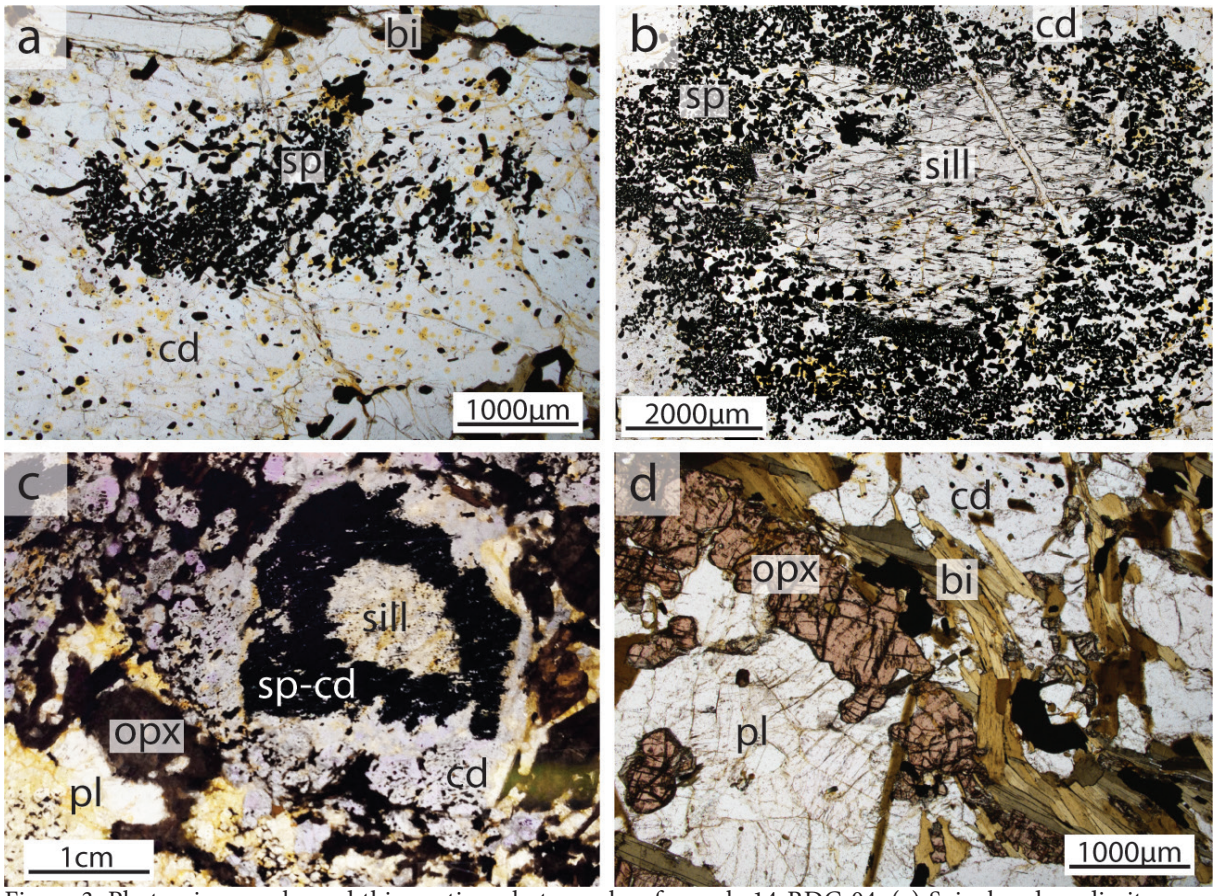


Figure 3. Photomicrographs and thin section photographs of sample 14-RDC-04. (a) Spinel and cordierite symplectites. (b) Relict sillimanite grain, showing typical crosshatching andalusite replacement texture, surrounded by symplectic corona of spinel and cordierite. (c) Relict sillimanite surrounded by a cordierite-spinel corona. (d) Anhedral orthopyroxene grains adjacent to semi-oriented biotite. Biotite becomes unoriented and has an anhedral shape when in contact with cordierite.

interpret the peak assemblage present in this sample to be plagioclase + biotite + orthopyroxene + cordierite + spinel + magnetite + ilmenite. The rare, coarse-grained domains of sillimanite enclosed within spinel–cordierite symplectites are interpreted to be textural relics from replacement of prograde andalusite. Although sillimanite and orthopyroxene are in close proximity (Figure 3d) we do not interpret them to represent former stable coexistence.

MATERIALS AND METHODS

The pelitic orthopyroxene-bearing domains that make up sample 14-RDC-04 are thin and irregularly shaped, meaning that rock slabs cut for whole rock geochemistry contain a mixture of residual pelite and the surrounding wall rock, and thus may not provide a valid composition for the purposes of phase equilibria modelling. Instead, a chemical composition of the orthopyroxene-bearing domains was determined by combining average measured mineral chemistry and density with estimates of mineral proportions in these domains. In the domain used for the determination of mineral modal abundances, sillimanite is almost completely replaced by blocky aggregates of cordierite–spinel, so was not considered as part of the composition. Estimations of the proportions of minerals present in the sample were determined by pixel counting minerals in thin section images using Adobe Photoshop. The area of thin section used for pixel counting was quite large, at approximately 7.5 x 3.5 cm. As the domains that were sampled were quite thin, we believe that this 2D area is representative of the equilibrium volume. The use of individual mineral chemistry to determine a

bulk composition is a relatively common practice [e.g. 40,41]; however, it should be noted that this method may produce different results than compositions acquired using XRF [see 42]. Mineral chemical analyses were obtained using a Cameca SXFive electron microprobe at Adelaide Microscopy, with standard operating procedures. The mineral modes and average mineral chemical analyses and densities used for the determination of the residual pelite composition are provided in Table 1.

One of the uncertainties of pseudosection modelling is determining the bulk composition that relates to the formation of the peak metamorphic mineral assemblage, particularly the amount of H_2O and Fe_2O_3. *P–MO*, *P–*M_{H_2O} and *T–*M_{H_2O} sections (where the oxidation state (MO) or amount of water (M_{H_2O}) is varied as a function of pressure (P) or temperature (T); Appendix 2B) were calculated to assess the sensitivity of the compositions of the sample to changing H_2O content and oxidation state (O), and determine appropriate values for the domain composition. The P–MO and P–M_{H_2O} sections were drawn at a constant temperature of 750 °C, which was chosen based on a first pass estimate of the likely metamorphic conditions of the suprasolidus assemblage and the assumed sensitivity of the assemblage to pressure. A T–M_{H_2O} section was modelled after the P–M_{H_2O} to better assess the H_2O content of the sample due to the greater sensitivity of H_2O-dependent equilibria to temperature. The T–M_{H_2O} section was calculated at a fixed pressure of 4.2 kbar, which was chosen based on the pressure of the peak field on the P–MO and P–M_{H_2O} sections. Maximum H_2O values used on the x-axis of P–M_{H_2O} and T–M_{H_2O} sections were chosen to be 1.5 wt%. Compositions chosen along the x–axis from the peak fields of *P–X* and *T–X* diagrams for *P–T* modelling

Table 1. Mineral modal proportions and average mineral chemistry used to obtain a chemical composition of the orthopyroxene-bearing domains for the purposes of phase equilibria modelling. Individual mineral analyses can be found in Appendix 1A.

	Bi	**Cd**	**Opx**	**Sp**	**Pl**	**Total**	
Mode (wt%)	9.93	34.59	21.41	6.41	27.67	100	
Mineral Density (kg/m^3)	2.9	2.6	3.5	4.1	2.6		
wt%	**Bi**	**Cd**	**Opx**	**Sp**	**Pl**	**Ave comp**	**Final comp**
SiO_2	37.99	49.39	52.65	0.09	68.77	51.16	**50.61**
TiO_2	3.48	0	0.09	0.01	0	0.37	**0.37**
Al_2O_3	15.17	33.06	2.22	58.04	19.68	22.58	**22.34**
Cr_2O_3	0.1	0	0.04	0.04	0	0.02	**0.02**
FeO	14.36	5.06	24.2	33.72	0	10.52	**10.41**
MnO	0.02	0.05	0.24	0.12	0	0.08	**0.08**
MgO	15.89	11.14	21.71	7.89	0	10.58	**10.47**
ZnO	0.01	0.01	0.02	0.13	0	0.02	**0.02**
CaO	0	0	0.02	0.01	1.5	0.42	**0.42**
Na_2O	0.08	0	0	0	10.04	2.79	**2.76**
K_2O	8.68	0	0.03	0	0	0.86	**0.85**
Cl	0.49	0.16	0	0	0	0.11	**0.11**
F	0.02	0	0	0	0	0	**0.00**
Total	**96.29**	**98.87**	**101.22**	**100.05**	**99.99**	**101.08**	**100**

were selected based on modal proportions of minerals that best suited the estimated modes. Further information on the methods for the selection of compositions from these diagrams can be found in Appendix 2B.

Phase equilibria models were calculated for sample 14-RDC-04 using THERMOCALC 3.40 [43,44] in the chemical system MnO–Na_2O–CaO–K_2O–FeO–MgO–Al_2O_3–SiO_2–H_2O–TiO_2–O (MnNCKFMASHTO), where 'O' is a proxy for Fe_2O3, using the internally-consistent thermodynamic dataset ds62' [43] and activity–composition models reparametrised for Mn [8-10]. Completed pseudosections were contoured for the modal proportions of minerals using TCInvestigator [45]. The chemical composition of the discontinuous orthopyroxene-bearing pelitic layers (sample 14-RDC-04, see Figure 4) was used to constrain the peak metamorphic conditions at Reedy Creek.

Melt reintegration was undertaken after calculation of the *P–T* pseudosection using the original residual composition (Figure 4a) as a starting point, following the method of Korhonen, Brown, Clark and Bhattacharya [18]. This stepwise melt reintegration method is now well-established and has been used to remove melt or to rebuild protolith compositions in numerous studies [e.g. 11,12,17,18,46]. This method adds 6 mol% melt to the system when the modal proportion of melt in the initial

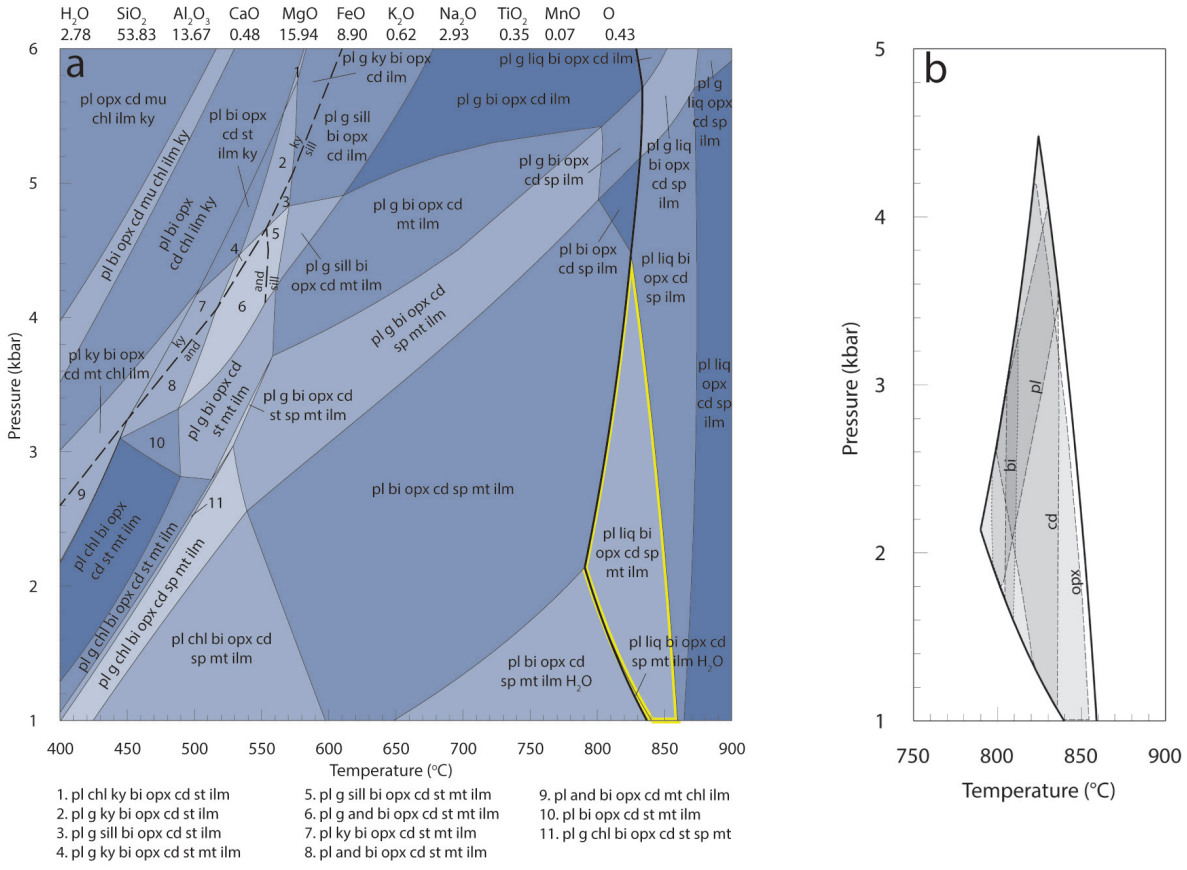


Figure 4. (a) Calculated *P–T* pseudosection using the composition of the residual orthopyroxene-bearing domain. The bulk composition (in mol%) is given above the pseudosection. The bold black line represents the solidus and the field outlined in yellow is the interpreted peak assemblage. (b) Overlay of modal contours on the peak field of Figure 4a. To avoid making the diagram overly complex, only the most abundant phases were included on the overlay. The contours of each mineral on the peak field of the *P–T* section represent the modal abundances of the major phases in sample 14-RDC-04, including plagioclase, biotite, orthopyroxene and cordierite. Primary overlap of phases occurs between 2–4 kbar in the peak field. Individual modal proportion plots for each mineral can be found in Appendix 1C.

composition reaches 1 mol%, equivalent to the 7% melt connectivity transition (MCT) of Rosenberg and Handy (2005). This 7% threshold is interpreted as the point at which there is enough melt present in the rock to create a connected grain boundary network, resulting in the rapid decrease of rock strength and likely melt loss [47]. The composition of the melt that is reintegrated back into the rock corresponds to the composition of the 1% melt contour, which is interpreted to be the amount of melt remaining on grain boundaries after a melt loss event. The resulting composition is then normalised and can be used to calculate further *P–T* pseudosections until the composition produces a wet solidus. It is assumed that as a rock crosses the solidus any remaining free H2O will be immediately used up during production of the first vestiges of melt. Therefore, melt reintegration modelling aims to reintegrate melt until the solidus is just H2O-saturated, to model the point at which a subsolidus composition would begin to melt. The *P–T* path during the Delamerian Orogeny is not well constrained. Therefore, for the purpose of simplifying melt reintegration modelling, an isobaric heating path of 3.5 kbar was assumed, based on the peak pressures inferred from the *P–T* pseudosection, the presence of andalusite pseudomorphs in the Reedy Creek area and the metamorphic pressures that are recorded elsewhere in the Delamerian Orogen [e.g. 35,48,49].

RESULTS

Peak P–T conditions

The peak assemblage in sample 14-RDC-04 of plagioclase + biotite + orthopyroxene + cordierite + spinel + magnetite + ilmenite occurs at conditions of 1.0–4.4 kbar and 790–860 °C (Figure 4a). Mineral abundance contouring of this pseudosection indicates that peak *P–T* conditions would have likely occurred between 2–4 kbar, where the modelled mineral

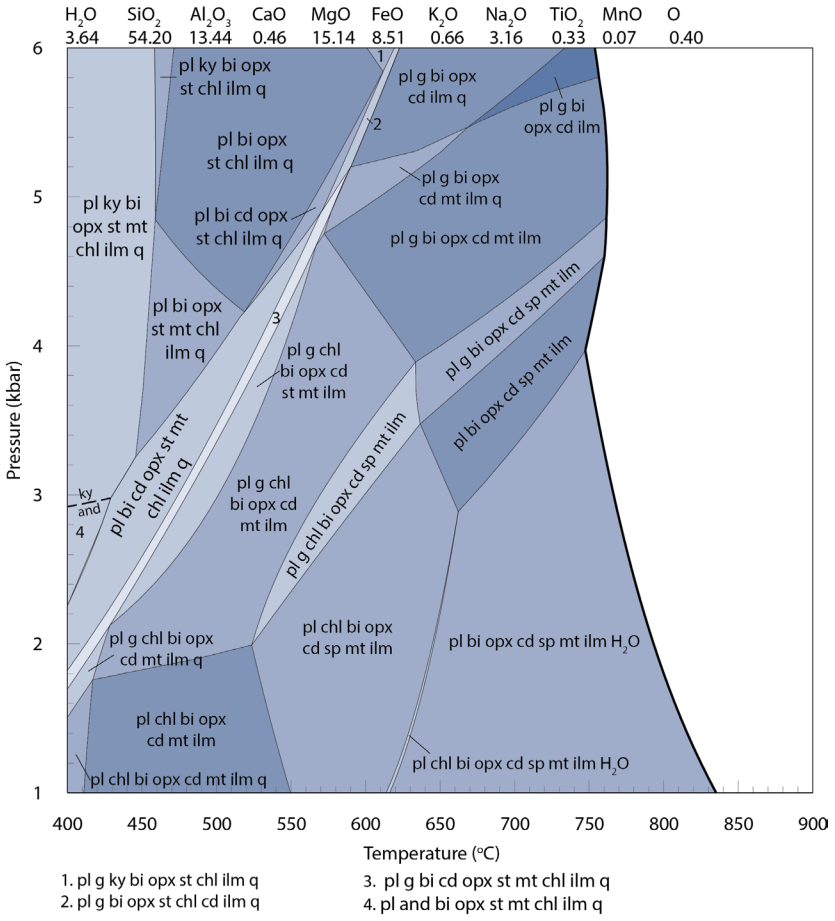


Figure 5. Calculated *P–T* pseudosection after the first melt reintegration (6% melt reintegrated). The bulk composition (in mol%) was calculated with the addition of 6% melt into the original granulite composition (Figure 4a) and is given above the pseudosection. The bold black line represents the solidus.

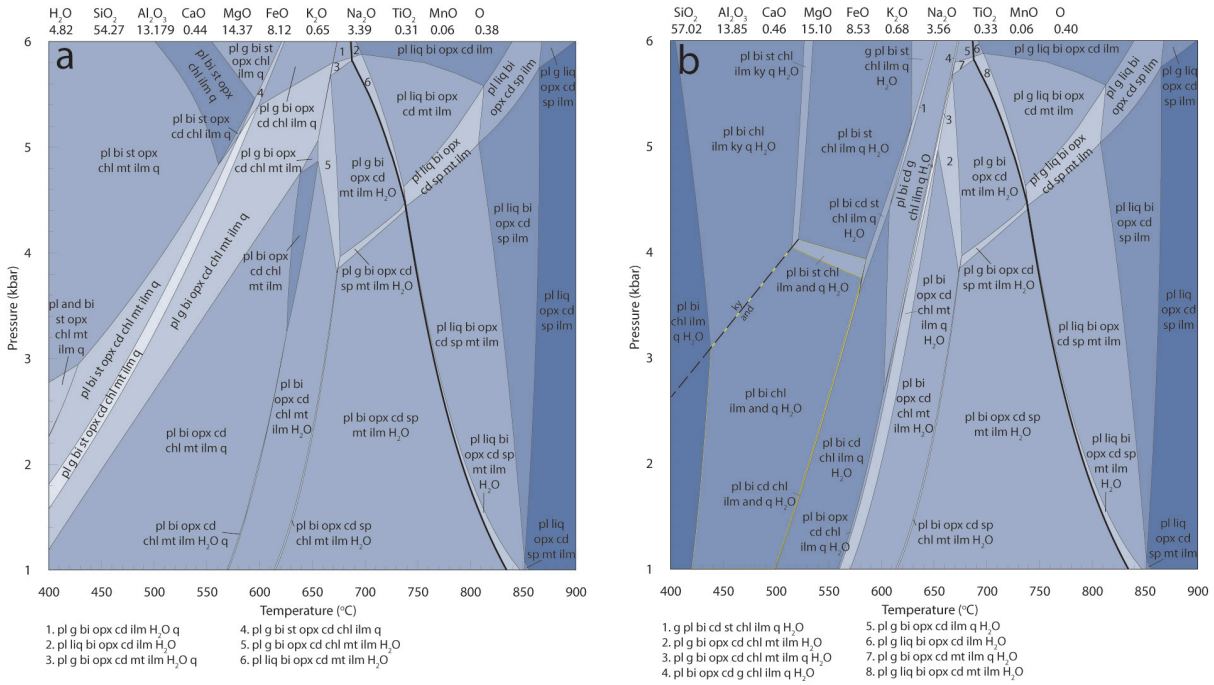


Figure 6. Calculated *P–T* pseudosections after the second melt reintegration (12% melt reintegrated). The bulk composition (in mol%) was calculated with the addition of a further 6% melt into the composition after the first melt reintegration (Figure 4a) and is given above each pseudosection. The bold black line represents the solidus. (a) H_2O was not set to excess below the solidus, instead subsolidus equilibria were calculated using the H_2O content of the melt reintegrated composition. (b) H_2O was set to excess below the solidus. Setting H_2O to excess allows calculation of equilibria with a free water phase at subsolidus temperatures and results in significant changes to the stability of andalusite.

modal abundance contours best correspond to the observed mineral abundances in thin section (Figure 4b). Observed abundances of minerals in thin section (determined through point counting) are provided in Table 1.

Melt reintegration

Melt was reintegrated into the residual pelite composition in two stages (Figures 5 and 6), for a total of 12%. The addition of 12% melt results in a solidus that is water saturated at peak metamorphic conditions (1.0–4.4 kbar; Figure 6), with ~1.4 mol% H2O present at 3.5 kbar. The addition of 12% melt results in a decrease in the temperature of the solidus at 3.5 kbar from ~810 ˚C to ~750 ˚C. After the reintegration of 12% melt, the peak assemblage above the solidus is still present and occurs at similar *P–T* conditions, but subsolidus assemblages have been significantly changed. However, notably, subsolidus equilibria calculated using the H2O content of the melt reintegrated composition do not contain andalusite (Figure 6a). The H_2O content of the melt reintegrated composition also does not allow for a free H2O phase at temperatures below 570–670 ˚C (with increasing pressure). However, if H_2O is set to excess below the solidus, which is an approach commonly used for modelling subsolidus rocks, then mineral assemblages containing andalusite can be produced at temperatures below ~570 °C using the melt reintegrated composition (Figure 6b). Setting H_2O to be in excess also supresses the modelled stability of orthopyroxene.

DISCUSSION

The aim of this study is to test the veracity of melt reintegration calculations by reintegrating melt into a compositionally residual rock whose precursor mineralogy is partly known. We interpret andalusite to have been present during the subsolidus prograde evolution of the rock, based on blocky mineral aggregates cored by sillimanite that are rimmed by cordierite-spinel intergrowths, as well as the

widespread presence of andalusite in lower grade stratigraphic equivalents. Sillimanite cores in the cordierite–spinel coronae are rare throughout the rock and were likely no more than metastable relics of the andalusite porphyroblasts that were unable to be completely replaced during metamorphism to higher temperatures due to sluggish diffusion of Al [e.g. 50,51]. However, they do indicate that blocky domains of cordierite–spinel symplectites likely represent the complete replacement of andalusite porphyroblasts along the prograde path. As such, the localised occurrence of spinel–cordierite symplectites in the sample used in this study can be used to estimate the abundance of subsolidus andalusite. On this basis approximately 5% andalusite was present, allowing for volume loss associated with melt loss in the subsolidus protolith.

The *P–T* pseudosection calculated for the original residual composition already has stable andalusite prior to any melt reintegration (Figure 7a). However, it is well established that residual bulk compositions are not appropriate for modelling the prograde evolution of a rock [12,18,52]. The melting and melt loss that has occurred in the field area would have altered the composition of the rocks so that the subsolidus part of the pseudosection does not represent real prograde assemblages. Therefore, we have used the presence of ~5% subsolidus andalusite as a target to evaluate the viability of the melt reintegration procedure for predicting subsolidus assemblages.

Melt was reintegrated into the original residual composition in two separate batches of 6%, for a total of 12% melt until the solidus was H_2O saturated at peak conditions (1.0–4.4 kbar, and up to pressures of 6 kbar). The solidus in the final melt reintegrated bulk composition remains at a high temperature (750 °C at 3.5 kbar), which likely reflects the absence of quartz above 650 °C. It is common practice for petrologists to model subsolidus equilibria with H_2O in excess. Evidence of decreasing H_2O content with increasing metamorphic grade at subsolidus conditions can be found in most metamorphic terranes, suggesting that H_2O is typically lost from the system during prograde dehydration reactions, prior to melting [53-56]. Therefore, when the rock reaches the solidus, it is likely to contain very little free H_2O, and less H_2O than was present during the development of the lower temperature mineral assemblages [57]. Subsolidus andalusite could not be produced using the H_2O content of the final melt reintegrated composition except at very low temperatures; however, when H_2O was modelled to be in excess below the solidus, the reintegrated bulk composition was able to produce subsolidus assemblages that include andalusite (plagioclase–biotite–staurolite–chlorite–ilmenite–andalusite–quartz–H_2O, plagioclase–biotite–chlorite–ilmenite–andalusite–quartz–H_2O and plagioclase–biotite–cordierite–chlorite–ilmenite–andalusite–quartz–H_2O) with an andalusite abundance of 1–5%. The absence of andalusite in a fluid-undersaturated system suggests that H_2O plays a large role in its stability, at least using the dataset and activity models used in this study [8-10,43]. It should be noted that the use of different activity–composition models can result in differences in mineral stability [58]. Whereas modelling with subsolidus H_2O saturation arguably represents a closed system from which H_2O produced from dehydration reactions is unable to escape [57], a fluid-rich composition appears to be necessary to reproduce the subsolidus andalusite that we interpret was present. Therefore, to model the subsolidus andalusite-bearing mineral assemblages melt was reintegrated until a wet solidus was reached and H_2O was then assumed to be in excess below the solidus.

Limitations of the modelling

While the modelling of melt reintegrated composition predicts the presence of prograde andalusite, there are several limitations to the

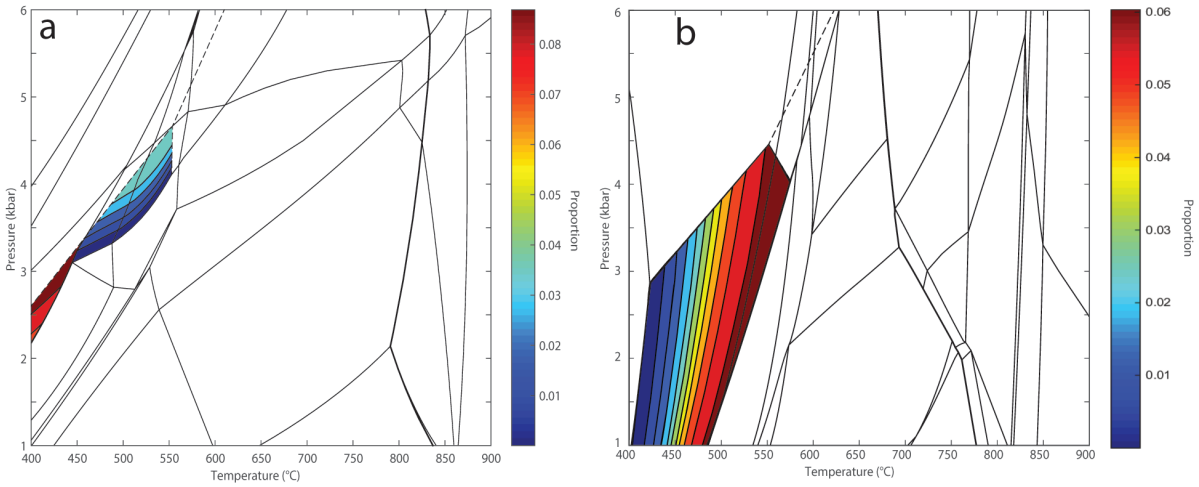


Figure 7. (a) TCInvestigator [45] plot of the modal proportion of andalusite present in the residual *P–T* pseudosection (Figure 4a) prior to melt reintegration. (b) TCInvestigator [45] plot of the modal proportion of andalusite present in the ds55 *P–T* pseudosection after 12% melt reintegration and with H_2O in excess.

modelling that was undertaken in this study. Some limitations relate to the uncertainties associated with the internally consistent thermodynamic data [43] and the activity–composition models [8-10] used in THERMOCALC to calculate the mineral stability fields [e.g. 10]. The simplifications that are necessary to model phase equilibria in naturally complex chemical systems are also a limiting factor. The model chemical system used in this study does not take into account minor components, such as chlorine and fluorine in biotite and ZnO and Cr_2O_3 in spinel, which are present in minor amounts [Table 1; 59,60]. Although the effects of these minor components are unlikely to greatly influence the outcomes of the modelling, they are real and will slightly modify of the positions of reactions in *P–T* space [5]. The uncertainties in determining the effective chemical composition that relates to the formation of the peak mineral assemblages are also a limitation. The composition obtained by whole-rock geochemistry was not appropriate to model to the development of the pelitic orthopyroxene-bearing domains, as these occur in thin, discontinuous layers within metapsammitic rock. Instead, a composition for the purposes of phase equilibria modelling was determined by combining mineral abundances and average chemical compositions of minerals. A two-dimensional domainal composition is necessarily limited, but for the purposes of modelling we have assumed that it is a realistic composition.

The melt reintegration modelling is limited by simplifications to the modelled *P–T* path. An isobaric *P–T* path at 3.5 kbar was chosen for melt reintegration modelling on the basis of peak pressures reached by other locations during the Delamerian Orogeny and the presence of andalusite in lower grade successions within the Kanmantoo Group. In all likelihood, the sample used in this study would have experienced a change in pressure during prograde metamorphism, driven by the 10–20% shortening recorded in the southern part of the Delamerian Orogen [61]. However, due to the steep inclination of the solidus and liquid modal abundance contours (e.g. Figure 4a), minor changes in the pressure during heating do not significantly change the results of this study.

Despite successfully recreating subsolidus assemblages with andalusite in the presence of excess H_2O after melt reintegration, a more critical issue is that the orthopyroxene-bearing subsolidus assemblages in the final model produced in this study (Figure 6b) are unlike-

ly to have existed, as subsolidus orthopyroxene does not appear to occur in sub-granulite grade metapelitic rocks. If it is assumed that the model shown in Figure 6b represents the amphibolite facies prograde metamorphic assemblages prior to melting and melt loss, subsolidus orthopyroxene would have formed on the prograde path. Tilley [62] described the apparent occurrence of subsolidus orthopyroxene in metapelites in the Comrie aureole in the Scottish Highlands. However, later evidence of subtle partial melting was found [63], suggesting the orthopyroxene-bearing assemblages formed at suprasolidus conditions. Although some studies have recorded mineral assemblages with prograde subsolidus orthopyroxene [e.g. 64,65], these situations generally involve infiltration of a low H_2O activity fluid (aH_2O), such as CO_2-rich fluids or highly concentrated brines, and occur in rocks that have experienced granulite facies temperatures. An example of this is the formation of fine-grained orthopyroxene–andalusite symplectites at low aH_2O conditions during retrogression of pelitic granulites, described by Ballèvre, et al. [66]. The sources of low aH2O fluids could include magmatic dykes, volatile-rich carbonates, or tectonic structures such as fractures or shear zones that may act as channels for fluid to move over large distances [67-69]. However, such sources are not relevant to the prediction of orthopyroxene as shown in Figure 6b, since the modelling does not incorporate a low aH_2O fluid and therefore it is unlikely that subsolidus orthopyroxene would form in the abundances predicted by our models in prograde metapelites at amphibolite facies conditions.

Instead we suggest the appearance of subsolidus orthopyroxene in our models is an artefact created by the absence of an activity–composition model for orthoamphibole in ds62 [10]. This means that Mg and Al cannot be incorporated into orthoamphibole and instead stabilises other minerals, resulting in the formation of unrealistic assemblages. Orthopyroxene can form by the breakdown of orthoamphibole in K-poor protoliths [70]. Occurrences of orthoamphibole in andalusite-bearing metapelites are rare; however, one such occurrence is also within the Kanmantoo Group, in the Springton region, approximately 30 km north of Reedy Creek [71]. Although the Springton region rocks are thought to have been metasomatised, their final bulk compositions contain low proportions of K2O and CaO, and also contain a high Na_2O/K_2O ratio [71], which is similar to the composition of the sample used in this study.

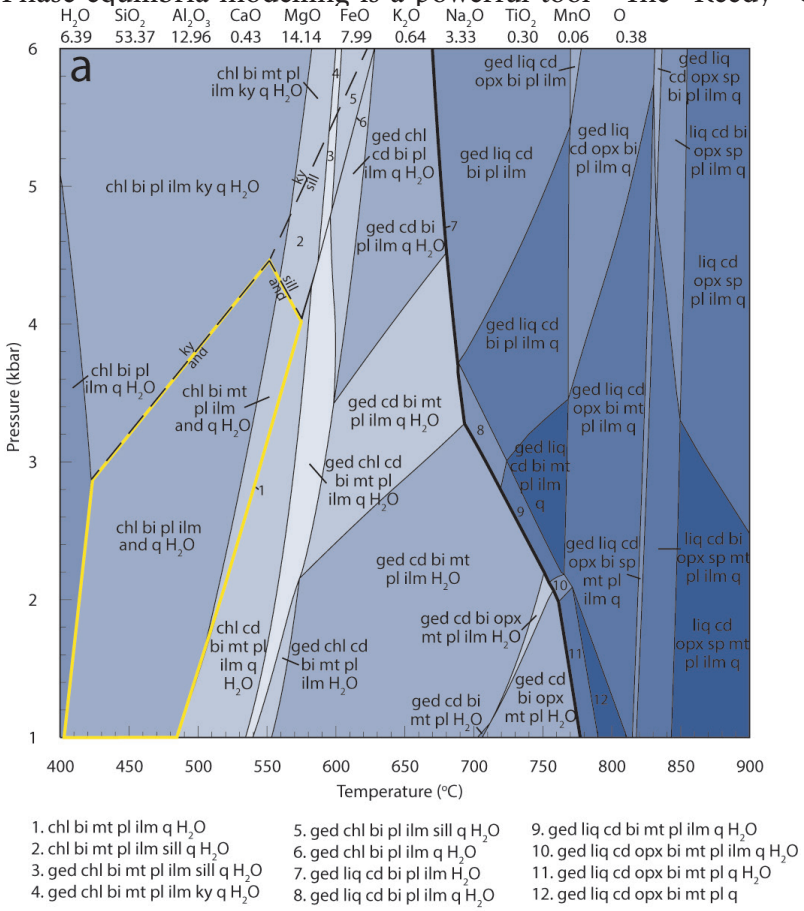
The modelling undertaken in this study used the most recent internally-consistent thermodynamic dataset ds62 [43]. However, our attempts to incorporate orthoamphibole into the ds62 modelling failed to reproduce any subsolidus equilibria that could be rationalised with the incoming solidus or mineral assemblages that could plausibly have existed at subsolidus conditions. Therefore, at this stage we cannot incorporate orthoamphibole into the modelling with ds62 with any confidence. It should also be noted that low–P subsolidus equilibria involving porphyroblastic cordierite like in this study have been known to be problematic to model in ds62 [e.g. 9,58,72]. Instead, the final composition produced after melt reintegration modelling (Figure 6b) was used to model the subsolidus assemblages in the previous THERMOCALC dataset ds55 [73], to investigate the effects of incorporating orthoamphibole into the modelling [e.g. 70,74]. The following activity relationships were used for modelling in ds55: silicate melt and biotite [5]; chlorite [75,76]; cordierite [73]; plagioclase [77]; gedrite [74]; orthopyroxene,spinel and magnetite [78]; ilmenite [6]. Using ds55 the subsolidus assemblages were again modelled with H_2O in excess (Figure 8). While we acknowledge the apparent logic disconnect in using a melt reintegrated composition created using ds62 followed by modelling in ds55, no

subsolidus orthopyroxene was found to be stable using ds55, and instead, orthoamphibole (gedrite)-bearing assemblages were modelled to be stable (Figure 8). Despite the differences between the ds62 and ds55 subsolidus models, the melt reintegrated composition in ds55 was able to produce a number of assemblages containing andalusite at similar conditions to the ds62 model (1.0–4.1 kbar and 400–550 °C; Figure 8) and in similar modal proportions (Figure 7b; 1–6%). Furthermore, although the melt reintegrated composition is specific to the sample we have used, the prediction of gedrite-bearing assemblages is consistent with the presence of orthoamphibole-bearing assemblages in lower grade areas of the Kanmantoo Group [71], suggesting that while ds62 is now widely used, ds55 still provides realistic predictions.

Implications of the melt reintegration modelling

Phase equilibria modelling is a powerful tool for investigating the chemical changes that occur as a result of partial melting and melt loss during high-grade metamorphism. It is one of the few methods that allows investigation of the petrological and chemical evolution of deep-crustal rocks, as it provides an opportunity to define equilibrium relationships between melt and solid mineral species for particular bulk compositions at a given set of *P*–*T* conditions [e.g. 13,14]. Several previous studies have utilised this technique to explore the effects of reintegrating melt back into lower-crustal rocks [16,18,41,46,79,80]. However, rarely do studies attempt to assess the veracity of the melt reintegration process to create valid subsolidus rock compositions. Reedy Creek presents an opportunity in which a partially known subsolidus mineral assemblage can be used as a reference point for the assessment of the outcome of melt reintegration modelling on a granulite facies rock.

The Reedy Creek metasedimentary rocks



1. chl bi mt pl ilm q H_2O
2. chl bi mt pl ilm sill q H_2O
3. ged chl bi mt pl ilm sill q H_2O
4. ged chl bi mt pl ilm ky q H_2O
5. ged chl bi pl ilm sill q H_2O
6. ged chl bi pl ilm q H_2O
7. ged liq cd bi pl ilm H_2O
8. ged liq cd bi pl ilm q H_2O
9. ged liq cd bi mt pl ilm q H_2O
10. ged liq cd opx bi mt pl ilm q H_2O
11. ged liq cd opx bi mt pl q H_2O
12. ged liq cd opx bi mt pl q

Figure 8. *P*–*T* pseudosection calculated using the same melt reintegrated composition as in Figure 6, but using ds55 rather than ds62 to explore the stability of orthoamphibole. The fields highlighted in yellow contain andalusite. The bold black line represents the solidus. H_2O is set to excess below the solidus. Differences in the subsolidus and suprasolidus magnetite models in ds55 resulted in differences in fields across the solidus.

preserve intact relict, centimetre-scale sedimentary layering. This suggests that melt loss from the rock was likely to have been incremental and efficient, without the accumulation of large amounts of melt that would have resulted in catastrophic melt loss and disruption of the sedimentary layering [81,82]. The melt connectivity transition [approximately 7%, 47] was used as a maximum for the melt loss that would have occurred in any one melt extraction event. However, we acknowledge that in the presence of syn-anatectic deformation, melt extraction may well occur at a lower threshold [83-86].

In the modelled sample the sillimanite is not interpreted to have been part of the equilibrium mineral assemblage at peak metamorphic conditions, or likely at any stage throughout the sample's prograde history. In most cases, the cordierite–spinel Symplectites that are seen surrounding sillimanite on rare occasion have completely replaced sillimanite, indicating that it is not part of the peak assemblage. It cannot be said for certain that sillimanite was never stable throughout any of the rock's history. However, the models in this study (all of which were derived from the composition of the peak mineral assemblage in the sample) are not able to form stable sillimanite at any point, suggesting that it may not have occurred at all on the prograde path. Instead, we suggest that the sillimanite that we observe in the sample is simply a compositional relic of incomplete continuous reactions involving the progressive formation of cordierite and orthoamphibole at the expense of andalusite, biotite and chlorite as the rock traversed the narrow set of fields between andalusite-bearing assemblages and orthoamphibole–cordierite-bearing assemblages. We suggest that residual metastable aluminosilicate in micro-compositional domains underwent a reaction that cannot be sequentially tracked across phase fields in our *P–T* models. The calculation of *P–T* models relies on the assumption that all phases are in equilibrium at any given point across the diagram. However, in reality this is rarely the case. Reactions may not proceed to completion, leaving behind minerals that should have reacted out to play a role in new reactions and restricting the growth of new minerals. This results in further reactions that involve metastable minerals that are not reflected on *P–T* diagrams [e.g. 87,88-90]. This overstepping displaces the location of the boundary of a metamorphic reaction in *P–T* space, resulting in a phase diagram that does not necessarily reflect the sequence of prograde reactions that occurred in the rock. In this study, we interpret the small relics of aluminosilicate remaining in the granulite to be metastable with respect to the modelled bulk compositions. However, they play a critical role in our analysis because they allow us to confidently interpret the presence of a subsolidus mineral. Furthermore, the spinel–cordierite symplectites form clearly delineated domains in the rock that allow us to make an estimate of the approximate amount of subsolidus andalusite.

The predicted occurrence of andalusite at subsolidus conditions indicates that melt reintegration modelling is a viable way to reproduce protolith bulk rock compositions. However, it should be noted that in cases where low-grade mineral assemblages are unclear or textural evidence of compositional domains not preserved, there may still be a significant amount of uncertainty involved in selecting a potential prograde *P–T* path.

An important application of melt loss modelling is the interpretation of inclusion assemblages. A large number of studies have used inclusion assemblages to provide information about prograde history, even in rocks that have undergone partial melting and melt loss [e.g. 91,92,93]. While these inclusions may offer an insight into the existence of potential prograde minerals, interpreting prograde conditions based on modelling a bulk composition

that existed prior to modification due to melt loss is illogical, and unlikely to result in meaningful constraints. Furthermore, a number of workers have also used the compositions of individual minerals to make inferences about prograde histories [e.g. 94,95,96]. Where rocks have experienced high temperature evolutions, any such compositions will only be fortuitously the same as they were at the time of capture due to diffusion-driven compositional modification of the inclusion. However, melt reintegration modelling does offer an avenue for the interpretation of inclusion assemblages providing a window into the prograde conditions of rocks, despite extensive melt extraction compositional modification.

CONCLUSIONS

Phase equilibria modelling undertaken on the Kanmantoo sediments at Reedy Creek indicate that peak *P–T* conditions of 790–860 °C and 1.0–4.4 kbar were reached. From these peak conditions, melt reintegration modelling of the pelitic granulites was able to reproduce several viable subsolidus mineral assemblages containing andalusite, which was known to have existed in these rocks at lower grade. This indicates that current melt reintegration methods may have the potential to effectively recreate valid protolith bulk rock compositions, but do require some knowledge of the protolith to be certain. However, the absence of orthoamphibole in the current ds62 model does, in this case, restrict our ability to accurately predict many subsolidus reactions that may have occurred in this rock

ACKNOWLEDGMENTS

Jade Anderson is thanked for her assistance with data collection. This work was supported by ARC DP160101006 (DEK), ARC LP160100578 and DP160104637 (MH). The University of Adelaide is also thanked for research support funding. KLA acknowledges the support of an Australian Government Research Training Program Scholarship.

REFERENCES

1. Brown, M. Crustal melting and melt extraction, ascent and emplacement in orogens: mechanisms and consequences. Journal of the Geological Society 2007, 164, 709-730.
2. Heier, K.S. Metamorphism and the chemical differentiation of the crust. GFF 1965, 87, 249-256.
3. Sighinolfi, G.P.; Gorgoni, C. Chemical evolution of high-grade metamorphic rocks—anatexis and remotion of material from granulite terrains. Chemical Geology 1978, 22, 157-176.
4. Holland, T.; Powell, R. Calculation of phase relations involving haplogranitic melts using an internally consistent thermodynamic dataset. J. Petrol. 2001, 42, 673-683.
5. White, R.; Powell, R.; Holland, T. Progress relating to calculation of partial melting equilibria for metapelites. J. Metamorph. Geol. 2007, 25, 511-527.
6. White, R.; Powell, R.; Holland, T.; Worley, B. The effect of TiO~ 2 and Fe~ 2O~ 3 on metapelitic assemblages at greenschist and amphibolite facies conditions: mineral equilibria calculations in the system K~ 2O-FeO-MgO-Al~ 2O~ 3-SiO~ 2-H~ 2O-TiO~ 2-Fe~ 2O~ 3. J. Metamorph. Geol. 2000, 18, 497-512.
7. Johnson, T.; White, R.; Powell, R. Partial melting of metagreywacke: a calculated mineral equilibria study. J. Metamorph. Geol. 2008, 26, 837-853.
8. Powell, R.; White, R.; Green, E.; Holland, T.; Diener, J. On parameterizing thermodynamic descriptions of minerals for petrological calculations. J. Metamorph. Geol. 2014, 32, 245-260.
9. White, R.; Powell, R.; Holland, T.; Johnson, T.; Green, E. New mineral activity–composition relations for thermodynamic calculations in metapelitic systems. J. Metamorph. Geol. 2014, 32, 261-286.

10. White, R.; Powell, R.; Johnson, T. The effect of Mn on mineral stability in metapelites revisited: New a–x relations for manganese-bearing minerals. J. Metamorph. Geol. 2014, 32, 809-828.
11. Morrissey, L.J.; Hand, M.; Lane, K.; Kelsey, D.E.; Dutch, R.A. Upgrading iron-ore deposits by melt loss during granulite facies metamorphism. Ore Geology Reviews 2016, 74, 101-121.
12. Diener, J.; White, R.; Powell, R. Granulite facies metamorphism and subsolidus fluid-absent reworking, Strangways Range, Arunta Block, central Australia. J. Metamorph. Geol. 2008, 26, 603-622.
13. Yakymchuk, C.; Brown, M. Consequences of open-system melting in tectonics. Journal of the Geological Society 2014, 171, 21-40.
14. Yakymchuk, C.; Brown, M. Behaviour of zircon and monazite during crustal melting. Journal of the Geological Society 2014, 171, 465-479.
15. Diener, J.F.; Fagereng, Å. The influence of melting and melt drainage on crustal rheology during orogenesis. Journal of Geophysical Research: Solid Earth 2014, 119, 6193-6210.
16. Koblinger, B.M.; Pattison, D.R. Crystallization of Heterogeneous Pelitic Migmatites: Insights from Thermodynamic Modelling. J. Petrol. 2017, 58, 297-326.
17. Bartoli, O. Phase equilibria modelling of residual migmatites and granulites: an evaluation of the melt-reintegration approach. J. Metamorph. Geol. 2017.
18. Korhonen, F.; Brown, M.; Clark, C.; Bhattacharya, S. Osumilite–melt interactions in ultrahigh temperature granulites: phase equilibria modelling and implications for the *P*–*T*–t evolution of the Eastern Ghats Province, India. J. Metamorph. Geol. 2013, 31, 881-907.
19. White, R.; Powell, R.; Halpin, J. Spatially-focussed melt formation in aluminous metapelites from Broken Hill, Australia. J. Metamorph. Geol. 2004, 22, 825-845.
20. Redler, C.; White, R.W.; Johnson, T.E. Migmatites in the Ivrea Zone (NW Italy): Constraints on partial melting and melt loss in metasedimentary rocks from Val Strona di Omegna. Lithos 2013, 175, 40-53.
21. Yakymchuk, C.; Brown, M.; Clark, C.; Korhonen, F.; Piccoli, P.; Siddoway, C.; Taylor, R.; Vervoort, J. Decoding polyphase migmatites using geochronology and phase equilibria modelling. J. Metamorph. Geol. 2015, 33, 203-230.
22. Goodge, J.W. Latest Neoproterozoic basin inversion of the Beardmore Group, central Transantarctic Mountains, Antarctica. Tectonics 1997, 16, 682-701.
23. Stump, E. The Ross Orogen of the Transantarctic Mountains. Cambridge University Press: 1995.
24. Milnes, A.; Compston, W.; Daily, B. Pre-to syn-tectonic emplacement of early Palaeozoic granites in southeastern South Australia. Journal of the Geological Society of Australia 1977, 24, 87-106.
25. Preiss, W.V. The Adelaide Geosyncline: Late Proterozoic stratigraphy, sedimentation, palaeontology and tectonics. Department of Mines and Energy: 1987.
26. Haines, P.W.; Flöttmann, T. Delamerian Orogeny and potential foreland sedimentation: a review of age and stratigraphic constraints. Aust. J. Earth Sci. 1998, 45, 559-570.
27. Foden, J.; Elburg, M.A.; Dougherty-Page, J.; Burtt, A. The timing and duration of the Delamerian Orogeny: correlation with the Ross Orogen and implications for Gondwana assembly. The Journal of Geology 2006, 114, 189-210.
28. Flöttmann, T.; James, P.; Rogers, J.; Johnson, T. Early Palaeozoic foreland thrusting and basin reactivation at the Palaeo-Pacific margin of the southeastern Australian Precambrian Craton: a reappraisal of the structural evolution of the Southern Adelaide Fold-Thrust Belt. Tectonophysics

1994, 234, 95-116.
29. Mancktelow, N.S. The structure of the southern Adelaide fold belt, South Australia. The evolution of a Late Precambrian–Early Palaeozoic Rift Complex: The Adelaide Geosyncline 1990, 16, 369-395.
30. Offler, R.; Fleming, P. A synthesis of folding and metamorphism in the Mt Lofty Ranges, South Australia. Journal of the Geological Society of Australia 1968, 15, 245-266.
31. Foden, J.; Sandiford, M.; Dougherty-Page, J.; Williams, I. Geochemistry and geochronology of the Rathjen Gneiss: implications for the early tectonic evolution of the Delamerian Orogen. Aust. J. Earth Sci. 1999, 46, 377-389.
32. Foden, J.; Elburg, M.; Turner, S.; Sandiford, M.; O'Callaghan, J.; Mitchell, S. Granite production in the Delamerian orogen, South Australia. Journal of the Geological Society 2002, 159, 557-575.
33. Turner, S.; Foden, J. Magma mingling in late-Delamerian A-type granites at Mannum, South Australia. Mineralogy and Petrology 1996, 56, 147-169.
34. Turner, S.; Kelley, S.; VandenBerg, A.; Foden, J.; Sandiford, M.; Flöttmann, T. Source of the Lachlan fold belt flysch linked to convective removal of the lithospheric mantle and rapid exhumation of the Delamerian-Ross fold belt. Geology 1996, 24, 941-944.
35. Sandiford, M.; Eraser, G.; Arnold, J.; Foden, J.; Farrow, T. Some causes and consequences of high-temperature, low-pressure metamorphism in the eastern Mt Lofty Ranges, South Australia. Aust. J. Earth Sci. 1995, 42, 233-240.
36. Moeller, T. The Petrology and Geochemistry of the Reedy Creek Granitoids and Migmatites. University of Adelaide, Department of Geology: 1980.
37. Sando, M. The Granitic and Metamorphic Rocks of the Reedy Creek Area, Mannum, South Australia. University of Adelaide: 1957.
38. White, R.; Powell, R. Melt loss and the preservation of granulite facies mineral assemblages. J. Metamorph. Geol. 2002, 20, 621-632.
39. Dymoke, P.; Sandiford, M. Phase relationships in Buchan facies series pelitic assemblages: calculations with application to andalusite-staurolite parageneses in the Mount Lofty Ranges, South Australia. Contributions to Mineralogy and Petrology 1992, 110, 121-132.
40. Carson, C.; Powell, R.; Clarke, G. Calculated mineral equilibria for eclogites in CaO-Na 2 O-FeO-MgO-Al 2 O 3-SiO 2-H 2 O: application to the Pouébo Terrane, Pam Peninsula, New Caledonia. J. Metamorph. Geol. 1999, 17, 9-24.
41. Indares, A.; White, R.; Powell, R. Phase equilibria modelling of kyanite-bearing anatectic paragneisses from the central Grenville Province. J. Metamorph. Geol. 2008, 26, 815-836.
42. Palin, R.M.; Weller, O.M.; Waters, D.J.; Dyck, B. Quantifying geological uncertainty in metamorphic phase equilibria modelling; a Monte Carlo assessment and implications for tectonic interpretations. Geoscience Frontiers 2016, 7, 591-607.
43. Holland, T.; Powell, R. An improved and extended internally consistent thermodynamic dataset for phases of petrological interest, involving a new equation of state for solids. J. Metamorph. Geol. 2011, 29, 333-383.
44. Powell, R.; Holland, T. An internally consistent thermodynamic dataset with uncertainties and correlations: 3. Applications to geobarometry, worked examples and a computer program. J. Metamorphic Geol. 1988, 6, 173-204.
45. Pearce, M.A.; White, A.J.R.; Gazley, M.F. TCInvestigator: automated calculation of mineral mode and composition contours for thermocalc pseudosections. J. Metamorph. Geol. 2015, 33, 413-425.

46. White, R.; Powell, R.; Halpin, J.A. Spatially-focussed melt formation in aluminous metapelites from Broken Hill, Australia. J. Metamorph. Geol. 2004, 22, 825-845.
47. Rosenberg, C.L.; Handy, M.R. Experimental deformation of partially melted granite revisited: implications for the continental crust. J. Metamorph. Geol. 2005, 23, 19-28.
48. Jenkins, R.J.F.; Sandiford, M. Observations on the tectonic evolution of the southern Adelaide Fold Belt. Tectonophysics 1992, 214, 27-36.
49. Alias, G.; Sandiford, M.; Hand, M.; Worley, B. The *P–T* record of synchronous magmatism, metamorphism and deformation at Petrel Cove, southern Adelaide Fold Belt. J. Metamorph. Geol. 2002, 20, 351-363.
50. White, R.; Powell, R. Retrograde melt–residue interaction and the formation of near-anhydrous leucosomes in migmatites. J. Metamorph. Geol. 2010, 28, 579-597.
51. Mongkoltip, P.; Ashworth, J. Quantitative estimation of an open-system symplectite-forming reaction: restricted diffusion of Al and Si in coronas around olivine. J. Petrol. 1983, 24, 635-661.
52. Kelsey, D.E.; Hand, M. On ultrahigh temperature crustal metamorphism: phase equilibria, trace element thermometry, bulk composition, heat sources, timescales and tectonic settings. Geoscience Frontiers 2015, 6, 311-356.
53. Ague, J.J. Evidence for major mass transfer and volume strain during regional metamorphism of pelites. Geology 1991, 19, 855-858.
54. Clemens, J.D.; Droop, G.T.; Stevens, G. High-grade metamorphism, dehydration and crustal melting: a reinvestigation based on new experiments in the silica-saturated portion of the system KAlO2–MgO–SiO2–H2O–CO2 at P≤ 1.5 GPa. Contributions to Mineralogy and Petrology 1997, 129, 308-325.
55. Huang, W.; Wyllie, P. Muscovite dehydration and melting in deep crust and subducted oceanic sediments. Earth Planet. Sci. Lett. 1973, 18, 133-136.
56. Miyashiro, A. Evolution of metamorphic belts. J. Petrol. 1961, 2, 277-311.
57. Webb, G.; Powell, R.; McLaren, S. Phase equilibria constraints on the melt fertility of crustal rocks: the effect of subsolidus water loss. J. Metamorph. Geol. 2015, 33, 147-165.
58. Pattison, D.; DeBuhr, C. Petrology of metapelites in the Bugaboo aureole, British Columbia, Canada. J. Metamorph. Geol. 2015, 33, 437-462.
59. Peterson, J.; Chacko, T.; Kuehner, S. The effects of fluorine on the vapor-absent melting of phlogopite+ quartz; implications for deep-crustal processes. Am. Miner. 1991, 76, 470-476.
60. Nichols, G.T.; Berry, R.F.; Green, D.H. Internally consistent gahnitic spinel-cordierite-garnet equilibria in the FMASHZn system: geothermobarometry and applications. Contributions to Mineralogy and Petrology 1992, 111, 362-377.
61. Paul, E.; Flöttmann, T.; Sandiford, M. Structural geometry and controls on basement-involved deformation in the northern Flinders Ranges, Adelaide Fold Belt, South Australia. Aust. J. Earth Sci. 1999, 46, 343-354.
62. Tilley, C.E. Contact-metamorphism in the Comrie area of the Perthshire Highlands. Quarterly Journal of the Geological Society 1924, 80, 22-71.
63. Pattison, D.R.; Tracy, R.J. Phase equilibria and thermobarometry of metapelites. Reviews in Mineralogy and Geochemistry 1991, 26, 105-206.
64. Droop, G.R.; Bucher-Nurminen, K. Reaction textures and metamorphic evolution of sapphirine-bearing granulites from the Gruf Complex, Italian Central Alps. J. Petrol. 1984, 25, 766-803.

65. Harlov, D.E.; Johansson, L.; Van Den Kerkhof, A.; FÖRSTER, H.-J. The role of advective fluid flow and diffusion during localized, solid-state dehydration: Söndrum Stenhuggeriet, Halmstad, SW Sweden. J. Petrol. 2006, 47, 3-33.
66. Ballèvre, M.; Hensen, B.J.; Reynard, B. Orthopyroxene-andalusite symplectites replacing cordierite in granulites from the Strangways Range (Arunta block, central Australia): A new twist to the pressure-temperature history. Geology 1997, 25, 215-218.
67. Knudsen, T.-L.; Lidwin, A. Magmatic CO2, brine and nitrogen inclusions in Sveconorwegian enderbitic dehydration veins and a gabbro from the Bamble sector, Southern Norway. European Journal of Mineralogy 1996, 1041-1064.
68. Harlov, D.E.; Förster, H.-J. High-grade fluid metasomatism on both a local and a regional scale: the Seward peninsula, Alaska, and the Val Strona di Omegna, Ivrea–Verbano Zone, Northern Italy. Part I: petrography and silicate mineral chemistry. J. Petrol. 2002, 43, 769-799.
69. Radhika, U.; Santosh, M. Shear-zone hosted graphite in southern Kerala, India: implications for CO 2 infiltration. Journal of Southeast Asian Earth Sciences 1996, 14, 265-273.
70. Diener, J.; Powell, R.; White, R. Quantitative phase petrology of cordierite–orthoamphibole gneisses and related rocks. J. Metamorph. Geol. 2008, 26, 795-814.
71. Arnold, J.; Sandiford, M. Petrogenesis of cordierite-orthoamphibole assemblages from the Springton region, South Australia. Contributions to Mineralogy and Petrology 1990, 106, 100-109.
72. Pattison, D.; Spear, F.; Debuhr, C.; Cheney, J.; Guidotti, C. Thermodynamic modelling of the reaction muscovite+ cordierite→ Al2SiO5+ biotite+ quartz+ H2O: constraints from natural assemblages and implications for the metapelitic petrogenetic grid. J. Metamorph. Geol. 2002, 20, 99-118.
73. Holland, T.; Powell, R. An internally consistent thermodynamic data set for phases of petrological interest. J. Metamorph. Geol. 1998, 16, 309-343.
74. Diener, J.; Powell, R.; White, R.; Holland, T. A new thermodynamic model for clino-and orthoamphiboles in the system Na2O–CaO–FeO–MgO–Al2O3–SiO2–H2O–O. J. Metamorph. Geol. 2007, 25, 631-656.
75. Mahar, E.M.; Baker, J.; Powell, R.; Holland, T.; Howell, N. The effect of Mn on mineral stability in metapelites. J. Metamorph. Geol. 1997, 15, 223-238.
76. Holland, T.; Baker, J.; Powell, R. Mixing properties and activity-composition relationships of chlorites in the system MgO-FeO-Al2O3-SiO2-H2O. European Journal of Mineralogy 1998, 10, 395-406.
77. Holland, T.; Powell, R. Activity–composition relations for phases in petrological calculations: an asymmetric multicomponent formulation. Contributions to Mineralogy and Petrology 2003, 145, 492-501.
78. White, R.; Powell, R.; Clarke, G. The interpretation of reaction textures in Fe-rich metapelitic granulites of the Musgrave Block, central Australia: constraints from mineral equilibria calculations in the system K2O–FeO–MgO–Al2O3–SiO2–H2O–TiO2–Fe2O3. J. Metamorph. Geol. 2002, 20, 41-55.
79. Guilmette, C.; Indares, A.; Hébert, R. High-pressure anatectic paragneisses from the Namche Barwa, Eastern Himalayan Syntaxis: Textural evidence for partial melting, phase equilibria modeling and tectonic implications. Lithos 2011, 124, 66-81.
80. Palin, R.; Searle, M.; Waters, D.; Parrish, R.; Roberts, N.; Horstwood, M.; Yeh, M.W.; Chung, S.L.; Anh, T. A geochronological and petrological study of anatectic paragneiss and associated granite dykes from the Day Nui Con Voi metamorphic

core complex, North Vietnam: constraints on the timing of metamorphism within the Red River shear zone. J. Metamorph. Geol. 2013, 31, 359-387.

81. Johnson, T.; White, R.; Brown, M. A year in the life of an aluminous metapelite xenolith—the role of heating rates, reaction overstep, H 2 O retention and melt loss. Lithos 2011, 124, 132-143.
82. Pattison, D.; Harte, B. Evolution of structurally contrasting anatectic migmatites in the 3-kbar Ballachulish aureole, Scotland. J. Metamorph. Geol. 1988, 6, 475-494.
83. White, R.W.; Powell, R.; Holland, T.J.B. Calculation of partial melting equilibria in the system Na2O-CaO-K2O-FeO-MgO-Al2O3-SiO2-H2O (NCKFMASH). J. Metamorph. Geol. 2001, 19, 139.
84. White, R.W.; Powell, R.; Holland, T.J.B. Progress relating to calculation of partial melting equilibria for metapelites. J. Metamorph. Geol. 2007, 25, 511-527.
85. Korhonen, F.J.; Brown, M.; Clark, C.; Bhattacharya, S. Osumilite–melt interactions in ultrahigh temperature granulites: phase equilibria modelling and implications for the *P*–*T*–t evolution of the Eastern Ghats Province, India. J. Metamorph. Geol. 2013, 31, 881-907.
86. Brown, M. The spatial and temporal patterning of the deep crust and implications for the process of melt extraction. Philosophical Transactions: Mathematical, Physical and Engineering Sciences 2010, 368, 11-51.
87. Pattison, D.R.; De Capitani, C.; Gaidies, F. Petrological consequences of variations in metamorphic reaction affinity. J. Metamorph. Geol. 2011, 29, 953-977.
88. Waters, D.; Lovegrove, D. Assessing the extent of disequilibrium and overstepping of prograde metamorphic reactions in metapelites from the Bushveld Complex aureole, South Afri*ca.* J. Metamorph. Geol. 2002, 20, 135-149.
89. Zeh, A.; Holness, M. The effect of reaction overstep on garnet microtextures in metapelitic rocks of the Ilesha Schist Belt, SW Nigeria. J. Petrol. 2003, 44, 967-994.
90. Spear, F.S.; Pattison, D.R. The implications of overstepping for metamorphic assemblage diagrams (MADs). Chemical Geology 2017.
91. Guo, J.; O'Brien, P.; Zhai, M. High-pressure granulites in the Sanggan area, North China craton: metamorphic evolution, *P–T* paths and geotectonic significance. J. Metamorph. Geol. 2002, 20, 741-756.
92. Liu, D.; Jian, P.; Kröner, A.; Xu, S. Dating of prograde metamorphic events deciphered from episodic zircon growth in rocks of the Dabie–Sulu UHP complex, China. Earth Planet. Sci. Lett. 2006, 250, 650-666.
93. Parkinson, C.D. Coesite inclusions and prograde compositional zonation of garnet in whiteschist of the HP-UHPM Kokchetav massif, Kazakhstan: a record of progressive UHP metamorphism. Lithos 2000, 52, 215-233.
94. Inui, M.; Toriumi, M. Prograde pressure–temperature paths in the pelitic schists of the Sambagawa metamorphic belt, SW Japan. J. Metamorph. Geol. 2002, 20, 563-580.
95. Schertl, H.-P.; Schreyer, W.; Chopin, C. The pyrope-coesite rocks and their country rocks at Parigi, Dora Maira Massif, Western Alps: detailed petrography, mineral chemistry and PT-path. Contributions to Mineralogy and Petrology 1991, 108, 1-21.
96. Spear, F.S.; Selverstone, J.; Hickmott, D.; Crowley, P.; Hodges, K. PT paths from garnet zoning: A new technique for deciphering tectonic processes in crystalline terranes. Geology 1984, 12, 87-90.

CHAPTER 3

This chapter has been publised in *Geology* as:
Alessio K. L., Hand M., Kelsey D. E., Williams M. A., Morrissey L. J. & Barovich K. 2018 Conservation of deep crustal heat production, Geology.

Statement of Authorship

Title of Paper	Conservation of deep crustal heat production
Publication Status	☑ Published ☐ Accepted for Publication ☐ Submitted for Publication ☐ Unpublished and Unsubmitted w ork w ritten in manuscript style
Publication Details	Alessio, K.L., Hand, M., Kelsey, D.E., Williams, M.A., Morrissey, L.J., Barovich, K., 2018. Conservation of deep crustal heat production. Geology.

Principal Author

Name of Principal Author (Candidate)	Kiara Alessio
Contribution to the Paper	Fieldwork Data collection and modelling Manuscript writing
Overall percentage (%)	65
Certification:	This paper reports on original research I conducted during the period of my Higher Degree by Research candidature and is not subject to any obligations or contractual agreements with a third party that would constrain its inclusion in this thesis. I am the primary author of this paper.
Signature	Date: 30/07/2019

Co-Author Contributions

By signing the Statement of Authorship, each author certifies that:

i. the candidate's stated contribution to the publication is accurate (as detailed above);
ii. permission is granted for the candidate in include the publication in the thesis; and
iii. the sum of all co-author contributions is equal to 100% less the candidate's stated contribution.

Name of Co-Author	Martin Hand
Contribution to the Paper	Manuscript editing Ideas for manuscript Fieldwork Data collection
Signature	Date: 30/07/2019

Name of Co-Author	David Kelsey
Contribution to the Paper	Manuscript editing Ideas for manuscript Fieldwork Data collection

Signature		Date	25/07/2019

Name of Co-Author	Megan Williams
Contribution to the Paper	Manuscript editing Fieldwork Data collection
Signature	Date: 25/07/19

Name of Co-Author	Laura Morrissey
Contribution to the Paper	Manuscript editing Fieldwork Data collection
Signature	Date: 25/07/2019

Name of Co-Author	Karin Barovich
Contribution to the Paper	Manuscript editing Fieldwork Data collection
Signature	Date: 22/07/2019

ABSTRACT
Partial melting of continental crust is generally considered to produce granitic rocks that have high radiogenic heat production rates when compared to their inferred sources and average continental crust. If this idea is correct, then granulite-facies rocks, which are the sources for crustally derived melt, and comprise the residual material left behind after melt loss, should have depleted heat production rates with respect to crustally derived granites. However, K–U–Th measurements from metapelitic compositions in five metamorphic terranes show that crustal heat production rates do not change significantly between subsolidus and formerly suprasolidus domains that have undergone fluid-absent partial melting and experienced significant (>20 vol%) melt loss. In some cases, crustal heat production rates increase in the residual granulite-facies rocks. This suggests fluid-absent partial melting does not deplete concentrations of heat-producing elements in residual metapelitic-derived granulite-facies rocks. Consequently, basement terranes may retain elevated concentrations of heat-producing elements and therefore be more susceptible to thermo-mechanical reactivation than typically expected.

INTRODUCTION
Metamorphism involving partial melting and melt loss is a fundamental process leading to the compositional differentiation of Earth's crust (e.g., Taylor and McLennan, 1995; Sawyer et al., 2011). The primary expression of this process within continents is the formation of crustally derived granitoids, and the associated generation of granulite-facies metamorphic rocks that reflect the residuum left behind after extraction of melts. Crustally derived granitoids typically have radiogenic heat production rates of ~2.4 μW m^{-3} (Bea, 2012), whereas average continental crust has a radiogenic heat production rate of 1.0–1.2 μW m^{-3} (Hacker et al., 2011; Bea, 2012). As a result, residual granulite-facies rocks are commonly inferred to be depleted in radiogenic heat-producing elements (HPEs) with respect to crustally derived granites. However, there are cases where residual granulite-facies rocks retain high radiogenic heat-production values. Regional-scale examples of granulite-facies terranes with high radiogenic heat-production values compared to average continental crust occur in the Eastern Ghats Belt and Southern Granulite Terrane, India (Kumar et al., 2007; Roy et al., 2008); the Namaqualand Complex, South Africa (Andreoli et al., 2006); and the Jequié Terrane, Brazil (Alexandrino and Hamza, 2008). These examples demonstrate that high-temperature metamorphism and melt extraction does not necessarily deplete concentrations of HPEs with respect to average crust.

Such examples are contradictory to the widely held view that there is a downward decrease in the concentration of radiogenic HPEs in the crust, driven by large-scale fluid-absent partial melting and melt loss (e.g., Heier and Adams, 1965; Jaupart et al., 2016). Despite this view, there have been remarkably few studies that have attempted to determine how partial melting and melt loss affects the concentration of HPEs in the crust. The studies that have been done (Bea and Montero, 1999; Kumar and Reddy, 2004; Vilà et al., 2010) have employed small data sets and/or have compiled data from different terranes and lithologies, obscuring the consequences of granitoid generation on the heat-production rates of the residual source materials. The logical way to determine the effect of partial melting and melt extraction on the redistribution of HPEs is to systematically determine HPE concentrations in melt-fertile rocks that have been subjected to progressive metamorphism culminating in extensive fluid-absent partial melting. In this study, for five metamorphic terranes, we determine the concentration of HPEs in metapelitic rocks that record subsolidus to suprasolidus (granulite-facies) metamorphism associated with melt loss, to assess the effect of these pro-

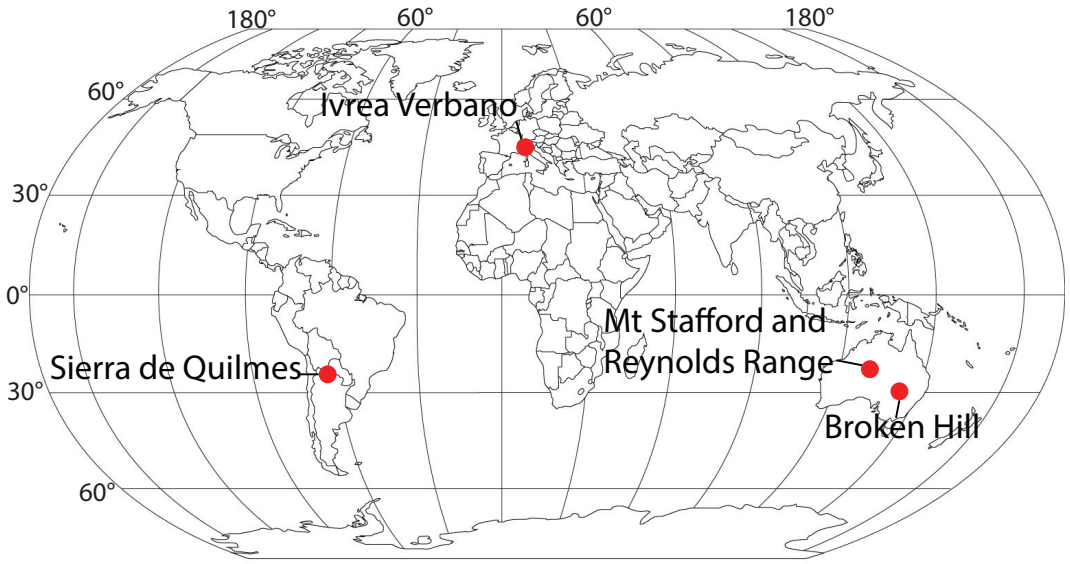


Figure 1. World map showing the locations of the five terranes used in this study. More detailed maps and sample locations are given in Appendix 2A.

cesses on the distribution of HPEs in the crust.

BACKGROUND

In the present-day continental crust, ~80% of surface heat flow can be attributed to the decay of radioactive isotopes within the crust, with the remaining 20% coming from residual heat from the cooling of the Earth (Jaupart et al., 2016). The primary mechanism of heat production within Earth's lithosphere comes from the decay of the three major HPEs: potassium, uranium and thorium. Heat-production rates for each of these elements are 0.074 μW m^{-3} $wt\%^{-1}$ (K2O), 0.265 μW m^{-3} ppm^{-1}, and 0.072 μ W m^{-3} ppm^{-1}, respectively (Bea, 2012). Uranium produces more heat due to its multiple radiogenic isotopes and faster decay rate when compared with Th. However, the ratio of Th to U in continental crust is ~3.7, so the global contribution of U and Th to heat generation is similar (Taylor and McLennan, 1985; Jaupart and Mareschal, 2005; Vilà et al., 2010; Bea, 2012). Due to its much lower heat production, K provides <20% of the radiogenic heat generated within the crust today, so it does not significantly impact crustal heat-production rates. The combined concentrations of these elements determines the radiogenic heat production generated in a particular area.

This study is focused on five metamorphic terranes that record progressive metamorphism from subsolidus to suprasolidus conditions: the Reynolds Range and Mount Stafford in central Australia (Morrissey et al., 2014); Broken Hill in the Curnamona Province in southern Australia (White et al., 2004); the Ivrea–Verbano Zone in northern Italy (Redler et al., 2013); and the Sierra de Quilmes in northwest Argentina (Büttner et al., 2005) (Fig. 1). All of these terranes consist of multiple rock types, but this study was focused on the metapelitic units, as they are most prone to compositional changes as a result of melting and melt loss. The Reynolds Range and Broken Hill systems allow a single metapelitic stratigraphic unit to be sampled across increasing metamorphic grade, from subsolidus conditions to suprasolidus, now residual granulite-facies, conditions (Willis, 1989; Morrissey et al., 2014). In the other terranes, the stratigraphic framework is unknown. Nonetheless, the similar aluminous bulk compositions of the rocks suggest they approximate similar protolith materials. In each terrane, peak metamorphic conditions in the deepest exposed sections were at least 825 °C, with suprasolidus conditions interpreted to be associated with fluid-absent partial melt-

ing and significant (>20%) melt loss (Morrissey et al., 2014; White et al., 2003; White et al., 2004; Redler et al., 2013; Finch et al., 2017).

RESULTS

The methods that were used in this study are given in Appendix 2B. HPE concentrations are given in the the GSA Data Repository (item 2018095 at http://www.geosociety.org/datarepository/2018/ or on request from editing@geosociety.org). Overall, the heat-production rate data show either a conservation or an increase from subsolidus greenschist-facies and amphibolite-facies protoliths to formerly suprasolidus, now residual granulite-facies rocks (Fig. 2). The Reynolds Range and the Ivrea–Verbano Zone both show similar heat production rates before and after melting and melt loss. In the Reynolds Range, protolith heat production is 2.52 ± 0.06 μW m^{-3}, compared to the residual granulite-facies average of 2.53 ± 0.10 μW m^{-3} (Fig. 2a). Similarly, the Ivrea–Verbano Zone shows virtually identical protolith (2.26 ± 0.13 μW m^{-3}) and residual granulite-facies heat-production rates (2.29 ± 0.5 μW m^{-3}; Fig. 2B). The data from Sierra de Quilmes show a small increase in heat-production rates from the protolith rocks to the residual granulite-facies rocks (2.01 ± 0.09 to 2.17 ± 0.09 μW m^{-3}; Fig. 2C). The transition from protolith rocks to residual granulite-facies rocks in the Mount Stafford and Broken Hill terranes has an increase in heat production rates (2.57 ± 0.05 to 2.81 ± 0.06 μW m^{-3} in Mount Stafford, Fig. 2D; and 2.65 ± 0.08 to 3.30 ± 0.07 μWm^{-3} in Broken Hill, Fig. 2E).

DISCUSSION

The distribution of HPEs, and hence the overall distribution of heat production in continental crust, relies on the growth or breakdown (stability) of the minerals in which they are contained, and the ability of these HPEs to move into the melt or remain in the residue. These minerals are not necessarily uniformly distributed throughout the protolith, meaning that some areas of a terrane may have higher heat-production rates before any melt loss has occurred. Melting during high-grade metamorphism involves the dissolution of U–Th-bearing minerals, so the ability of U- and Th-rich minerals to remain in the granulite-facies residue, rather than be dissolved into the extracted melt, will also largely control whether heat-production rates are higher in the residuum or in the melts that are extracted.

Protolith Composition

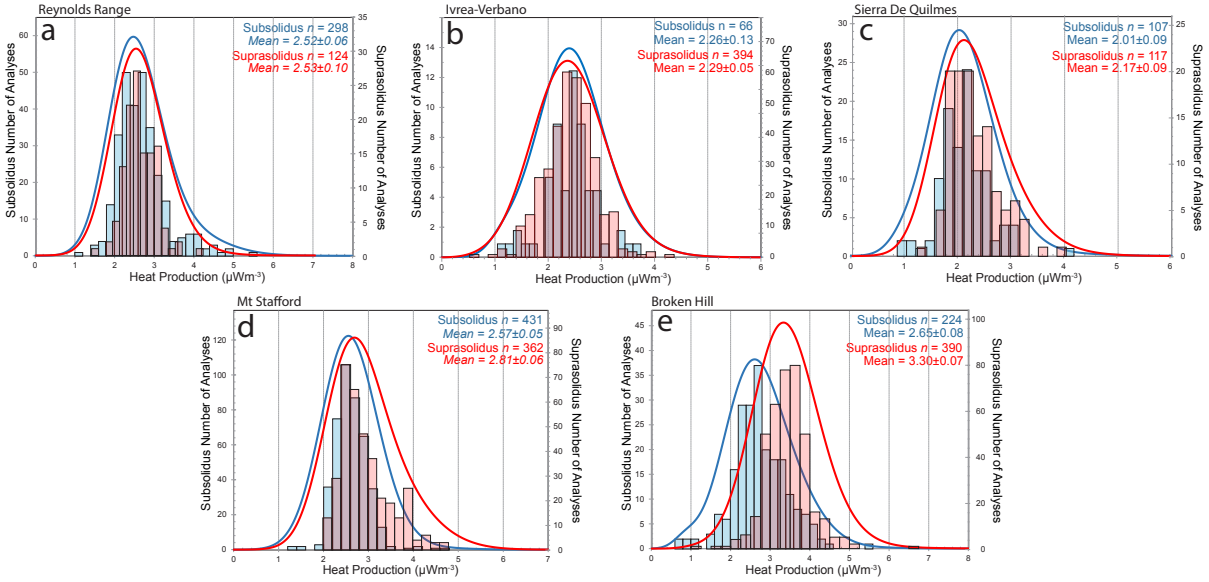


Figure 2. Probability density plot of heat production in protolith (blue) and residual granulite-facies (red) rocks of Reynolds Range, central Australia (A), Ivrea–Verbano Zone, northern Italy (B), Sierra de Quilmes, northwest Argentina (C), Mount Stafford, central Australia (D), and Broken Hill, southern Australia (E).

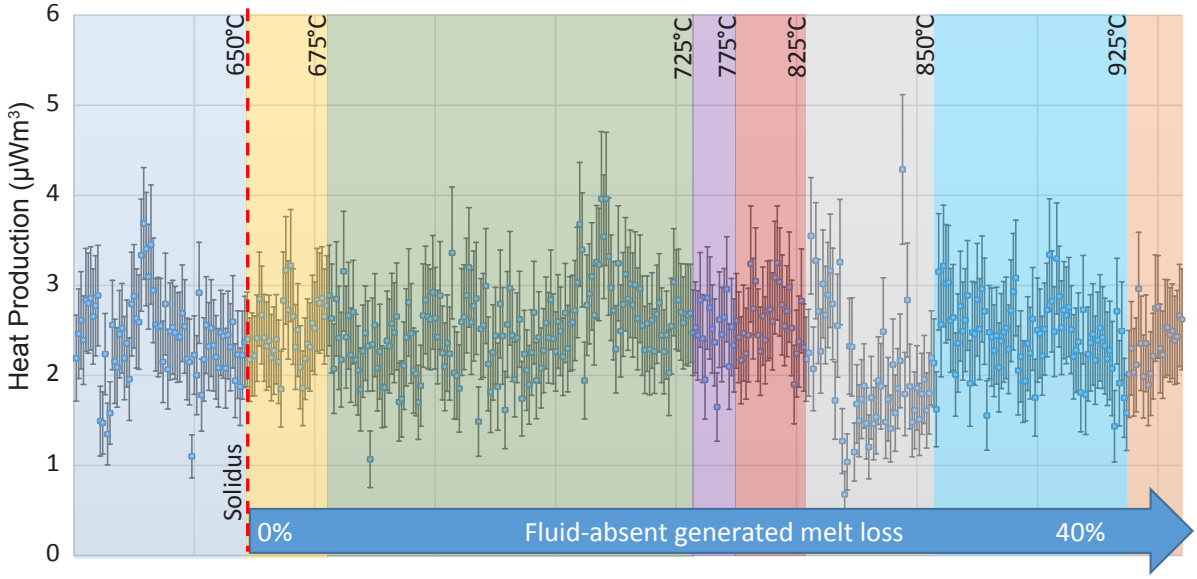


Figure 3. The detailed relationship between heat-production rate and increasing metamorphic grade along the same transect in the Ivera– Verbano Zone (northern Italy) described by Bea and Montero (1999), with metamorphic and melt loss constraints from Redler et al. (2013). Each point represents one analysis, and error bars represent 1 standard deviation.

In each terrane, the transition from subsolidus protolith to residual granulite conditions was associated with no change (or even an increase) in heat-production rate, despite significant melt loss (e.g., White et al., 2003; Büttner et al., 2005; Redler et al., 2013; Morrissey et al., 2014). Conceivably, this pattern may reflect differences in protolith composition. This possibility is evident in Figure 3, which is a transect across strike in the Ivera–Verbano Zone. It shows a localized drop in the heat production rate in rocks metamorphosed between 825 °C and 850 °C that likely reflects a change in protolith composition. However, given that the terranes in this study are geologically unrelated, with metamorphic ages ranging between Palaeoproterozoic and Phanerozoic, and that in the Reynolds Range and Broken Hill examples, a single stratigraphic unit recording the change in metamorphic grade was sampled, we consider it unlikely that the higher-grade areas in each terrane coincidentally had higher protolith concentrations of HPEs.

Role of Accessory Minerals in HPE Distribution

Uranium and Th are primarily hosted within accessory minerals (Bea, 1996). The dominant mineral repositories for U and Th in metapelitic rocks are monazite and zircon (Bea, 1996), with lesser contributions from apatite, xenotime, and allanite. Survival of these accessory minerals is governed by a number of factors relating to bulk rock chemistry, pressure-temperature (*P–T*) conditions, stability of other accessory minerals, microstructural location, and volume and composition of fluids, including melt (Kelsey et al., 2008; Hetherington et al., 2010; Spear, 2010; Harlov et al., 2011; Yakymchuk and Brown, 2014).

In high-grade metapelites, monazite is generally the primary Th host (e.g., Bea, 1996, 2012). Therefore, the stability of monazite during partial melting and melt loss will largely dictate the concentration of Th lost during melt extraction. Fluid-absent partial melting conditions in the five terranes of this study (White et al., 2003; White et al., 2004; Redler et al., 2013; Morrissey et al., 2014; Finch et al., 2017) are widely interpreted to be responsible for large-scale partial melting of the crust (e.g., Clemens, 1990; Brown, 2013). Due to its low solubility in fluid-absent anatectic conditions (Bea, 1996; Stepanov et al., 2012; Yakymchuk and Brown, 2014; Yakymchuk, 2017) monazite

is likely to remain as a stable residual mineral during partial melting, unless the protoliths had extremely low amounts of monazite to begin with (e.g., Kelsey et al., 2008). Further, Stepanov et al. (2012) found that Th has a far stronger partitioning preference for monazite over melt, suggesting that as long as monazite remains stable in the residue during melting, Th will be retained in the granulitic residue following melt loss. However, the modelling of Yakymchuk and Brown (2014) implies that melt loss will lead to depletion of HPEs in the residuum, as long as the drained melt is saturated in HPEs. Our results are contrary to the latter conclusion, but may reflect that the inferred lost melts were undersaturated in U and Th, although it seems unlikely this would have been the case in all five locations. Studies show that monazite and zircon dissolution occurs over very short time scales in hydrous melts, suggesting that kinetic barriers to U and Th entering melt are not significant (e.g., Rapp and Watson, 1986). Conceivably, melt generation and extraction might have occurred so rapidly that mineral–melt interaction was inhibited, although in some of the studied terranes (e.g., Reynolds Range, Broken Hill), the duration of high-grade metamorphism exceeded 10 m.y. (e.g., Morrissey et al., 2014).

Like monazite, zircon also has low solubility in melts that are typically generated from metapelites (e.g., Watson and Harrison, 1983). The widespread presence of detrital zircon, as well as the growth of metamorphic zircon in high-grade metapelites, shows zircon is a significant refractory repository of U, and to a lesser extent, Th (Bea, 1996; Bea and Montero, 1999).

Implicit in consideration of the behaviour of zircon and monazite, with respect to retention of HPEs in the residuum, is that U–Th hosted in zircon and monazite becomes dissolved in melt as a function of zircon and monazite stability (i.e., a function of Zr and P–LREE [light rare earth element] solubility in melt). Conceivably, in anatectic systems, U–Th liberated from dissolution of zircon and monazite could be accommodated by substitution into solid residuum minerals, including monazite and zircon. Data from the Reynolds Range (K.L. Alessio, unpublished data) show that monazite that experienced suprasolidus conditions is significantly richer in Th compared to subsolidus monazite; supporting the notion that solid solutions may buffer the amount of U–Th in the melt.

Distribution of Heat Production in the Crust

Numerous geophysical studies have depicted heat-production rates as a function of depth within Earth's crust (e.g., Lachenbruch, 1968; Pinet and Jaupart, 1987; Singh and Manglik, 2000). These models typically show an exponential decrease in heat production with increasing depth, suggesting the lower crust, which is primarily composed of granulite-facies rocks, is depleted in HPEs. However, as in the five terranes in this study, previous studies—although limited and non-systematic—have found that melt loss (the process that forms residual granulite-facies rocks) results in the conservation or even enrichment of U and Th in the residual granulite-facies material (e.g., Bea and Montero, 1999). Bea (2012) suggested the decrease in heat-production rates in the deep crust was likely due to differences in lithology, and not the processes that create granulite-facies rocks. Overall, the deep crust contains a much higher abundance of mafic rock that is inherently depleted in HPEs (e.g., Bea, 2012; but see also Hacker et al., 2011). This suggests there is not so much a relationship between HPE concentration and large-scale redistribution associated with melting and melt migration, but rather between the abundance of HPE-rich lithologies and depth.

The results of this study suggest that it stands to reason that fluid-absent partial melting of metasedimentary crust will not inherently

generate comparatively HPE-enriched melts and, therefore, HPE-depleted lower crust. Instead, HPE depletion in the granulitic residuum versus enrichment in the melt will largely be controlled by the original HPE concentration of the protolith. Fluid-absent partial melting is only likely to lead to depletion of lower crustal HPE concentrations in terranes where the protoliths to the metasedimentary rocks were derived from HPE-depleted sources. Terranes that have protolithic HPE concentrations above a critical threshold, controlled by the ratio between the HPE saturation in melt versus the concentration in the protolith, will retain or even concentrate HPEs during melt loss. It is important to note that this threshold will be affected by a number of factors that influence HPE saturation and effective removal of the melt, including pressure and temperature gradients, and the composition of both the protolith and the melt (particularly their fluid content).

The redistribution of HPEs within the crust has important implications for long-term lithospheric thermal regime and strength. For example, Sandiford et al. (2002) showed that loss of heat production from the lower crust will lead to long-term crustal cooling and strengthening, creating a feedback process leading to cratonization. Our results show that melt extraction does not necessarily deplete HPE concentrations in the lower crust, thereby limiting the long-term thermomechanical consequences of melt loss from the lower crust. This may explain why some continental regions appear to exhibit long-standing propensity for tectonic rejuvenation (e.g., Raimondo et al., 2014).

CONCLUSIONS

Fluid-absent partial melting and melt loss during high-grade metamorphism of metapelites does not reduce the concentration of HPEs in residual granulite-facies rocks. Therefore, the observed and/or assumed decrease in crustal heat production rate with increasing depth in the crust simply reflects protolithic compositional control, and has little to do with compositional differentiation associated with melting and melt extraction. Because the concentration of HPEs is an important control on the thermomechanical stability of the crust, there is no inherent reason why highly metamorphosed crust should not be tectonically responsive.

ACKNOWLEDGMENTS

We thank Justin Payne and Christopher Kemp for their assistance with data collection. This work was supported by Australian Research Council grants DP160101006 (Kelsey), LP160100578 (Hand) and DP160104637 (Hand). We also thank the University of Adelaide (Australia) for research support funding. Alessio and Williams acknowledge the support of an Australian Government Research Training Program Scholarship.

REFERENCES

Alexandrino, C.H., and Hamza, V.M., 2008, Estimates of heat flow and heat production and a thermal model of the São Francisco craton: International Journal of Earth Sciences, v. 97, p. 289–306, https://doi.org/10.1007/s00531-007-0291-y.

Andreoli, M.A., Hart, R.J., Ashwal, L.D., and Coetzee, H., 2006, Correlations between U, Th content and metamorphic grade in the western Namaqualand Belt, South Africa, with implications for radioactive heating of the crust: Journal of Petrology, v. 47, p. 1095–1118, https://doi.org/10.1093/petrology/egl004.

Bea, F., 1996, Residence of REE, Y, Th and U in granites and crustal protoliths: Implications for the chemistry of crustal melts: Journal of Petrology, v. 37, p. 521–552, https://doi.org/10.1093/petrology/37.3.521.

Bea, F., 2012, The sources of energy for crustal melting and the geochemistry of heat-producing elements: Lithos, v. 153, p. 278–291, https://doi.org/10.1016/j.lithos.2012.01.017.

Bea, F., and Montero, P., 1999, Behavior of accessory phases and redistribution of Zr, REE, Y, Th and U during metamorphism and partial melting of metapelites in the lower crust: An example from the Kinzigite Formation of Ivrea-Verbano, NW Italy: Geochimica et Cosmochimica Acta, v. 63, p. 1133–1153, https://doi.org/10.1016/S0016-7037(98)00292-0.

Brown, M., 2013, Granite: From genesis to emplacement: Geological Society of America Bulletin, v. 125, no. 7-8, p. 1079-1113, https://doi.org/10.1130/B30877.1.

Büttner, S., Glodny, J., Lucassen, F., Wemmer, K., Erdmann, S., Handler, R., and Franz, G., 2005, Ordovician metamorphism and plutonism in the Sierra de Quilmes metamorphic complex: Implications for the tectonic setting of the northern Sierras Pampeanas (NW Argentina): Lithos, v. 83, p. 143–181, https://doi.org/10.1016/j.lithos.2005.01.006.

Clemens, J., 1990, The granulite—granite connexion, Granulites and crustal evolution, Springer, p. 25-36.

Finch, M., Weinberg, R., Hasalová, P., Becchio, R., Fuentes, G., and Kennedy, A., 2017, Tectono-metamorphic evolution of a convergent back-arc: The Famatinian orogen, Sierra de Quilmes, Sierras Pampeanas, NW Argentina: Geological Society of America Bulletin, v. 129, p. 1602–1621.

Hacker, B.R., Kelemen, P.B., and Behn, M.D., 2011, Differentiation of the continental crust by relamination: Earth and Planetary Science Letters, v. 307, p. 501–516, https://doi.org/10.1016/j.epsl.2011.05.024.

Harlov, D.E., Wirth, R., and Hetherington, C.J., 2011, Fluid-mediated partial alteration in monazite: The role of coupled dissolution–reprecipitation in element redistribution and mass transfer: Contributions to Mineralogy and Petrology, v. 162, p. 329–348, https://doi.org/10.1007/s00410-010-0599-7.

Heier, K., and Adams, J., 1965, Concentration of radioactive elements in deep crustal material: Geochimica et Cosmochimica Acta, v. 29, p. 53–61, https://doi.org/10.1016/0016-7037(65)90078-5.

Hetherington, C.J., Harlov, D.E., and Budzyń, B., 2010, Experimental metasomatism of monazite and xenotime: mineral stability, REE mobility and fluid composition: Mineralogy and Petrology, v. 99, p. 165–184, https://doi.org/10.1007/s00710-010-0110-1.

Jaupart, C., Mareschal, J.-C., and Iarotsky, L., 2016, Radiogenic heat production in the continental crust: Lithos, v. 262, p. 398–427, https://doi.org/10.1016/j.lithos.2016.07.017.

Jaupart, C., and Mareschal, J., 2005, Constraints on crustal heat production from heat flow data, in Rudnick, R.L., ed., Treatise on Geochemistry, The Crust: New York, Permagon, v. 3, p. 65–84.

Kelsey, D.E., Clark, C., and Hand, M., 2008, Thermobarometric modeling of zircon and monazite growth in melt-bearing systems: Examples using model metapelitic and metapsammitic granulites: Journal of Metamorphic Geology, v. 26, p. 199–212, https://doi.org/10.1111/j.1525-1314.2007.00757.x.

Kumar, P.S., Menon, R., and Reddy, G., 2007, The role of radiogenic heat production in the thermal evolution of a Proterozoic granulite-facies orogenic belt: Eastern Ghats, Indian Shield: Earth and Planetary Science Letters, v. 254, p. 39–54, https://doi.org/10.1016/j.epsl.2006.11.018.

Kumar, P.S., and Reddy, G., 2004, Radioelements and heat production of an exposed Archaean crustal cross-section, Dharwar craton, south India: Earth and Planetary Science Letters, v. 224, p. 309–324, https://doi.org/10.1016/j.epsl.2004.05.032.

Lachenbruch, A.H., 1968, Preliminary geothermal model of the Sierra Nevada: Journal of Geophysical Research, v. 73, p. 6977–6989, https://doi.org/10.1029/JB073i022p06977.

Morrissey, L.J., Hand, M., Raimondo, T., and

Kelsey, D.E., 2014, Long-lived high-T, low-P granulite facies metamorphism in the Arunta Region, central Australia: Journal of Metamorphic Geology, v. 32, p. 25–47, https://doi.org/10.1111/jmg.12056.

Pinet, C., and Jaupart, C., 1987, The vertical distribution of radiogenic heat production in the Precambrian crust of Norway and Sweden: Geothermal implications: Geophysical Research Letters, v. 14, p. 260–263, https://doi.org/10.1029/GL014i003p00260.

Raimondo, T., Hand, M., and Collins, W.J., 2014, Compressional intracontinental orogens: Ancient and modern perspectives: Earth-Science Reviews, v. 130, p. 128–153, https://doi.org/10.1016/j.earscirev.2013.11.009.

Rapp, R. P., and Watson, E. B., 1986, Monazite solubility and dissolution kinetics: implications for the thorium and light rare earth chemistry of felsic magmas: Contributions to Mineralogy and Petrology, v. 94, no. 3, p. 304-316.

Redler, C., White, R.W., and Johnson, T.E., 2013, Migmatites in the Ivrea Zone (NW Italy): Constraints on partial melting and melt loss in metasedimentary rocks from Val Strona di Omegna: Lithos, v. 175–176, p. 40–53, https://doi.org/10.1016/j.lithos.2013.04.019.

Roy, S., Ray, L., Bhattacharya, A., and Srinivasan, R., 2008, Heat flow and crustal thermal structure in the Late Archaean Closepet Granite batholith, south India: International Journal of Earth Sciences, v. 97, p. 245–256, https://doi.org/10.1007/s00531-007-0239-2.

Sandiford, M., McLaren, S., and Neumann, N., 2002, Long-term thermal consequences of the redistribution of heat-producing elements associated with large-scale granitic complexes: Journal of Metamorphic Geology, v. 20, p. 87–98, https://doi.org/10.1046/j.0263-4929.2001.00359.x.

Sawyer, E.W., Cesare, B., and Brown, M., 2011, When the continental crust melts: Elements, v. 7, p. 229–234, https://doi.org/10.2113/gselements.7.4.229.

Singh, R., and Manglik, A., 2000, Identification of radiogenic heat source distribution in the crust: A variational approach: Sadhana, v. 25, p. 111–118, https://doi.org/10.1007/BF02703753.

Spear, F.S., 2010, Monazite–allanite phase relations in metapelites: Chemical Geology, v. 279, p. 55–62, https://doi.org/10.1016/j.chemgeo.2010.10.004.

Stepanov, A.S., Hermann, J., Rubatto, D., and Rapp, R.P., 2012, Experimental study of monazite/melt partitioning with implications for the REE, Th and U geochemistry of crustal rocks: Chemical Geology, v. 300–301, p. 200–220, https://doi.org/10.1016/j.chemgeo.2012.01.007.

Taylor, S. R., and McLennan, S. M., 1985, The continental crust: its composition and evolution. United States: Blackwell Scientific Pub.,Palo Alto, *CA.*

Taylor, S.R., and McLennan, S.M., 1995, The geochemical evolution of the continental crust: Reviews of Geophysics, v. 33, p. 241–265, https://doi.org/10.1029/95RG00262.

Vilà, M., Fernández, M., and Jiménez-Munt, I., 2010, Radiogenic heat production variability of some common lithological groups and its significance to lithospheric thermal modeling: Tectonophysics, v. 490, p. 152–164, https://doi.org/10.1016/j.tecto.2010.05.003.

Watson, E.B., and Harrison, T.M., 1983, Zircon saturation revisited: Temperature and composition effects in a variety of crustal magma types: Earth and Planetary Science Letters, v. 64, p. 295–304, https://doi.org/10.1016/0012-821X(83)90211-X.

Watt, G., Burns, I., and Graham, G., 1996, Chemical characteristics of migmatites: accessory phase distribution and evidence for fast melt segregation rates: Contributions to Mineralogy and Petrology, v. 125, no. 1, p. 100-111, https://doi.org/10.1007/s004100050209.

White, R., Powell, R., and Halpin, J., 2004, Spatially-focussed melt formation in aluminous metapelites from Broken Hill, Australia: Journal of Metamorphic Geology, v. 22, p. 825–845, https://doi.org/10.1111/j.1525-1314.2004.00553.x.

White, R.W., Powell, R., and Clarke, G.L., 2003, Prograde metamorphic assemblage evolution during partial melting of metasedimentary rocks at low pressures: Migmatites from Mt Stafford, Central Australia: Journal of Petrology, v. 44, p. 1937–1960, https://doi.org/10.1093/petrology/egg065.

Willis, I. L., 1989, Broken Hill Stratigraphic 1:100 000 Geological Sheet: Geological Survey of New South Wales.

Yakymchuk, C., 2017, Behaviour of apatite during partial melting of metapelites and consequences for prograde suprasolidus monazite growth: Lithos, v. 274, p. 412-426, https://doi.org/10.1016/j.lithos.2017.01.009

Yakymchuk, C., and Brown, M., 2014, Behaviour of zircon and monazite during crustal melting: Journal of the Geological Society, v. 171, no. 4, p. 465-479, https://doi.org/10.1144/jgs2013-115.

CHAPTER 4

This chapter has been approved for publication to *Lithos* as:
Alessio K. L., Hand M., Hasterok D., Morrissey L. J., Kelsey D. E. & Raimondo T. 2019 Thermal modelling of very long-lived (>140 Myr) high thermal gradient metamorphism as a result of radiogenic heating in the Reynolds Range, central Australia, Lithos.

Statement of Authorship

Title of Paper	Thermal modelling of very long-lived high thermal gradient metamorphism
Publication Status	☐ Published ☐ Accepted for Publication ☑ Submitted for Publication ☐ Unpublished and Unsubmitted w ork w ritten in manuscript style
Publication Details	Alessio, K.L., Hand, M., Hasterok, D., Morrissey, L.J., Kelsey, D.E., Raimondo, T., 2019. Thermal modelling of very long-lived high thermal gradient metamorphism. Lithos.

Principal Author

Name of Principal Author (Candidate)	Kiara Alessio
Contribution to the Paper	Fieldwork Data collection and modelling Manuscript writing Ideas for manuscript
Overall percentage (%)	60
Certification:	This paper reports on original research I conducted during the period of my Higher Degree by Research candidature and is not subject to any obligations or contractual agreements with a third party that would constrain its inclusion in this thesis. I am the primary author of this paper.
Signature	[redacted] Date 30/07/2019

Co-Author Contributions

By signing the Statement of Authorship, each author certifies that:

i. the candidate's stated contribution to the publication is accurate (as detailed above);

ii. permission is granted for the candidate in include the publication in the thesis; and

iii. the sum of all co-author contributions is equal to 100% less the candidate's stated contribution.

Name of Co-Author	Martin Hand
Contribution to the Paper	Manuscript editing Ideas for manuscript Fieldwork Data collection
Signature	[redacted] Date 30/07/2019

Name of Co-Author	Derrick Hasterok
Contribution to the Paper	Manuscript editing Coding of modelling software
Signature	[redacted] Date 26/07/2019

Name of Co-Author	Laura Morrissey		
Contribution to the Paper	Manuscript editing Data modelling		
Signature		Date	30/07/2019

Name of Co-Author	David Kelsey		
Contribution to the Paper	Manuscript editing Data modelling		
Signature		Date	25/07/2019

Name of Co-Author	Tom Raimondo		
Contribution to the Paper	Manuscript editing Data modelling		
Signature		Date	26/07/2019

ABSTRACT

The Reynolds Range in the Paleo-Mesoproterozoic Aileron Province of central Australia exposes a differentially exhumed metamorphic rock system varying from greenschist- to granulite-facies. Calculated *P–T* pseudosections indicate that peak metamorphic conditions in greenschist-facies areas reached temperatures of ~480 °C and pressures of 3.2–5 kbar. Peak conditions at amphibolite-facies are constrained to 500–620 °C and 1.3–3.8 kbar. *P–T* modelling of two petrologically different granulite-facies samples indicate that peak conditions in the exhumed granulite-facies rocks reached 780–920 °C and 3.5–5.4 kbar, corresponding to high apparent thermal gradients of 152–218 °C/kbar. In the amphibolite-facies rocks, in situ LA–ICP–MS U–Pb monazite geochronology records ages that range between 1680–1550 Ma. In contrast, in the granulite-facies rocks, monazite records ages of ca. 1560 Ma. The terrane contains significantly elevated rates of crustal heat production compared to global norms, and when incorporated into lithospheric thermal models with reasonable boundary conditions and average thermal properties, can plausibly account for the long-lasting metamorphic conditions. The thermal modelling shows that the long lasting (>100 Myr) record of monazite U–Pb ages, supported by previous studies, reflects a continuous duration of elevated crustal temperatures, an interpretation consistent with texturally simple mineral assemblages that lack any evidence for polymetamorphism. In high-crustal heat production terranes, high thermal gradients and high temperatures will persist until exhumation removes the upper crust. This physical reality provides a basis for the existence of arbitrarily long-lived metamorphic systems, even under high thermal gradients that are generally considered to be thermally anomalous. However, such thermal anomalism is not remarkable, as there is abundant evidence for elevated rates of crustal heat production in the Reynolds Range and worldwide. In terranes where accessory minerals record large continuous ranges of age, robust volumetric measurements of crustal heat production rates are a necessary step in evaluating the potential thermal significance of such geochronological records. Failure to document rates of crustal heat generation invalidates many interpretations for drivers of metamorphism.

INTRODUCTION

Crustal environments that record high-temperature–low-pressure (HT–LP) metamorphism at granulite-facies conditions require significant energy to facilitate such geothermal gradients. Generally these requirements either demand that the lithosphere is significantly thinned, that metamorphism was accompanied by voluminous magmatism, or that high thermal gradients were generated during rapid exhumation of hot, deeply buried rocks (e.g. Okay et al., 2014; Sisson et al., 1989; Wickham and Oxburgh, 1985). Importantly these mechanisms typically create metamorphic–geologic associations (for example syn-metamorphic high-temperature magmas, large extensional detachment systems etc.) that clarify the thermal drivers, and create characteristic time scales for the duration of the high temperature conditions. In comparison to external thermal inputs or structural drivers, the concentration of heat producing elements in the crust is often overlooked as a driver for high-grade metamorphic conditions. However, it has been recognised that in some regions, the concentration of heat producing elements contained in metasedimentary and granitic reservoirs may be sufficiently high to generate high-grade metamorphism at comparatively shallow depths (e.g. Anderson et al., 2013; Andreoli et al., 2006; Clark et al., 2011; Horton et al., 2016; Jaupart et al., 2016; McLaren and Powell, 2014; McLaren et al., 1999; Morrissey et al., 2014; Sandiford and Hand, 1998). High thermal gradient terranes largely heated by internal heat sources will only cool significantly if they are exhumed or undergo significant melt loss (Alessio et

al., 2018), and so have the potential to be extremely long-lived in regions that do not experience significant deformation. However, one of the challenges in deciphering the duration of metamorphism in high-grade terranes, and therefore the likely thermal driver, is that the prograde evolution (and its geochronology) is commonly obliterated or obscured by the peak and high-temperature retrograde conditions. Furthermore, the growth of accessory minerals typically used to constrain the duration of high–grade metamorphism is biased toward the end of the thermal evolution because their physiochemical behaviours appear to be governed largely by melt crystallisation (Kelsey et al., 2008; Rubatto et al., 2006; Schaltegger et al., 1999; Williams, 2001; Yakymchuk and Brown, 2014). Therefore, temporal records using accessory minerals in high-grade rocks are commonly incomplete. One way to better determine the durations of energetic metamorphic regimes is to use natural laboratories where low-grade regions and their unambiguously higher-grade equivalents are preserved. Such terranes preserve a more complete picture of the thermal duration. Furthermore, reactive minerals such as monazite have a greater potential to record prograde metamorphism in subsolidus rocks than in anatectic rocks (e.g. Kelsey et al., 2008).

The Reynolds Range in the Aileron Province of the North Australian Craton provides an uncommon and fortuitous situation in which a metapelitic stratigraphic unit can be continuously followed from greenschist- to granulite-facies conditions over a distance of ~100 km (Dirks et al., 1991; Hand and Buick, 2001; Stewart, 1981). There have been a number of studies focused on the metamorphic and temporal evolution of the high-grade parts of the Reynolds Range and the neighbouring Anmatjira Range (Anderson et al., 2013; Buick et al., 1998; Clarke and Powell, 1991; Dirks et al., 1991; Morrissey et al., 2014; Rubatto et al., 2001; Vry et al., 1996; Williams et al., 1996). In high-grade areas geochronology suggests that HT–LP anatectic conditions were maintained for at least 70 Myr (Anderson et al., 2013; Morrissey et al., 2014; Vry and Baker, 2006; Williams et al., 1996), and that elevated levels of crustal heat production played a critical role in generating the high thermal gradient regime (e.g. Anderson et al., 2013; Hand and Buick, 2001; Morrissey et al., 2014; Sandiford and Hand, 1998). However, there have been few studies that seek to understand the metamorphic record contained in the lower grade parts of the terrane (cf. Dirks et al., 1991; Dirks and Wilson, 1990). We present calculated metamorphic phase diagrams and new geochronology from the low-grade and high-grade parts of the Reynolds Range to obtain a more complete picture of the potential duration and conditions of metamorphism. We also present thermal models built on estimations of crustal heat generation to assess the possibility of radiogenic-driven metamorphism in the region.

GEOLOGICAL BACKGROUND

The Reynolds–Anmatjira Ranges form a northwest-trending region of outcrop within the Aileron Province in central Australia (Figure 1). They are primarily composed of metasedimentary and granitic rocks. The oldest rocks are pelitic and psammitic metasedimentary rocks of the Lander Rock Formation, which have depositional ages between 1840 and 1806 Ma (Claoué-Long et al., 2008; Hand and Buick, 2001). Voluminous granitic magmatism between 1810 and 1790 Ma resulted in localised high thermal gradient metamorphism of the Lander Rock Formation (Collins and Williams, 1995; Rubatto et al., 2001; Worden et al., 2008). The 1810–1790 Ma granitic rocks and the Lander Rock Formation are unconformably overlain by shallow marine successions of the Reynolds Range Group, which were deposited between 1800 and 1780 Ma (Claoué-Long et al., 2008; Dirks, 1990; Hand and Buick, 2001). The Reynolds Range Group was intruded by voluminous felsic magmas towards the

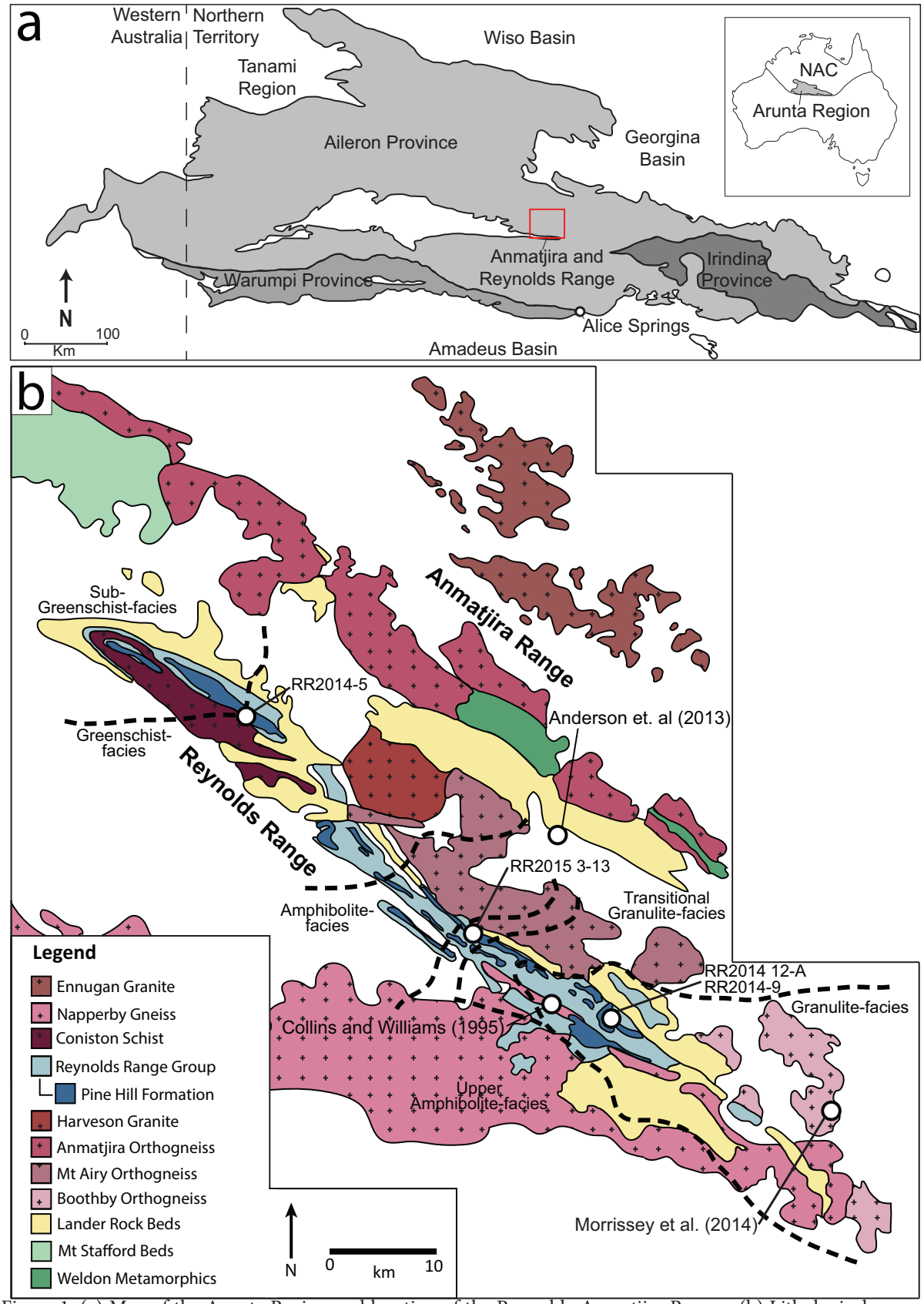


Figure 1. (a) Map of the Arunta Region and location of the Reynolds-Anmatjira Ranges. (b) Lithological map of Reynolds Range (simplified from Stewart 1981). Locations of samples used in this study and those from other relevant studies are represented by white circles.

end of its deposition at approximately 1780 Ma (Hand and Buick, 2001; Howlett et al., 2015). The subsequent Chewings Orogeny at 1595–1520 Ma resulted in long-lived, high thermal gradient metamorphism and pervasive deformation associated with NE–SW shortening that created the dominant structures in the Reynolds–Anmatjira Ranges (Dirks and Wilson, 1990; Hand and Buick, 2001; Morrissey et al., 2014; Rubatto et al., 2001; Vry et al., 1996; Williams et al., 1996). The metamorphic record of the Chewings Orogeny in the Reynolds–Anmatjira Ranges varies from greenschist facies in the northwest to granulite facies in the southeast (Figure 1b). The final event affecting the region was the 450–320 Ma Alice Springs Orogeny, which exhumed the Precambrian metamorphic sequences and exposed the regional HT–LP metamorphic gradient observed today (Cartwright et al., 1999; Raimondo et al., 2011).

Previous P–T work in the Reynolds Range region suggests the greenschist-facies rocks at the northwest end of the range reached maximum peak pressures of <3 kbar and temperatures of <400 °C (Dirks et al., 1991; Dirks and Wilson, 1990). Moving southeast, amphibolite-facies rocks record temperatures of <600 °C (Dirks et al., 1991; Hand and Buick, 2001) and have a monazite age of 1576 ± 5 Ma, derived from grain separates (Rubatto et al., 2001). In the southeastern part of the range, metamorphism is granulite-grade with conditions of 6.0–7.0 kbar and 750–870 °C (Buick et al., 1998; Morrissey et al., 2014). Metasedimentary granulites have U–Pb monazite ages of ca. 1585–1557Ma (grain separates; Rubatto et al., 2001) and 1580–1520 Ma (in situ; Morrissey et al., 2014; Prent et al., 2019). Zircon grain separates yield U–Pb ages of ca. 1587 Ma (Rubatto et al., 2001). In addition to the dominant 1580–1520 Ma ages, Collins and Williams (1995) reported an age of 1659 ± 6 Ma from metamorphic zircon grain separates from granulite-facies granitic orthogneiss rocks (shown in Figure 1b).

The nearby Anmatjira Range shows a similar regional metamorphic gradient to the Reynolds Range. With the exception of localised ca. 1800 Ma high-grade metamorphism in the Mt Stafford area in the westernmost part of the range (Greenfield et al., 1996; Rubatto et al., 2006; Wang et al., 2014; White et al., 2003), the lowest metamorphic grades occur in the northwest Anmatjira Range, with conditions of <3 kbar and <400 °C (Hand and Buick, 2001). The high-grade area in the SE part of the range records peak conditions of 870–920 °C and 6.5–7.2 kbar, (Anderson et al., 2013). Peak to post-peak metamorphism is interpreted to have occurred at ca. 1580–1555 Ma, based on monazite U–Pb data (Anderson et al., 2013). In addition, Anderson et al. (2013) also found additional discrete monazite age peaks between 1700–1630 Ma, largely confined to inclusions in garnet. These older age populations have not been definitively attributed to any particular event.

Field Relationships

This study focuses on metapelitic rocks in the Pine Hill Formation, within the Reynolds Range Group. In the northwest-most part of the Reynolds Range the Pine Hill Formation is sub-greenschist and is a fine-grained muscovite–chlorite–quartz slate, interlayered with psammite (Figure 2a). To the south, biotite appears with increasing metamorphic grade. At amphibolite facies, the rocks contain andalusite porphyroblasts that are enclosed by the regional foliation, defining the assemblage andalusite–biotite–muscovite–quartz ± magnetite ± ilmenite (Figure 2b). The upper amphibolite-facies rocks contain sillimanite–muscovite–K-feldspar, rather than andalusite. The rocks in this region also contain small volumes of leucosome (<1 %) consisting of K-feldspar–plagioclase–quartz ± muscovite ± tourmaline, interpreted to reflect the onset of partial melting. With increasing metamorphic grade further

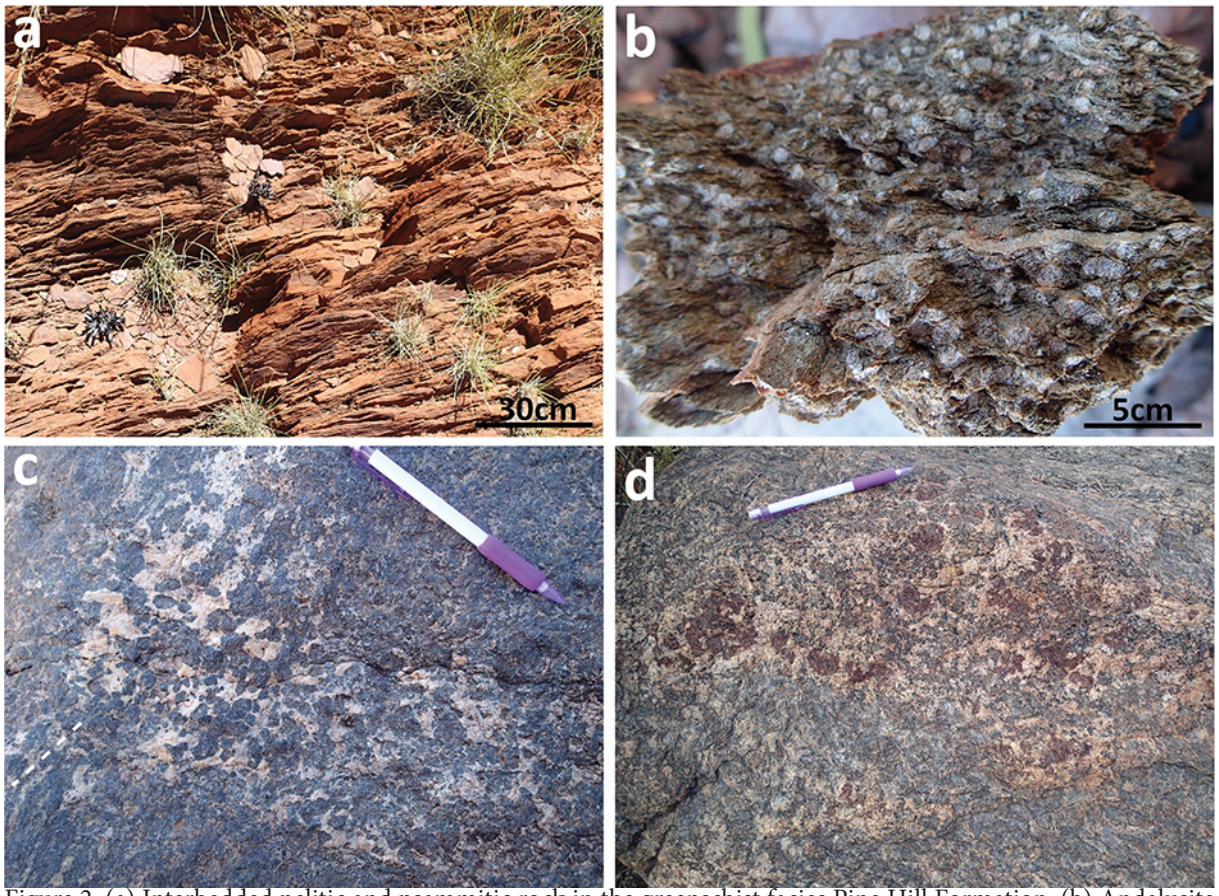


Figure 2. (a) Interbedded pelitic and psammitic rock in the greenschist facies Pine Hill Formation. (b) Andalusite porphyroblasts enclosed by a biotite-muscovite foliation that is the axial surface to the regional SE-trending upright isoclinal folds that deform the Reynolds Range Group (Dirks and Wilson 1990, Hand and Buick 2001). (c) Cordierite porphyroblasts in a K-feldspar–quartz leucosome in the granulite facies Pine Hill Formation. (d) Garnet porphyroblasts in a K-feldspar–quartz–sillimanite leucosome in the granulite facies Pine Hill Formation.

to the southeast, leucosomal segregations become more common and the rocks dominantly contain biotite–sillimanite–quartz–magnetite–ilmenite ± K-feldspar assemblages. At the highest metamorphic grades, the Pine Hill Formation contains cordierite or garnet-bearing leucosomes that both parallel and overprint the fabric (Figure 2c, d). The resulting peak granulite-facies assemblages are cordierite–biotite–sillimanite–K-feldspar–quartz–ilmenite–(melt) and garnet–biotite–sillimanite–K-feldspar–quartz–ilmenite–(melt).

Petrography

This study focuses on four samples of different metamorphic grade from the Pine Hill Formation. The samples are: one greenschist-facies rock (RR2014-5), one subsolidus amphibolite-facies rock (RR2015 3-13), and two granulite-facies rocks of different mineralogy (RR2014-9 and RR2014-12A). The foliation carries the change in metamorphic grade from greenschist- to granulite-facies. Sample locations are shown in Figure 1b.

Greenschist-facies (RR2014-5; Lat: -22° 13' 10.84" Long: 132° 43' 18.21")

This sample contains biotite, muscovite, chlorite, quartz, rutile and minor tourmaline. The sample is fine-grained (<0.25 mm) and homogeneous (Figure 3a). The rock is intensely foliated, with the fabric defined by aligned muscovite–biotite–chlorite. The rutile and tourmaline are minor (<2%), but are uniformly distributed. The sample is dominated by muscovite and quartz. The interpreted peak assemblage is biotite–muscovite–chlorite–quartz–rutile.

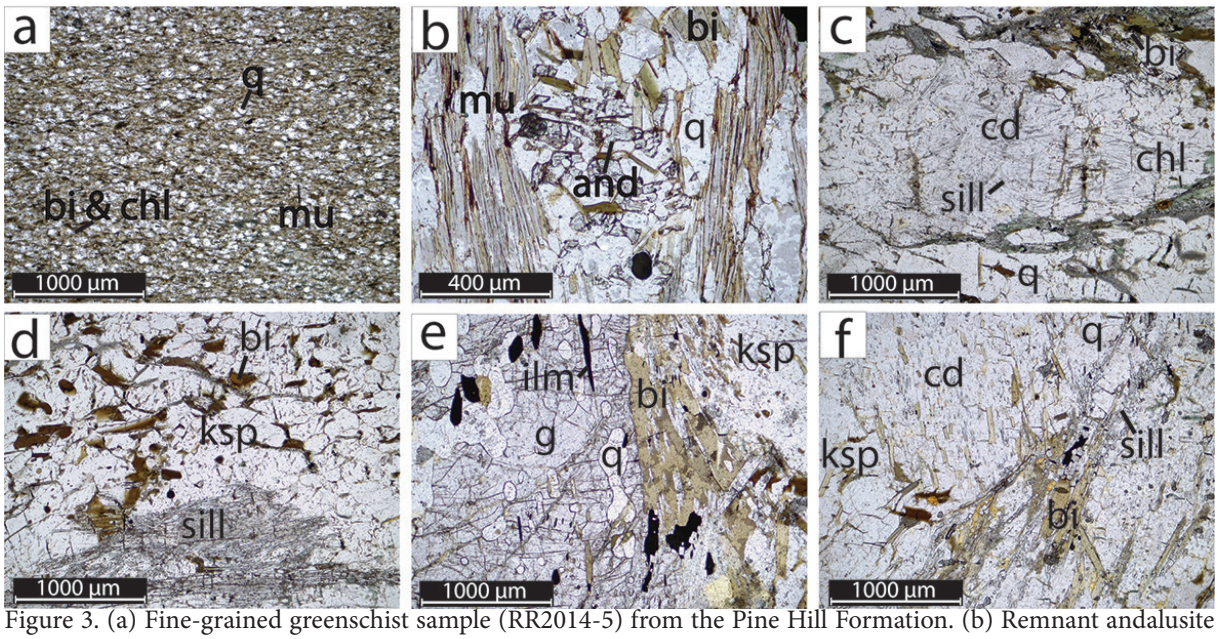


Figure 3. (a) Fine-grained greenschist sample (RR2014-5) from the Pine Hill Formation. (b) Remnant andalusite porphyroblast wrapped by a muscovite–biotite foliation in amphibolite-facies sample RR2015 3-13. (c) Cordierite porphyroblasts with sillimanite inclusions are wrapped by a weak sillimanite–biotite foliation in the sample of cordierite-rich granulite (RR2014-9). (d) Biotite intergrown with K–feldspar and clusters of randomly oriented sillimanite in the cordierite-rich granulite (RR2014-9). (e) Garnet porphyroblast rimmed by biotite in the garnet-bearing granulite (RR2014 12-A). (f) Cordierite with quartz, biotite and some sillimanite inclusions in the garnet-bearing granulite. Biotite is anhedral and coarser-grained than sillimanite (RR2014-12A). Mineral abbreviations after Holland and Powell (2011).

Amphibolite-facies (RR2015 3-13; Lat: -22° 23' 20.99' Long: 132° 53' 8.72")

This sample contains biotite, muscovite, andalusite, quartz and minor pyrite. Alternating mica-rich and quartz-rich layers are present throughout the sample. Andalusite porphyroblasts (5–10 mm) occur throughout the matrix and contain small inclusions of quartz, biotite and muscovite (<1 mm). Biotite and muscovite form a strong foliation that constitutes the regional northwest-southeast trending foliation, and wraps andalusite grains containing curvilinear inclusion patterns, suggesting that andalusite grew during the development of the enclosing foliation (Figure 3b). The interpreted peak metamorphic assemblage is biotite–muscovite–andalusite–quartz.

Cordierite granulite (RR2014-9; Lat: -22° 31' 19.57" Long: 133° 5' 59.13")

This sample contains biotite, cordierite, magnetite, ilmenite, sillimanite, quartz and K-feldspar. The sample is compositionally layered on the cm-scale, with foliation defined by biotite-sillimanite-rich and cordierite-rich domains. The foliation itself is defined by aligned sillimanite and minor biotite (Figure 3c). Cordierite is abundant (~40% of the sample volume), and generally occurs as large (3–6 mm) poikiloblastic grains with inclusions of sillimanite and quartz (<1 mm; Figure 3c). K-feldspar grains (1–5 mm), occur in contact with biotite and sillimanite and contain inclusions of biotite, sillimanite and quartz (Figure 3d). Biotite is foliated in some parts of the rock, but more commonly it occurs as anhedral grains at the margins of sillimanite clusters and between K-feldspar grains (Figure 3c, d). Although foliated in some parts of the rock, biotite does not occur within cordierite and has a tendency to mantle sillimanite, and is therefore interpreted as a retrograde mineral. Minor ilmenite and magnetite occur as small grains (<1mm) throughout the matrix of the sample, primarily bordering biotite.

Late stage chlorite is largely anhedral and only occurs adjacent to clusters of sillimanite and biotite. The interpreted peak metamorphic

assemblage is sillimanite–cordierite–K-feldspar–quartz–magnetite–ilmenite.

Garnet granulite (RR2014-12A; Lat: -22° 31' 35.00" Long: 133° 5' 55.10")
This sample contains garnet, biotite, cordierite, ilmenite, sillimanite, quartz and K-feldspar, and comes from an outcrop with garnet-bearing leucosomes. Coarse-grained garnet (10–25 mm) occurs throughout the matrix surrounding the leucosomes, in addition to occurring in leucosomes. Garnet commonly contains inclusions of quartz and ilmenite, but also rarely sillimanite (<1 mm; Figure 3e). Coarse-grained K-feldspar (10–15 mm) has abundant fine-grained biotite and quartz inclusions (1–2 mm; Figure 3f). Poikiloblastic cordierite (5–15 mm) contains quartz, sillimanite and biotite inclusions (<2mm; Figure 3f). Biotite occurs as both randomly orientated, anhedral grains in the matrix and at the margins of garnet and sillimanite, and less commonly as euhedral grains that are aligned, defining the regional foliation (Figure 3e, f). Quartz (1–3 mm) is present throughout the matrix. Small ilmenite grains (1–2 mm) typically occur in contact with biotite and garnet grains. Minor chlorite occurs adjacent to biotite and sillimanite grains.
The peak assemblage is interpreted to be biotite–garnet–K-feldspar–cordierite–sillimanite–quartz –ilmenite. Some biotite is included in cordierite and occurs as a foliation-defining mineral, but some of the biotite also occurs mantling garnet and sillimanite, suggesting that there are two generations of biotite, one of which is peak and the other being retrograde.

ANALYTICAL METHODS

Bulk Rock and Mineral Chemistry

Whole-rock geochemical analyses were obtained for each sample. These data were used for phase equilibria modelling. The data were obtained using X-ray Fluorescence (XRF) spectrometry at the Earth and Environmental Department, Franklin and Marshall College, Lancaster PA, USA. Bulk rock analyses are given in Table 1.

Mineral compositions were obtained using a Cameca Electron MicroProbe SXFive hosted by Adelaide Microscopy, at the University of Adelaide. A beam size of 3 μm was used with beam conditions of 15 kV and 20 nA. All microprobe analyses are presented in Appendix A.

Phase Equilibria Modelling and Mineral Modal Proportions

Phase equilibria models were calculated for four samples of different metamorphic grade from the Pine Hill Formation. Phase equilibria models were calculated using the phase equilibria modelling program THERMOCALC 3.40 (Holland and Powell, 2011; Powell and Holland, 1988) in the chemical system $MnO–Na^2O–CaO–K^2O–FeO–MgO–Al^2O^3–SiO^2–H^2O–TiO^2–O$ (MnNCKFMASHTO), where 'O' is Fe^2O^3, using the latest internally-consistent thermodynamic dataset 'ds62' (Holland and Powell, 2011) and activity–composition models reparameterised for Mn (Powell et al., 2014; White et al., 2014a; White et al., 2014b). Calculated models were contoured for the modal proportions of minerals using the program TCInvestigator (Pearce et al., 2015). Mineral modes used for phase equilibria modelling were determined by pixel counting of thin section for opaque minerals, biotite and garnet. Proportions of the remaining minerals were calculated using averaged mineral chemistry and the bulk rock composition. Volumetric modal proportions were then converted into 1 atom normalised molar proportions to equate them with modal outputs generated by THERMOCALC v3.40 (Holland and Powell, 2011; Powell and Holland, 1988). Normalised proportions are given in Table 2 for the amphibolite- and granulite-facies samples, but were not calculated for the greenschist, as it was extremely fine-grained.

Table 1. Modal proportions of peak minerals present in each sample converted into 1 atom normalised molar proportions to equate with modal outputs generated by THERMOCALC v3.40.

Table 1. Bulk rock XRF analyses used for phase equilibria modelling each of the samples. Analyses are given in wt%.

Sample	RR2014-5	RR2015 3-13	RR2014-9	RR2014-12A
SiO_2	66.05	65.69	66.07	62.53
TiO_2	0.56	0.60	0.88	0.71
Al_2O_3	17.51	19.06	18.51	21.5
MnO	0.02	0.02	0.06	0.04
MgO	1.48	1.59	4.38	1.61
CaO	0.03	0.03	0.08	0.18
Na_2O	0.14	0.18	0.03	0.36
K_2O	5.87	6.11	2.83	6.31
P_2O_5	0.07	0.05	0.04	0.12
LOI	3.07	2.59	1.34	1.36
Fe_2O_3T	4.95	6.35	5.95	5.55
Total	99.75	102.27	100.17	100.27

The oxidation state and water content of the samples were determined by T–M_O and T–M_{H2O} sections (see White et al., 2000). Morrissey et al. (2014) suggest peak pressures of 6.5 kbar in the easternmost Reynolds Range, approximately 20 km east of sample RR2014-9 and RR2014-12A (Figure 1b). In the central Reynolds Range, andalusite has been pseudomorphed by sillimanite, suggesting maximum pressures of approximately 3.8 kbar at ~550 °C, prior to sillimanite growth. A constant P–T gradient was assumed between the northwest greenschist-facies end of the range and the granulite facies rocks at in the easternmost Reynolds Range to determine the pressures for the calculation of T–M_O and T–M_{H2O} sections. The T–M_O section for the greenschist-facies sample was calculated at a pressure of 2 kbar, the amphibolite-facies sample at 3 kbar and the granulite-facies samples at 4.5 kbar. The greenschist and amphibolite-facies models were calculated with water in excess. Water content for the granulite-facies samples was selected based on T–M_{H2O} sections. The oxidation state and water content for each sample were selected to best represent the modal proportions of minerals observed in the peak assemblage in the T–MO and T–M_{H2O} sections. All T–MO and T–MH2O sections and relevant TCInvestigator v2.0 models are given in Appendix B.

U–Pb monazite geochronology

U–Pb monazite dating was done using Laser¬-Ablation-Inductively Coupled Plasma-Mass Spectrometry (LA-ICP-MS) at the University of Adelaide. Several attempts were made to locate and analyse monazite in the amphibolite-facies sample (RR2015 3-13) in thin section and in mineral separates. However, neither of these methods were successful, likely due to the small size of monazite grains (<14 μm). Instead, amphibolite-facies monazites were analysed in polished rock-blocks mounted in resin. In the granulite-facies samples (RR2014-9 and RR2014-12A), monazite grains are typically <20 μm and so were analysed in situ in thin sections. All samples were imaged using a back-scattered electron (BSE) detector on a FEI Quanta 600 Scanning Electron Microscope (SEM) accompanied with Mineral Liberation Analysis (MLA) software in order to locate monazite in the thin sections. Prior to U–Pb analysis, monazite was imaged in situ using BSE on the same SEM to characterise the microstructural location and compositional

Table 2. Modal proportions of peak minerals present in each sample converted into 1 atom normalised molar proportions to equate with modal outputs generated by THERMOCALC v3.40.

Amphibolite-facies		Cordierite granulite		Garnet granulite	
Mineral	**Mol.%**	**Mineral**	**Mol.%**	**Mineral**	**Mol.%**
Biotite	18.0	Biotite	5.2	Biotite	14.4
Quartz	50.5	Quartz	38.1	Quartz	23.4
Muscovite	30.3	Sillimanite	2.4	Sillimanite	13.4
Andalusite	1.1	K-feldspar	14.6	K-feldspar	35.5
Opaques	0.1	Cordierite	39.4	Cordierite	9.1
		Opaques	0.3	Garnet	4.1

variation of each grain. The textural locations of representative monazites from each sample are given in Appendix C.

U–Pb isotopic analyses of monazite were obtained in situ using a Resonetics (now Australian Scientific Instruments) M50 ArF Excimer laser in a He ablation atmosphere, coupled to an Agilent 7700cs ICP–MS at Adelaide Microscopy, the University of Adelaide. Monazite grains were ablated with a spot size of 13 μm and a frequency of 5 Hz. Total analysis time was 90 seconds and included 30 seconds of background measurement and 60 seconds of ablation. Monazite data were reduced using the correction program 'Iolite' (Paton et al., 2011). The full dataset of LA–ICP–MS monazite analyses collected in this study are provided in Appendix D. U–Pb fractionation was corrected for using the primary standard MAdel (TIMS normalisation data: $^{207}Pb/^{206}Pb$ = 491 ± 2.7 Ma, $^{206}Pb/^{238}U$ = 518.37 ± 0.99 Ma and $^{207}Pb/^{235}U$ = 513.13 ± 0.19 Ma; Payne et al., 2008). Data accuracy was monitored using the in house monazite standard 94-222 ($^{206}Pb/^{238}U$ age = 449.7 ± 3.4 Ma; Maidment, 2005). Throughout the analytical sessions, the 222 standard yielded a weighted mean 206Pb/238U age of 448.2 ± 1.4 Ma (MSWD = 3.1). Data were plotted using Isoplot (Ludwig, 2003).

RESULTS

Phase Equilibria Modelling

Greenschist-facies metapelite

The interpreted peak assemblage in sample RR2014–5 is biotite–muscovite–chlorite–quartz–rutile. This assemblage does not occur in P–T the pseudosection. However, this assemblage is likely best represented by the field containing epidote–biotite–muscovite–chlorite–quartz–rutile. In this field epidote is modelled to be present in very low abundances (<0.1%), which may be a result of Ca from accessory minerals, such as apatite, that cannot be modelled in THERMOCALC. Therefore modelling stabilises Ca-rich minerals that may not necessarily exist in the rock. The most reasonable choice of peak field is modelled to occur at conditions of 1–6 kbar and 400–490 °C (Figure 4a). This field does not offer any constraint on pressure. The upper temperature boundary is constrained by the presence of margarite and ilmenite (Figure 4a).

Amphibolite-facies metapelite

TThe interpreted peak assemblage for sample RR2015 3-13 is biotite–muscovite–quartz–andalusite. The assemblage biotite–muscovite–quartz–andalusite–ilmenite occurs at conditions of 1.3–3.8 kbar and 500–620 °C (Figure 4b). Modelled modal abundances of ilmenite indicate that it is present in proportions of <1% in the peak field. It is therefore possible that ilmenite may not have been present in the thin section, but is present as a minor component of the rock sample used for geochemistry.

Cordierite-rich granulite-facies metapelite

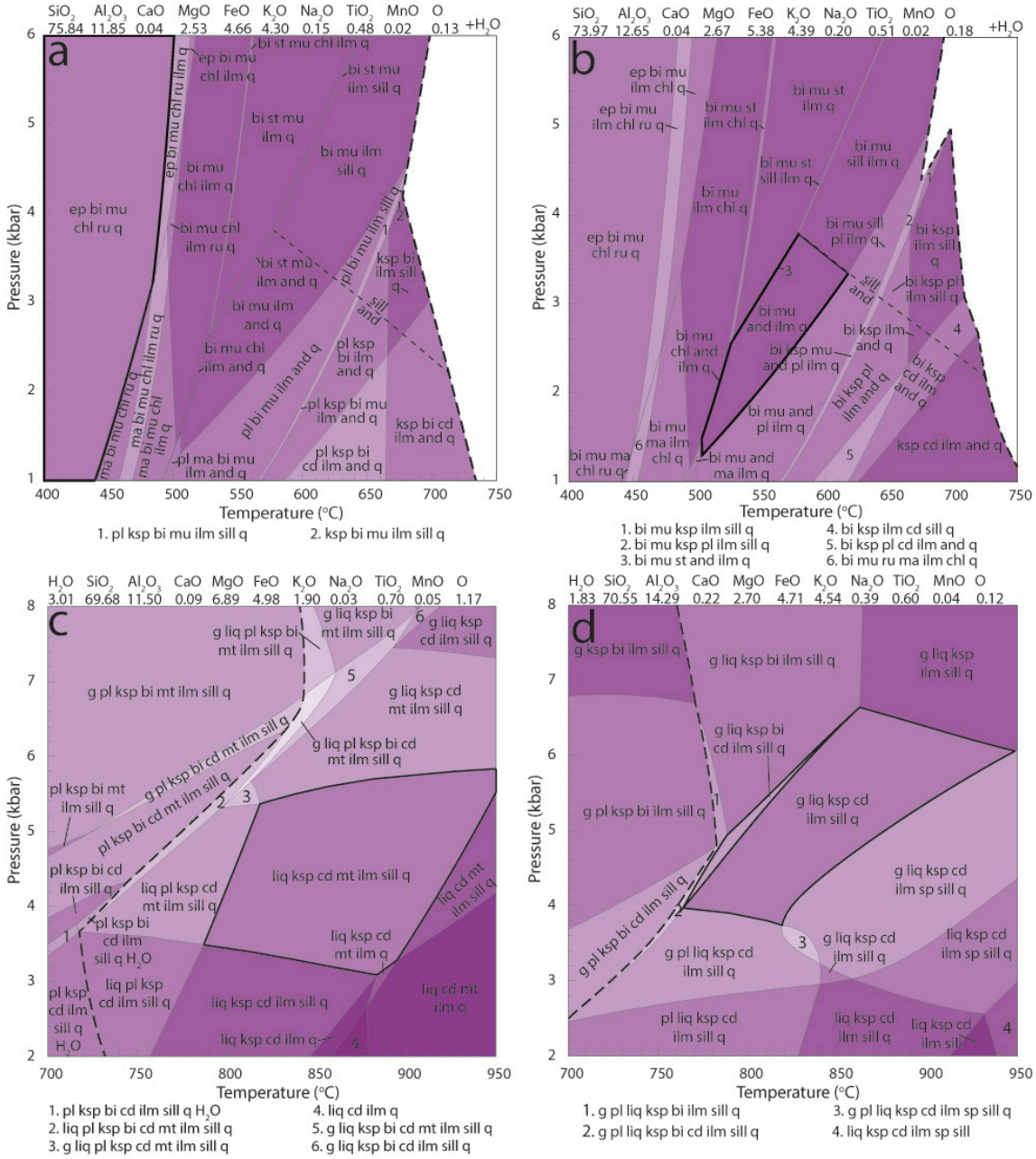


Figure 4. Calculated *P–T* pseudosections for samples of the Pine Hill Formation. The bulk composition (in mol%) is given above the pseudosection. The bold dashed line represents the solidus and the field outlined in bold is the interpreted peak assemblage. (a) Greenschist-facies sample RR2014-5. (b) Amphibolite-facies sample RR2015 3-13. (c) Cordierite-rich granulite sample RR2014-9. (d) Garnet-bearing granulite sample RR2014-12A. Mineral abbreviations after Holland and Powell (2011).

The interpreted peak assemblage in sample RR2014-9 is cordierite–sillimanite–K-feldspar–quartz–magnetite–ilmenite–melt. The peak assemblage is stable over a large range of P–T conditions (3.1–5.6 kbar and 780–950 °C; Figure 4c). The absence of garnet in the rock provides an upper pressure constraint, whereas the absence of plagioclase provides a lower temperature constraint.

Garnet-bearing granulite-facies metapelite

The interpreted peak assemblage in sample RR2014-12A is garnet–cordierite–K-feldspar–sillimanite–quartz–ilmenite–melt ± biotite.

This peak assemblage with biotite only occurs over a very small range of *P–T* space in an extremely narrow field (~760-840 °C and 4-6 kbar, <10 °C wide; Figure 4d). Alternatively, a much larger, biotite-absent field exists next to this field in our modelled *P–T* section (3.7–6.6 kbar and 760–950 °C; Figure 4d). The majority of biotite in this sample mantles sillimanite and garnet and therefore we interpret much of the biotite to be retrograde. However, some of the biotite is foliated and texturally appears to be peak. To account for this ambiguity, two peak fields have been selected to represent the possible peak *P–T* conditions, one with biotite and one without. The combination of these fields occur over the range of ~760–950 °C and 3.7–6.6 kbar (Figure 4d).

Samples 2014-9 and 2014 12-A come from outcrops ~400 m apart and are not separated by any known shear zones or faults. Therefore, these samples almost certainly experienced the same *P–T* conditions. The peak *P–T* conditions of the granulite-facies samples overlap at ~780–920 °C and 3.5–5.4 kbar.

Monazite Geochronology

In situ monazite U-Pb geochronology was collected from one amphibolite-facies sample and two granulite-facies samples. The amphibolite-facies sample was analysed with the aim of providing temporal constraints on the prograde evolution of the Reynolds Range Group, whereas the granulite-facies samples were analysed to constrain the timing of peak to post-peak metamorphism. Analyses that are not within 2σ uncertainty of concordia (using $^{206}Pb/^{238}U$ and $^{207}Pb/^{235}U$, as depicted visually on the concordia plots) were excluded from age calculations but are depicted on the concordia plots as grey dashed ellipses (Figure 5).

A*mphibolite-facies metapelite*

The monazite grains in sample RR2015 3-13 are small, typically 13–15 μm in diameter, and vary from rounded to anhedral in shape. No zoning was observed through BSE imaging in any of the grains. Thirty-four analyses were collected from 34 grains. None of the analysed grains occur as inclusions in the silicate minerals. Six analyses were excluded on the basis of discordance. Three analyses yield concordant older $^{207}Pb/^{206}Pb$ ages of 1720–1680 Ma. The remaining 25 analyses range in 207Pb/206Pb age between 1680–1560 Ma (Figure 5a, b). It is not possible to calculate a meaningful weighted mean age because of the large spread in the age data.

Cordierite granulite-facies metapelite (RR2014-9)

Analysed monazite grains in sample RR2014-9 are typically 14–20 μm in diameter and vary in shape from rounded to anhedral. No zoning was observed in any of the grains. Fifteen analyses were collected from 14 grains. Two analyses were excluded on the basis of discordance. The remaining 13 analyses range between $^{207}Pb/^{206}Pb$ ages of 1580–1500 Ma and have a $^{207}Pb/^{206}Pb$ weighted mean age of 1545 ± 7 Ma (Figure 5c, d; MSWD = 1.17, probability = 0.30).

Garnet granulite-facies metapelite (RR2014-12A)

Monazite grains in sample RR2014-12A are typically 10–25 μm in diameter and vary in shape from rounded to anhedral. No zoning was observed in any of the grains. Twenty-one analyses were collected from 21 grains. Six analyses were excluded on the basis of discordance. Two outlying analyses have older $^{207}Pb/^{206}Pb$ ages of 1589 ± 14 Ma and 1612 ± 18 Ma. The weighted mean $^{207}Pb/^{206}Pb$ age of the remaining 13 analyses is 1553 ± 5 Ma (Figure 5e, f; MSWD = 1.7, probability = 0.065). However, the MSWD of 1.7 suggests the analyses do not form one population.

DISCUSSION

Pressure–temperature–time constraints on

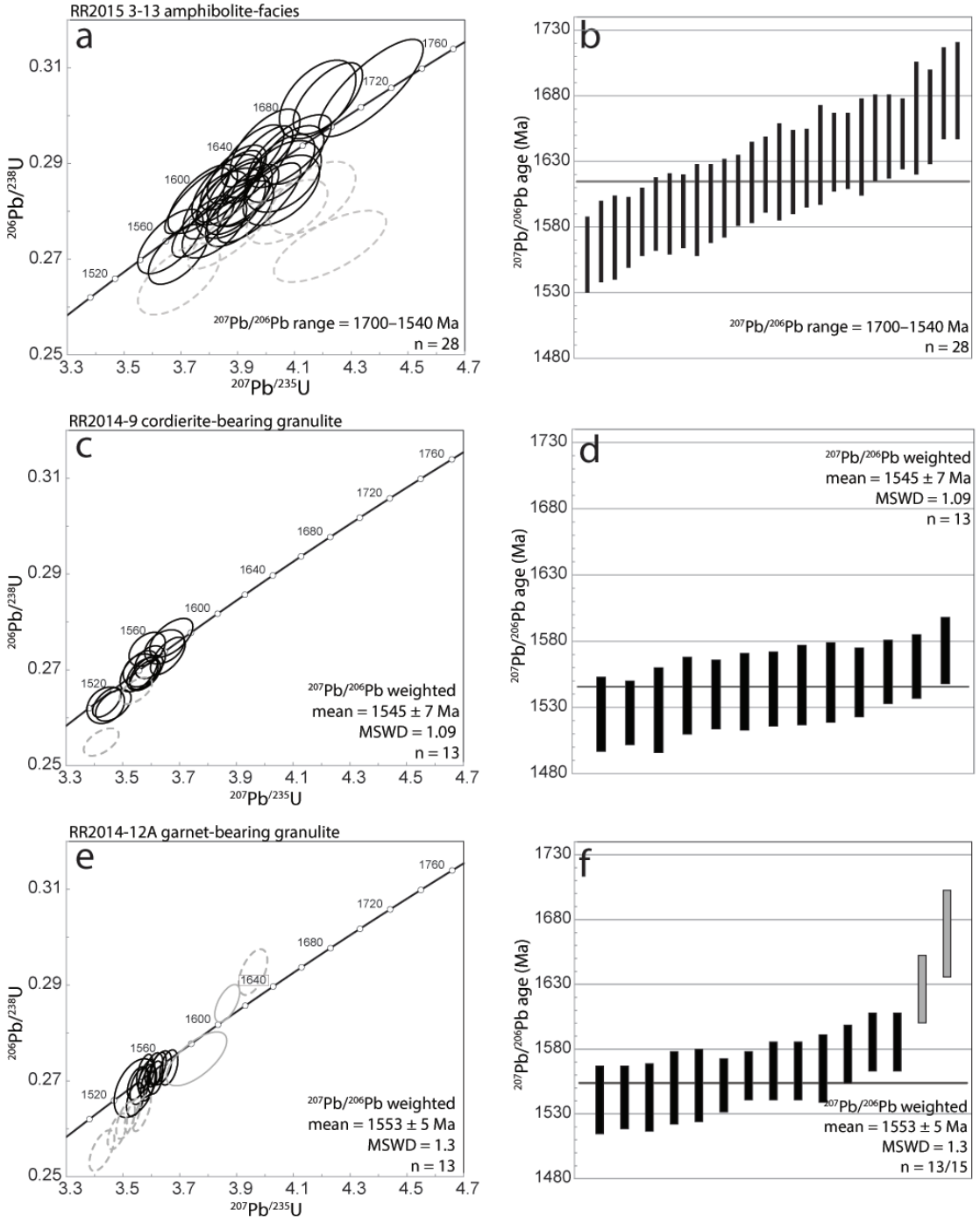


Figure 5. Concordia and weighted average plots of in situ U–Pb monazite analyses for samples (a, b) RR2015 3-13, (c, d) RR2014-9 and (e, f) RR2014-12A. Outlying data that was excluded from weighted average age calculations is represented by grey ellipses/columns and discordant analyses are shown in the grey, dashed ellipses (not included in weighted average plots). Remaining analyses are shown in black and the ellipses each represent 2σ errors.

metamorphism

PPressure–temperature constraints from the samples in this study highlight the metamorphic progression from greenschist-facies to granulite-facies along the length of the Reynolds Range. The greenschist-facies rocks in this study reached conditions of ~480 °C and 3.2–5 kbar. These samples do not contain metamorphic monazite, and so do not provide temporal constraints on metamorphism. The amphibolite-facies metapelitic rocks reached metamorphic conditions of 500–620 °C and

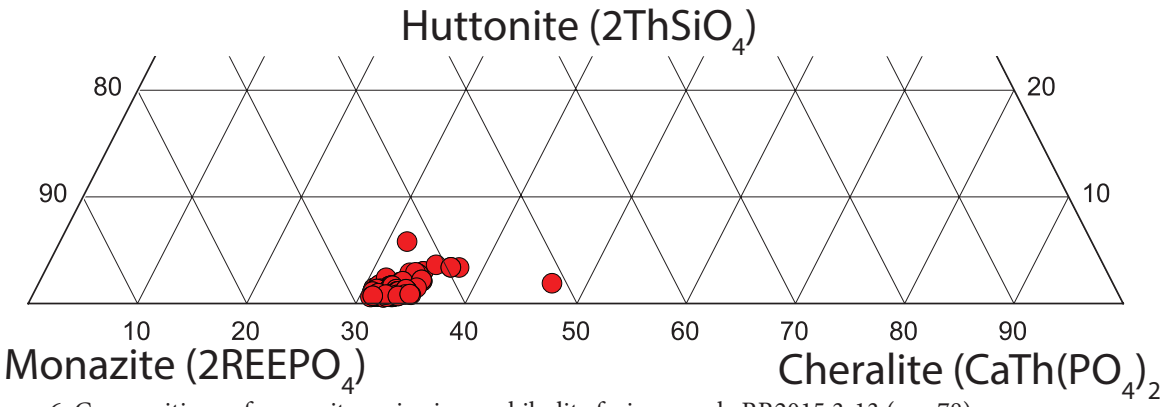


Figure 6. Compositions of monazite grains in amphibolite facies sample RR2015 3-13 (n = 78).

1.3–3.8 kbar and give a broad range of concordant monazite ages between ca. 1700–1540 Ma (Figure 5). The granulite-facies samples in this study reached peak conditions of 780–920 °C and 3.5–5.4 kbar and record $^{207}Pb/^{206}Pb$ ages between 1570–1500 Ma. This results in a geothermal gradient of 152–218 °C/kbar. The calculated metamorphic conditions for each of the samples suggests a similar, high thermal gradient along the length of the Reynolds Range. The thermal gradients and metamorphic ages recorded by the granulite samples align with the well-established *P–T* conditions and timing of the 1595–1520 Ma Chewings Orogeny (Anderson et al., 2013; Hand and Buick, 2001; Morrissey et al., 2014; Prent et al., 2019; Rubatto et al., 2001; Williams et al., 1996). However, the amphibolite-facies sample records significantly older ages (1690–1560 Ma; Figure 5a, b) than the granulite-facies rocks, and these ages do not correspond to the currently defined interval of the Chewings Orogeny.

During the early stages of prograde metamorphism, detrital monazite is commonly interpreted to be replaced by metamorphic allanite or apatite at temperatures approximating the biotite isograd (Janots et al., 2008; Rasmussen and Muhling, 2007; Tomkins and Pattison, 2007; Yakymchuk, 2017), and detrital monazite is only rarely observed in rocks that reach mid-amphibolite- to granulite-facies metamorphic conditions (e.g. Kohn and Malloy, 2004; Rubatto et al., 2006; Wing et al., 2003). The specific temperature at which metamorphic monazite in metapelites forms is a function of whole rock Ca and Al content (e.g. Spear, 2010; Wing et al., 2003). Specifically, bulk rock compositions with CaO <1.08 wt% (such as all samples modelled in this study) tend to undergo the allanite–monazite transition at ~450°C (Spear, 2010; Spear and Pyle, 2010). The amphibolite-facies sample (RR2015 3–13) records minimum temperatures of ~500 °C (Figure 4b), suggesting the monazite is likely to be metamorphic. In addition, the Pine Hill Formation has a depositional age of 1800–1785 Ma (Claoué-Long et al., 2008; Dirks, 1990; Hand and Buick, 2001), supporting the idea that the 1690–1560 Ma monazite ages in the amphibolite facies sample are metamorphic rather than detrital. EPMA data collected from 78 monazite grains in the amphibolite-facies sample shows reasonable consistency in composition (Figure 6), uncharacteristic of detrital grains. This compositional consistency indicates that these monazites likely grew together in the same approximate bulk composition, and so the range of ages is also unlikely to reflect partial resetting of older detrital grains. Therefore, we interpret the monazites in the amphibolite-facies sample to record growth during metamorphism.

The metamorphic ages older than ca. 1610 Ma are not within error of any other known event in the Reynolds–Anmatjira Ranges. However, similar ages have been found in other studies from the central Aileron Province (Anderson et al., 2013; Collins and Williams, 1995). Col-

lins and Williams (1995) described a population of zircons that formed at 1659 ± 6 Ma in the granulite-facies Napperby Gneiss, in the SE Reynolds Range (Figure 1b). The Napperby Gneiss is a deformed and metamorphosed S-type granite with garnet–biotite–sillimanite-bearing metamorphic assemblages (Hand and Dirks, 1992). The zircons with ca. 1660 Ma ages are colourless, multi-faceted grains with low Th/U ratios, typical of metamorphic zircon (Corfu et al., 2003). They form a group that is morphologically distinct from protolith 1780 Ma magmatic zircons and Chewings Orogeny-aged zircon rims in the sample (see also Dirks et al., 1991). The origin of the ca. 1660 Ma zircons is unclear, and Collins and Williams (1995) did not attribute them to any particular metamorphic event. In the adjacent Anmatjira Range, Anderson et al. (2013) noted metamorphic monazite with ages between *ca.* 1670–1630 Ma in three granulite-facies metapelites that also contain 1580–1560 Ma monazite (Figure 1b). The older ages come from monazite mostly armoured in garnet, and comprise ~30% of all the monazites analysed by Anderson et al. (2013). The monazite ages from RR2015 3-13, combined with existing data from Collins and Williams (1995) and Anderson et al. (2013), suggest that metamorphic monazite and zircon growth in the central Aileron Province occurred over the interval ca. 1680–1550 Ma. A significant proportion of these monazite and zircon ages are older than the currently defined duration of the Chewings Orogeny.

The presence of older monazite and zircon ages in the Reynolds–Anmatjira Ranges can be interpreted in two ways: (1) the Reynolds Range Group sequences have undergone a polymetamorphic history, or (2) they experienced a single continuous, long-lived metamorphic event. Polymetamorphism could result in variable mixing between distinct metamorphic events and so may be difficult to identify purely from geochronological data. Some previous studies have interpreted the isograds in the Reynolds Range Group to have formed through a single metamorphic event (e.g. Dirks et al., 1991; Hand and Buick, 2001). However, other structural and metamorphic work has highlighted the possibility of a polymetamorphic history. Dirks and Wilson (1990) and Hand and Buick (2001) described a structural event, which preceded the main SE-trending foliation in the region that is associated with peak metamorphism. There is also abundant evidence of inclusion-trail assemblages within cordierite–K-feldspar–garnet porphyroblasts in the granulite-facies rocks (Collins and Vernon, 1991; Collins and Williams, 1995; Dirks et al., 1991; Dirks and Wilson, 1990), suggesting an earlier metamorphic history. Collins and Vernon (1991) also interpreted the area to have experienced a foliation-forming deformation event prior to the upright folds that define the present regional structural trends. Howlett et al. (2015) attribute these earlier structures to deformation at ca. 1780 Ma, but it is possible that this pre-peak deformation stage may have been associated with a discrete metamorphic event somewhere between ca. 1670–1630 Ma. However, Dirks et al. (1991) showed that the inclusion assemblages in metamorphic porphyroblasts within the Pine Hill Formation in the Reynolds Range Group increase in grade sympathetically with the pattern of peak metamorphic grade change, strongly suggesting the inclusion assemblages formed during the same thermal event that created the peak assemblages. Furthermore, there is no textural evidence for the growth, dissolution and regrowth of metamorphic porphyroblasts that might be expected to occur with polymetamorphism. Nor is there any evidence for magmatic events that might have driven a series of short-lived thermal events. Therefore, our preferred interpretation is that the pre-Chewings Orogeny ages (>1610 Ma) record the early stages of a long-lived event, with a maximum thermal expression recorded in the comparatively deeply exhumed, granulite-facies SE Anmatjira and

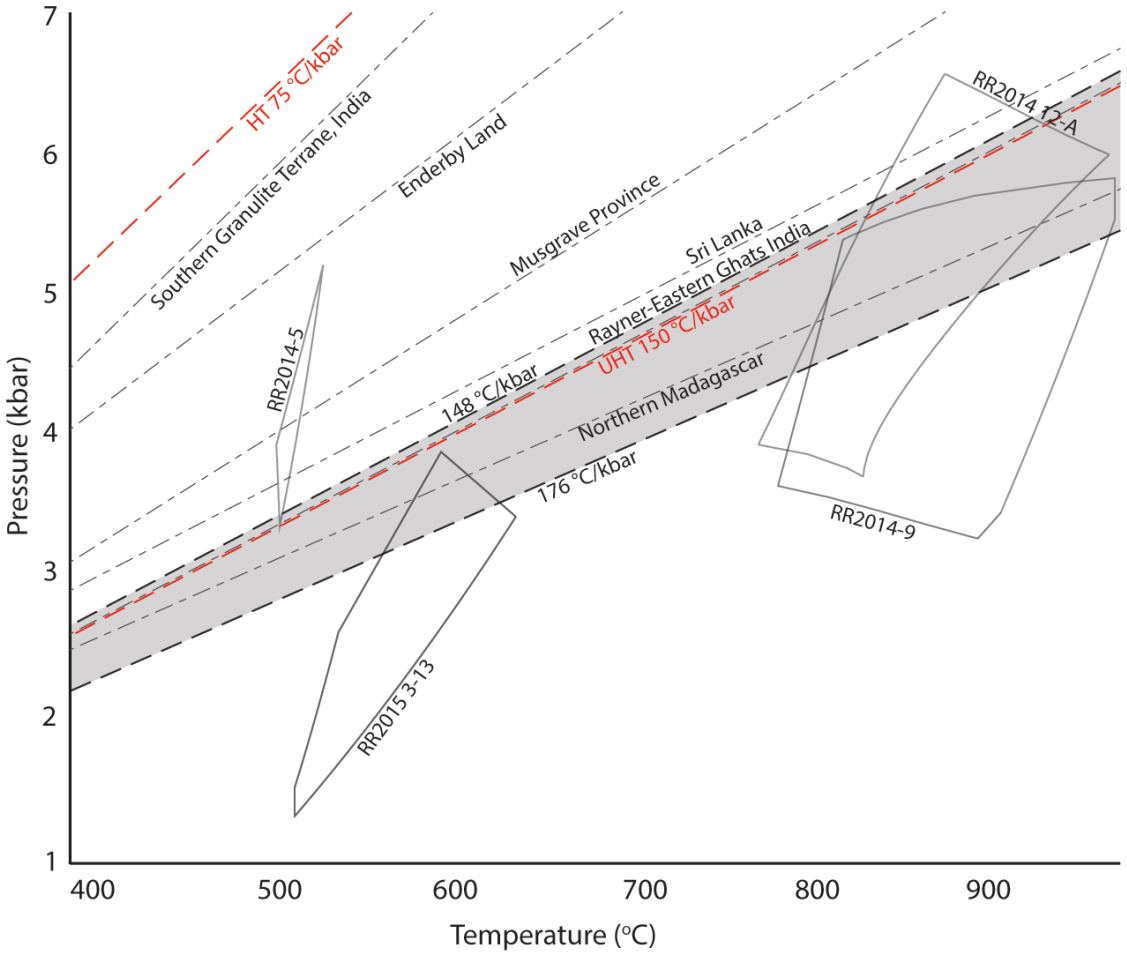


Figure 7. Peak *P–T* conditions calculated for each of the four representative samples of increasing metamorphic grade along the Reynolds Range. Minimum and maximum thermal gradients are based on overlap between the granulite-facies samples and are highlighted by the lightly shaded area between the long-dashed lines. The red dashed lines represent the high temperature (HT) and ultra-high temperature (UHT) thermal gradient boundaries from Brown and Johnson (2018). Other dashed lines represent the thermal gradients of other long-lived, high geothermal gradient terranes including: the Southern Granulite Terrane (Brandt et al. 2011); Enderby Land (Ellis et al. 1980); Musgrave Province (Tucker et al. 2015); Sri Lanka (He et al. 2016); Rayner–Eastern Ghats (Korhonen et al. 2013, Morrissey et al. 2015) and; Northern Madagascar (Nicollet 1990).

Reynolds Ranges. Existing thermochronological data from granulites in the Reynolds Range points to a long cooling history, with rocks cooling through ~500 °C at 1450 Ma (Buick et al., 1999; Morrissey et al., 2014; Vry et al., 1996; Williams et al., 1996), suggesting the terrane experienced a prolonged thermal event, despite being characterised by high thermal gradients.

Given that the terrane appears to have experienced prolonged cooling under high geothermal gradient conditions, in principal there is no reason why it could not also have experienced prolonged prograde heating. If maximum prograde to peak metamorphic conditions were reached at amphibolite-facies as early as 1690–1670 Ma, then it could be assumed that metamorphic monazite growth also began in the granulite-facies rocks at this time, but was overprinted by ongoing high–T metamorphism. The range of older ages observed by this study, Anderson et al. (2013) and Collins and Williams (1995) supports a prolonged prograde evolution in this region. Morrissey et al. (2014) interpreted monazite U–Pb data from the easternmost Reynolds Range to record a minimum of 60 Myr of HT–

LP metamorphism from 1576 ± 10 Ma to 1513 ± 15 Ma. The combination of these studies appears to suggest that the Reynolds–Anmatjira Ranges record almost continuous metamorphic ages from ca. 1690–1500 Ma. Including the age errors on these studies, this information shows the area records a period of metamorphism from ~140 Myr, up to potentially ~190 Myr.

Long-lived high–T low–P metamorphism

High temperature–low pressure crustal environments that reach granulite-facies conditions, such as the central Aileron Province, have extreme energy requirements that sustain rapid changes in temperature with depth, and these tectonic settings are commonly associated with relatively short-lived metamorphism. However, there are a number of high temperature, high thermal gradient terranes where metamorphism has been interpreted to have persisted for upwards of 50 Myr (Figure 7). Korhonen et al. (2013) suggested that ultra-high temperature metamorphism in the Eastern Ghats Province may have persisted for upwards of 200 Myr, recorded by monazite and zircon growth during prograde, peak and post-peak metamorphism. Similarly in the Musgrave Province in central Australia, granulite-facies conditions were associated with long-lived A-type magmatism over a period of at least 150 Myr (Smithies et al., 2011; Tucker et al., 2015). The thermal gradients of these, as well as other well-known examples of long-lived HT–LP terranes are compared with the gradients in the central Aileron Province calculated in this and other studies (Figure 7). Although recording similar thermal gradients to the central Aileron Province, metamorphism in many of these examples was associated with regional extension and voluminous, high temperature magmatism. In contrast, there is no evidence of extension or magmatism in the Aileron Province during the Chewings Orogeny, with the exception of the ca. 1620 Ma Ennugan Mountains Granite (Kositcin et al., 2013). However, this granite was emplaced after the ca. 1670–1650 Ma onset of metamorphism in the amphibolite-facies sample RR2015 3-13, and so cannot be the primary thermal driver for metamorphism. Additionally, it intruded greenschist- to lower amphibolite-grade rocks ~20 km from the extent of the Reynolds Range Group, and therefore was not an agent of significant heating at the exposed crustal level. The general absence of syn-metamorphic magmatism, particularly in the highest-temperature rocks, and lack of evidence for lithospheric extension or rapid exhumation (Clarke and Powell, 1991; Dirks et al., 1991; Dirks and Wilson, 1990; Hand and Buick, 2001), leaves few options for generating the long-lived high thermal gradient conditions. Morrissey et al. (2014) suggested that the ca. 60 Myr period of metamorphism in the eastern Reynolds Range was the result of conductive heating from highly radiogenic pre-metamorphic granites and slow exhumation rates. The Reynolds Range, and central Australia in general, contains voluminous granitic rocks with high radiogenic heat production that have been proposed as the thermal driver for metamorphism (McLaren et al., 2003; McLaren et al., 2005; Sandiford and Hand, 1998). None of these studies have attempted to model the generation of high thermal gradients during burial of highly radiogenic crust using realistic estimates of the amount of crustal heat production in the terrane. However, using a small K–U–Th dataset, and considering only a steady state thermal regime, Sandiford & Hand (1998) showed that high thermal gradient granulite conditions in the central Aileron Province could largely be generated by in situ crustal heat production.

Metamorphism driven by high radiogenic heat production

To explore the suggestion of Sandiford and Hand (1998) that in situ crustal heat production may be the causative agent in generating long-lived high thermal gradient metamor-

phism we produced one-dimensional thermal models to calculate the temperatures arising from the burial of highly radiogenic crust. This was used to assess the validity of radiogenic heating as the primary driver for HT–LP metamorphism in the central Aileron Province. The SE-Reynolds Range has undergone higher pressure metamorphism than the northwest end (Figure 1b). Despite a difference in pressure of around 3 kbar, the unconformity at the base of the Reynolds Range Group can be continuously traced from the low-grade rocks in the northwest to the granulites in the SE. Dirks and Wilson (1990) suggest that the entire length of the range underwent approximately similar amounts of shortening, indicating the northwest to SE increase in pressure of the Reynolds Range Group was not primarily a function of deformation. Therefore, it appears that differential burial occurred after deposition of the Reynolds Range Group between 1800–1785 Ma and before the earliest evidence for prograde metamorphism recorded in the amphibolite-facies rocks (ca. 1670 Ma). The burial mechanism is unknown but we suggest it might have occurred during the formation of a now completely inverted sedimentary basin. We note that sedimentary successions were deposited elsewhere in the southern Aileron Province between 1780–1730 Ma (Scrimgeour, 2013). We therefore speculate that at the onset of metamorphism the upper crust was comprised of a sedimentary basin that had a thickness equivalent to the metamorphic pressure difference between the northwest and southeast ends of the Reynolds Range (~4 km).

We acknowledge there are a number of unknowns associated with constructing a thermal model for the central Aileron Province. However, for the purposes of the modelling we propose a simple three-layered crustal model similar to that of Sandiford et al. (2001), comprising: (1) a thin, residual lower crust; (2) a mixture of granites and metasedimentary rocks in the middle crust; and (3) a generic shale–sandstone sedimentary system for the upper crust. The argument for a thin compositionally residual lower crust is a petrological one. The central Aileron Province contains extremely voluminous K–U–Th-rich 1810–1780 Ma granites that are mostly aluminous and contain abundant inherited zircon (Scrimgeour, 2013). The volume of these largely crustally derived granites implies that the lower crust of the central Aileron Province is volumetrically and chemically depleted. As there is no outcrop from which to directly assess the composition of the lower crust in the central Aileron Province, the heat production rate for our model was set to an average lower crustal value of 1.6 μWm^{-3} at 1650 Ma. This value was chosen based on the higher than average crustal heat production values present in the middle and upper crust, which would presumably have been at least partially derived from a high heat producing lower crust. Lower crustal rocks from Mt Hay and Mt Chapple in the southern Aileron Province also have similar heat production rates to this value (e.g. Sandiford et al., 2001). The middle crust metasedimentary–granite layer in our model is based on the obliquely exposed Reynolds–Anmatjira Ranges, encompassing the entire area shown in Figure 1b. To calculate the bulk heat production value for this layer, the levelled airborne radiometric grid compiled by Geoscience Australia (Minty et al., 2009) was used to obtain K (%), U (ppm) and Th (ppm) values at 100 m resolution over the outcropping geology (Figure 8). Lithologies not represented in the crustal column at 1650 Ma (i.e. all rock units younger than this age and all regolith material) were removed from the radiometric dataset using map polygons from the Geoscience Australia 1:1 million scale surface geology of Australia (Raymond et al., 2012). Heat production rates at 1650 Ma for the remaining polygons were then calculated following Turcotte and Schubert (2014), using the measured concentrations of U, Th and K and an assumed rock density of 2700 kg m^{-3}. Mean heat produc-

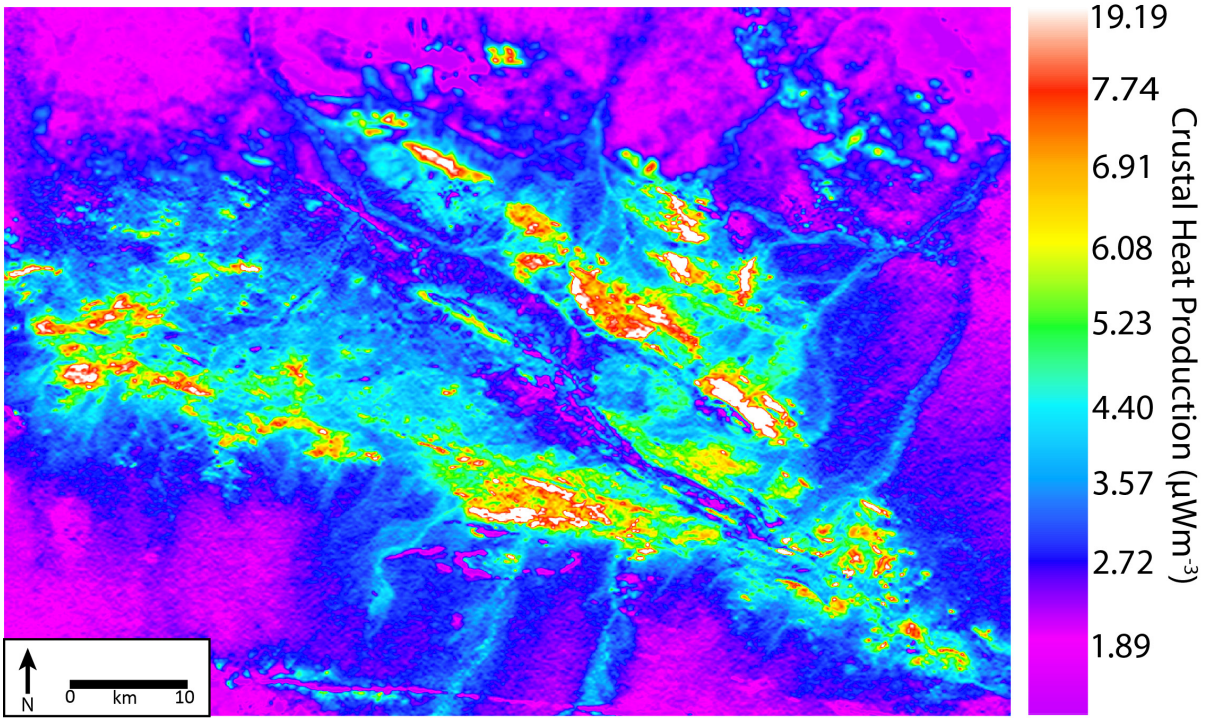


Figure 8. Radiogenic heat production map of the Reynolds–Anmatjira Ranges at 1650 Ma, constructed using the levelled radiometric grid compiled by Geoscience Australia (Minty et al. 2009) and the Geoscience Australia 1:1 million scale surface geology of Australia map (Raymond et al. 2012). Lithologies in this map are shown in Stewart (1981).

tion values for each lithology estimated using zonal statistics are detailed in Appendix E, and were subsequently applied to equivalent lithologies and their areal extents as represented in the Reynolds–Anmatjira Ranges solid geology map (Stewart, 1981). This approach yielded an average heat production value of 4.97 μWm^{-3} for the composite metasedimentary–granitic mid crustal volume at 1650 Ma. These values are essentially identical to outcrop-scale heat production measurements made in the terrane (Alessio et al., 2018).

The Reynolds–Anmatjira Ranges have significantly higher radiogenic heat production values than those of average continental crust (1.0–1.2 μWm^{-3}; Bea, 2012; Hacker et al., 2011). This has been identified in numerous studies (Anderson et al., 2013; Hand and Buick, 2001; Morrissey et al., 2014; Sandiford and Hand, 1998) and is the result of voluminous high-heat producing granites and extensive comparatively U-Th rich pelitic lithologies, as lithology has been shown to be the primary control on HPE distribution (Alessio et al., 2018; Bea, 2012). These lithologies are also highly fertile, and so would have lost some of their HPEs during granulite-grade melting. However, Alessio et al. (2018) showed that the loss of HPEs from the residual material (at least during fluid-absent melting), is proportional to the volume of melt loss, so the concentration of these elements in the residual lithologies would have remained high, even after melting.

Due to denudation, there is also no record of the upper crust above the granulites, but using the logic outlined above, it is interpreted to have been a sedimentary basin. A generic shale–sandstone layer, comprising 50% sandstone and 50% shale was chosen. The heat production value of this sedimentary system was taken to be 1.25 μWm^{-3} based on global averages (Hasterok et al., 2017), but was conceivably higher based on the generally K–U–Th enriched Proterozoic crust in North Australia compared to global averages (Alessio et al.,

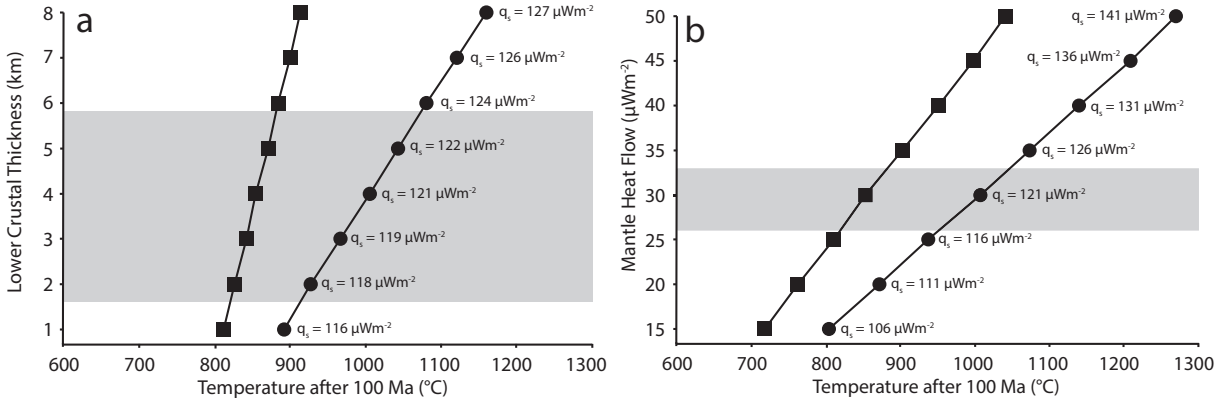


Figure 9. Plots made from the values generated from modelling the instantaneous burial and heating over 100 Ma of a crustal section through the central Aileron Province at 1650 Ma. In all models the upper crust is 4 km thick and the middle crust is 16 km thick. The squares represent temperatures at 16.5 km (5 kbar), where the granulite-facies rocks from this study would be located. The circles represent temperatures at the base of the crust. The grey boxes represent regions in which the temperatures of the granulite-facies rocks correspond to observed metamorphic conditions. (a) Lower crustal thickness plotted against the temperature of the crust after 100 Ma, with a constant mantle heat flow of 30 mWm^{-2}. (b) Mantle heat flow plotted against the temperature of the crust after 100 Ma, with a constant lower crustal thickness of 4 km.

2018). A full description of the thermal modelling code is given in Appendix F.

Aside from the hypothetical composition and heat production values of the upper and lower crust, two variables that are largely unknown are the mantle heat flow and total crustal thickness. Current mantle heat flow in central Australia appears to be low, resulting in a very thick lithospheric mantle (Fichtner et al., 2009; Pollack and Chapman, 1977). It is not clear when this thick mantle lithosphere was established, so we used a conservative mantle heat flow value of 30 mWm^{-2} (Hasterok and Gard, 2016). The effect of total crustal thickness on the mid-crustal thermal regime is indirect. High mid-crustal temperatures require high upper-crustal thermal gradients. The effect of these high thermal gradients when propagated into the lower crust will lead to very high temperatures if the crust is too thick, logically resulting in the generation of dry, high-temperature melts from lower crust previously depleted by extraction of the voluminous 1810–1780 aluminous crustally-derived granites in the central Aileron Province. The overall lack of evidence for magmatism during metamorphism in the Reynolds–Anmatjira Ranges indicates the lower crust did not undergo extreme metamorphism, and therefore the crust cannot have been significantly thick, suggesting the 25–40% shortening determined by Dirks and Wilson (1990) occurred in previously thin crust.

To accommodate the factors mentioned above, a viable thermal model for late Paleoproterozoic–early Mesoproterozoic metamorphism in the central Aileron Province has to account for (1) high (800–850 °C) mid-crustal temperatures that appear to have been sustained for an extremely long duration, (2) an absence of magmatic inputs to drive the metamorphism, (3) lower crustal temperatures less than ~950–1000 °C, to account for the absence of significant felsic magmatic inputs into the mid-crust during metamorphism and (4) unremarkable mantle heat flow to account for the absence of mafic magmas. The lack of obvious external thermal inputs and the duration of metamorphism strongly point to a thermal system generated largely by the crust itself, likely as a consequence of its bulk radiogenic heat generation rate. This inference is consistent with the highly elevated heat production rates of rocks in the central Aileron Province.

As discussed above, two of the most unknown

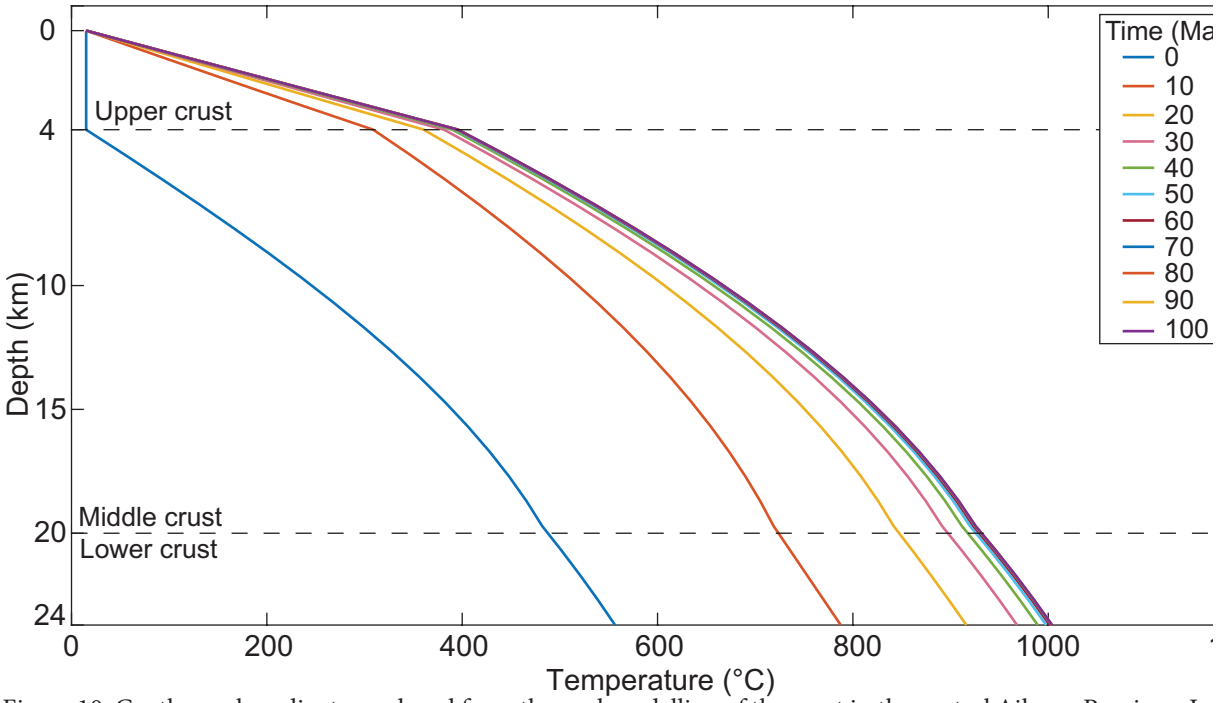


Figure 10. Geothermal gradients produced from thermal modelling of the crust in the central Aileron Province. In this model, the crust was buried under 4 km of sediment, representing the upper crust, almost instantaneously (in 1 Myr) and allowed to incubate for a further 99 Ma, where equilibrium is essentially reached. The mantle heat flow for this model was set to 30 mWm^{-2}. Each coloured curve represents the geotherm at a different point in time after burial. The dashed lines represent the boundaries of the upper, middle and lower crustal sections used in the model (properties are given in Appendix E).

variables are mantle heat flow and total crustal thickness. Figure 9 explores the effect of variations in crustal thickness and mantle heat flow on lower crustal temperatures using the heat production values outlined above. Initial sensitivity tests showed that varying crustal thickness has a significant impact on lower crustal temperatures. The base of the mid-crust is represented by the granulite-facies rocks in the easternmost Reynolds Range, which record burial to depths of 20–23 km (Morrissey et al., 2014). Therefore, for all models the upper crust was set to be 4 km thick and the middle crust was set to be 16 km thick. There are no geological constraints on the thickness of the lower crust. The modelling shows that a range of lower crustal thicknesses for the lower crust are compatible with the *P–T* conditions recorded by the granulite-facies samples in this study (Fig. 10). However, the temperatures at the base of the crust begin to exceed 1000 °C once the total crustal thickness exceeds around 25 km. The absence of magmatism corresponding to the timing of granulite-facies metamorphism suggests that if our models are representative, the lower crust did not exceed 5 km in thickness. The effect of mantle heat flow on crustal temperatures was investigated using a constant lower crustal thickness of 4 km, as determined above (Figure 9b). The modelling shows that only a small range of mantle heat flow values (~26–33 μWm^{-2}) result in mid crustal temperatures consistent with our *P–T* modelling without creating excessively high (>1000 °C) lower crustal temperatures. Therefore, the parameters that best fit the geological constraints include a total crustal thickness of 24 km, mantle heat flow of 30 μWm-2 and the heat production rates outlined in Appendix F.

The results shown in Figure 10 using the parameters outlined above show the evolving geotherm for the simple end-member situation of instantaneous burial followed by thermal relaxation. In reality, burial is likely to have occurred in at least two stages; firstly

deeper burial of the SE part of the Reynolds Range Group prior to the onset of metamorphism, conceivably by an overlying eastwards thickening sedimentary basin, and then burial during shortening associated with deformation coeval with metamorphism (Dirks and Wilson, 1990; Hand and Buick, 2001). Therefore, the geotherm would have evolved more slowly than shown in Figure 10. This geotherm evolution is consistent with the highest temperatures being reached after Chewings Orogeny shortening (Hand and Buick, 2001; Morrissey et al., 2014). Nonetheless, burial must have been underway before 1650 Ma to allow monazite to begin growing in amphibolite-facies rocks in the central-western Reynolds Range by ca. 1650 Ma. Plausibly the presence of 1650–1630 Ma monazite in granulites in the Anmatjira Range (Anderson et al., 2013) and metamorphic zircon in migmatised granitic gneiss in the eastern Reynolds Range (Collins and Williams, 1995) reflects this burial. Therefore, based on the rate of the evolving geotherm (Figure 10), burial and possibly even deformation-induced burial would have been underway by around 1670 Ma, some 70 Ma before the Chewings Orogeny is considered to have begun (Scrimgeour, 2013).

Unlike thermally-driven high thermal gradient metamorphism, terranes heated dominantly by radiogenic heat production can only cool significantly if they are exhumed. Anderson et al. (2013) showed that granulites in the Anmatjira Range underwent a cooling pressure-decreasing retrograde P–T path that tracked along a retrograde gradient of around 1300 °C/GPa, ultimately leading to the formation of retrograde andalusite after cordierite. Based on existing geochronology from the region (Morrissey et al., 2014; Vry et al., 1996; Williams et al., 1996), the duration of this cooling path is likely to have been at least 100 Myr. Rutile U–Pb ages in the terrane are ca. 1554 ± 8 Ma (Vry and Baker, 2006), and Rb–Sr muscovite ages are ca. 1485 ± 6 Ma (Vry and Baker, 2006), indicating the terrane cooled through the interval ~600–500 °C some 80 to 100 Myr after the peak granulite-facies conditions were reached. Morrissey et al. (2014) also recorded aluminous and boron-rich pegmatites in the eastern Reynolds Range at ca. 1520 Ma, suggesting the terrane was still at anatectic conditions (ca. 650 °C) at this time. However, it should be noted that halogens in pegmatites may decrease the solidus temperature somewhat (e.g. Bailey, 1977).

The thermal modelling not only suggests that high grade Paleo-Mesoproterozoic metamorphism in the central Aileron Province as a result of crustal heat production was possible, but that the crust needed to be relatively thin (<25 km with a mantle heat flow of <35 mWm-2) in order to keep lower crustal temperatures cool enough to prevent significant magma genesis. We acknowledge that some of the thermal values used in the models shown in Figure 9 rely on a number of assumptions, but they serve as a rough guide to the crustal character prior to metamorphism. Regardless, it is evident that the apparent duration of high thermal gradient metamorphism and cooling in the central Aileron Province requires a long-lived, high-energy thermal driver. Based on the high measured rates of crustal heat production, the essentially amagmatic character of the metamorphism, the evident duration of high-T conditions, and the lack of evidence for polymetamorphism, we argue this thermal driver was crustal heat production. Consequently, long-lived high thermal gradient conditions in other terranes may be able to be explained by radiogenic heat production, with the caveat that the crust must be relatively thin in situations where heat production rates are high to prevent excessive melting in the lower crust. In terranes that record apparently long durations of accessory mineral growth, a necessary step in evaluating their potential significance is to make realistic estimates of the rates of crustal heat production and the crustally

generated heat flow. Only when this energy source is manifestly insufficient, should external thermal inputs be considered.

In areas of thickened crust, extreme temperatures may be able to be avoided if radiogenic elements are concentrated in the upper crust (Mareschal and Jaupart, 2013; Sandiford et al., 2002). However, Alessio et al. (2018) have recently shown that the distribution of these elements is largely controlled by lithology, not depth, so these situations would only occur in terranes where the lower crust is dominated by lithologies that are naturally low in heat producing elements.

CONCLUSIONS

Monazite U–Pb geochronology collected from amphibolite-facies pelites in the Reynolds Range suggest that metamorphism during the Chewings Orogeny may have begun as early as 1670 Ma. This data, combined with other metamorphic ages that have been compiled in this study, suggest that the Reynolds Range and the neighbouring Anmatjira Range and Napperby Gneiss underwent a single, long-lived event that may have lasted up to 190 Ma. This event resulted from high concentrations of radiogenic heat production contained within pre-metamorphic granites and the central Australian crust. The attainment of granulite-facies temperatures in the mid-lower crust but absence of significant syn-metamorphic magmatism provide important constraints on crustal thickness prior to the Chewings Orogeny; and indicate that crustal thickness likely did not exceed 24 km. These results indicate that radiogenic heating of the crust was likely the primary driver for high-temperature metamorphism in the Reynolds–Anmatjira Ranges. The HPE-enriched granites and tectonically stable environment permitted significant radiogenic heating during the Chewings Orogeny. These same conditions are likely common in the middle crust elsewhere, so radioactive decay may be a more important source of heat for metamorphism than typically thought.

ACKNOWLEDGEMENTS

This work was supported by ARC DP160101006 (DEK), ARC LP160100578 and DP160104637 (MH). The University of Adelaide is also thanked for research support funding. KLA acknowledges the support of an Australian Government Research Training Program Scholarship. Staff at Adelaide Microscopy are thanked for their assistance in operating equipment and data collection.

REFERENCES

Alessio, K.L., Hand, M., Kelsey, D.E., Williams, M.A., Morrissey, L.J., Barovich, K., 2018. Conservation of deep crustal heat production. Geology.

Anderson, J.R., Kelsey, D.E., Hand, M., Collins, W.J., 2013. Conductively driven, high-thermal gradient metamorphism in the Anmatjira Range, Arunta region, central Australia. Journal of Metamorphic Geology 31, 1003-1026.

Andreoli, M.A., Hart, R.J., Ashwal, L.D., Coetzee, H., 2006. Correlations between U, Th content and metamorphic grade in the western Namaqualand Belt, South Africa, with implications for radioactive heating of the crust. Journal of Petrology 47, 1095-1118.

Brandt, S., Schenk, V., Raith, M.M., Appel, P., Gerdes, A., Srikantappa, C., 2011. Late Neoproterozoic PT evolution of HP-UHT granulites from the Palni Hills (South India): New constraints from phase diagram modelling, LA-ICP-MS zircon dating and in-situ EMP monazite dating. Journal of Petrology 52, 1813-1856.

Brown, M., Johnson, T., 2018. Secular change in metamorphism and the onset of global plate tectonics. American Mineralogist 103, 181-196.

Brown, M., Raith, M., 1996. First evidence of ultrahigh-temperature decompression from the granulite province of southern In-

dia. Journal of the Geological Society 153, 819-822.

Buick, I.S., Cartwright, I., Harley, S., 1998. The retrograde *P–T–*t path for low-pressure granulites from the Reynolds Range, central Australia: petrological constraints and implications for low-P/high-T metamorphism. Journal of Metamorphic Geology 16, 511-529.

Buick, I.S., Frei, R., Cartwright, I., 1999. The timing of high-temperature retrogression in the Reynolds Range, central Australia: constraints from garnet and epidote Pb-Pb dating. Contributions to Mineralogy and Petrology` 135, 244-254.

Cartwright, I., Buick, I., Foster, D., Lambert, D., 1999. Alice Springs age shear zones from the southeastern Reynolds Range, central Australia. Australian Journal of Earth Sciences 46, 355-363.

Claoué-Long, J., Edgoose, C., Worden, K., 2008. A correlation of Aileron Province stratigraphy in central Australia. Precambrian Research 166, 230-245.

Clark, C., Fitzsimons, I.C., Healy, D., Harley, S.L., 2011. How does the continental crust get really hot? Elements 7, 235-240.

Clarke, G.L., Powell, R., 1991. Proterozoic granulite facies metamorphism in the southeastern Reynolds Range, central Australia: geological context, *P–T* path and overprinting relationships. Journal of Metamorphic Geology 9, 267-281.

Collins, W.J., Vernon, R.H., 1991. Orogeny associated with anticlockwise P-T-t paths: evidence from low-P, high-T metamorphic terranes in the Arunta inlier, central Australia. Geology 19, 835-838.

Collins, W.J., Williams, I.S., 1995. SHRIMP ionprobe dating of short-lived Proterozoic tectonic cycles in the northern Arunta Inlier, central Australia. Precambrian Research 71, 69-89.

Corfu, F., Hanchar, J.M., Hoskin, P.W., Kinny, P., 2003. Atlas of zircon textures. Reviews in Mineralogy and Geochemistry 53, 469-500.

Dirks, P., 1990. Intertidal and subtidal sedimentation during a mid-Proterozoic marine transgression, reynolds range group, Arunta block, central Australia. Australian Journal of Earth Sciences 37, 409-422.

Dirks, P., Hand, M., Powell, R., 1991. The P-T-deformation path for a mid Proterozoic, low-pressure terrane - the Reynolds range, central Australia. Journal of Metamorphic Geology 9, 641-661.

Dirks, P., Wilson, C.J.L., 1990. The geological evolution of the Reynolds Range, central Australia - evidence for 3 distinct structural-metamorphic cycles. Journal of Structural Geology 12, 651-665.

Ellis, D., Sheraton, J., England, R., Dallwitz, W., 1980. Osumilite-sapphirine-quartz granulites from Enderby Land Antarctica—mineral assemblages and reactions. Contributions to Mineralogy and Petrology 72, 123-143.

Fichtner, A., Kennett, B.L., Igel, H., Bunge, H.-P., 2009. Full seismic waveform tomography for upper-mantle structure in the Australasian region using adjoint methods. Geophysical Journal International 179, 1703-1725.

Greenfield, J., Clarke, G., Bland, M., Clark, D., 1996. In-situ migmatite and hybrid diatexite at Mt Stafford, central Australia. Journal of Metamorphic Geology 14, 413-426.

Hand, M., 1993. Structural and metamorphic evolution of two Proterozoic terrains: southeastern Anmatjira Range (central Australia) and Jetty Peninsula (east Antarctica), School f Earth Sciences. University of Melbourne, Melbourne.

Hand, M., Buick, I.S., 2001. Tectonic evolution of the Reynolds-Anmatjira Ranges: a case study in terrain reworking from the Arunta Inlier, central Australia, in: Miller, J., Holdsworth, R.E., Buick, I.S., Hand, M. (Eds.), Continental Reactivation and Reworking, pp. 237-260.

Hand, M., Dirks, P.H., 1992. The influence of deformation on the formation of axial-

planar leucosomes and the segregation of small melt bodies within the migmatitic Napperby Gneiss, central Australia. Journal of Structural Geology 14, 591-604.

Harley, S., Hensen, B., Sheraton, J., 1990. Two-stage decompression in orthopyroxene–sillimanite granulites from Forefinger Point, Enderby Land, Antarctica: implications for the evolution of the Archaean Napier Complex. Journal of Metamorphic Geology 8, 591-613.

Hasterok, D., Gard, M., 2016. Utilizing thermal isostasy to estimate sub-lithospheric heat flow and anomalous crustal radioactivity. Earth and Planetary Science Letters 450, 197-207.

Hasterok, D., Gard, M., Webb, J., 2017. On the radiogenic heat production of metamorphic, igneous, and sedimentary rocks.

He, X.-F., Santosh, M., Tsunogae, T., Malaviarachchi, S.P., 2016. Early to late Neoproterozoic magmatism and magma mixing–mingling in Sri Lanka: implications for convergent margin processes during Gondwana assembly. Gondwana Research 32, 151-180.

Holland, T., Powell, R., 2011. An improved and extended internally consistent thermodynamic dataset for phases of petrological interest, involving a new equation of state for solids. Journal of Metamorphic Geology 29, 333-383.

Horton, F., Hacker, B., Kylander-Clark, A., Holder, R., Jöns, N., 2016. Focused radiogenic heating of middle crust caused ultrahigh temperatures in southern Madagascar. Tectonics 35, 293-314.

Howlett, D., Raimondo, T., Hand, M., 2015. Evidence for 1808–1770 Ma bimodal magmatism, sedimentation, high-temperature deformation and metamorphism in the Aileron Province, central Australia. Australian Journal of Earth Sciences 62, 831-852.

Janots, E., Engi, M., Berger, A., Allaz, J., Schwarz, J.O., Spandler, C., 2008. Prograde metamorphic sequence of REE minerals in pelitic rocks of the Central Alps: implications for allanite–monazite–xenotime phase relations from 250 to 610 °C. Journal of Metamorphic Geology 26, 509-526.

Jaupart, C., Mareschal, J.-C., Iarotsky, L., 2016. Radiogenic heat production in the continental crust. Lithos 262, 398-427.

Kelsey, D.E., Clark, C., Hand, M., 2008. Thermobarometric modeling of zircon and monazite growth in melt-bearing systems: examples using model metapelitic and metapsammitic granulites. Journal of Metamophic Geology 26, 199-212.

Kohn, M.J., Malloy, M.A., 2004. Formation of monazite via prograde metamorphic reactions among common silicates: implications for age determinations. Geochimica Et Cosmochimica Acta 68, 101-113.

Korhonen, F., Clark, C., Brown, M., Bhattacharya, S., Taylor, R., 2013. How long-lived is ultrahigh temperature (UHT) metamorphism? Constraints from zircon and monazite geochronology in the Eastern Ghats orogenic belt, India. Precambrian Research 234, 322-350.

Kositcin, N., Beyer, E., Close, D., Hallett, L., DJ, D., Whelan, J., 2013. Summary of Results: Joint NTGS-GA Geochronology Project: Arunta Region, Ngalia Basin, Tanami Region and Murphy Province July 2011-June 2012. Northern Territory Geological Survey.

Ludwig, K.R., 2003. User's manual for Isoplot 3.00: a geochronological toolkit for Microsoft Excel. Kenneth R. Ludwig.

Maidment, D.W., 2005. Palaeozoic high-grade metamorphism within the Centralian Superbasin, Harts Range region, central Australia.

Mareschal, J.-C., Jaupart, C., 2013. Radiogenic heat production, thermal regime and evolution of continental crust. Tectonophysics.

McLaren, S., Powell, R., 2014. Magmatism, orogeny and the origin of high-heat-producing granites in Australian Proterozoic terranes. Journal of the Geological Society

171, 149-152.

McLaren, S., Sandiford, M., Hand, M., 1999. High radiogenic heat–producing granites and metamorphism—An example from the western Mount Isa inlier, Australia. Geology 27, 679-682.

McLaren, S., Sandiford, M., Hand, M., Neumann, N., Wyborn, L., Bastrakova, I., 2003. The hot southern continent: heat flow and heat production in Australian Proterozoic terranes. Geological Society of America Special Papers 372, 157-167.

McLaren, S., Sandiford, M., Powell, R., 2005. Contrasting styles of Proterozoic crustal evolution: a hot-plate tectonic model for Australian terranes. Geology 33, 673-676.

Minty, B., Franklin, R., Milligan, P., Richardson, M., Wilford, J., 2009. The Radiometric Map of Australia. Exploration Geophysics 40, 325-333.

Morrissey, L.J., Hand, M., Kelsey, D.E., 2015. Multi-stage metamorphism in the Rayner–Eastern Ghats Terrane: *P–T–*t constraints from the northern Prince Charles Mountains, east Antarcti*ca.* Precambrian Research 267, 137-163.

Morrissey, L.J., Hand, M., Raimondo, T., Kelsey, D.E., 2014. Long-lived high-T, low-P granulite facies metamorphism in the Arunta Region, central Australia. Journal of Metamorphic Geology 32, 25-47.

Nicollet, C., 1990. Crustal evolution of the granulites of Madagascar, Granulites and crustal evolution. Springer, pp. 291-310.

Okay, A., Sunal, G., Tüysüz, O., Sherlock, S., Keskin, M., Kylander-Clark, A., 2014. Low-pressure–high-temperature metamorphism during extension in a Jurassic magmatic arc, Central Pontides, Turkey. Journal of Metamorphic Geology 32, 49-69.

Paton, C., Hellstrom, J., Paul, B., Woodhead, J., Hergt, J., 2011. Iolite: Freeware for the visualisation and processing of mass spectrometric data. Journal of Analytical Atomic Spectrometry 26, 2508-2518.

Payne, J., Hand, M., Barovich, K., Wade, B., 2008. Temporal constraints on the timing of high-grade metamorphism in the northern Gawler Craton: implications for assembly of the Australian Proterozoic. Australian Journal of Earth Sciences 55, 623-640.

Pearce, M.A., White, A.J.R., Gazley, M.F., 2015. TCInvestigator: automated calculation of mineral mode and composition contours for thermocalc pseudosections. Journal of Metamorphic Geology 33, 413-425.

Pollack, H.N., Chapman, D.S., 1977. Mantle heat flow. Earth and Planetary Science Letters 34, 174-184.

Powell, R., Holland, T., 1988. An internally consistent thermodynamic dataset with uncertainties and correlations: 3. Applications to geobarometry, worked examples and a computer program. J. Metamorphic Geol. 6, 173-204.

Powell, R., White, R.W., Green, E.C.R., Holland, T.J.B., Diener, J.F.A., 2014. On parameterizing thermodynamic descriptions of minerals for petrological calculations. Journal of Metamorphic Geology 32, 245-260.

Prent, A.M., Beinlich, A., Morrissey, L.J., Raimondo, T., Clark, C.F., Putnis, A., 2019. Monazite as a Monitor for Melt-Rock Interaction during Cooling and Exhumation. Journal of Metamorphic Geology.

Raimondo, T., Clark, C., Hand, M., Faure, K., 2011. Assessing the geochemical and tectonic impacts of fluid–rock interaction in mid-crustal shear zones: a case study from the intracontinental Alice Springs Orogen, central Australia. Journal of Metamorphic Geology 29, 821-850.

Rasmussen, B., Muhling, J.R., 2007. Monazite begets monazite: evidence for dissolution of detrital monazite and reprecipitation of syntectonic monazite during low-grade regional metamorphism. Contributions to Mineralogy and Petrology 154, 675-689.

Raymond, O.L., Liu, S., Gallagher, R., Higher, L.M., Zhang, W., 2012. Surface Geology of Australia, 1:1 000 000 scale, 2012 edition [Digital Dataset]. Geoscience Australia,

Commonwealth of Australia, Canberra.

Rubatto, D., Hermann, J., Buick, I.S., 2006. Temperature and bulk composition control on the growth of monazite and zircon during low-pressure anatexis (Mount Stafford, central Australia). Journal of Petrology 47, 1973-1996.

Rubatto, D., Williams, I.S., Buick, I.S., 2001. Zircon and monazite response to prograde metamorphism in the Reynolds Range, central Australia. Contributions to Mineralogy and Petrology 140, 458-468.

Sandiford, M., Hand, M., 1998. Australian Proterozoic high-temperature, low-pressure metamorphism in the conductive limit. Geological Society, London, Special Publications 138, 109-120.

Sandiford, M., Hand, M., McLaren, S., 2001. Tectonic feedback, intraplate orogeny and the geochemical structure of the crust: a central Australian perspective, in: Miller, J., Buick, I.S., Hand, M., Holdsworth, R.E. (Eds.), Polyphase tectonism and reactivation mechanisms in metamorphic belts. Geological Society of London, London.

Sandiford, M., McLaren, S., Neumann, N., 2002. Long-term thermal consequences of the redistribution of heat-producing elements associated with large-scale granitic complexes. Journal of Metamorphic Geology 20, 87-98.

Schaltegger, U., Fanning, C., Günther, D., Maurin, J., Schulmann, K., Gebauer, D., 1999. Growth, annealing and recrystallization of zircon and preservation of monazite in high-grade metamorphism: conventional and in-situ U-Pb isotope, cathodoluminescence and microchemical evidence. Contributions to Mineralogy and Petrology 134, 186-201.

Scrimgeour, I., 2013. Geology and mineral resources of the Northern Territory, in: M, A., TJ, M. (Eds.). Northern Territory Geological Survey, pp. 12:11-12:74.

Sisson, V., Hollister, L., Onstott, T., 1989. Petrologic and age constraints on the origin of a low-pressure/high-temperature metamorphic complex, southern Alaska. Journal of Geophysical Research: Solid Earth 94, 4392-4410.

Smithies, R., Howard, H., Evins, P., Kirkland, C., Kelsey, D., Hand, M., Wingate, M., Collins, A., Belousova, E., 2011. High-temperature granite magmatism, crust–mantle interaction and the Mesoproterozoic intracontinental evolution of the Musgrave Province, Central Australia. Journal of Petrology 52, 931-958.

Spear, F.S., 2010. Monazite–allanite phase relations in metapelites. Chemical Geology 279, 55-62.

Spear, F.S., Pyle, J.M., 2010. Theoretical modeling of monazite growth in a low-Ca metapelite. Chemical Geology 273, 111-119.

Stewart, A., 1981. Reynolds Range Region, Northern Territory, 1: 100 000 Geological Map Commentary. Bureau of Mineral Resources, Geology and Geophysics, Canberra, ACT.

Tomkins, H., Pattison, D., 2007. Accessory phase petrogenesis in relation to major phase assemblages in pelites from the Nelson contact aureole, southern British Columbia. Journal of Metamorphic Geology 25, 401-421.

Tucker, N.M., Hand, M., Payne, J.L., 2015. A rift-related origin for regional medium-pressure, high-temperature metamorphism. Earth and Planetary Science Letters 421, 75-88.

Turcotte, D.L., Schubert, G., 2014. Geodynamics. Cambridge University Press.

Vry, J., Compston, W., Cartwright, I., 1996. SHRIMP II dating of zircons and monazites: Reassessing the timing of high-grade metamorphism and fluid flow in the Reynolds Range, northern Arunta Block, Australia. Journal of Metamorphic Geology 14, 335-350.

Vry, J.K., Baker, J.A., 2006. LA-MC-ICPMS Pb–Pb dating of rutile from slowly cooled

granulites: Confirmation of the high closure temperature for Pb diffusion in rutile. Geochimica Et Cosmochimica Acta 70, 1807-1820.

Wang, W., Dunkley, E., Clarke, G., Daczko, N., 2014. The evolution of zircon during low-P partial melting of metapelitic rocks: theoretical predictions and a case study from Mt Stafford, central Australia. Journal of Metamorphic Geology 32, 791-808.

White, R.W., Powell, R., Clarke, G.L., 2003. Prograde metamorphic assemblage evolution during partial melting of metasedimentary rocks at low pressures: migmatites from Mt Stafford, Central Australia. Journal of Petrology 44, 1937-1960.

White, R.W., Powell, R., Holland, T.J.B., Johnson, T.E., Green, E.C.R., 2014a. New mineral activity–composition relations for thermodynamic calculations in metapelitic systems. Journal of Metamorphic Geology 32, 261-286.

White, R.W., Powell, R., Johnson, T.E., 2014b. The effect of Mn on mineral stability in metapelites revisited: new a–x relations for manganese-bearing minerals. Journal of Metamorphic Geology 32, 809-828.

Wickham, S.M., Oxburgh, E.R., 1985. Continental rifts as a setting for regional metamorphism. Nature 318, 330.

Williams, I., 2001. Response of detrital zircon and monazite, and their U–Pb isotopic systems, to regional metamorphism and host-rock partial melting, Cooma Complex, southeastern Australia. Australian Journal of Earth Sciences 48, 557-580.

Williams, I., Buick, I., Cartwright, I., 1996. An extended episode of early Mesoproterozoic metamorphic fluid flow in the Reynolds Range, central Australia. Journal of Metamorphic Geology 14, 29-47.

Wing, B.A., Ferry, J.M., Harrison, T.M., 2003. Prograde destruction and formation of monazite and allanite during contact and regional metamorphism of pelites: petrology and geochronology. Contributions to Mineralogy and Petrology 145, 228-250.

Worden, K.E., Carson, C.J., Close, D.F., Donnellan, N., Scrimgeour, I.S., 2008. Summary of results: Joint NTGS-GA geochronology: Tanami Region, Arunta Region, Pine Creek Orogen and Halls Creek Orogen correlatives, January 2005-March 2007, Darwin.

Yakymchuk, C., Brown, M., 2014. Behaviour of zircon and monazite during crustal melting. Journal of the Geological Society 171, 465-479.

CHAPTER 5

This chapter has not been submitted but has been prepared in manuscript style as: Alessio K., Hand M., Morrissey L., Raimondo T. & Kelsey D. 2019. Contrasting temperature–time records in interlayered granulites.

Statement of Authorship

Title of Paper	Thermal modelling of very long-lived high thermal gradient metamorphism
Publication Status	☐ Published ☐ Accepted for Publication ☐ Submitted for Publication ☑ Unpublished and Unsubmitted w ork w ritten in manuscript style
Publication Details	NA

Principal Author

Name of Principal Author (Candidate)	Kiara Alessio
Contribution to the Paper	Data modelling Manuscript writing Data collection
Overall percentage (%)	80
Certification:	This paper reports on original research I conducted during the period of my Higher Degree by Research candidature and is not subject to any obligations or contractual agreements with a third party that would constrain its inclusion in this thesis. I am the primary author of this paper.
Signature	Date: 30/07/2019

Co-Author Contributions

By signing the Statement of Authorship, each author certifies that:

i. the candidate's stated contribution to the publication is accurate (as detailed above);

ii. permission is granted for the candidate in include the publication in the thesis; and

iii. the sum of all co-author contributions is equal to 100% less the candidate's stated contribution.

Name of Co-Author	Martin Hand
Contribution to the Paper	Manuscript editing Ideas for manuscript Fieldwork Data collection
Signature	Date: 30/07/2019

Name of Co-Author	Laura Morrissey
Contribution to the Paper	Manuscript editing Data modelling Ideas for manuscript
Signature	Date: 30/07/2019

Name of Co-Author	Tom Raimondo		
Contribution to the Paper	Manuscript editing Data analysis		
Signature		Date	29/07/2019

Name of Co-Author	David Kelsey		
Contribution to the Paper	Manuscript editing Data modelling		
Signature		Date	25/07/2019

ABSTRACT

Interlayered metapelitic and metabasic granulite-facies rocks in the northern Harts Range, central Australia record different components of long-lived early Palaeozoic high-temperature metamorphism. Pressure–temperature-mineral mode modelling of hornblende-rich mafic rocks containing garnet-bearing leucosomes record *pressure–temperature* (*P–T*) conditions between of ~790–900 °C and 9.8–12.6 kbar. In the interlayered metapelitic rocks, *P–T* conditions are 690–800 °C and 7.0–9.8 kbar. The modelled differences in *P–T* conditions overlap at the edge of computed uncertainty. However, mineral mode modelling suggests the commonality in estimated *P–T* ranges lie at approximately 780 °C and 9.8 kbar. The range of metamorphic zircon ages in both lithologies are similar, ranging between ~520–440 Ma. Zircon-garnet REE compositions show garnet growth in both rock compositions preceded zircon growth. However, in contrast to metabasite, garnet modes in metapelite continued to increase after metamorphic zircon began to form. In metapelitic garnet, REE compositions diverge from apparent equilibrium with zircon within rims characterised by MREE enrichment, minor Ca and Zr enrichment. The relative change in garnet rim composition is consistent with apatite breakdown. Inferred apatite breakdown is interpreted to have resulted in monazite formation. This interpretation is supported by the approximate equilibrium partitioning of REE between monazite and the garnet rims. The monazite in the metapelite gives a U–Pb age of 451.9 ± 2.1 Ma. Combined with zircon U-Pb-REE data, the monazite U–Pb data from metapelite indicates that garnet grew over the interval *ca.* 520-450 Ma. Therefore, the metapelite and metabasic lithologies grew garnet at different times, with garnet in the metabasite growing to modal completion prior to onset of zircon growth at *ca.* 520 Ma, but garnet in metapelite continuing to grow until *ca.* 450 Ma. Consequently, the modelled difference in *P–T* conditions between metabasite and metapelite represents different points in the *P–T* evolution, with the recorded ~790–900 °C and 9.8–12.6 kbar metabasic peak conditions occurring well before the peak *P–T* conditions recorded in the metapelitic rocks. It appears that the rate of heating was different in metapelitic and metabasic compositions, resulting in differing *P–T*–t paths occurring in the two samples. Taking a conservative view on the combined *P–T* modelling and zircon-garnet-HREE results from both lithologies, the conditions of 790–900 °C and 9.8–12.6 kbar recorded by the mineral assemblage in mafic gneiss were achieved at or before 520 Ma. In contrast, the metapelite records its peak *P–T* conditions of 690–800 °C and 7.0–9.8 kbar at *ca.* 450 Ma. Speculatively this large time lag between recording of peak conditions in interlayered metabasic and metapelitic lithologies reflects an extremely slowly evolving thermobarometric regime, in which thermal buffering of mineral assemblages competed effectively with the rate of change of externally imposed *P–T* conditions.

INTRODUCTION

The combination of petrography, geochemistry and geochronology, known as the recently emerging field of petrochronology, has quickly become an important area of Earth Science. Petrochronology forms a powerful toolkit to link timing or rates to deep and mid crustal processes, whether it be to determine the longevity of a widespread metamorphic event (e.g. Donaldson et al. 2013) or to unravel complex tectonic histories (e.g. Mottram et al. 2014). However, the timing of metamorphism or even its apparent intensity may be recorded differently in rocks of differing composition and mineralogy (e.g. Schorn and Diener 2019), so it is important that petrochronological analysis is applied to a wide range of rock types in order to capture as much of the history as possible. The release of the mafic melt models for incorporation in phase equilibria modelling (Green et al. 2016), has for the first time allowed for phase equilibria modelling of suprasolidus metabasic rocks. Combined with techniques utilised by petrochronol-

ogy, this now gives petrologists the ability to compare the similarities/differences recorded by rocks of varying compositions to develop our understanding of high-temperature processes in mafic rocks and how these may differ from the better understood processes that occur in pelitic rocks. In combination, mafic and metapelitic rocks potentially record a greater extent of the thermal evolution.

This study focusses on an interlayered section of granulite-facies metabasic and metapelitic rocks in Mallee Bore, northern Harts Range, central Australia. Previous work on these rocks indicate that they experienced the same metamorphic events (Miller et al. 1997, Buick et al. 2001, Buick et al. 2005), and so can be used to explore whether rocks of differing compositions record metamorphic events differently. In the following chapter a combination of phase equilibria modelling, geochronology, geochemistry and petrography are used to compare a sample of mafic and metapelitic granulite from Mallee Bore. The results show that garnet growth continued much longer in the metapelitic rocks than in the mafic rocks, recording approximately 40 Myr of high-temperature early Palaeozoic metamorphism.

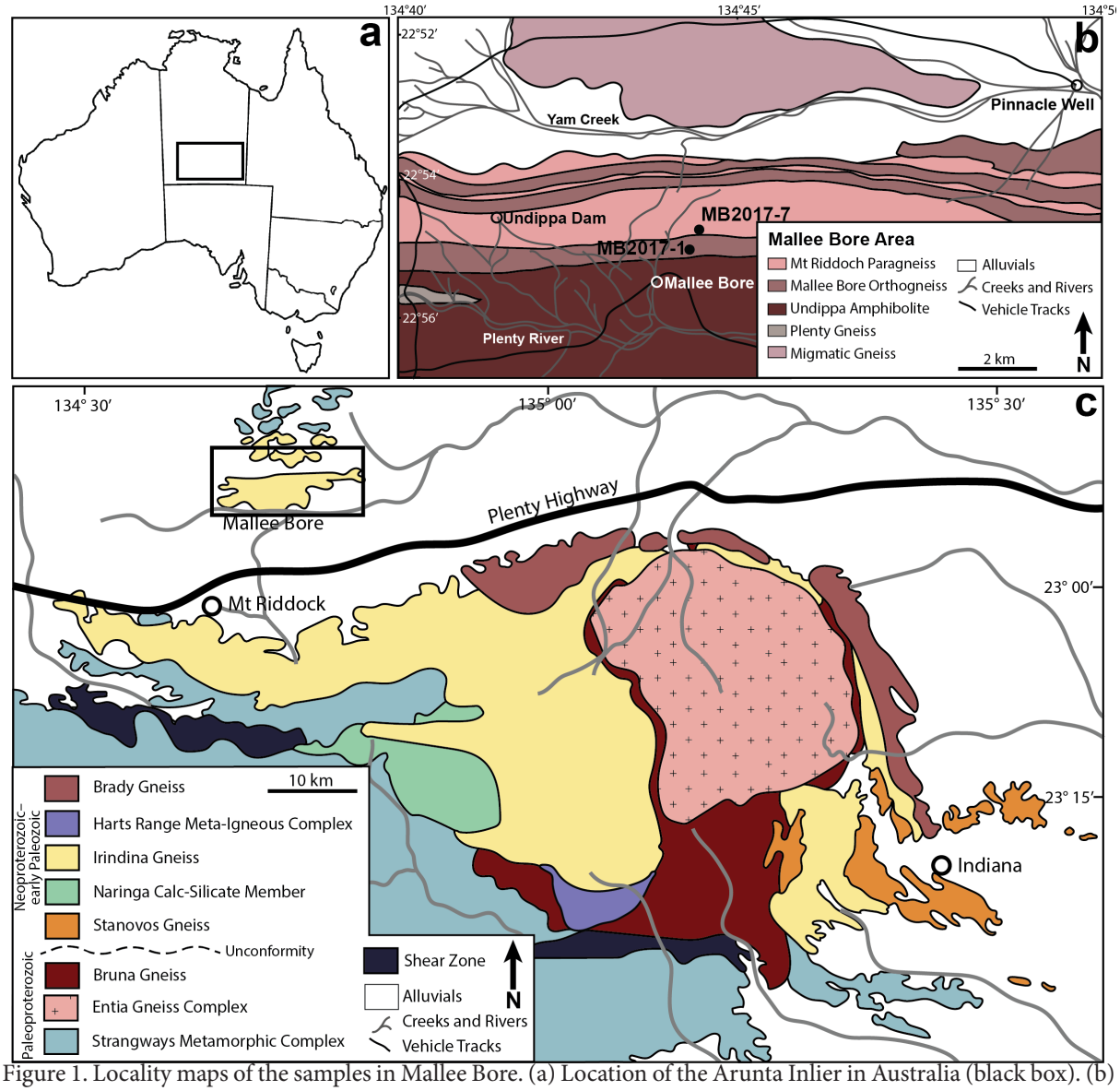


Figure 1. Locality maps of the samples in Mallee Bore. (a) Location of the Arunta Inlier in Australia (black box). (b) The geology of Mallee Bore showing the locations of the mafic sample (MB2017-1) and the pelite sample (MB2017-7). (c) The geology of the Harts Range area, showing the location of Mallee Bore. After Miller et al. (1997).

GEOLOGICAL BACKGROUND

Regional Geology

The Arunta Region in central Australia consists primarily of high-grade Paleoproterozoic–Palaeozoic (*ca.* 1900–300 Ma) metamorphic rocks and has a complex polymetamorphic history (Collins and Shaw 1995, Mawby et al. 1999, Buick et al. 2005, Maidment et al. 2005, Scrimgeour 2013, Tucker et al. 2015). The Harts Range Group forms part of the Irindina Province in the south-eastern Arunta Region, approximately 150 km north-east of Alice Springs, and is surrounded by the Georgina Basin to the north and the Amadeus Basin to the south, both of which are essentially unmetamorphosed (Lindsay 1991, Walter et al. 1995, Sandiford and Hand 1998). The Harts Range Group consists of 5 major stratigraphic units, all with depositional ages in the Neoproterozoic and Cambrian (Buick et al. 2005, Maidment et al. 2013). Despite the intensity pf metamorphism and deformation, the overall sequence in the Harts Range Group appears regionally right way up. The structurally and stratigraphically lowest member within the Harts Range Group (Figure 1) is the Naringa Calcareous Member, which outcrops primarily in the western Harts Range and consists primarily of quartzites, calc-silicates, marbles, calcareous quartzofeldspathic gneisses and metapelites (Shaw et al. 1979, Maidment et al. 2013). The Stanovos Gneiss Member outcrops in the south-eastern Harts Range and is potentially related to the Naringa Calcareous Member (Hand et al. 1999). It has been separated into an upper unit, consisting metapelitic rocks, amphibolites, quartzofeldspathic gneisses and quartzites, and a lower unit, consisting of quartzites, marble, calc-silicates and metapelitic rocks. Within the Stanovos Gneiss member ~520 Ma granites (Maidment et al. 2005), which show mingling relationships with mafic intrusives, suggest that mafic magmatism also occurred at this time. The Irindina Gneiss outcrops across much of the Harts Range (Figure 1) and comprises primarily metapelitic rocks with minor marbles, calc-silicates and quartzites. Within the Irindina Gneiss are a number of mafic units, which make up the bulk of the Harts Range Meta Igneous Complex (Scrimgeour 2013). The structurally and stratigraphically highest member of the Harts Range Group is the Brady Gneiss, which outcrops primarily in the north-east and is separated into an upper unit comprising mainly calc-silicate rocks, metapelitic rocks and psammites, and a lower unit of metapelites and minor amphibolites (Maidment et al. 2013, Scrimgeour 2013).

U–Pb dating of detrital zircon from the metasedimentary rocks of the Harts Range Group indicate the sedimentary protoliths were deposited during the Neoproterozoic to Cambrian (Buick et al. 2001, Buick et al. 2005, Maidment et al. 2013). Detrital zircon spectra for the Harts Range Group are similar to the adjacent, unmetamorphosed Georgina and Amadeus basin sediments (Maidment et al. 2013). U–Pb dating of metamorphic zircon overgrowths and Sm–Nd dating of metamorphic garnet-bearing assemblages from the structurally lowest parts of the Harts Range Group show two distinct peaks at 480 Ma and 460 Ma (Hand et al. 1999, Mawby et al. 1999, Buick et al. 2001, Buick et al. 2005, Maidment et al. 2013). These age peaks may represent a single prolonged period of metamorphism, where different parts of the thermal evolution have been recorded at different times in different rocks, or alternatively the prograde and retrograde phases of high-grade metamorphism (Mawby et al. 1999, Buick et al. 2005, Maidment et al. 2013, Tucker et al. 2015). At the base of the Harts Range Group, in the Brady Gneiss, the peak conditions are 800–820 °C and 9–10 kbar through conventional thermobarometery and phase equilibria modelling (Miller et al. 1997, Mawby et al. 1999, Buick et al. 2001, Storkey et al. 2005, Tucker et al. 2015). Coeval with metamorphism, shallow marine sediments were being deposited in the Geor-

Table 1. One atom normalised molar proportions of minerals observed in the samples from Mallee Bore.

MB2017-1		MB2017-7	
Mineral	**Mode**	**Mineral**	**Mode**
Garnet	11	Garnet	22
Plagioclase	29	Plagioclase	36
Quartz	17	Quartz	29
Hornblende	26	Biotite	9
Clinopyroxene	11	Rutile	2
Titanite	1	Sillimanite	0.2
Ilmenite	6		

gina and Amadeus basins, surrounding the Harts Range, suggesting that metamorphism within the Harts Range Group took place in an extensional setting (Hand et al. 1999, Mawby et al. 1999, Buick et al. 2005). Termination of the extensional setting occurred at 450 Ma with the onset of exhumation of the Harts Range Group during the Alice Springs Orogeny (450–320 Ma; Mawby et al. 1999, Haines et al. 2001, Buick et al. 2005, Raimondo et al. 2011).

Study Area

This study focusses on the Mallee Bore area in the northern Harts Range (Figure 1), approximately 30 km north-west of the Entia Dome (Figure 1c). The Mallee Bore area comprises metasedimentary and metabasic lithologies that underwent granulite-facies metamorphism (Miller et al. 1997). The Mallee Bore area has two major metasedimentary sequences; (1) the more abundant Mt Riddoch Paragneiss, consists of garnetiferous metapelite, garnet–biotite–felsic gneisses and garnet–cordierite-bearing quartzite. (2) The less abundant Plenty Gneiss, distinguished from the Mt Riddoch Paragneiss by the presence of large porphyroblasts of sillimanite (Miller et al. 1997). These contain distinct leucocratic layering and abundant garnet, likely resulting from high-grade partial melting (Miller et al. 1997). Conventional thermobarometry has previously estimated the peak pressure–temperature (*P–T*) conditions in the Mt Riddoch Paragneiss at approximately 820 ± 90 °C and 8.1 ± 1 kbar and the Mallee Bore Orthogneiss at approximately 730 ± 80 °C and 9.4 ± 1 kbar (Miller et al. 1997). The close proximity of the mafic and pelitic units at Mallee Bore provides an excellent opportunity to assess how the differing bulk compositions record the same metamorphic event, both thermobarometrically and geochronologically.

Field geology and petrography

Two samples were chosen for this study. The samples came from ~75 m apart across strike and are not separated by any major structures. Sample locations are shown in Fig. 1b. The mineral modes given below and in Table 1 were determined by pixel counting of field photographs and BSE thin section images using commercial image analysis software. Volumetric modal proportions were then converted into 1 atom normalised molar proportions to equate them with modal outputs generated by THERMOCALC v3.40 (Powell and Holland 1988a, Holland and Powell 2011).

Sample MB2017-1 is taken from a migmatised hornblende-rich gneiss that forms part of the Mallee Bore Orthogneiss. The sample contains plagioclase-rich segregations up to 20cm x 5cm, with garnet grains up to 1 cm and clinopyroxene up to 3 mm (Figure 2a). Garnet is significantly more abundant than clinopyroxene in the plagioclase-rich segregations. Overall in outcrop, the garnet-bearing segregations make up 5 % of the rock, with garnet comprising ~30% of the segregations. The rock around the segregations consists of coarse-grained hornblende–plagioclase–clinopyrox-

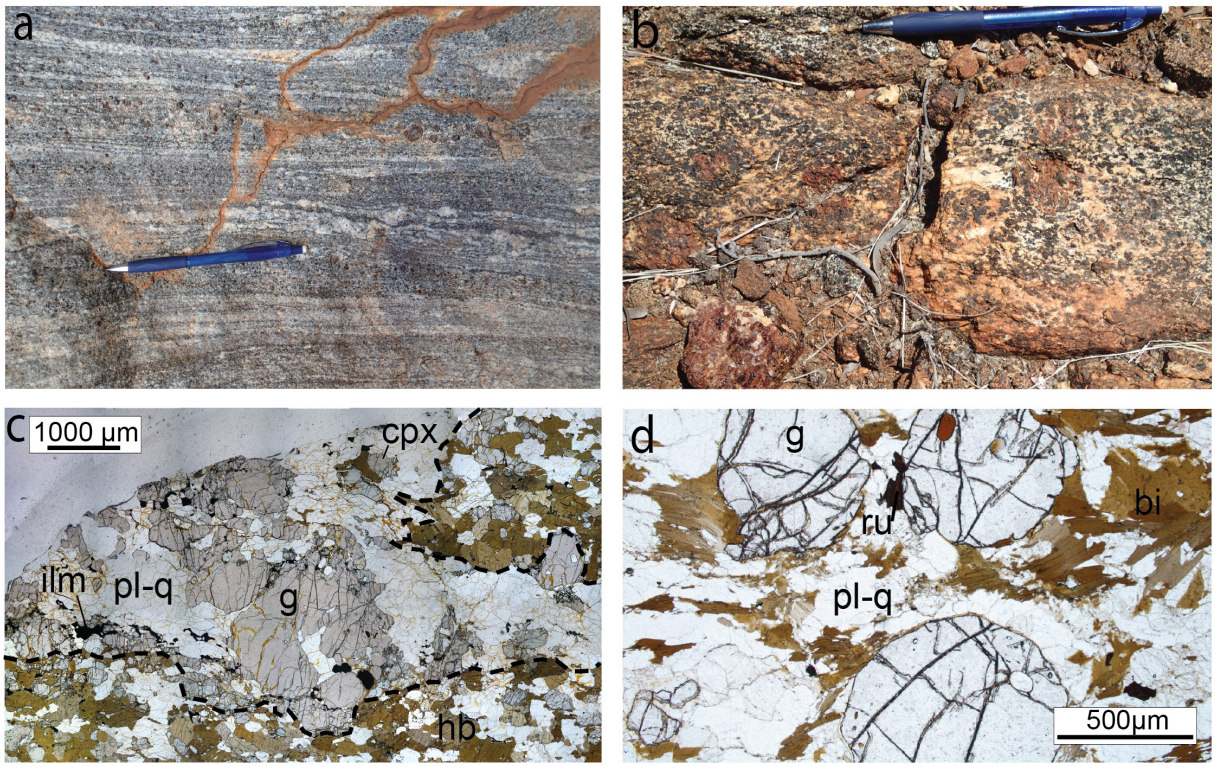


Figure 2. (a) Field photograph of MB2017-1 showing small, garnet-bearing leucosomes and alternating layers dominated by hornblende or quartz and plagioclase. (b) Field photograph of MB2017-7 showing large garnet grains surrounded by a poorly aligned foliation defined primarily by biotite. (c) Photomicrograph of MB2017-1 showing a portion of a garnet-bearing leucosome with palaeosome. The boundary of the leucosome is shown by the white dotted line. It contains coarse garnet, plagioclase, minor quartz, clinopyroxene and ilmenite. The palaeosome contains the assemblage hornblende, clinopyroxene, plagioclase, quartz, ilmenite and titanite, which occurs as abundant small grains within hornblende and at matrix grain boundaries. (d) Photomicrograph of MB2017-7 showing small, euhedral garnet grains wrapped by a weak gneissic foliation defined by layers of biotite, quartz and plagioclase.

ene gneiss. The garnet-bearing segregations are interpreted to have formed during partial melting (Miller et al. 1997). For the purpose of metamorphic analysis, the outcrop was sampled in such a way that the proportion of leucosome to palaeosome were proportional to the original outcrop proportions. Sample MB2017-7 comes from a migmatitic garnet–biotite gneiss Figure 2b). Garnet occurs both with plagioclase–quartz segregations that are parallel to a biotite-defined foliation. The foliation is parallel to the hornblende-defined foliation in MB2017-1.

MB2017-1 (-22° 55′ 5.95969″, 134° 44′ 57.39604″)

This sample contains hornblende, clinopyroxene, garnet, plagioclase, titanite, ilmenite and quartz.

There are alternating domains of garnet-rich—hornblende-absent leucosome and garnet-absent—hornblende-rich melanosome (Figure 2c). The hornblende-rich melanosome consists of hornblende–clinopyroxene–plagioclase–quartz–ilmenite–titanite. Hornblende forms large (2–8mm) subhedral grains that are generally in contact with quartz, plagioclase and clinopyroxene. Grains of clinopyroxene are often rimmed by hornblende and form large (4-10 mm) anhedral grains. Quartz and plagioclase grains occur between hornblende grains and plagioclase is commonly found in contact with clinopyroxene. The garnet-rich leucosomes consist of garnet–plagioclase–quartz–ilmenite–titanite. Garnet forms large (6–20 mm) anhedral grains that are surround-

ed by moats of quartz and plagioclase (Figure 2c). Medium sized (0.5–1.5 mm) grains of ilmenite are present throughout the sample and are commonly surrounded by plagioclase and clinopyroxene or plagioclase and hornblende. Titanite is present as inclusions in all minerals, as well as at grain boundaries. The peak assemblage is interpreted to be hornblende–garnet–clinopyroxene–plagioclase–quartz–ilmenite–titanite–melt.

MB2017-7 (-22° 55′ 2.87196″, 134° 44′ 58.49003″)

This sample contains garnet, biotite, plagioclase, sillimanite, rutile, quartz and minor ilmenite.

This sample contains some layers that are almost entirely composed of plagioclase and minor quartz separate layers dominated by biotite and garnet (Figure 2d). Garnet is euhedral to subhedral, 2–5 mm in diameter and contains inclusions of rutile, biotite, plagioclase and quartz. The garnet grains are wrapped by a foliation defined by biotite and rare sillimanite. Biotite forms elongate, euhedral grains (0.2–0.6 mm) that define the fabric in the sample, with some later grains crosscutting the foliation. Clusters of sillimanite occur rarely with biotite and are parallel to the foliation. Rutile is present as small (0.1–1 mm) anhedral grains that generally occur around the edges of biotite, garnet and plagioclase (Figure 2d). The peak assemblage of this sample is interpreted to be garnet–biotite–plagioclase–sillimanite–rutile–quartz. Assuming the sparsely garnet-bearing leucosomes formed during partial melting, the peak assemblage additionally contained melt.

Table 2. Bulk rock compositions of Mallee Bore samples. Major elements in wt% and minor elements in ppm.

	MB2017-1	MB2017-7
SiO2	50.27	63.14
TiO2	1.46	1.09
Al2O3	14.53	16.04
Fe2O3T	13.34	9.48
MnO	0.52	0.18
MgO	6.23	3.84
CaO	10.68	2.22
Na2O	2.52	3.08
K2O	0.29	0.97
P2O5	0.16	0.1
Total	**100**	**100.14**
LOI	1.38	0.97

METHODS

Bulk rock and mineral chemistry

Whole-rock geochemical analyses were obtained for each sample that was used for phase equilibria modelling using Wavelength Dispersive X-ray Fluorescence spectrometry at the Earth and Environmental Department, Franklin and Marshall College, Lancaster PA, USA. Major elements were analysed by XRF on fused disks prepared using a lithium tetraborate flux. Minor elements were analysed by XRF in briquettes prepared using copolywax. Whole rock compositions of samples used in this study are given in Table 2. Bulk samples were chosen to replicate the lithological proportions of leucosome and the surrounding palaeosome that occur in the outcrop at the m-scale.

Mineral chemical analyses were obtained using a Cameca Electron Microprobe SXFive at Adelaide Microscopy, with a beam size of 3 μm and beam conditions of 15 kV and 20 nA. Linear transects across garnet were collected from each sample to normalise REE concentrations obtained via LA-ICP-MS. EPMA maps of garnet grains were obtained using a Camera SX-51 electron microprobe with a focused electron beam at an accelerating voltage of 15 kV and a beam current of 20 nA. Individual EPMA mineral analyses are presented in Appendix 4A.

Phase equilibria modelling

Phase equilibria models were calculated for the mafic sample MB2017-1 and pelitic sample MB2017-7. For the mafic sample (MB2017-1)

phase equilibria models were calculated using the phase equilibrium modelling program THERMOCALC 3.45 (Holland and Powell 2011) in the chemical system Na_2O–CaO–K_2O–FeO–MgO–Al_2O_3–SiO_2–H_2O–TiO_2–O (NCKFMASHTO), where 'O' is Fe_2O_3, using the internally-consistent thermodynamic dataset 'ds62' and activity–composition (a–x) models of Green et al. (2016). For the metapelitic sample (MB2017-7) phase equilibria models were calculated using the phase equilibrium modelling program THERMOCALC 3.40 (Powell and Holland 1988b, Holland and Powell 2011) in the chemical system MnO–Na_2O–CaO–K_2O–FeO–MgO–Al_2O_3–SiO_2–H_2O–TiO_2–O (MnNCKFMASHTO), where 'O' is Fe_2O_3, using the thermodynamic dataset 'ds62' (Holland and Powell 2011) and a–x

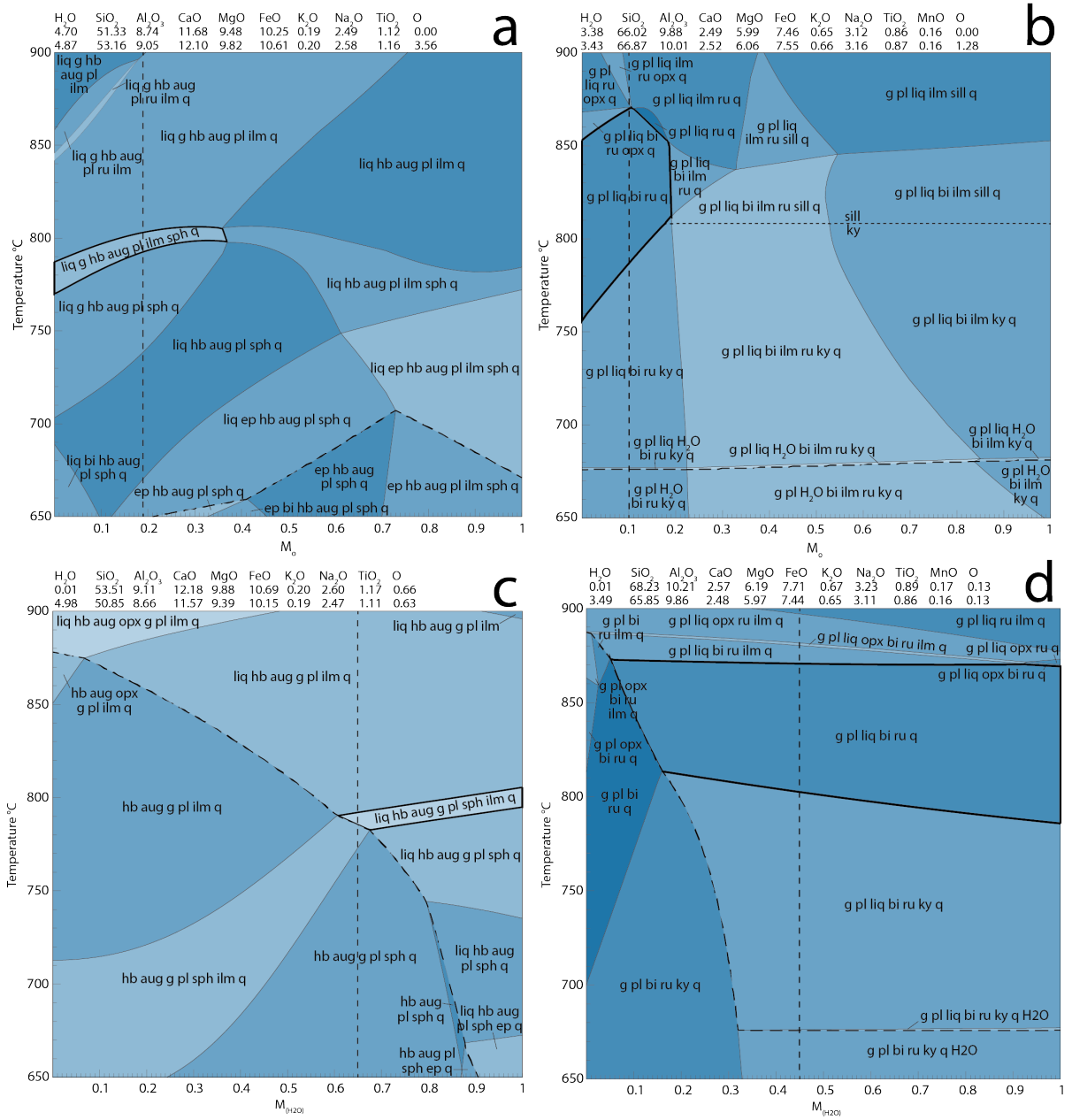


Figure 3. T–X sections used to calculate the final composition of each sample for *P–T* modelling (Figure 5). (a, b) TMo sections for samples (a) MB2017-1 and (b) MB2017-7, and (c, d) TM_{H_2O} sections for samples (c) MB2017-1 and (d) MB2017-7. In all sections the compositions are displayed on top of the diagram and the interpreted peak mineral assemblage field is outlined in bold. The solidus is represented by the long-dashed line and the composition that was chosen for further modelling is represented by the vertical short-dashed lines. All T–X sections were calculated at 10 kbar.

models of White et al. (2014a), reparameterised for Mn (Powell et al. 2014, White et al. 2014b).

The oxidation state and water content of the samples were determined via TMo and TM-H_2O models to assess the sensitivity of the assemblages to H_2O and oxidation state (Figure 3).The *T–X* sections were calculated at a pressure of 10 kbar, based on *P–T* estimates from other samples within the Harts Range Group (Tucker et al. 2015). The oxidation state of the peak fields in these models is well constrained by the presence of rutile (Figure 3a, b). Although the modelled peak assemblage in sample MB2017-7 contains kyanite rather than sillimanite, the oxidation state is well constrained by the absence of ilmenite in the rock and the presence of kyanite likely reflects that the TMo section was calculated at too high a pressure (Figure 3b).The water content of both samples is less well constrained by the TM_{H_2O} sections(Figure 3c, d). For the mafic sample MB2017-1, the water content was selected so that the peak assemblage was bound to lower temperatures by the solidus, as it is commonly inferred that that strongly foliated granulite-facies rocks do not retain large volumes of melt at peak conditions. In metapelitic sample MB2017-7, the there are no sillimanite-bearing fields in the TM_{H_2O} section, but the peak assemblage with kyanite is stable over a large range of H_2O contents. In this case the H_2O content was chosen based on the calculated amount of water in biotite, the only hydrous mineral in the peak assemblage.

Geochronology and REE analysis

U–Pb geochronology and REE analysis was undertaken on zircon and monazite in sample MB2017-7, and zircon in sample MB2017-1. Samples were crushed using a jaw crusher and sieved to collect the 79–300 μm fraction. Minerals were concentrated by panning and using a Frantz magnetic separator, before hand picking to obtain pure separates. Grains were then mounted in epoxy disks and polished to expose the grain centres. All grains were imaged on a back-scattered electron (BSE) detector on an FEI Quanta 600 Scanning Electron Microscope (SEM) to identify any inclusions or zoning. Zircon was also imaged on the same SEM with an attached Gatan cathodoluminescence (CL) detector. Representative BSE and CL images of each mineral are shown in Figure 4. All U–Pb geochronology was done using Laser¬-Ablation-Inductively Coupled Plasma-Mass Spectrometry (LA-ICP-MS) at the University of Adelaide. U–Pb isotopic analyses were obtained using a Resonetics M50 ArF Excimer laser in a He ablation atmosphere, coupled to an Agilent 7700cs ICP–MS at Adelaide Microscopy, the University of Adelaide. All isotopic data were reduced using Iolite version 3 (Paton et al. 2011), and are provided in Appendix 4B.

Zircon Geochronology

Zircon grains were ablated with a spot size of 29 μm beam and a frequency of 5 Hz. Total analysis time was 60 Seconds and included 30 seconds of background measurements and 30 seconds of ablation. The full dataset of LA–ICP–MS zircon analyses collected in this study are provided in Appendix 4B. U–Pb fractionation was corrected for using the primary standard GJ-1 ($^{207}Pb/^{206}Pb$ = 608.3 Ma, $^{206}Pb/^{23}8U$ = 600.7 Ma and $^{207}Pb/^{235}U$ = 602.2 Ma Jackson et al. 2004). Accuracy of the age measurements was checked during processing against the unknown analyses using the zircon standards Plesovice ($^{206}Pb/^{238}Pb$ age of 337.1 ± 0.37 Ma; Sláma et al. 2008) and 91500 ($^{207}Pb/^{206}Pb$ age= 1065.4 ± 0.3 Ma, $^{206}Pb/^{238}U$ age = 1062.4 ± 0.4 Ma; Wiedenbeck et al. 1995). Throughout the analytical session the Plesovice standard yielded an average $^{206}Pb/^{238}U$ age of 340.8 ± 1.5 Ma (n = 24, MSWD = 2.5) and the 91500 standard yielded an average $^{207}Pb/^{206}Pb$ age of 1040 ± 44 Ma (n = 16, MSWD = 5.9) and an average $^{206}Pb/^{238}U$ age of 1060.6 ± 6.3 Ma (n =

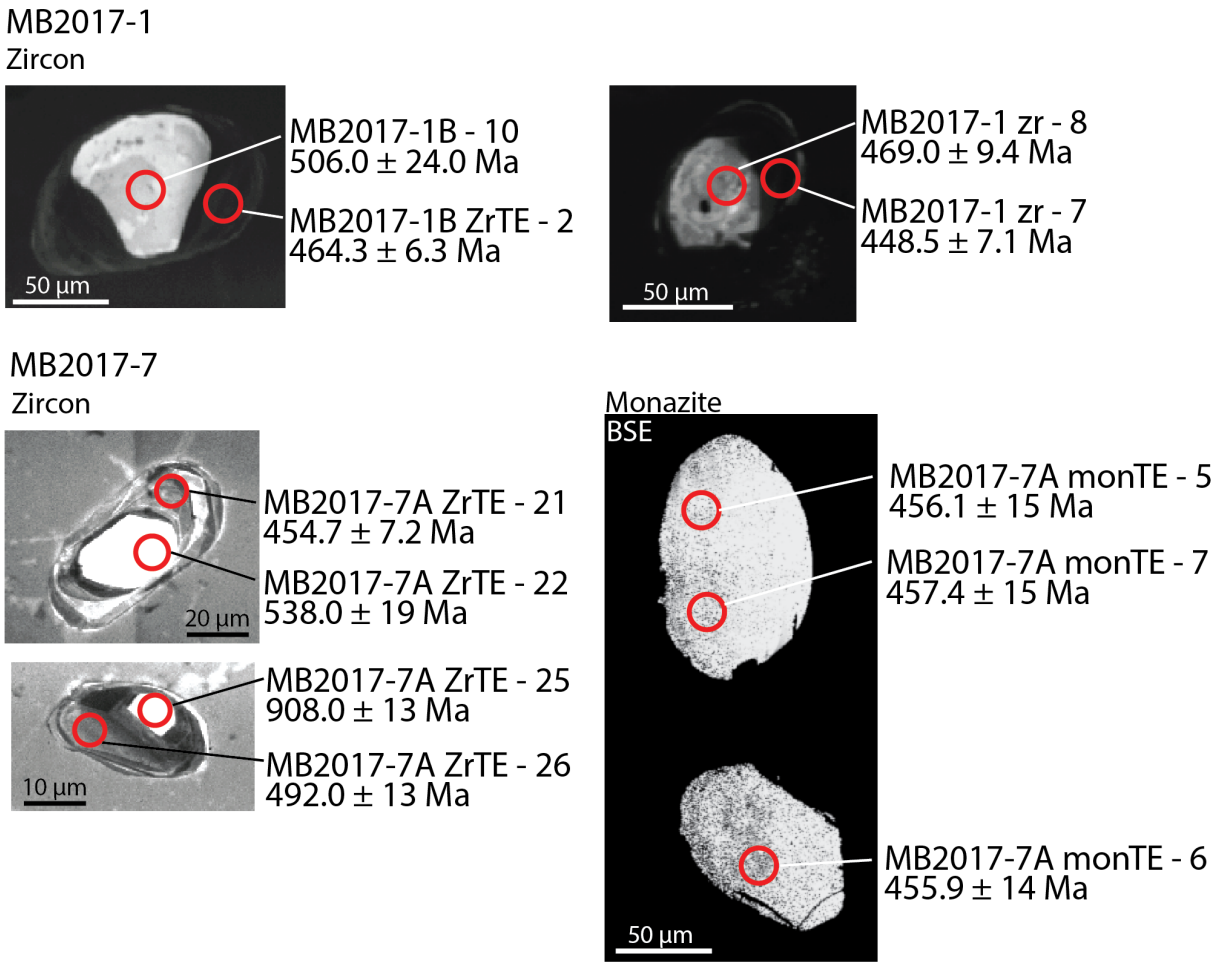


Figure 4. Representitive CL images of zricon and BSE images of monazite grains that were analysed for sample MB2017-1 and MB2017-7.

16, MSWD = 1.9) throughout all analyses. No analyses were corrected for common Pb due to extremely low ^{204}Pb counts in all unknown analyses. Data were then plotted using Isoplot (Ludwig 2003).

Monazite Geochronology

Monazite grains were ablated with a spot size of 19 µm beam and a frequency of 5 Hz. Total analysis time was 60 Seconds and included 30 seconds of background measurements and 30 seconds of ablation. The full dataset of LA–ICP–MS monazite analyses collected in this study are provided in Appendix 4B. U–Pb fractionation was corrected for using the primary standard MAdel (TIMS normalisation data: ^{207}Pb/^{206}Pb = 491 ± 2.7 Ma, ^{206}Pb/^{238}U = 518.37 ± 0.99 Ma and ^{207}Pb/^{235}U = 513.13 ± 0.19 Ma; updated from Payne et al. 2008 with additional TIMS analyses). Accuracy of the age measurements was checked during processing against the unknown analyses using the in house monazite standard 94-222 (^{206}Pb/^{238}U age = 449.7 ± 3.4 Ma; Payne et al. 2008). Throughout the analytical session the 94-222 standard yielded an average ^{206}Pb/^{238}U age of 458 ± 7.6 Ma (n = 10, MSWD = 2.4).

Garnet trace element mapping

Trace element mapping of garnet was done insitu on standard polished thin sections. As with the U–Pb geochronology, LA–ICP–MS trace element maps were acquired using a Resonetics (now Australian Scientific Instruments) M50 ArF Excimer laser in a He ablation atmosphere, coupled to an Agilent 7700cs ICP–MS at Adelaide Microscopy, the University of Adelaide. Linear traverses of single point

analyses were initially measured to gain quantitative data and an understanding of any compositional zoning prior to mapping. The traverses were analysed using a 29 µm spot size, 5 Hz frequency, and a total acquisition time of 60 s, inclusive of 30 s of background measurement. The reference glass NIST610 was used as the external standard and electron microprobe analyses of Al in these garnets served as an internal standard (Appendix 4A).

After zoning was shown to be present by the traverses, full LA-ICP-MS mapping of the garnet grains was undertaken. Instrument conditions and protocols that were used in this study have been outlined by several previous studies from this laboratory on silicate minerals (Sharrad et al. 2014, Xu et al. 2016, Raimondo et al. 2017). A beam diameter of 23 µm with a laser repetition rate of 10 Hz was used, along with a scan speed of 23 µm s-1 and line spacing of 23 µm. The reference glass NIST612 (Pearce et al. 1997, Jochum et al. 2011) and the garnet standard GSD-1G (Jochum et al. 2005) were analysed throughout the runs.

RESULTS

Phase equilibria modelling

Phase equilibria modelling of sample MB2017-1 constrains the peak assemblage of melt–hornblende–augite–garnet–plagioclase–ilmenite–titanite–quartz to conditions of ~790–900 ± 15 °C and 9.8–12.6 ± 0.6 kbar. The upper pressure boundary of this peak assemblage is constrained by ilmenite, whereas the lower pressure boundary is constrained by titanite (Figure 5a). The upper and lower temperature boundaries of this field are constrained by hornblende and the solidus, respectively (Figure 5a). The temperature of the solidus and thus the minimum peak temperature is largely controlled by H_2O content as modelled in the TM_{H_2O} section.

The peak assemblage in sample MB2017-7, melt–garnet–sillimanite–plagioclase–biotite–rutile–quartz, is constrained to ~690–800 ± 3 °C and 7.0–9.8 ± 0.1 kbar, not inclusive of errors. The upper pressure boundary of this field is well-constrained by the kyanite–sillimanite boundary, whereas the lower pressure boundary is constrained by the absence of cordierite and ilmenite in the rock (Figure 5b). The up-

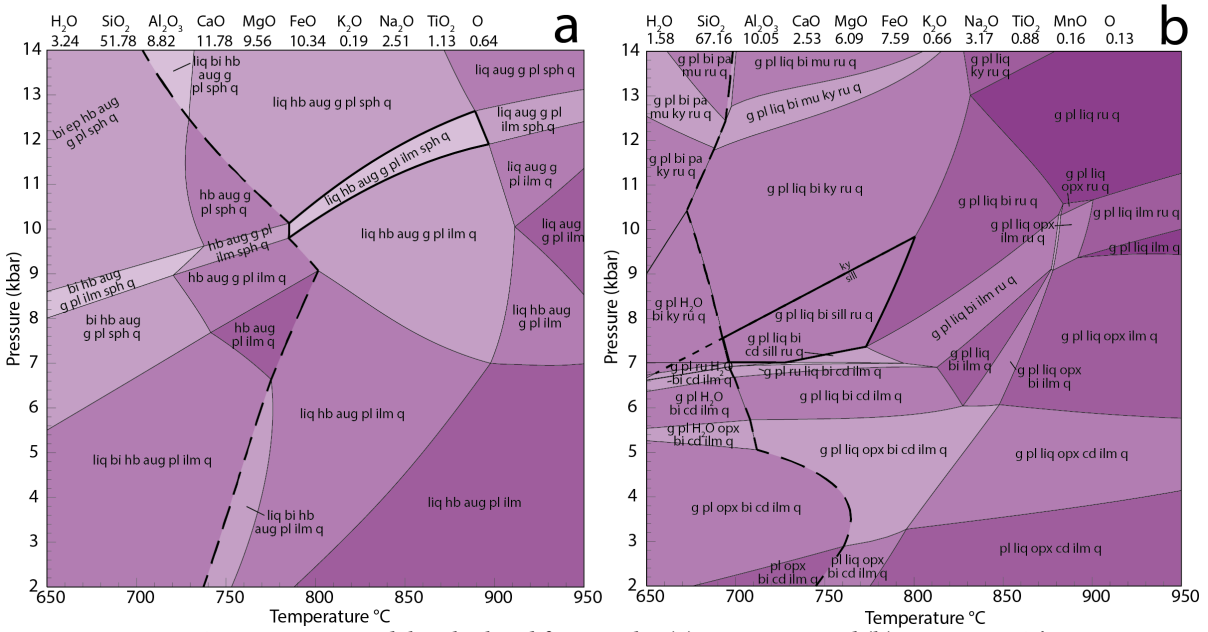


Figure 5. Pressure–Temperature models calculated for samples (a) MB2017-1 and (b) MB2017-7. The compositions are shown at the top of the diagrams and the peak mineral assemblage fields are outlined in bold. The solidus is represented by the dashed lines.

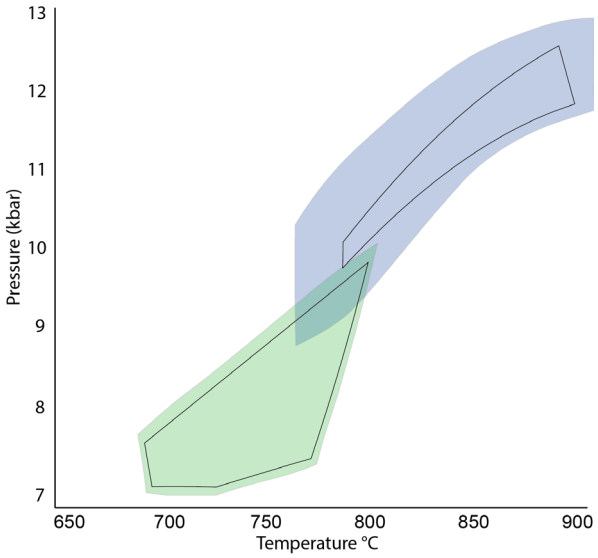


Figure 6. Peak *P–T* fields of sample MB2017-1 (blue) and MB2017-7 (green) taken from the *P–T* sections in Figure X. The coloured areas around the fields represent the errors on the field boundaries calculated in THERMOCALC (Holland and Powell 2011).

per temperature boundary of the peak field is constrained by sillimanite, whereas the lower temperature boundary is constrained by the wet solidus (Figure 5b). Explorative modelling of different H_2O contents in this sample revealed that lower H_2O contents supressed the occurrence of sillimanite, requiring the presence of a wet solidus.

The peak conditions from the two samples do not directly overlap. However, when the 2σ uncertainties on the field boundaries are taken into account, there is a small region of overlap between 760–800 °C and 8.8–9.9 kbar (Figure 6). This indicates that the maximum geothermal gradient in this area was ~90 °C/kbar.

U–Pb geochronology and REE analysis

The maximum depositional age of the Harts Range Group has been identified as 545–500 Ma (Buick et al. 2001, Buick et al. 2005, Maidment et al. 2013, Scrimgeour 2013), so any ages older than the early Cambrian are assumed to be inherited detrital ages. In both samples data was collected in two separate analytical sessions; one session with only U–Pb and one including U–Pb and REEs. This was done to assess how the collection of REEs affected the quality of U–Pb data in a single analysis. There was no significant difference in age or error in U–Pb data between either set of analyses, suggesting that the collection of REE does not significantly affect U–Pb data quality. Only analyses within uncertainty of concordia were used for interpretation. All zircon analyses are given in Appendix 4B.

MB2017-1

The amount of zircon present in sample MB2017-1 was limited, despite processing ~5kg of sample, and so only a total of 23 analyses were analysed from 16 zircon grains. Zircons range in size from ~40–200 μm and are either rounded or euhedral in shape (Figure 4). Most zircons in this sample are zoned in some way, with older ages recorded in the cores of the grains and slightly younger ages recorded in the rims. One analysis was discarded due to discordance and three analyses were discarded as they were older than the maximum depositional age. Of the remaining 19 concordant analyses, only 13 were analysed with REEs. Some analyses had extremely low 238U counts, resulting in large errors. The ages acquired range from ~520–420 Ma (Figure 7a). A weighted average age yields a high MSWD (9.2) and probability of zero, suggesting that these analyses do not form one population.

The thirteen zircon REE analyses that were collected show consistent patterns in chondrite normalised spider plots (Figure 8a). Most of these grains are largely depleted in LREEs, with many analyses below detection limit, and enriched in HREEs. Some grains show a slight negative Eu anomaly, but this is largely absent. There is some correlation between HREE enrichment with age, with the more HREE-enriched grains largely being older.

MB2017-7

In sample MB2017-7 zircons range in size from ~30–150 μm and generally form elon-

gate, euhedral grains, with some of the smaller grains being rounder in shape (Figure 4). Most zircons in this sample contain inherited cores with interpreted metamorphic rims. Detrital ages are mainly recorded in the cores of the grains and younger ages recorded in the rims. A total of 110 analyses were obtained from 62 zircon grains. Of these, 69 analyses were interpreted to be detrital, on the basis of the maximum depositional age in the Mallee Bore area. The 41 remaining interpreted metamorphic analyses gave a spread in ages from ~500–450 Ma (Figure 7b). A weighted average age gives a high MSWD and probability of zero, suggesting that these analyses do not define a single population. Six of these analyses have high Th/U ratios (>0.1) for metamorphic zircons in a metapelitic rock. These analyses have been kept for all age calculations but have been highlighted in Figure 7b.

Thirty-four zircon REE analyses were collected from MB2017-7 and have variable trace element patterns and concentrations. Some of the zircons are mildly depleted in LREEs, whereas others are enriched in these elements. Negative Eu anomalies of varying magnitudes are present in some analyses but are completely absent in others. Overall the zircons show some enrichment in HREEs, with some correlation between age and HREE-enrichment showing that younger zircons are less enriched. HREE slopes were much more variable than the mafic sample (Figure 8b).

Monazite was analysed as separates in MB2017-7, with a total of 23 analyses from 12 grains. Monazite grains vary from ~20–120 µm in diameter (Figure 4). No zoning was observed in any of the monazite grains using BSE imaging. The analyses have a much smaller age range than zircon (~470–440 Ma) and give a weighted average age of 451.9 ± 2.1 Ma (MSWD = 1.8, probability = 0.012; Figure 7c). All grains have a moderate negative Eu anomaly, suggesting growth occurred during a time

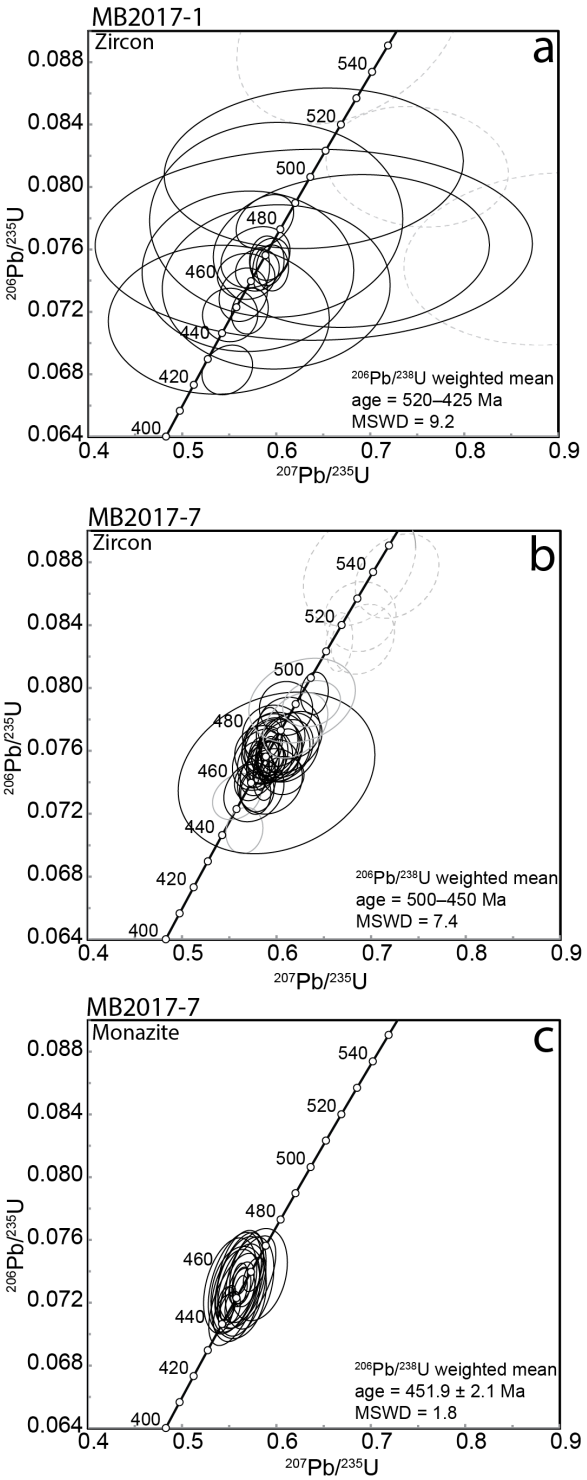


Figure 7. Zircon U–Pb geochronology concordia plots from sample (a) MB2017-1 and (b) MB2017-7. Solid grey ellipses represent analyses with high Th/U (Th/U = >0.1) and dashed grey ellipses represent analyses that were discordant or detrital. (c) Monazite U–Pb geochronology concordia plot for sample MB2017-7.

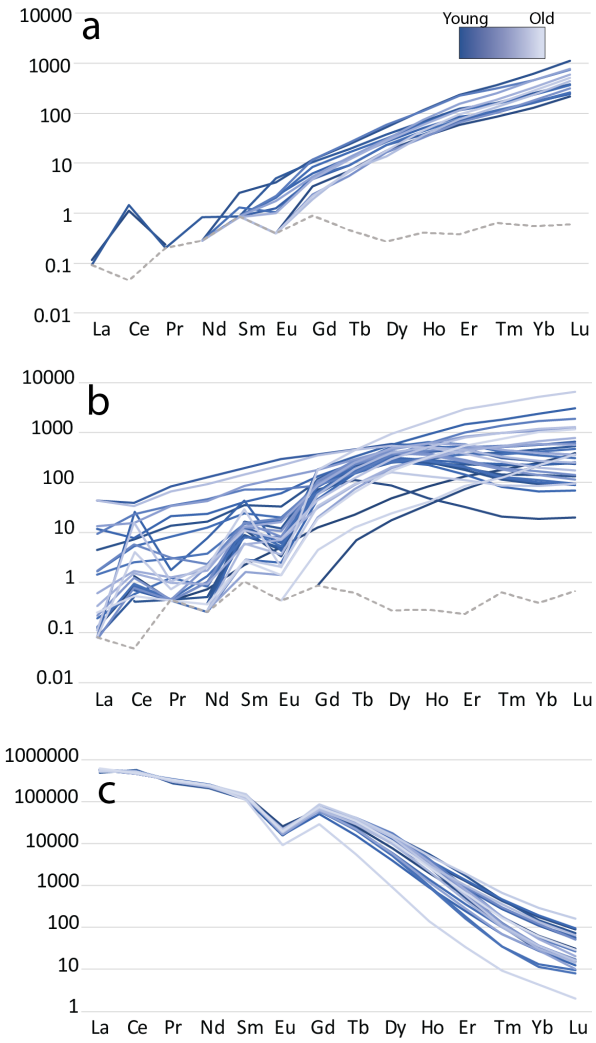


Figure 8. Chondrite normalised REE patterns of LA-ICP-MS spots on zircon grains in (a) MB2017-1 and (b) MB2017-7, and monazite grains in MB2017-7 (c). All REE concentrations are in ppm. The dashed line represents the detection limit of each set of analyses for each element from Iolite. Normalisation after Sun and McDonough (1989).

when plagioclase was stable. There is a range of HREE contents, but all grains are largely depleted in HREEs (Figure 8c).

Garnet REE mapping and analysis

LA-ICP-MS major element maps from MB2017-1 and MB2017-7 show good correspondence to EPMA X-ray maps for each sample (Figure 9). From the suite of 31 elements collected for garnet LA-ICP-MS mapping, a subset the maps that are most indicative of growth patterns are given in Figure 10. All of the elemental maps and their concentrations are given in Appendix 4C. In this study, individual spot analyses have been used to gather a transect of data across garnets from both samples. This was done to assess zoning in the grains prior to mapping but was also used to calculate more accurate linear transects in Figure 11, without the effects of signal smearing or compromised detection limits. Garnet LA-ICP-MS analyses are given in Appendix 4D.

MB2017-1

The analysed garnet in sample MB2017-1 has an embayed/irregular grain shape (Figure 10). The primarily smooth zoning patterns of the major elements are decoupled from the REEs. The major elements are relatively consistent across the interior of the grain, with a thin outer rim that enriched in Mn and Fe and depleted in Ca and Mg (Figure 10). Garnet REE analyses in sample MB2017-1 all behave in a similar way. Most analyses are depleted in LREEs, with a slight negative Eu anomaly (Figure 12a). LREE values are approaching or are at detection limits, making detection of any zoning patterns difficult. The MREEs (Eu–Gd) display faint zoning, shown as mainly an increase in concentration in the mantle zone of the garnet with a drop in concentration towards the outer edges in this sample. All analyses are enriched in HREEs and show a pattern of decreasing HREE concentration from core to rim (Figure 12a). HREEs and Y show relatively flat zoning patterns in the core and mantle of the garnet, with oscillatory zoning and a sharp increase in concentration at the edge of the grain, similar to V and Cr.

MB2017-7

The analysed garnet in sample MB2017-7 has a euhedral grain boundary with some minor irregularities (Figure 10). The garnet is unzoned in Fe and Mg except for a thin zone at the edge of the grain that is enriched in Fe and depleted in Mg, whereas there is a gradual decrease in Mn from core to rim. In contrast, Ca and V have more complex zoning, with

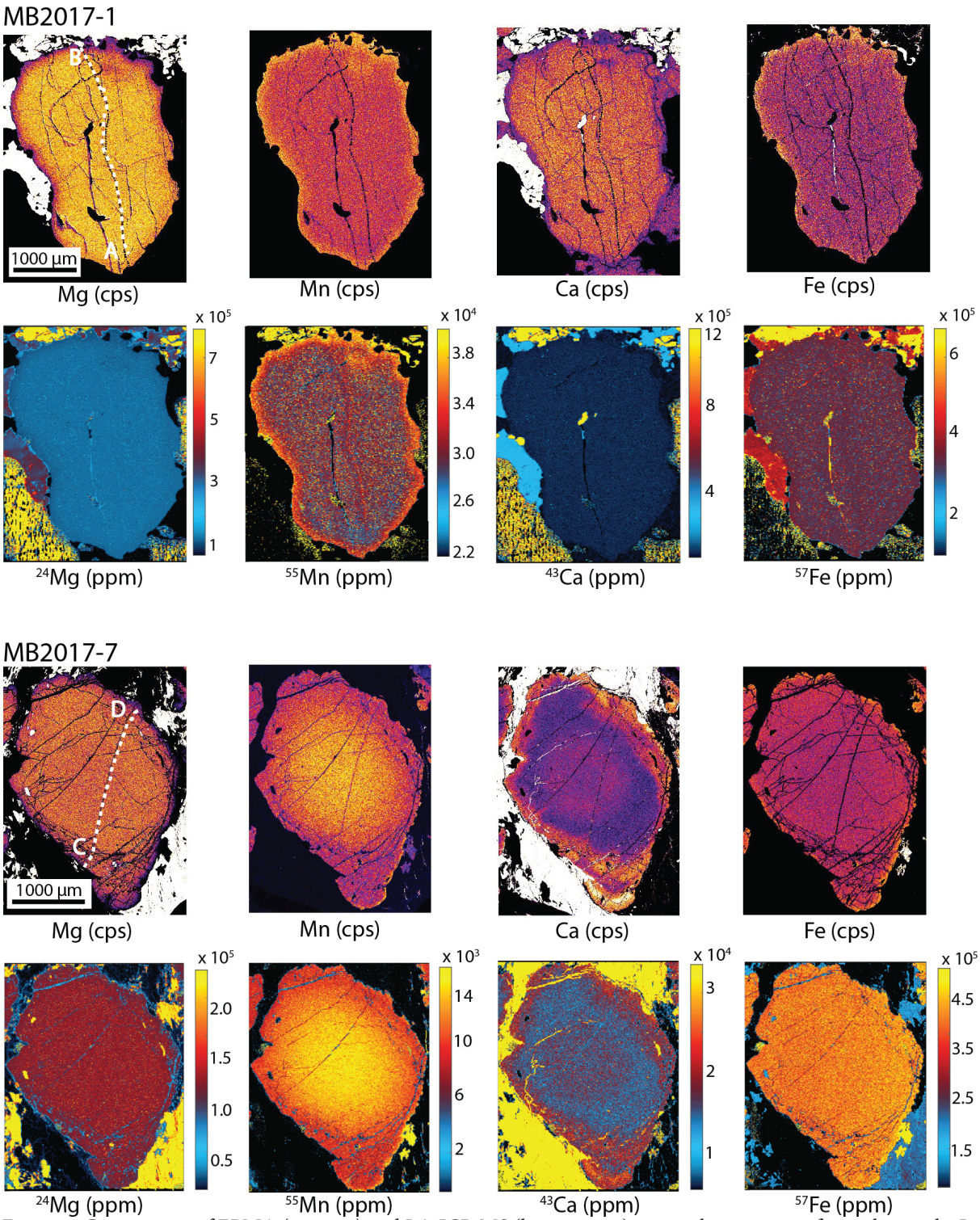


Figure 9. Comparison of EPMA (top row) and LA-ICP-MS (bottom row) major element maps for each sample. In the EPMA maps yellow represents high abundances and purple represents low abundances, whereas in the LA-ICP-MS maps warmer colours represent high abundances and coolers colours represent lower abundances. The dashed red line on the first EPMA map for each sample represents the line over which a LA-ICP-MS linear transect was analysed prior to mapping and correspond to the lines used in Figure 12.

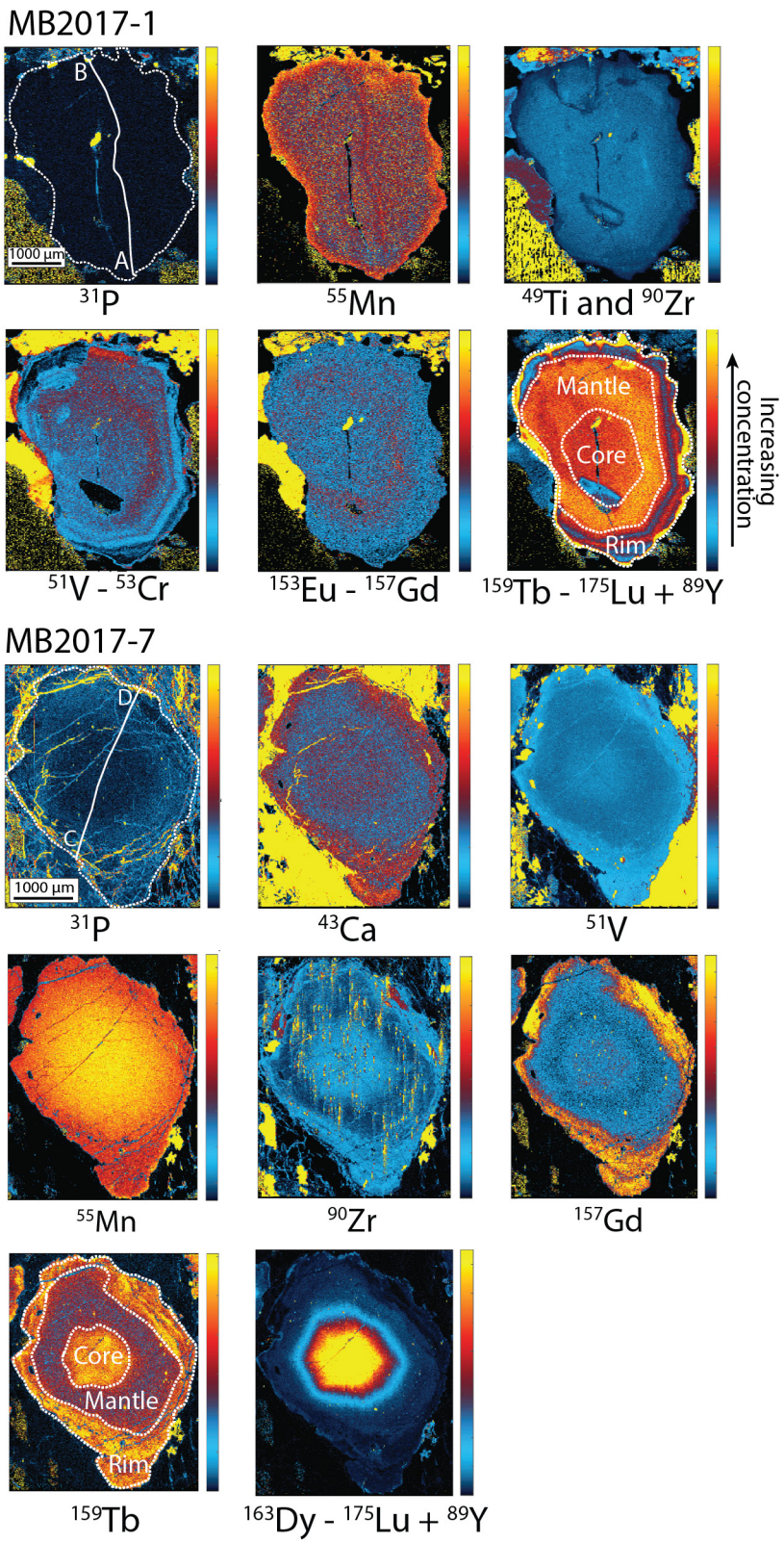


Figure 10. Quantified representative LA-ICP-MS garnet trace element maps from sample MB2017-1 and MB2017-7. Where maps are representative of patterns that occur for more than one element, the rage of elements represented by the map are given. All quantitative maps are given in Appendix 4C. The dashed outline in the first map represents the boundary of the garnet that was analysed. Line A–B in the first map of sample MB2017-1 shows the core-rim transect of individual LA-ICP-MS analyses shown in Figure 12, and Line C–D in the first map of sample MB2017-7 shows the core-rim transect of individual LA-ICP-MS analyses shown in Figure 11.

multiple zones of increasing and decreasing concentration. This zoning pattern can also be seen in Zr and MREE but is best highlighted by Tb and Gd (Figure 10). REE analyses from the garnet in sample MB2017-7 have far more variable compositions than those from the garnet analysed in sample MB2017-1. All analyses are depleted in LREEs, with a negative Eu anomaly (Figure 12b). The data show a pattern of decreasing HREE concentration from core

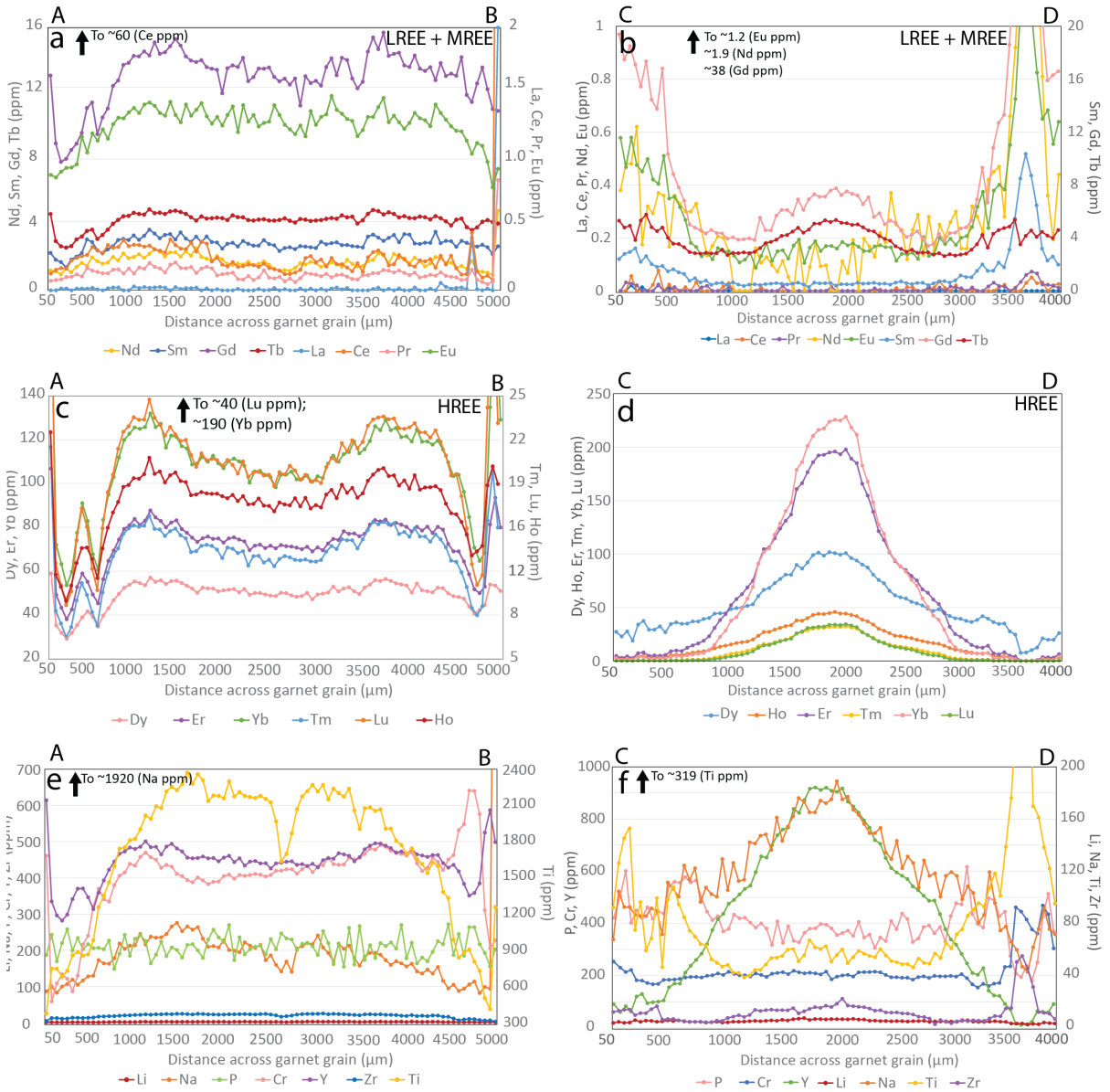


Figure 11. LA-ICP-MS transects across line A–B in sample MB2017-1 (a, c, e) and line C–D (Figure 10) in sample MB2017-7 (b, d, f).

to rim, with the outermost rim becoming very HREE-depleted (Figure 12b). Zr concentrations decrease from the core to the mantle layer, then increase again towards the rim. LREEs are largely approaching or at detection limit, so no real zoning can be observed in these elements. MREEs sharply increase in concentration towards the garnet rims, with Gd and Tb showing a lower concentration zone towards the core of the grain. HREEs and Y all show a similar trend of high concentrations in the centre of the grain, which gradually decrease towards the rim. This garnet appears to have a growth-zoned core, with a gradual decrease in HREEs, and a distinct rim, which is best highlighted by Tb (Figure 10).

DISCUSSION

The aim of this study is to gain a greater understanding of the ways that rocks of differing compositions record high-grade metamorphism, through looking at the timing of growth of accessory minerals relative to major silicate minerals such as garnet. This has been done through the integration of U–Pb zircon geochronology, phase equilibria modelling

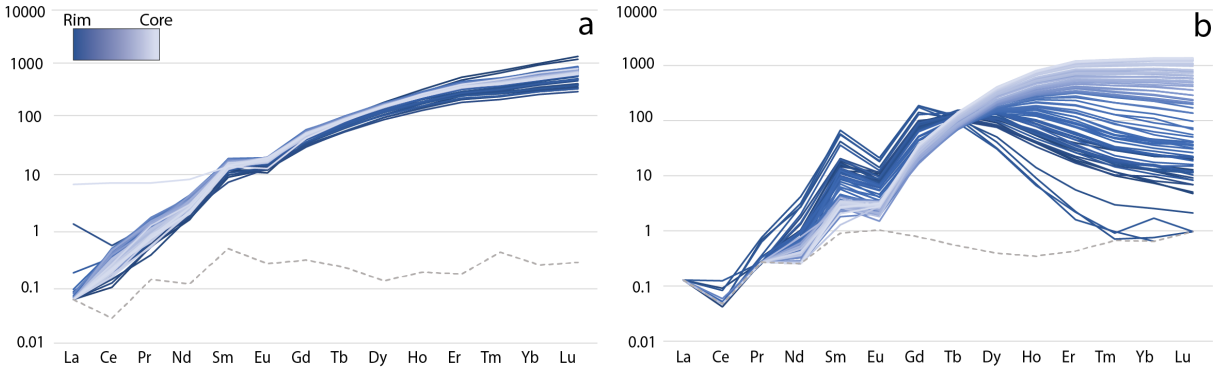


Figure 12. Chondrite normalised REE patterns of the LA-ICP-MS individual spot transects across the garnet grains in (a) MB2017-7 and (b) MB2017-7. All REE concentrations are in ppm. The dashed line represents the detection limit of each set of analyses for each element from Iolite. Normalisation after Sun and McDonough (1989).

and mineral chemistry and mapping of two samples are located within ~75 m of one another.

Peak Metamorphic Conditions

We recognise that the discussion that follows is heavily leveraged against modelling realistic bulk compositions. In this context we recognise the bulk composition of MB2017-7 is very reduced. However, we believe the approach of using mineral analyses and mineral modes to be superior to whole rock chemistry because it removes any oxidative processes on grain boundaries. We note that the bulk composition of MB2017-7 is reduced, relative to even Archaean sedimentary rocks, which formed in a low aO_2 environment. However, we note that the vast bulk of whole rock geochemistry is taken from the Earth's surface, where oxidation is almost unavoidable. By constructing a whole rock Fe_2/Fe_3 ratio from analysis of stoichiometrically valid mineral analysis, we believe we are determining a robust rock Fe2/Fe3. This reduced value is consistent with the presence of rutile, and the absence of ilmenite anywhere in the textural evolution of the rock. The reduced nature is also consistent with the deep rift marine depositional setting (Maidment et al. 2013, Tucker et al. 2015). In $T–M_o$ space, the chosen O stabilises kyanite. However, this is likely to be because the chosen pressure is slightly too high, despite using pressures determined from previous studies (Tucker et al. 2015). We note that reducing pressure of the $T–M_o$ by 0.5 kbar will stabilise sillimanite, consistent with the paragenesis.

The peak fields of samples MB2017-1 and MB2017-7 modelled in THERMOCALC do not overlap directly, but when errors are included on the fields there is a small overlap at 760–800 °C and 8.8–9.9 kbar (Figure 6). The overlap between the errors on these peak fields agree well with previous work, including individual geothermometers and geobarometers, and average *P–T* calculations, in Mallee Bore and the Harts Range (Miller et al. 1997, Hand et al. 1999, Buick et al. 2001, Buick et al. 2005, Tucker et al. 2015). These errors were calculated in THERMOCALC, using the same internally consistent datasets that was used to calculate the original fields (Powell and Holland 1988a, Holland and Powell 2011). However, as can be seen in Figure 6, the errors associated with the peak field of MB2017-1 (blue) are much larger than those associated with MB2017-7 (green). However, these phase equilibria models highlight the importance of modelling multiple compositions in order to better constrain *P–T* conditions, as mafic and metapelitic compositions generally stabilise different minerals that are influenced by different factors. For example, the kyanite–sillimanite boundary constraining the peak pressure in the pelite sample (MB2017-7; Figure 5b) is a robust pressure constraint that is not affected by compositional variables. However, many of the other peak field boundaries in both sam-

ples are constrained by mineral stability that may be influenced by H_2O and O concentrations, which are chosen through *T–X* modelling.

Relationship between garnet zoning and accessory mineral growth

When plotted on a chondrite normalised spider plot, the garnet composition in the mafic sample MB2017-1 is far less variable than in the metapelitic sample MB2017-7. The garnet HREE content of MB2017-7 changes over several orders of magnitude from the core to the rim, whereas all of the REEs in MB2017-1 only change slightly across the diameter of the grain (Figure 12). These same patterns in concentration are also reflected in the zircon REE compositions for both samples, although not all zircons preserve a Eu anomaly like the garnets (Figure 8a, b).

The REE garnet zoning in MB2017-1 displays a slight depletion in REE, particularly HREE, in the core of garnet, with most trace elements then increasing to peaks in a relatively symmetrical pattern in the mantle, before again dropping in concentration at the rims (Figure 10). In the mafic composition (MB2017-1), primary accessory phases that may have broken down during garnet growth to liberate REE could include zircon, apatite, xenotime or titanite. There are no corresponding changes in Zr, Ca and P contents in the garnet, suggesting that breakdown of any of these minerals is unlikely to explain the trace element enrichment patterns (Figure 10 and 11a). The outer edge of garnet is very irregular in shape, compared to the very euhedral zoning within, and has a thin, highly Mn- and HREE-enriched rim, suggesting garnet has undergone resorption to some extent (Hwang et al. 2003).

The metapelitic sample preserves different zoning patterns to the mafic sample, in particular in Mn and Ca and the M–HREEs. The bell-shaped decrease in HREEs and Y from core to rim of the garnet in metapelitic sample MB2017-7 (Figure 11d, f) are very typical of prograde garnet growth (Hickmott et al. 1987, Caddick et al. 2010). In contrast to the apparent prograde zoning patterns displayed by the HREEs and Mn, some elements point to a more complex growth history. There is a distinct rim that is enriched in Gd, Tb, Ca and to some extent, P (Figure 10), indicating that breakdown of another mineral occurred towards the end of garnet growth and liberated these elements for garnet uptake. The combination of elements that became available are typical of apatite breakdown (Nagasawa 1970, Fujimaki 1986, Yakymchuk 2017) and so likely reflect the breakdown of apatite during the late stages of garnet growth.

The age range defined by metamorphic zircon growth is the same in both samples. However, the REE patterns in the garnets and zircons in

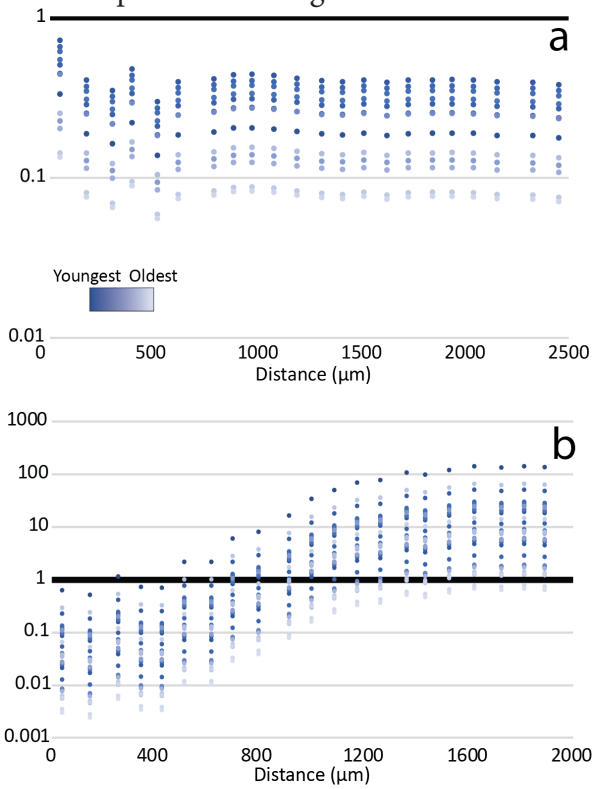


Figure 13. Scatter plot showing DREE(zircon–garnet) for all zircon analyses against garnet analyses on a log scale from rim (left) to core (right) in (a) MB2017-1 and (b) MB2017-7. The plot shows the changing age of the zircons growing in equilibrium (the bold line at 1) with different garnet zones.

both samples show different trends, indicating that garnet growth relative to zircon growth occurred at different times between the samples. To investigate the relationship between garnet and zircon growth, REE partition coefficients (DREE) were calculated for every zircon across a garnet transect from rim to core in both samples to determine whether zircon and garnet were growing in equilibria at any stage. As thoroughly discussed by Taylor et al. (2017), the visualisation of large DREE datasets can be difficult, so we have summarised the data into the plot in Figure 13. In Figure 13, each vertical column of points represents all the zircon analyses obtained with REEs for that sample against one garnet analysis, and are colour coded from oldest (lightest) to youngest (darkest) in age. Each point is representative of the slope of the HREE line for that particular zircon analysis relative to the garnet analyses ($DREE_{(zircon-garnet)Gd/Yb}$). Points that lie close to one (bold line; Figure 13) are thought to represent zircons that were growing in equilibrium with garnet at that time. Points that lie below one suggest that garnet was more HREE-enriched than zircon and points that lie above one suggest that zircon was more HREE-enriched than garnet. The Gd/Yb slope of each DREE(zircon–garnet) line was calculated using the methods of Taylor et al. (2017) and were plotted from rim–core. In the pelitic sample MB2017-7, there is a very clear trend with zircons of changing ages growing in equilibrium with different zones of the garnet (Fig. 14b). In general, the youngest zircons are in equilibrium with the rim and the older zircons with the core, as to be expected. The zircon closest to equilibrium with the rim of the garnet is spaced quite far from the other points and so it is difficult to tell whether zircon was truly in equilibrium with the garnet rim. Garnet may have been growing for the entire 50 Myr period recorded by zircon (500-450 Ma; Figure 7a, b), or alternatively, zircon may have only been growing with the garnet core and mantle. This is also reflected in the

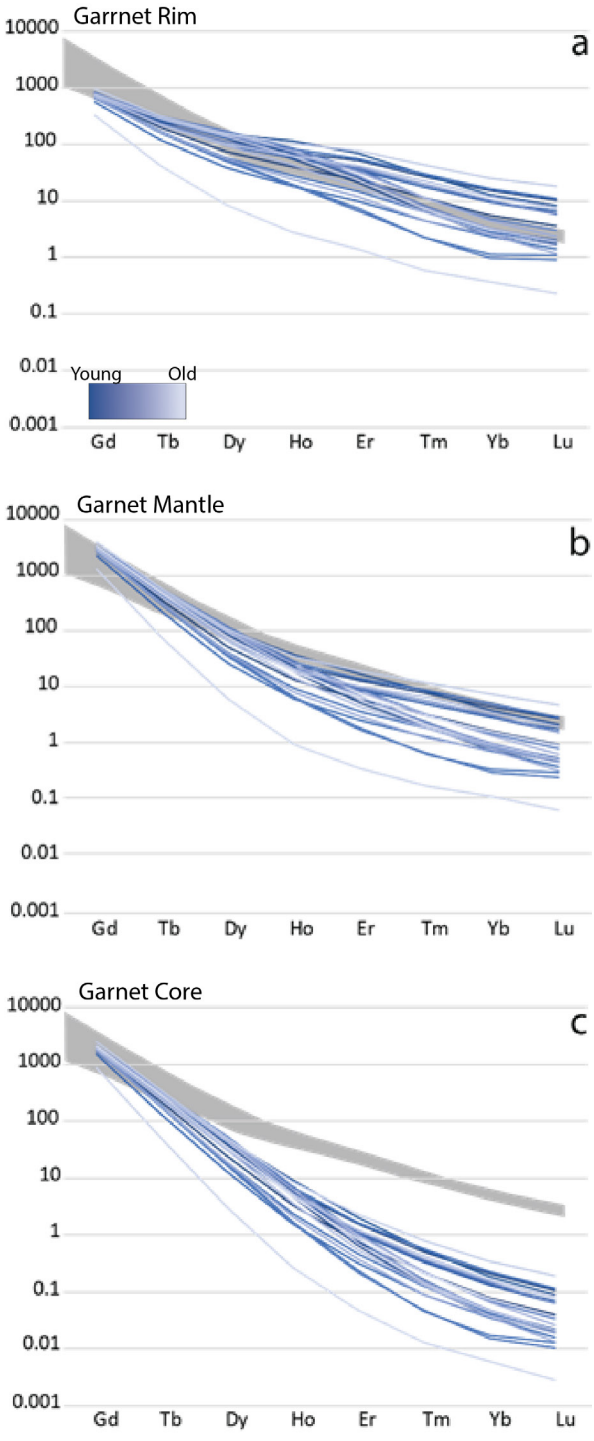


Figure 14. REE partitioning between monazite analyses in sample MB2017-7 and the garnet (a) rim, (b) mantle and (c) core. Each line represents an individual monazite analysis that has been coloured from youngest-oldest. The grey zone represents approximate equilibrium partitioning conditions (Hermann and Rubatto, 2003; Buick et al., 2006; Rubatto et al., 2006).

Zr garnet map in Figure 10, which shows high concentrations of Zr in the garnet core, where both minerals were just beginning to grow, which slowly decreases outward until there is once again a sudden increase in Zr around the garnet rim, suggesting that either a Zr reservoir has broken down and released Zr back into the system, or that garnet is no longer competing for Zr in the rock. Some zircons do not perfectly follow the age trend this may be the result of resetting during the Alice Springs Orogeny or potentially minor local chemical differences between different domains of the rock that developed during progressive metamorphism.

Monazite analyses in sample MB2017-7 give a much more consistent and younger age than zircon (451.9 ± 2.1 Ma; Figure 5c), and so were presented as more traditional spider plots against garnet compositions. Figure 14 shows that the monazite compositions are partially in equilibrium with the garnet mantle and rim, which is consistent with U–Pb ages for monazite coinciding with the latest stages of zircon growth and slightly beyond.

In contrast to the pelite sample, DREE (zircon–garnet) from MB2017-1 show that garnet and zircon were not growing in equilibrium at any point (Figure 13a). The fact that the data is sitting below equilibrium also suggests that garnet was dominating HREE consumption over zircon for all of its growth, except perhaps the outermost rim. However, this rim has been resorbed and has elevated concentrations of HREEs in comparison to its original growth composition. Assuming that the garnet in this sample had essentially grown to completion prior to any zircon growth, it would have finished growing by ~500 Ma, which is the age of the oldest zircon.

Conditions of zircon and monazite growth in Mallee Bore

In the mafic gneiss, there are no direct constraints on the *P–T* conditions of zircon growth. However, the depleted HREE composition of zircon suggests it formed after garnet grew. Based on mineral equilibria modelling constraints (Figure 5), garnet in leucosomes in low modal abundance is estimated to have formed at around 10 kbar and 780 °C. Garnet shows evidence for resorption which is marked by rimward Mn and HREE enrichment. Speculatively, if zircon grew during garnet resorption, it would have provided a sink for HREE. Instead, the enrichment of HREE at the garnet rims implies there was no mineralogical sink for HREE, suggesting zircon grew

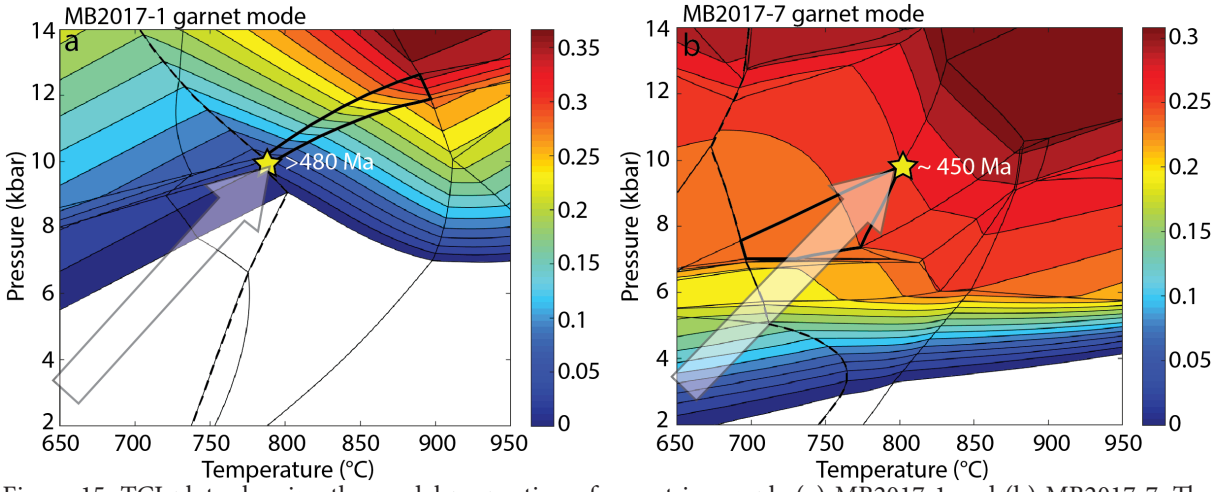


Figure 15. TCI plots showing the modal proportion of garnet in sample (a) MB2017-1 and (b) MB2017-7. The fields outlined in bold are the peak fields identified in Figure 5 and the bold dashed lines represent the solidus. The arrows represent the same prograde *P–T* path. The stars represent the proposed peak *P–T* point with the time that each sample reached that point.

Table 3. Ti-in-zircon thermometry results using the methods of Watson et al. (2006).

Zircon analysis	^{49}Ti (ppm)	Temperature (°C)	Error (°C)	Age (Ma)
MB2017_7_7	3.6	658	34	456.9
MB2017_7_27	2.9	642	30	460.5
MB2017_7_6	4	666	30	468.9
MB2017_7_2	3	644	31	470.8
MB2017_7_20	3.6	658	25	472.4
MB2017_7_5	4.9	682	23	472.5
MB2017_7_4	4	667	26	473.1
MB2017_7_25	5.7	694	28	473.5
MB2017_7_12	3.1	648	32	474.4
MB2017_7_9	3.3	652	27	474.6
MB2017_7_11	4	666	26	475.5
MB2017_7_14	2.9	641	30	477.9
MB2017_7_3	6	698	26	480.9
MB2017_7_10	3.8	662	25	481.9

before garnet was resorbed. Therefore, by logical extension, zircon grew at around the *P–T* conditions corresponding to the maximum garnet mode for the mafic bulk composition. If this logic is correct, it suggests that zircon grew at around 10 kbar and 780 °C, but after garnet had formed. Furthermore, the consistency of zircon composition over the measured age range implies the *P–T* conditions associated with zircon growth were maintained for *ca.* 480-450 Ma.

In contrast in the metapelite, zircon-garnet REE compositions suggest that zircon across virtually its entire measured range of ages appears to have been in equilibrium with garnet. The exception to this general statement is the outer parts of garnet which do not appear to have formed in equilibrium with zircon. This rimward garnet domain is characterised by a marked increase in Ca, MREE and relative enrichment in Zr (Figure 10). These data are consistent with the breakdown of apatite (MREE enrichment; Tribuzio et al. 1996, Krenn et al. 2009, Yakymchuk 2017), and the cessation of zircon growth (Johnson et al. 2015). While the breakdown of apatite can't be directly linked to the growth of monazite, the approximate coincidence between the monazite age and the cessation of zircon growth is striking. Additionally, monazite-garnet REE partitioning suggests the outer part of garnet, marked by MREE enrichment, grew in equilibrium with monazite (Figure 10). Taken collectively with the total range of zircon and monazite ages (Figure 7), the U–Pb data indicate that garnet continued to grow in the metapelite between *ca.* 480-450 Ma.

Based on the above reasoning, the modal evolution (i.e. over time) of garnet in the mafic and metapelitic compositions was very different. In the mafic gneiss, approximate peak garnet mode (Table 1) was achieved before *ca.* 480 Ma, whereas in the metapelite it was achieved by *ca.* 450 Ma (Figure 15). At face value these statements are not reconcilable because, based on the *P–T* models shown in Figure 5, they imply the mafic and metapelitic gneiss had different *P–T–t* evolutions, despite being interlayered. To state this more clearly, the mafic gneiss reached its maximum *P–T* before the metapelitic gneiss reached its maximum *P–T*. There is no evidence in the geology for any structural break between the two outcrops. Therefore, the suggestion that the different lithologies reached their maximum temperatures (as measured by garnet modal abun-

dance in mineral equilibria models), at different times implies that the metapelite and the mafic lithology heated at different rates. There is no suggestion the mafic rock is a syn-metamorphic intrusive (Miller et al. 1997, Buick et al. 2001, Buick et al. 2005), and further, the formation of garnet-bearing leucosomes from a hornblende-bearing precursor is consistent with heating. Therefore, the thermal evolution of the mafic gneiss was not influenced by magmatic heat.

The results of Ti-in-zircon thermometry support the suggestion the mafic gneiss and felsic gneiss experienced different temperature evolutions (Table 3). The metapelite contains abundant quartz and rutile. The bulk of the zircons are around 480–470 Ma in age, with a minor tail to around 455 Ma. Ti-in-zircon thermometry gives a mean temperature of 660 °C for zircons in the age range *ca.* 480–470 Ma. Since garnet appears to have been in equilibrium with zircon for a significant part of its growth history, the Ti-in-zircon data imply the metapelite was undergoing prograde heating, indicated by increasing garnet mode, at temperatures around 660 °C. The final modal maximum of garnet in the metapelite is expressed by the formation of rims with elevated MREE and Ca that appear to have formed in equilibrium with monazite at *ca.* 450 Ma (Figure 14). The inferred *P–T* conditions from the garnet modes are around 9 kbar and 780 °C, within error of the *P–T* conditions estimated from the mafic gneiss. Therefore, it appears that although the metapelite initially lagged behind the mafic gneiss thermally, by *ca.* 450 Ma it recorded *P–T* conditions similar to that recorded in the mafic gneiss.

A speculative case for thermal buffering in the Northern Harts Range Metamorphic Complex

The inference that the mafic gneiss reached its metamorphic peak prior to the metapelite is disconcerting. However, the inference appears to have a sound basis:

(i) Zircon appears to have begun growing at around 480 Ma in the mafic gneiss.
(ii) The HREE depleted zircon compositions in the mafic gneiss zircons are consistent with garnet already having formed.
(iii) Garnet-bearing leucosomes are modelled to form in low modal abundance at around 780 °C and 10 kbar in the mafic gneiss.
(iv) Zircons in the metapelite that are 480-470 Ma in age formed in equilibrium with garnet.
(v) The final garnet mode in the metapelite formed in equilibrium with monazite at around 450 Ma, and based on *P–T* modelling, gives conditions similar to those recorded by the mafic gneiss.

Even allowing for the possibility that the Ti-in-zircon temperature calculated from the metapelitic zircons are too low for some reason, the garnet-zircon REE partitioning data indicates the pelite was forming the bulk of its garnet at around 480–470 Ma and after the mafic gneiss had formed its peak assemblage. Assuming the *P–T* modelling is realistic; it means the mafic gneiss and the metapelite were at different temperatures at around 480–470 Ma. The magnitude of the apparent temperature difference is hard to quantify. This is because the *P–T* model for the metapelite does not take into account melt reintegration, which means the prograde garnet modes are likely to be overestimated. However, based on the Ti-in-zircon thermometry from the metapelite and the *P–T* modelling for the mafic gneiss, the temperature difference may have been as much as 80–100 °C.

Most workers assume that over comparatively small distances *P–T* conditions in metamorphic terranes are the same. Where *P–T* differences appear to exist, these are generally interpreted to reflect variable retrograde re-equilibration or differences in thermobarometric methods. However, in principal, variations in temperature between different lithologies

could arise due to the energetics of prograde mineral reactions. It is well known that both sub-solidus dehydration and supra-solidus partial melting are endothermic (Ridley 1986, Stüwe 1995). Melting in particular consumes significant amounts of heat, with around 400 kJ kg^{-1} (Bea 2012). Therefore, significant energy input is required to produce even small amounts of melt. Or put another way, melting may consume a significant amount of the input energy into a metamorphic rock system, rather than the energy going into temperature increase. Generally speaking, heats of reaction are considered to be subordinate to the overall energetics of metamorphic systems. However, where melt-fertile rocks are interlayered with less fertile rocks, heats of reaction leading to lithological controlled temperature variation may become important.

Schorn et al. (2018) showed that energy consumption associated with melting of modelled metapelite is similar in scale to typical magnitudes of external energy supply. Heat is consumed primarily via two reactions: (1) muscovite + quartz + plagioclase = garnet + sillimanite + biotite + K-spar + melt and (2) biotite + sillimanite + quartz + plagioclase = garnet + cordierite + K-spar + melt. Over the temperature interval of 650–950 °C at 5kbar, Schorn et al. (2018) calculated that a typical metapelite would consume the equivalent of ~ 80–100 °C in energy compared to a rock that did not undergo melting. Therefore, depending on the rate of heating, and the length scale of lithologies that melt and don't melt, rocks of contrasting composition may actually record different temperatures.

It is well recognised that in high-grade terranes melt infertile rocks commonly record higher temperature assemblages than magmatic rocks in the same areas. For example the Eastern Ghats in India where UHT assemblages are recorded in Mg-Al-rich lithologies, whereas the general overall metamorphic grade appears lower (e.g. Korhonen et al. 2013). In low-pressure rocks in the Namqua-Natal Metamorphic Complex Schorn and Diener (2019) inferred that anatectic metapelites record temperatures up to 70°C less than associated mafic rocks and ascribed this difference to thermal buffering within the metapelites due to melting.

At Mallee Bore, unlike the in the Namqua-Natal Metamorphic Complex (Schorn and Diener 2019), mafic and metapelitic assemblages record more or less the same *P–T* conditions. However, the evidence from mineral equilibria modelling and zircon-garnet REE partitioning suggests the mafic gneiss achieved its peak assemblage before *ca.* 480 Ma, whereas based on combined zircon-garnet and monazite-garnet REE partitioning, the metapelite achieved its peak assemblage at around 450 Ma (Figure 5 & 13).

If this suggestion is correct it implies the rate of heating in the metapelite was considerably slower than in the mafic. The prograde evolution is not well constrained based on the Mallee Bore outcrops. However, elsewhere in the Northern Harts Range Metamorphic Complex, extensive preservation of sillimanite pseudomorphs after andalusite (Tucker et al. 2015) provide a general prograde constraint. In the mafic gneiss, partial melting was coincident with the formation of volumetrically minor (~5%) garnet-bearing leucosomes. Because garnet is well preserved, it is likely these leucosomes lost melt. However, overall the amount of melting was minor, implying the present bulk composition is likely not that different to the prograde composition. Based on this composition, the *P–T* modelling indicates that the mafic rock did not undergo melting until the formation of garnet. Therefore, it traversed prograde *P–T* space where the rate of heating was essentially dictated solely by the rate of external energy supply.

In contrast the metapelite almost certainly

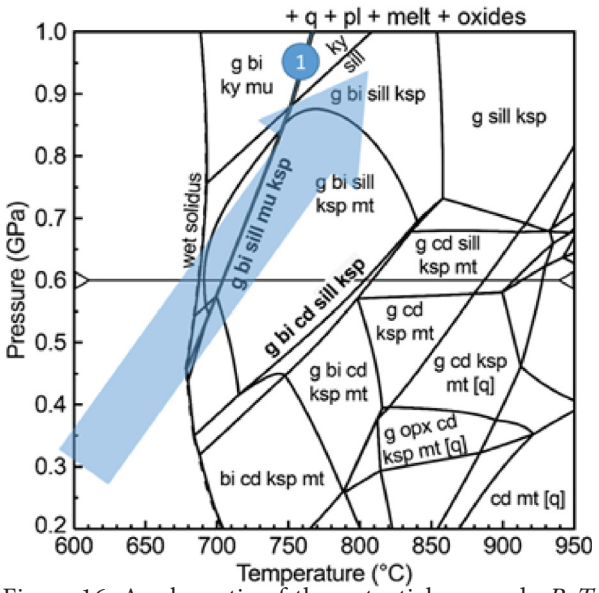


Figure 16. A schematic of the potential prograde *P–T* path of the metapelite sample MB2017-7 on a *P–T* pseudosection from Schorn and Diener (2019).

underwent melting. The present refractory composition of the metapelite is not suitable to understand its prograde melting evolution. In order to derive a more realistic prograde composition it is necessary to reintegrate melting back into the bulk composition (Alessio et al. 2017, Bartoli 2017). However, because amphibolite-granulite grade metapelite across a range of bulk compositions show the same melting reactions (e.g. White et al. 2001, White and Powell 2002, White et al. 2004, White et al. 2007) for the general purposes of discussion it isn't necessary to create a melt-reintegrated *P–T* model for the Mallee Bore metapelite.

Figure 16 shows a schematic prograde *P–T* path based on the regional presence of early andalusite and the peak *P–T* conditions at Mallee Bore. The *P–T* path has a steeply pressure increasing trajectory that would have tracked close to a typical wet solidus and the field garnet–biotite–muscovite–sillimanite–K-feldspar–melt (+ quartz + plagioclase + oxides). For a typical metapelite melting would commence at around 660–670 °C. This is identical to the temperature recorded by the Ti-in-zircon thermometry from the metapelite and seems to suggest that zircon grew on the prograde path, contrary to the normally assumed paradigm (Kelsey et al. 2008, Kelsey and Powell 2010).

Thermal buffering associated with reaction (1) would have slowed the rate of temperature increase in the metapelite compared to the mafic gneiss (e.g. Schorn et al. 2018, Schorn and Diener 2019) and may be an explanation for the different rates of prograde heating of the mafic gneiss and the metapelite. However, it must be acknowledged that applying the thermal buffering hypothesis to explain the apparently different rates of heating in different lithologies at Mallee Bore has shortcomings. Firstly, the amount of thermal buffering associated with crossing reaction (1) would lead to a temperature difference of no more than 30 °C (Schorn et al. 2018). Secondly, at the kilometre-scale the ratio of mafic gneiss to migmatitic metasediment is approximately 50-50 (Miller et al. 1997). The physical separation between the samples used in this study is ~75 m, and therefore the timescale difference over which each lithology reached its peak *P–T* conditions lateral heat flow would have thermally equilibrated both rocks to the same temperature. However, one possible mechanism to create a long-term temperature difference between melt-fertile metapelite and sub-solidus mafic gneiss is if the metapelite was a sink for fluid derived from dehydration of quartz-poor lithologies. Admittedly the existence of such lithologies is speculative. In this open-system scenario, melting of the metapelite may have been maintained for a longer period compared to a closed system. Another possibility is the metapelite was a long-lived transfer zone for melts generated deeper in the metamorphic pile. Melts transitioning to lower pressure may have exsolved fluid into the metapelite, facilitating on-going melting. If this process was ongoing, it would accentuate the evolving temperature difference between the melt-involved metapelite and the sub-solidus mafic gneiss. That the metapelite ultimately reached

similar *P–T* conditions to the mafic gneiss suggest the melt reaction in the metapelite ultimately completed, with external energy input then expressed as temperature increase.

The above suggestions are speculative. However, integrated *P–T* modelling and garnet-zircon and garnet-zircon-monazite U–Pb–REE chemistry strongly suggest that the sub-solidus mafic gneiss underwent faster rates of heating compared to partially melted metapelite. This study differs from previous studies in that the final *P–T* conditions of both mafic gneiss and metapelite are essentially the same. In contrast, studies such as Schorn and Diener (2019) suggest that melt-fertile rocks record lower *P–T* conditions than melt infertile rocks. The case study presented by Sandiford and Hand (1998) is implausible unless the metapelites they described continued to melt via open system processes because lateral heat conduction would have equalised temperatures between different lithologies.

CONCLUSION

The mafic and pelitic granulites from Mallee Bore provide a number of constraints on the peak conditions and timing of growth of several minerals throughout both samples and can be summarised as follows: (1) early garnet growth in the mafic sample MB2017-1, prior to zircon growth at *ca.* 520 Ma; (2) melting in the metapelitic sample buffers against heating, so the metabasite heats faster than the metapelite; (3) coeval zircon growth in both the mafic and the pelitic samples and growth of garnet in the metapelite from ~520–440 Ma; (4) apatite breakdown and garnet rim growth with monazite growth at 451.9 ± 2.1 Ma.

The two samples have minor overlap in the errors of their peak conditions at 760–800 °C and 8.8–9.9 kbar (Figure 6), but the maximum temperatures experienced by the pelitic sample may have been buffered by melting reactions, resulting in these conditions being reached later than the metabasite. The data from these two samples provide evidence for a consistent story but highlights the importance of assessing multiple samples in order to obtain a more complete understanding of the system.

ACKNOWLEDGEMENTS

This work was supported by ARC LP160100578 and DP160104637 (MH). The University of Adelaide is also thanked for research support funding. KLA acknowledges the support of an Australian Government Research Training Program Scholarship. Staff at Adelaide Microscopy are thanked for their assistance in operating equipment and data collection.

REFERENCES

Alessio K., Hand M., Morrissey L., Kelsey D. & Payne J. 2017 Melt Reintegration Modelling: Testing against a Subsolidus Reference Assemblage, Geosciences, vol. 7, no. 3, p. 75.

Bartoli O. 2017 Phase equilibria modelling of residual migmatites and granulites: an evaluation of the melt-reintegration approach, Journal of Metamorphic Geology.

Bea F. 2012 The sources of energy for crustal melting and the geochemistry of heat-producing elements, Lithos, vol. 153, no. 0, pp. 278-291.

Buick I., Miller J., Williams I. & Cartwright I. 2001 Ordovician high-grade metamorphism of a newly recognised late Neoproterozoic terrane in the northern Harts Range, central Australia, Journal of Metamorphic Geology, vol. 19, no. 4, pp. 373-394.

Buick I. S., Hand M., Williams I. S., Mawby J., Miller J. A. & Nicoll R. S. 2005 Detrital zircon provenance constraints on the evolution of the Harts Range Metamorphic Complex (central Australia): links to the Centralian Superbasin, Journal of the Geological Society, vol. 162, no. 5, pp. 777-787.

Caddick M. J., Konopásek J. & Thompson A. B. 2010 Preservation of garnet growth zoning and the duration of prograde metamor-

phism, Journal of Petrology, vol. 51, no. 11, pp. 2327-2347.

Collins W. & Shaw R. 1995 Geochronological constraints on orogenic events in the Arunta Inlier: a review, Precambrian Research, vol. 71, no. 1-4, pp. 315-346.

Donaldson D. G., Webb A. a. G., Menold C. A., Kylander-Clark A. R. & Hacker B. R. 2013 Petrochronology of Himalayan ultrahigh-pressure eclogite, Geology, vol. 41, no. 8, pp. 835-838.

Fujimaki H. 1986 Partition coefficients of Hf, Zr, and REE between zircon, apatite, and liquid, Contributions to Mineralogy and Petrology, vol. 94, no. 1, pp. 42-45.

Green E., White R., Diener J., Powell R., Holland T. & Palin R. 2016 Activity–composition relations for the calculation of partial melting equilibria in metabasic rocks, Journal of Metamorphic Geology, vol. 34, no. 9, pp. 845-869.

Haines P. W., Hand M. & Sandiford M. 2001 Palaeozoic synorogenic sedimentation in central and northern Australia: a review of distribution and timing with implications for the evolution of intracontinental orogens, Australian Journal of Earth Sciences, vol. 48, no. 6, pp. 911-928.

Hand M., Mawby J., Miller J., Ballevre M., Hensen B., Möller A. & Buick I. 1999 Tectonothermal evolution of the Harts and Strangways Range region, eastern Arunta Inlier, central Australia, Australia. SGGMP Eastern Arunta Field Guide N0, vol. 4.

Hickmott D., Shimizu N., Spear F. & Selverstone J. 1987 Trace-element zoning in a metamorphic garnet, Geology, vol. 15, no. 6, pp. 573-576.

Holland T. & Powell R. 2011 An improved and extended internally consistent thermodynamic dataset for phases of petrological interest, involving a new equation of state for solids, Journal of Metamorphic Geology, vol. 29, no. 3, pp. 333-383.

Hwang S., Shen P., Yui T. & Chu H. 2003 On the mechanism of resorption zoning in metamorphic garnet, Journal of Metamorphic Geology, vol. 21, no. 8, pp. 761-769.

Jackson S. E., Pearson N. J., Griffin W. L. & Belousova E. A. 2004 The application of laser ablation-inductively coupled plasma-mass spectrometry to in situ U–Pb zircon geochronology, Chemical Geology, vol. 211, no. 1, pp. 47-69.

Jochum K. P., Weis U., Stoll B., Kuzmin D., Yang Q., Raczek I., Jacob D. E., Stracke A., Birbaum K. & Frick D. A. 2011 Determination of reference values for NIST SRM 610–617 glasses following ISO guidelines, Geostandards and Geoanalytical Research, vol. 35, no. 4, pp. 397-429.

Jochum K. P., Willbold M., Raczek I., Stoll B. & Herwig K. 2005 Chemical Characterisation of the USGS Reference Glasses GSA-1G, GSC-1G, GSD-1G, GSE-1G, BCR-2G, BHVO-2G and BIR-1G Using EPMA, ID-TIMS, ID-ICP-MS and LA-ICP-MS, Geostandards and Geoanalytical Research, vol. 29, no. 3, pp. 285-302.

Johnson T. E., Clark C., Taylor R. J. M., Santosh M. & Collins A. S. 2015 Prograde and retrograde growth of monazite in migmatites: An example from the Nagercoil Block, southern India,

Kelsey D., Clark C. & Hand M. 2008 Thermobarometric modelling of zircon and monazite growth in melt-bearing systems: Examples using model metapelitic and metapsammitic granulites, Journal of Metamorphic Geology, vol. 26, no. 2, pp. 199-212.

Kelsey D. E. & Powell R. 2010 Progress in linking accessory mineral growth and breakdown to major mineral evolution in metamorphic rocks: a thermodynamic approach in the Na2O-CaO-K2O-FeO-MgO-Al2O3-SiO2-H2O-TiO2-ZrO2 system., Journal of Metamorphic Geology.

Korhonen F., Brown M., Clark C. & Bhattacharya S. 2013 Osumilite–melt interactions in ultrahigh temperature granulites: phase equilibria modelling and implications for

the *P–T–*t evolution of the Eastern Ghats Province, India, Journal of Metamorphic Geology, vol. 31, no. 8, pp. 881-907.

Krenn E., Janák M., Finger F., Broska I. & KonečNý P. 2009 Two types of metamorphic monazite with contrasting La/Nd, Th, and Y signatures in an ultrahigh-pressure metapelite from the Pohorje Mountains, Slovenia: Indications for pressure-dependent REE exchange between apatite and monazite?, American Mineralogist, vol. 94, no. 5-6, pp. 801-815.

Lindsay J. F. 1991 New evidence for ancient metazoan life in the late Proterozoic Heavitree, Amadeus Basin, central Australia, Geological and Geophysical Studies in the Amadeus Basin, Central Australia, Bulletin 236.

Ludwig K. R. 2003 User's manual for Isoplot 3.00: a geochronological toolkit for Microsoft Excel. Kenneth R. Ludwig.

Maidment D., Hand M. & Williams I. 2005 Tectonic cycles in the Strangways Metamorphic Complex, Arunta Inlier, central Australia: geochronological evidence for exhumation and basin formation between two high-grade metamorphic events, Australian Journal of Earth Sciences, vol. 52, no. 2, pp. 205-215.

Maidment D., Hand M. & Williams I. 2013 High grade metamorphism of sedimentary rocks during Palaeozoic rift basin formation in central Australia, Gondwana Research, vol. 24, no. 3-4, pp. 865-885.

Mawby J., Hand M. & Foden J. 1999 Sm-Nd evidence for Ordovician granulite facies metamorphism in an intraplate setting in the Arunta Inlier, central Australia, Journal of Metamorphic Geology, vol. 17, pp. 653-668.

Miller J., Cartwright I. & Buick I. 1997 Granulite facies metamorphism in the Mallee Bore area, northern Harts Range: implications for the thermal evolution of the eastern Arunta Inlier, central Australia, Journal of Metamorphic Geology, vol. 15, no. 5, pp. 613-629.

Mottram C. M., Warren C. J., Regis D., Roberts N. M., Harris N. B., Argles T. W. & Parrish R. R. 2014 Developing an inverted Barrovian sequence; insights from monazite petrochronology, Earth and Planetary Science Letters, vol. 403, pp. 418-431.

Nagasawa H. 1970 Rare earth concentrations in zircons and apatites and their host dacites and granites, Earth and Planetary Science Letters, vol. 9, no. 4, pp. 359-364.

Paton C., Hellstrom J., Paul B., Woodhead J. & Hergt J. 2011 Iolite: Freeware for the visualisation and processing of mass spectrometric data, Journal of Analytical Atomic Spectrometry, vol. 26, no. 12, pp. 2508-2518.

Payne J., Hand M., Barovich K. & Wade B. 2008 Temporal constraints on the timing of high-grade metamorphism in the northern Gawler Craton: implications for assembly of the Australian Proterozoic, Australian Journal of Earth Sciences, vol. 55, no. 5, pp. 623-640.

Pearce N. J., Perkins W. T., Westgate J. A., Gorton M. P., Jackson S. E., Neal C. R. & Chenery S. P. 1997 A compilation of new and published major and trace element data for NIST SRM 610 and NIST SRM 612 glass reference materials, Geostandards Newsletter, vol. 21, no. 1, pp. 115-144.

Powell R. & Holland T. 1988a An internally consistent thermodynamic dataset with uncertainties and correlations: 3. Applications to geobarometry, worked examples and a computer program, J. Metamorphic Geol., vol. 6, pp. 173-204.

Powell R. & Holland T. J. B. 1988b An internally consistent dataset with uncertainties and correlations: 3. Applications to geobarometry, worked examples and a computer program, Journal of Metamorphic Geology, vol. 6, no. 2, pp. 173-204.

Powell R., White R. W., Green E. C. R., Holland T. J. B. & Diener J. F. A. 2014 On parameterizing thermodynamic descriptions of minerals for petrological calculations,

Journal of Metamorphic Geology, vol. 32, no. 3, pp. 245-260.

Raimondo T., Clark C., Hand M. & Faure K. 2011 Assessing the geochemical and tectonic impacts of fluid–rock interaction in mid-crustal shear zones: a case study from the intracontinental Alice Springs Orogen, central Australia, Journal of Metamorphic Geology, vol. 29, no. 8, pp. 821-850.

Raimondo T., Payne J., Wade B., Lanari P., Clark C. & Hand M. 2017 Trace element mapping by LA-ICP-MS: assessing geochemical mobility in garnet, Contributions to Mineralogy and Petrology, vol. 172, no. 4, p. 17.

Ridley J. 1986 Modelling of the relations between reaction enthalpy and the buffering of reaction progress in metamorphism, Mineralogical Magazine, vol. 50, no. 357, pp. 375-384.

Sandiford M. & Hand M. 1998 Australian Proterozoic high-temperature, low-pressure metamorphism in the conductive limit, Geological Society, London, Special Publications, vol. 138, no. 1, pp. 109-120.

Schorn S., Diener J. F., Powell R. & Stüwe K. 2018 Thermal buffering in the orogenic crust, Geology, vol. 46, no. 7, pp. 643-646.

Schorn S. & Diener J. F. A. 2019 Seemingly disparate temperatures recorded in coexisting granulite facies lithologies, Journal of Metamorphic Geology, vol. 0, no. ja.

Scrimgeour I. 2013 Geology and mineral resources of the Northern Territory. In M A. & TJ M. eds. pp. 12:1-12:74. Northern Territory Geological Survey.

Sharrad K. A., Mckinnon-Matthews J., Cook N. J., Ciobanu C. L. & Hand M. 2014 The basil Cu–Co deposit, eastern Arunta Region, Northern Territory, Australia: a metamorphosed volcanic-hosted massive sulphide deposit, Ore Geology Reviews, vol. 56, pp. 141-158.

Shaw R., Langworthy A., Offe L., Stewart A., Allen A., Senior B. & Clarke D. 1979 Geological report on 1: 100,000-scale mapping of the southeastern Arunta Block, Northern Territory, Bureau of Mineral Resources, Australia, Geology and Geophysics, Record 1979/47.

Sláma J., Košler J., Condon D. J., Crowley J. L., Gerdes A., Hanchar J. M., Horstwood M. S. A., Morris G. A., Nasdala L., Norberg N., Schaltegger U., Schoene B., Tubrett M. N. & Whitehouse M. J. 2008 Plešovice zircon — A new natural reference material for U–Pb and Hf isotopic microanalysis, Chemical Geology, vol. 249, no. 1, pp. 1-35.

Storkey A., Hermann J., Hand M. & Buick I. 2005 Using in situ trace-element determinations to monitor partial-melting processes in metabasites, Journal of Petrology, vol. 46, no. 6, pp. 1283-1308.

Stüwe K. 1995 Thermal buffering effects at the solidus. Implications for the equilibration of partially melted metamorphic rocks, Tectonophysics, vol. 248, no. 1-2, pp. 39-51.

Taylor R., Clark C., Harley S., Kylander-Clark A., Hacker B. & Kinny P. 2017 Interpreting granulite facies events through rare earth element partitioning arrays, Journal of Metamorphic Geology, vol. 35, no. 7, pp. 759-775.

Tribuzio R., Messiga B., Vannucci R. & Bottazzi P. 1996 Rare earth element redistribution during high-pressure–low-temperature metamorphism in ophiolitic Fe-gabbros (Liguria, northwestern Italy): implications for light REE mobility in subduction zones, Geology, vol. 24, no. 8, pp. 711-714.

Tucker N. M., Hand M. & Payne J. L. 2015 A rift-related origin for regional medium-pressure, high-temperature metamorphism, Earth and Planetary Science Letters, vol. 421, no. Supplement C, pp. 75-88.

Walter M., Veevers J., Calver C. & Grey K. 1995 Neoproterozoic stratigraphy of the Centralian superbasin, Australia, Precambrian Research, vol. 73, no. 1-4, pp. 173-195.

Watson E. B., Wark D. A. & Thomas J. B. 2006 Crystallization thermometers for zircon and rutile, Contributions to Mineralogy

and Petrology, vol. 151, no. 4, p. 413.
White R. & Powell R. 2002 Melt loss and the preservation of granulite facies mineral assemblages, Journal of Metamorphic Geology, vol. 20, no. 7, pp. 621-632.
White R., Powell R. & Halpin J. 2004 Spatially-focussed melt formation in aluminous metapelites from Broken Hill, Australia, Journal of Metamorphic Geology, vol. 22, no. 9, pp. 825-845.
White R., Powell R. & Holland T. 2001 Calculation of partial melting equilibria in the system Na2O–CaO–K2O–FeO–MgO–Al2O3–SiO2–H2O (NCKFMASH), Journal of Metamorphic Geology, vol. 19, no. 2, pp. 139-153.
White R., Powell R. & Holland T. 2007 Progress relating to calculation of partial melting equilibria for metapelites, Journal of Metamorphic Geology, vol. 25, no. 5, pp. 511-527.
White R., Powell R., Holland T., Johnson T. & Green E. 2014a New mineral activity–composition relations for thermodynamic calculations in metapelitic systems, Journal of Metamorphic Geology, vol. 32, no. 3, pp. 261-286.
White R. W., Powell R. & Johnson T. E. 2014b The effect of Mn on mineral stability in metapelites revisited: new a–x relations for manganese-bearing minerals, Journal of Metamorphic Geology, vol. 32, no. 8, pp. 809-828.
Wiedenbeck M., Alle P., Corfu F., Griffin W., Meier M., Oberli F. V., Quadt A. V., Roddick J. & Spiegel W. 1995 Three natural zircon standards for U-Th-Pb, Lu-Hf, trace element and REE analyses, Geostandards newsletter, vol. 19, no. 1, pp. 1-23.
Xu J., Ciobanu C. L., Cook N. J., Zheng Y., Sun X. & Wade B. P. 2016 Skarn formation and trace elements in garnet and associated minerals from Zhibula copper deposit, Gangdese Belt, southern Tibet, Lithos, vol. 262, pp. 213-231.
Yakymchuk C. 2017 Behaviour of apatite during partial melting of metapelites and consequences for prograde suprasolidus monazite growth, Lithos, vol. 274, pp. 412-426.

CHAPTER 6

Summary of key outcomes and future research directions

This thesis endeavours to build upon previous knowledge of high-temperature metamorphic processes and increase our understanding of thermal drivers and element redistribution in the earth's crust. The preceding chapters in this thesis assess the chemical changes that occur with high-grade metamorphism at both a large and small scale to address the three principal aims presented in Chapter 1. The following discussion and conclusions highlight the important outcomes from these studies, along with the current state of knowledge in each area and the future research directions arising from this work.

1. Assess the validity of current phase equilibria modelling techniques to calculate protolith compositions for granulite-facies rocks.

With the increasing use of the newly emerging field of petrochronology, inverse phase equilibria modelling is becoming more important as it provides a means of rebuilding granulite-facies protolith compositions in which prograde reactions can be interpreted. Several methods of inverse, or melt reintegration modelling, currently exist. However, the method of incremental melt reintegration appears to be the most robust, as it most closely replicates the incremental style of melt loss thought to occur in most granulite-facies terranes and allows the user to assess when an appropriately water-saturated subsolidus composition has been reached. Chapter 2 confirms that this method is indeed able to reproduce viable protolith compositions from granulite-facies rocks that replicate appropriate subsolidus mineral assemblages. However, it also highlights the care that needs to be taken when applying this method to rocks with a truly unknown protolith composition and an uncertain *P*–*T* path, as these uncertainties may affect the modelled protolith composition.

The melt reintegration modelling undertaken in chapter 2 resulted in a composition that stabilised orthoamphibole, which cannot be modelled with the currently available activity-composition (a–x) models that are compatible with the most recent dataset, ds6 (Holland and Powell, 2011). This required that the final models were calculated using an older set of a-x models and the previous dataset, ds5 (Holland and Powell, 1998). The older models did produce the minerals that were identified to have existed at subsolidus conditions in the modelled composition. However, having to regress to a previous and somewhat outdated dataset and a–x models in order to produce these models is far from ideal. For ds6 to truly be a more generally applicable successor to ds5, all of the mineral a–x models and functionality that were previously available need to be incorporated into the new version.

2. Investigate how high-temperature metamorphism, and the partial melting and melt loss that accompanies it, redistributes heat producing elements (HPEs) and how these elements may contribute to high metamorphic temperatures.

The long-standing paradigm that high-grade metamorphic processes cause depletion of HPEs in granulite-facies crust has primarily been backed by geophysical models that attribute the decrease in HPE concentration with increasing depth in the crust (e.g. Lachenbruch, 1968; Oxburgh, 1980; Singh and Manglik, 2000). However, the extensive geochemical dataset provided in Chapter 3 clearly shows that there is no correlation between melt loss and HPE concentration, with the HPE concentrations in subsolidus rocks generally equalling HPE concentrations in suprasolidus areas of the same terrane. Instead, HPE concentration is more likely controlled by lithology, where protolith compositions that have a high concentration of HPEs will produce residual granulites with high HPE concentrations and vice versa. As partial melting does not necessarily result in large-scale redistribution of HPE in the crust, areas that are thought to be composed of residual granulitic crust may still

be thermomechanically reactive.

Chapter 4 showed that in areas where HPE concentrations are relatively high, such as the Reynolds–Anmatjira Range region in central Australia, radiogenic heat production may act as a primary driver for high temperature metamorphism. In the absence of obvious thermal drivers, such as magmatism or zones of crustal extension, it is clear that a larger catalogue of potential thermal drivers needs to be evaluated. Furthermore, radiogenic heating needs to be assessed in all cases when looking at metamorphic drivers, as its contribution to crustal temperatures is far more significant than it is currently given credit for.

To truly understand the effect that radiogenic heating can have on the crust, it is important to understand the processes behind how HPEs are distributed, as well as their spatial distribution in the crust. The work undertaken in Chapters 3 and 4 have provided a good basis for future work, but still leave many questions unanswered. For example, the origin of extremely radiogenic granites present in central Australia is still largely unknown and these granite bodies have a significant impact on later radiogenic heating of the mid-crust. A greater understanding of spatial distribution of HPEs and the processes behind this distribution may be able to shed some light on why these anomalously Th-U rich magmatic rocks exist.

3. Compare the way in which mineral growth and metamorphic events are recorded by granulite-facies rocks of differing composition.

Despite neighbouring lithologies undergoing the same thermobarometric evolution, certain compositions may record these events slightly differently or potentially not at all (Young and Kylander-Clark, 2015). Recently released metabasic melt models for use in THERMOCALC (Green et al., 2016) have allowed direct comparison of *P–T* conditions between suprasolidus rocks of mafic and metapelitic compositions (e.g. Schorn and Diener, 2019). These comparisons show that metabasic rocks may record higher temperatures than their pelitic counterparts (Schorn and Diener, 2019), as is shown in Chapter 5. This occurs as a result of temperature buffering in the, more melt fertile metapelitic composition. The apparent temperature difference recorded by the contrasting rock compositions highlights the importance of analysing multiple samples to fully understand the events that occurred in a given area. Beyond simple *P–T* comparison, the utilisation of petrochronology in Chapter 5 also highlights that there are key differences in the timing of mineral growth between mafic and metapelitic samples, despite similar U–Pb geochronology. Once again, this highlights the fact that compositionally different rocks record events in different ways and that it is important to thoroughly assess mineral relationships to determine what geochronological data actually means in the context of an evolving metamorphic system. Now with the ability to link mineral growth to age data and *P–T* paths, it is becoming necessary to do more than simply calculate phase equilibria models and acquire geochronological data. Instead it is now effectively compulsory to also determine the trace element compositions of the geochronological target minerals and their associated major rock forming minerals to determine the context of the accessory mineral growth. Combining all of these data types allows us to give far more meaning to the data we collect and therefore, make better interpretations about the timing and extent of metamorphic activities. The implementation of petrochronology in metamorphic terranes is a critical step towards providing robust constraints on their evolution, enabling geoscientists to further understand the way in which the formation of mineral assemblages constrains tectonic and geodynamic processes.

REFERENCES

Green, E., White, R., Diener, J., Powell, R., Holland, T., Palin, R., 2016. Activity–composition relations for the calculation of partial melting equilibria in metabasic rocks. Journal of Metamorphic Geology 34, 845-869.

Holland, T., Powell, R., 1998. An internally consistent thermodynamic data set for phases of petrological interest. Journal of Metamorphic Geology 16, 309-343.

Holland, T., Powell, R., 2011. An improved and extended internally consistent thermodynamic dataset for phases of petrological interest, involving a new equation of state for solids. Journal of Metamorphic Geology 29, 333-383.

Lachenbruch, A.H., 1968. Preliminary geothermal model of the Sierra Nevada. Journal of Geophysical Research 73, 6977-6989.

Oxburgh, E., 1980. Heat flow and magma genesis. Physics of magmatic processes, 161-199.

Schorn, S., Diener, J.F.A., 2019. Seemingly disparate temperatures recorded in coexisting granulite facies lithologies. Journal of Metamorphic Geology 0.

Singh, R., Manglik, A., 2000. Identification of radiogenic heat source distribution in the crust: A variational approach. Sadhana 25, 111-118.

Young, D., Kylander-Clark, A., 2015. Does continental crust transform during eclogite facies metamorphism? Journal of Metamorphic Geology 33, 331-357.

Appendix 1

Supplementary material for: Melt Reintegration Modelling: Testing against a Sub-solidus Reference Assemblage

Appendix A: Mineral compositions obtained on MicroProbe SXFive

	bi	bi	bi	bi	bi	AVE
SiO2	37.66	38.14	38.12	37.90	38.10	37.99
TiO2	3.41	3.43	3.49	3.50	3.55	3.48
Al2O3	15.24	15.11	15.29	15.21	14.99	15.17
Cr2O3	0.12	0.06	0.10	0.12	0.10	0.10
FeO	14.24	14.51	14.43	14.35	14.26	14.36
MnO	0.01	0.00	0.04	0.02	0.05	0.02
MgO	15.89	15.95	15.77	15.96	15.85	15.89
ZnO	0.00	0.00	0.00	0.00	0.04	0.01
CaO	0.00	0.00	0.00	0.00	0.00	0.00
Na2O	0.11	0.08	0.08	0.09	0.06	0.08
K2O	0.50	0.50	0.51	0.48	0.48	0.49
Cl	8.66	8.65	8.69	8.77	8.65	8.68
F	0.02	0.02	0.03	0.02	0.02	0.02

	cd	cd	cd	cd	cd	cd	cd	cd	cd	cd	AVE
SiO2	48.67	49.57	49.57	49.76	49.35	49.40	49.93	49.58	49.39	48.67	49.39
TiO2	0.00	0.00	0.00	0.01	0.01	0.01	0.00	0.00	0.00	0.00	0.00
Al2O3	32.53	32.85	32.93	33.63	33.23	33.56	33.18	33.29	32.86	32.53	33.06
Cr2O3	0.00	0.00	0.00	0.00	0.01	0.00	0.00	0.00	0.00	0.00	0.00
FeO	5.17	5.02	5.21	4.75	4.84	4.62	5.04	5.37	5.43	5.17	5.06
MnO	0.05	0.09	0.05	0.07	0.05	0.03	0.04	0.06	0.04	0.05	0.05
MgO	11.29	11.03	11.30	11.24	11.10	11.24	10.92	10.95	10.97	11.29	11.14
ZnO	0.00	0.00	0.00	0.00	0.00	0.06	0.03	0.00	0.05	0.00	0.01
CaO	0.00	0.00	0.00	0.01	0.00	0.00	0.00	0.00	0.00	0.00	0.00
Na2O	0.00	0.00	0.00	0.01	0.00	0.00	0.02	0.00	0.00	0.00	0.00
K2O	0.20	0.18	0.17	0.20	0.08	0.16	0.06	0.15	0.18	0.20	0.16
Cl	0.00	0.00	0.00	0.00	0.00	0.00	0.00	0.00	0.00	0.00	0.00
F	0.00	0.01	0.00	0.00	0.00	0.00	0.00	0.00	0.00	0.00	0.00

	opx	opx	opx	opx	opx	opx	opx	opx	opx	opx	AVE
SiO2	52.14	52.34	52.30	52.34	52.56	52.62	52.16	52.41	52.60	55.02	52.65
TiO2	0.08	0.10	0.09	0.10	0.07	0.08	0.09	0.08	0.07	0.09	0.09
Al2O3	2.50	2.44	2.01	2.27	1.99	1.99	1.95	1.90	1.92	3.18	2.22
Cr2O3	0.05	0.05	0.03	0.04	0.04	0.02	0.03	0.03	0.05	0.05	0.04
FeO	24.66	24.56	24.20	24.47	24.41	25.05	24.17	24.70	24.78	20.93	24.20
MnO	0.22	0.22	0.26	0.22	0.27	0.25	0.22	0.25	0.26	0.27	0.24
MgO	21.75	21.92	22.13	21.98	22.13	22.25	22.18	21.97	21.61	19.17	21.71
ZnO	0.00	0.02	0.06	0.03	0.00	0.03	0.02	0.00	0.02	0.04	0.02
CaO	0.02	0.01	0.03	0.01	0.01	0.01	0.02	0.02	0.01	0.03	0.02
Na2O	0.01	0.00	0.00	0.00	0.00	0.00	0.00	0.02	0.00	0.00	0.00
K2O	0.00	0.01	0.00	0.00	0.02	0.01	0.00	0.01	0.01	0.25	0.03
Cl	0.00	0.00	0.00	0.00	0.00	0.00	0.00	0.00	0.00	0.00	0.00
F	0.00	0.00	0.00	0.00	0.00	0.00	0.00	0.00	0.01	0.00	0.00

	sp	sp	sp	sp	sp	sp	AVE
SiO2	0.31	0.08	0.00	0.00	0.00	0.12	0.09
TiO2	0.03	0.00	0.01	0.00	0.02	0.01	0.01
Al2O3	57.40	57.86	57.99	58.59	58.24	58.13	58.04
Cr2O3	0.04	0.03	0.02	0.04	0.05	0.04	0.04
FeO	33.29	34.36	34.17	33.88	33.03	33.58	33.72
MnO	0.14	0.13	0.12	0.12	0.09	0.13	0.12
MgO	7.78	7.76	7.97	7.80	8.16	7.89	7.89
ZnO	0.07	0.09	0.15	0.17	0.15	0.18	0.13
CaO	0.01	0.00	0.00	0.01	0.00	0.00	0.01
Na2O	0.00	0.00	0.00	0.00	0.00	0.00	0.00
K2O	0.00	0.01	0.00	0.00	0.01	0.00	0.00
Cl	0.00	0.00	0.00	0.01	0.00	0.00	0.00
F	0.00	0.00	0.00	0.00	0.01	0.00	0.00

	pl	pl	pl	pl	pl	pl	pl	pl	pl	pl	pl	pl	AVE
SiO2	63.11	64.33	61.36	64.67	65.06	64.82	65.35	64.88	63.83	64.07	64.49	64.29	64.19
TiO2	0.00	0.02	0.00	0.00	0.00	0.01	0.00	0.05	0.01	0.00	0.01	0.02	0.01
Al2O3	21.29	20.36	19.96	20.46	20.76	20.51	20.29	20.51	20.20	20.36	20.49	20.56	20.48
Cr2O3	0.00	0.00	0.00	0.00	0.00	0.00	0.00	0.01	0.00	0.00	0.00	0.00	0.00
FeO	0.23	0.07	0.16	0.00	0.01	0.21	0.14	0.08	0.12	0.00	0.07	0.02	0.09
MnO	0.00	0.01	0.00	0.00	0.00	0.00	0.00	0.01	0.00	0.00	0.00	0.00	0.00
MgO	0.04	0.00	0.10	0.00	0.00	0.00	0.00	0.00	0.01	0.00	0.00	0.00	0.01
ZnO	0.00	0.03	0.00	0.01	0.00	0.03	0.00	0.01	0.01	0.03	0.01	0.01	0.01
CaO	1.00	0.97	2.70	1.12	1.20	0.96	0.98	0.95	0.86	1.22	1.15	1.06	1.18
Na2O	10.85	11.01	10.35	11.14	11.10	11.23	11.22	11.05	11.07	10.89	11.15	11.21	11.02
K2O	0.05	0.03	0.09	0.20	0.21	0.04	0.04	0.05	0.04	0.27	0.19	0.21	0.12
Cl	0.02	0.00	0.00	0.00	0.00	0.00	0.00	0.00	0.01	0.00	0.00	0.00	0.00
F	0.00	0.00	0.03	0.00	0.00	0.00	0.00	0.00	0.00	0.00	0.00	0.00	0.00

	Bi	Cd	Opx	Sp	Pl
Mineral Proportions (vol%)	9.77	38.26	17.51	4.44	30.02
Mineral Density (kg/m3)	2.9	2.58	3.49	4.12	2.63
Mode (wt%)	9.93	34.59	21.41	6.41	27.67

wt%	Bi	Cd	Opx	Sp	Pl	Ave comp	Final comp
SiO2	37.990	49.39	52.65	0.09	64.187625	51.16	49.90
TiO2	3.480	0	0.09	0.01	0.0093395	0.37	0.37
Al2O3	15.170	33.06	2.22	58.04	20.4789	22.58	22.80
Cr2O3	0.100	0	0.04	0.04	0.000823083	0.02	0.02
FeO	14.360	5.06	24.2	33.72	0.09372725	10.52	10.54
MnO	0.020	0.05	0.24	0.12	0.001722833	0.08	0.08
MgO	15.890	11.14	21.71	7.89	0.012792	10.58	10.59
ZnO	0.01	0.01	0.02	0.13	0.010407667	0.02	0.02
CaO	0	0	0.02	0.01	1.1809065	0.42	0.33
Na2O	0.08	0	0	0	11.0208	2.79	3.06
K2O	8.68	0	0.03	0	0.11935475	0.86	0.90
Cl	0.49	0.16	0	0	0.002831167	0.11	0.10
F	0.02	0	0	0	0.002411	0	0.00
Total	96.29	98.87	101.22	100.05	97.12164075	101.08	98.72

Appendix B: TX models

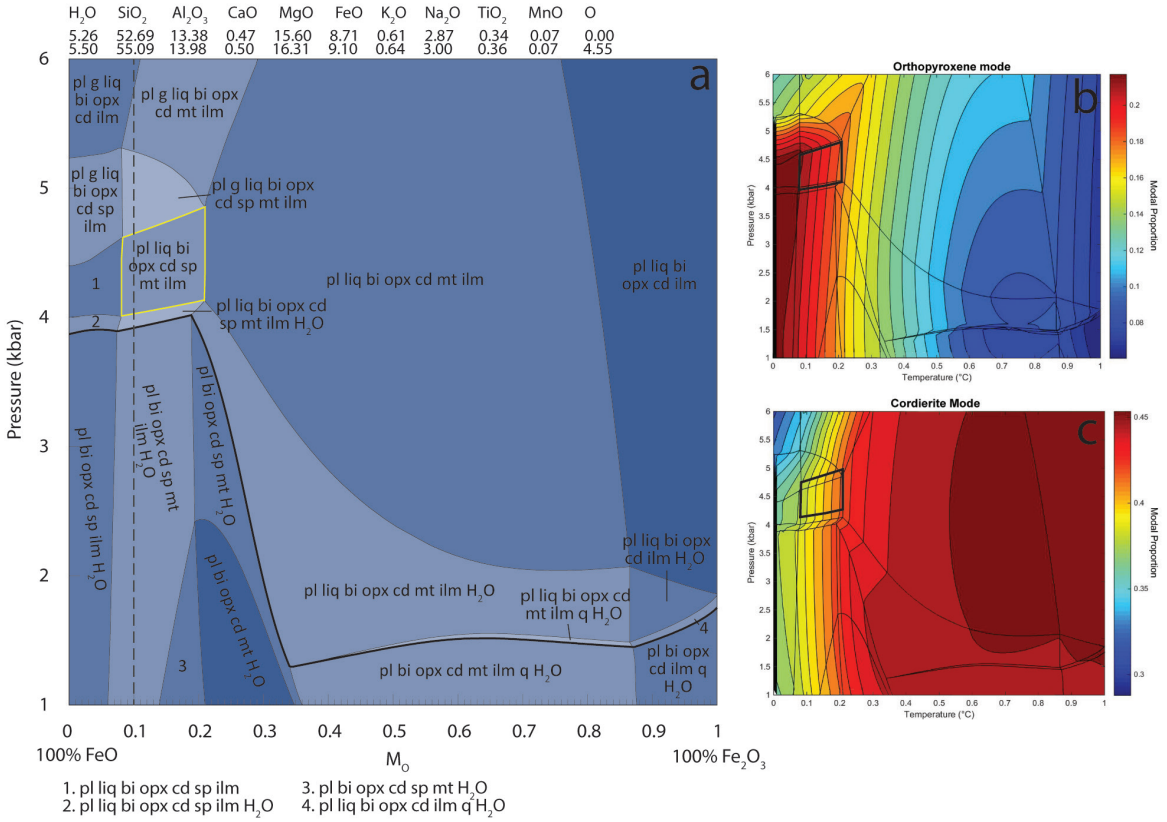


Figure B1. (a) *P–MO* model calculated to constrain the oxidation state of sample 14-RDC-04. The bold line represents the solidus. The field outlined in yellow represents the peak assemblage observed in the sample. The dashed line is the composition on the x–axis that was chosen for further modelling. (b) TCI output of modal proportion of orthopyroxene. The peak field is outlined in bold. (c) TCI output of modal proportion of cordierite. The peak field is outlined in bold.

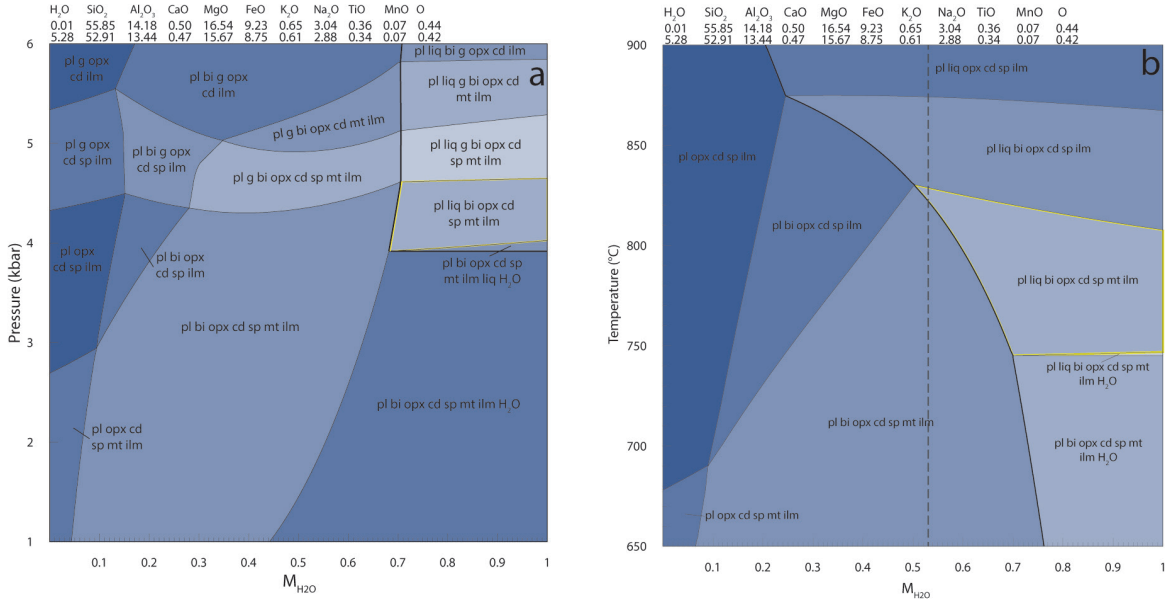


Figure B2. (a) P–M_{H_2O} model calculated to constrain the H_2O content of sample 14-RDC-04. The bold line represents the solidus. The field outlined in yellow represents the peak assemblage observed in the sample. a) T–M_{H_2O} model calculated to constrain the H_2O content of sample 14-RDC-04. The bold line represents the solidus. The field outlined in yellow represents the peak assemblage observed in the sample. The dashed line is the composition on the x–axis that was chosen for further modelling.

Appendix C: Mineral mode TCI outputs

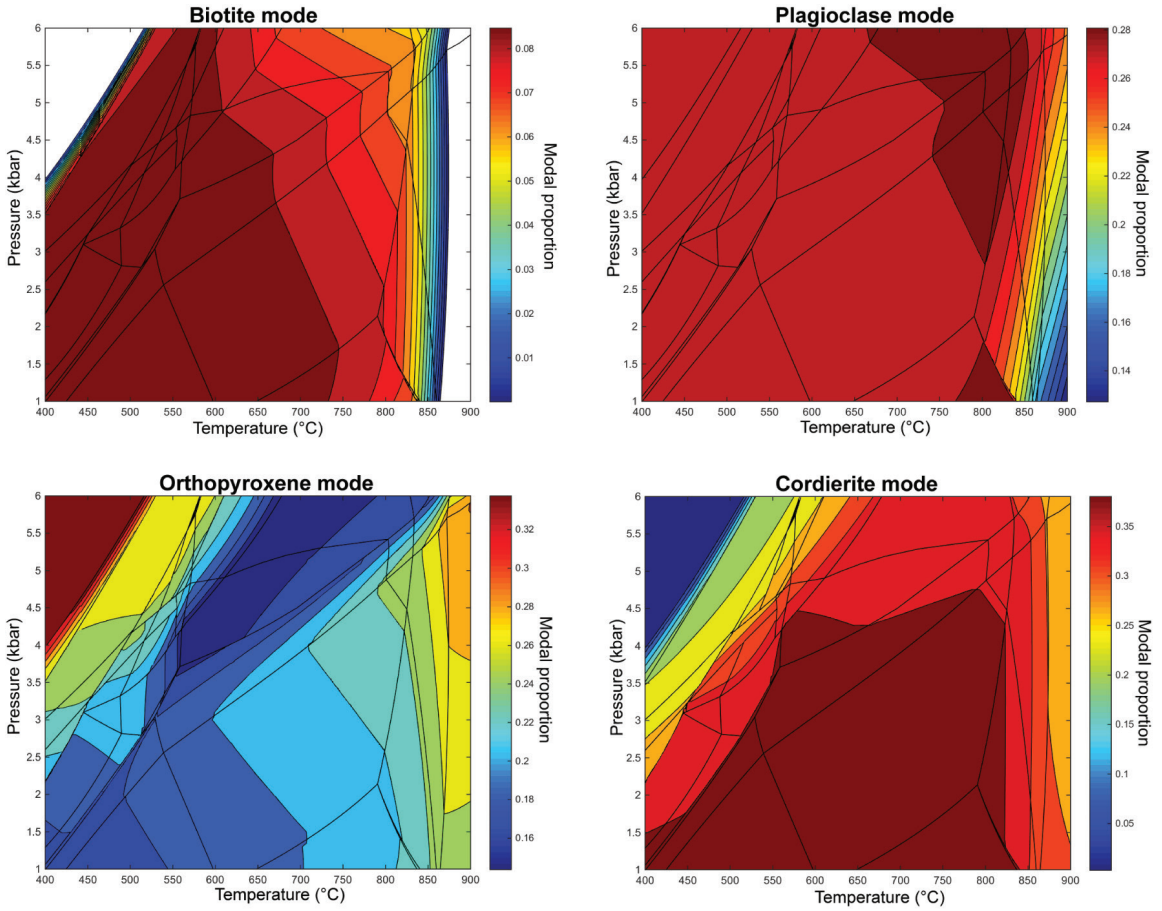


Figure C1. Mineral modal abundance contour diagrams produced using TCInvestigator [45] for the major phases that occur in the peak assemblage of sample 14-RDC-04. These diagrams were used to construct Figure 4b in the main text.

Appendix 2

Supplementary material for: Conservation of deep crustal heat production

Appeddix 2A: Detailed location and sample maps

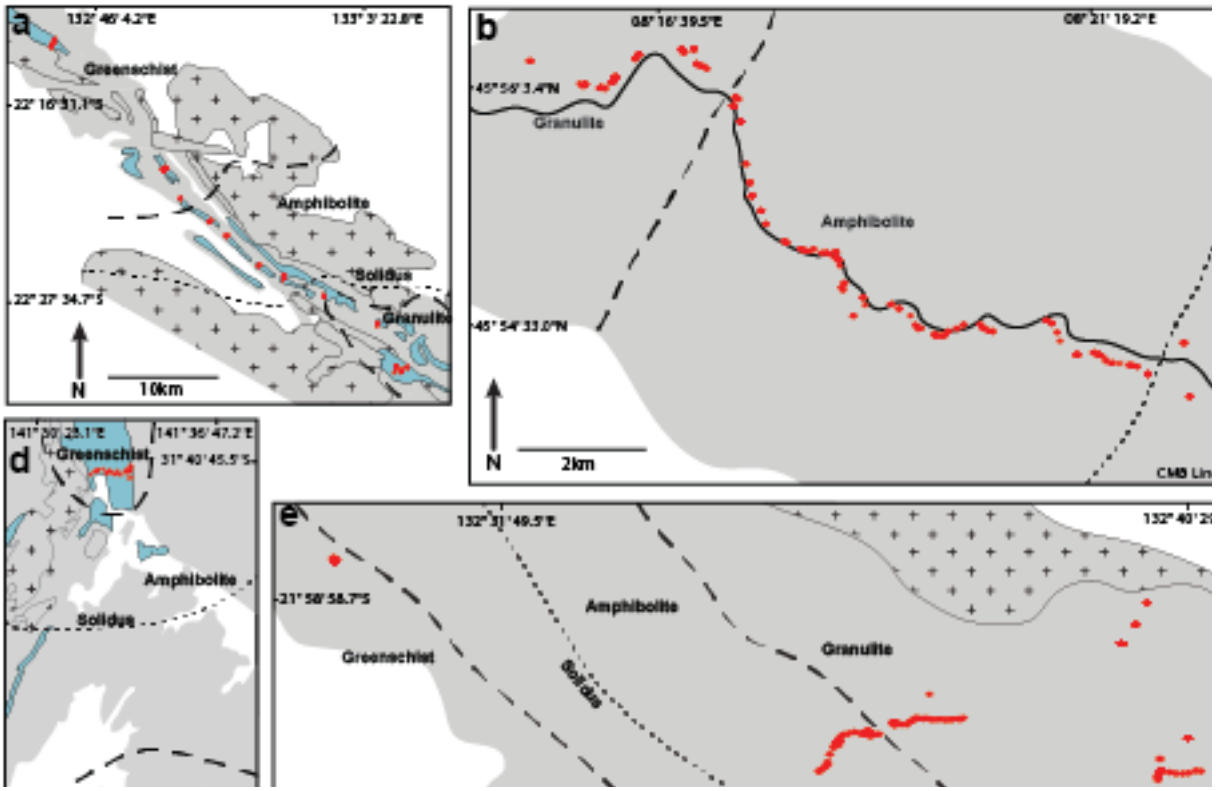


Figure 1. Location maps of the five terranes used in this study; (a) the Reynolds Range, (b) the Ivrea-Verbano Zone, (c) Sierra de Quilmes, (d) Broken Hill and (e) Mt Stafford. The red circles mark the locations where GRS measurements were taken. Long dashed lines represent changes in metamorphic facies and short dashed lines represent the solidus in each location. Crosses represent granites and, where applicable, blue units mark the particular lithology that was followed. Modified from (a) Morrissey et al. (2014), (b) Redler et al. (2013), (c) Büttner et al. (2005), (d) Willis (1989) and (e) White et al. (2003).

Appendix 2B: Comparison of GRS vs XRF data

Reynolds Range

	Subsolidus				Suprasolidus		
	Average	Stdev	n		Average	Stdev	n
GRS			298	GRS			124
K	4.71	1.17		K	4.4	0.96	
U	2.44	0.92		U	1.57	0.34	
Th	21.90	4.87		Th	24.33	4.53	
XRF			9	XRF			6
K	5.39	0.62		K	2.58	0.77	
U	0.91	0.45		U	1.57	0.59	
Th	31.01	2.62		Th	37.83	5.19	

Mt Stafford

	Subsolidus				Suprasolidus		
	Average	Stdev	n		Average	Stdev	n
GRS			431	GRS			124
K	3.90	0.97		K	4.4	0.96	
U	2.07	0.56		U	1.57	0.34	
Th	23.28	3.08		Th	24.33	4.53	
XRF			9	XRF			6
K	5.21	1.71		K	2.58	0.77	
U	2.80	1.39		U	1.57	0.59	
Th	33.48	3.13		Th	37.83	5.19	

Broken Hill

	Subsolidus				Suprasolidus		
	Average	Stdev	n		Average	Stdev	n
GRS			224	GRS			390
K	3.32	1.09		K	3.74	0.79	
U	2.71	1.59		U	2.36	0.75	
Th	23.46	5.80		Th	33.73	6.07	
XRF			7	XRF			6
K	4.88	1.36		K	3.69	0.78	
U	2.7	2.43		U	2.75	2.73	
Th	42.9	4.98		Th	45.83	14.93	

Ivera Zone

	Subsolidus				Suprasolidus		
	Average	Stdev	n		Average	Stdev	n
GRS			66	GRS			394
K	3.50	0.66		K	3.14	0.84	
U	2.52	0.55		U	1.99	0.64	
Th	19.73	4.97		Th	21.92	5.06	
XRF			11	XRF			8
K	2.88	1.02		K	2.27	0.64	
U	0.72	0.86		U	0.28	0.09	
Th	19.40	10.98		Th	23.61	10.1	

Sierra de Quilmes

	Subsolidus				Suprasolidus		
	Average	Stdev	n		Average	Stdev	n
GRS			107	GRS			117
K	3.35	0.94		K	3.34	0.68	
U	2.08	0.66		U	1.68	0.47	
Th	17.29	4.21		Th	20.91	5.83	
XRF			7	XRF			16
K	3.94	0.9		K	3.69	1.33	
U	3.56	0.47		U	2.92	1.32	
Th	15.29	1.49		Th	15.11	3.33	

Appendix 2C: Methods

Gamma Ray Spectrometer (GRS) Devices

All data used in this study were collected in situ using Radiation Solutions portable gamma ray spectrometer (GRS) devices (RS-230 and RS-330 models). The RS-230 models have a 103 cm3 bismuth germinate oxide crystal sensor whereas the RS-330 has a 344 cm3 sodium-iodide detector. The units were calibrated using concrete test pads, constructed by Radiation Solutions. The detectors housing the sensors were placed directly onto the outcrop and counts of K, U and Th were obtained over 120 seconds. The detectors collect data from a volume of ~0.5 m3, so only outcrops larger than this size were used. The outcrops that were chosen were the least weathered wherever possible. The uncertainties were calculated according to the manufacturer's specifications (Supplementary data). The different crystal sensors in the two models resulted in differences in their abilities to detect U and distinguish it from K and Th. This resulted in the overestimation of U concentrations in data collected from the RS-230 models. All of the data collected from the RS-230 models were normalized to the values from the RS-330 model, as the larger crystal in the RS-330 allows for more accurate determination of HPE concentrations. As a result, the U concentrations in the readings from the RS-230 GRS devices were lowered, but K and Th values remained the same. As the present study seeks to compare the HPE concentrations between subsolidus and suprasolidus rocks, the absolute values, while important, are secondary to the comparative concentration differences between subsolidus and suprasolidus conditions. The concentrations of K–U–Th collected by GRS in this study are in reasonably good agreement with whole-rock compositions determined by XRF for comparison. A comparison of average XRF and GRS K–U–Th is given in the supplementary data. However, given that the GRS devices sample a larger volume than can be practically sampled via conventional geochemical analysis, it is not surprising that there are some differences between the two different sampling methods. U and Th are concentrated primarily within accessory minerals, which are not solely controlled by major element bulk composition. This results in an non-uniform distribution of U and Th throughout the protolith, meaning that their concentrations may vary on the scale of a hand sample to an outcrop (Jaupart and Mareschal, 2005; Bea, 1996), resulting in different concentrations being present in small conventional geochemical samples and the 0.5 m3 volume sampled by the GRS units. Importantly, the GRS units are internally consistent and allow collection of large data sets that would be logistically and financially impractical to collect using conventional analytical methods. However, due to the large sample volume collected by the GRS devices, precision sampling was not able to be achieved in migmatitic rocks. As a result, rocks in which melt had segregated, but not yet left the residue were sampled as a whole, rather than just obtaining samples of the residual material.

Appendix 2D: GRS data

Broken Hill GRS Data

K (wt%)	U (ppm)	Th (ppm)	UTM Zone	Easting	Northing
2.4	2.4	18.4	54J	553537	6494756
2.2	2.0	18.7	54J	553537	6494756
4.6	3.6	23.9	54J	553537	6494756
2.6	1.9	18.5	54J	553537	6494756
1.6	1.5	14.9	54J	553537	6494756
2.2	2.4	21.4	54J	553537	6494756
3.9	2.4	24	54J	553490	6494814
2.5	2.2	16.8	54J	553490	6494814
0.7	1.1	6.1	54J	553490	6494814
4.8	2.3	22.5	54J	553490	6494814
0.8	1.3	6.3	54J	553475	6494767
0.8	2.4	9.9	54J	553475	6494767
2.3	1.8	18.8	54J	553397	6494724
2.8	1.9	18.7	54J	553397	6494724
2.6	1.5	14.7	54J	553397	6494724
2.1	2.5	14.2	54J	553319	6494711
3.6	2.1	24.5	54J	553319	6494711
3.6	3.0	25.6	54J	553319	6494711
3.9	3.4	24.9	54J	553319	6494711
3.4	2.5	23.1	54J	553319	6494711
2.8	2.6	23.1	54J	553319	6494711
2.8	1.7	23.2	54J	553319	6494711
2.6	2.1	20.9	54J	553319	6494711
3.9	3.0	30.1	54J	553263	6494297
3.2	2.3	20.8	54J	553263	6494297
2.6	1.9	21.1	54J	553263	6494297
3.8	2.6	24	54J	553263	6494297
3.5	1.3	28.1	54J	553263	6494297
3.8	3.6	28.9	54J	553263	6494297
4.3	2.8	30.1	54J	553263	6494297
3.9	2.9	27.6	54J	553263	6494297
3.9	1.8	25.4	54J	553219	6494539
3.6	2.6	21.9	54J	553219	6494539
3.4	2.5	23.7	54J	553219	6494539
3.3	1.9	23.7	54J	553219	6494539
3.5	1.3	28.4	54J	553167	6494321
3.6	1.4	22.6	54J	553167	6494321
2.7	1.0	22.3	54J	553167	6494321
4.9	2.2	31.8	54J	553167	6494321
3.4	1.2	23.7	54J	553167	6494321
1.4	1.7	11.4	54J	553128	6494284
3.8	2.5	26.4	54J	553128	6494284
4.2	1.7	25	54J	553128	6494284
3.8	1.7	20	54J	553128	6494284
5.4	3.5	29.3	54J	553128	6494284
5.4	2.1	25.4	54J	552967	6494232
1.7	1.5	14.5	54J	552967	6494232
4.7	3.1	28.9	54J	552967	6494232

4.6	3.0	26.2	54J	552967	6494232
4.2	3.4	25.4	54J	552967	6494232
3.1	1.3	21.9	54J	552926	6494226
3.3	1.2	24	54J	552926	6494226
3.4	1.4	27.1	54J	552926	6494226
3.6	1.6	21.2	54J	552926	6494226
4	1.8	25.5	54J	552926	6494226
3.4	1.8	21.3	54J	552887	6494243
3.1	2.3	24.3	54J	552887	6494243
3.7	2.8	22.6	54J	552887	6494243
3.3	3.2	34.9	54J	552887	6494243
2.1	2.3	17.3	54J	552887	6494243
2	1.6	20.5	54J	552887	6494243
2.5	2.1	22.2	54J	553365	6494105
3.1	2.6	29.7	54J	553365	6494105
3.3	2.3	24.4	54J	553365	6494105
3.5	1.9	22.1	54J	553365	6494105
2.8	1.7	25.7	54J	553365	6494105
3.1	2.0	21.7	54J	553365	6494105
2.6	2.3	20.9	54J	553365	6494105
2.8	2.4	23.5	54J	553365	6494105
3	1.7	17.9	54J	553365	6494105
2.9	3.1	18	54J	553365	6494105
2.6	3.9	19.1	54J	553365	6494105
3.3	3.3	20.1	54J	552292	6494091
2.7	3.0	22.7	54J	552292	6494091
2.5	3.7	31.5	54J	552292	6494091
2.4	3.3	32	54J	552292	6494091
2.1	3.6	30.4	54J	552292	6494091
3	4.4	23.7	54J	552237	6494094
3	4.2	23	54J	552237	6494094
2.1	2.1	16.1	54J	552237	6494094
3.5	3.0	30.6	54J	552237	6494094
4.2	4.3	33.1	54J	552181	6494088
3.5	3.6	25.8	54J	552181	6494088
3.6	3.6	22.9	54J	552181	6494088
4.8	5.8	31.6	54J	552181	6494088
2.9	2.5	22	54J	552181	6494088
4.4	3.1	33.3	54J	552107	6494084
3.9	5.1	24.2	54J	552107	6494085
4.4	2.5	23.6	54J	552107	6494086
4.6	2.6	33.5	54J	552107	6494087
1.8	1.4	18.7	54J	553537	6494103
1.9	2.8	20.3	54J	553537	6494103
1.6	2.1	21.7	54J	553537	6494103
2	1.7	16.6	54J	553537	6494103
2.7	2.1	20.7	54J	553537	6494103
1.1	1.2	8.3	54J	553490	6494814
0.8	1.1	8.4	54J	553490	6494814
0.8	1.7	9.3	54J	553475	6494767

0.5	1.1	5.5	54J	553475	6494767
2.3	1.1	15.9	54J	553397	6494724
2.2	1.2	26.4	54J	553397	6494724
4	2.2	24.1	54J	553319	6494711
3.7	3.0	29.3	54J	553319	6494711
2.8	2.4	22.2	54J	553319	6494711
3	2.0	22.6	54J	553319	6494711
2.9	2.2	30.6	54J	553319	6494711
2.1	1.8	21.4	54J	553319	6494711
3.4	1.5	23.9	54J	553263	6494297
3	1.5	29	54J	553263	6494297
3.2	2.1	23.7	54J	553263	6494297
3.3	1.8	28.5	54J	553263	6494297
3.1	1.8	23.7	54J	553263	6494297
3.2	1.9	23.4	54J	553263	6494297
4.2	2.9	29.9	54J	553263	6494297
3.8	2.9	29	54J	553263	6494297
2.1	1.6	19.2	54J	553219	6494539
3.4	2.1	26.3	54J	553219	6494539
3.1	2.3	25	54J	553219	6494539
3.4	2.6	22.5	54J	553219	6494539
3.8	1.8	30.5	54J	553167	6494321
3.8	1.8	31.3	54J	553167	6494321
2.4	1.5	15.6	54J	553167	6494321
4.1	2.6	31.5	54J	553167	6494321
3.9	2.6	24.1	54J	553128	6494284
2.9	1.6	24.9	54J	553128	6494284
2.9	2.5	23.6	54J	553128	6494284
4.1	1.9	22.8	54J	553128	6494284
2.8	1.7	22.8	54J	553128	6494284
3.9	1.8	28.1	54J	552967	6494232
1.6	1.6	15.2	54J	552967	6494232
3.9	2.6	24.3	54J	552967	6494232
4.7	2.8	34.2	54J	552967	6494232
4.8	2.6	33	54J	552967	6494232
3.7	1.6	27.7	54J	552926	6494226
3.8	1.4	29	54J	552926	6494226
3.2	1.7	22.6	54J	552926	6494226
3.3	1.8	23.4	54J	552926	6494226
3.6	1.4	20.1	54J	552926	6494226
3.3	2.6	21.3	54J	552887	6494243
2.3	1.8	21.2	54J	552887	6494243
2.4	1.4	24.1	54J	552887	6494243
2.1	1.7	16.4	54J	552887	6494243
2	2.1	19.9	54J	552887	6494243
3.2	1.8	28.6	54J	552887	6494243
2.9	2.6	25.3	54J	553365	6494105
3.3	2.4	27.2	54J	553365	6494105
3.2	2.8	22.9	54J	553365	6494105
2.9	2.3	20.1	54J	553365	6494105

3	2.1	24.5	54J	553365	6494105
2.4	1.9	20.6	54J	553365	6494105
2.9	1.8	26.5	54J	553365	6494105
3	2.3	25.9	54J	553365	6494105
2.8	1.9	24.5	54J	553365	6494105
2.7	2.4	22.2	54J	553365	6494105
2.2	2.4	17.9	54J	553365	6494105
2.9	1.7	19.3	54J	553365	6494105
2.8	2.5	20.1	54J	553365	6494105
2.9	5.0	24.7	54J	553365	6494105
3.1	5.2	22.5	54J	553365	6494105
3.3	6.2	21.7	54J	552292	6494091
3.1	5.6	21.9	54J	552292	6494091
2.8	4.9	21.3	54J	552292	6494091
2.6	3.3	27.4	54J	552292	6494091
2.6	3.4	22.3	54J	552237	6494094
3.8	2.9	29.5	54J	552237	6494094
2.4	2.0	27.1	54J	552237	6494094
4.3	4.8	32.5	54J	552181	6494088
4.3	4.4	30.7	54J	552181	6494088
3.8	2.5	31.7	54J	552181	6494088
4.2	2.3	32	54J	552181	6494088
4.8	2.8	31.7	54J	552107	6494084
3.9	2.9	27.8	54J	552107	6494084
4	2.0	28.8	54J	552107	6494084
4.5	3.0	33.2	54J	552107	6494084
4.1	3.2	35.3	54J	552107	6494084
3.41	7.4	26.1	54J	553537	6494601
3.25	8.6	21.6	54J	553537	6494601
2.01	4.8	18.2	54J	553537	6494601
2.04	5.0	29.3	54J	553537	6494601
1.49	5.7	17.8	54J	553537	6494601
3.95	4.3	20.2	54J	553490	6494814
0.75	5.2	5.9	54J	553490	6494814
3.04	2.9	21.2	54J	553490	6494814
3.40	11.2	32.1	54J	553490	6494814
1.77	8.8	15.4	54J	553475	6494767
2.75	7.9	18.6	54J	553475	6494767
2.12	3.3	22.3	54J	553397	6494724
2.27	7.6	16.4	54J	553397	6494724
3.61	4.0	22.9	54J	553397	6494724
3.52	8.6	25.9	54J	553319	6494711
2.79	2.9	21.3	54J	553319	6494712
3.07	8.1	25.4	54J	553319	6494713
2.92	7.6	23.4	54J	553319	6494714
6.11	1.9	32.47	54J	550627	6494129
5.68	5.3	28.33	54J	550810	6494217
5.48	7.1	24.1	54J	550870	6494253
3.12	2.9	13.85	54J	550979	6494289
4.89	3.4	24.71	54J	551035	6494305

5.09	1.6	25.09	54J	551200	6494284
5.57	2.4	27.9	54J	551345	6494211
5.84	1.9	35.48	54J	551429	6494230
6.13	3.5	33.27	54J	551619	6494342
4.88	1.6	25.36	54J	551661	6494230
2.54	1.8	14.14	54J	551805	6494099
2.6	0.8	14.44	54J	551833	6494110
3.85	1.9	21.01	54J	551914	6494142
5.26	1.3	26.12	54J	551961	6494162
6.36	3.2	32.8	54J	551995	6494192
6.71	2.1	38.69	54J	552082	6494199
5.43	2.6	27.37	54J	552155	6494194
4.53	2.8	24.5	54J	552203	6494216
4.15	4.0	20.56	54J	552681	6494339
4.51	2.8	14.22	54J	552717	6494344
4.18	1.6	21.61	54J	552758	6494349
4.48	2.0	20.03	54J	552831	6494360
3.33	0.8	20.2	54J	552880	6494360
4.6	1.1	22.59	54J	552934	6494333
4.76	1.3	23.27	54J	553069	6494331
4.25	2.6	19.55	54J	553133	6494360
4.08	1.1	23.56	54J	553210	6494392
4.89	2.1	24.87	54J	553261	6494428
4.51	1.2	23.25	54J	553313	6494436
3.48	1.5	20.53	54J	553358	6494454
3.73	1.8	20.51	54J	553456	6494489
3.8	2.6	27.7	54J	549308	6467198
4.2	2.5	30.6	54J	549308	6467198
4.1	3.6	29.5	54J	549308	6467198
4.9	3.5	34.9	54J	549308	6467198
3.7	2.4	27.1	54J	549287	6467238
3.7	2.0	26.8	54J	549287	6467238
4	2.6	26.3	54J	549258	6467245
5	2.6	27.9	54J	549258	6467245
3.8	2.8	30.1	54J	549258	6467245
2.9	2.5	29.3	54J	549177	6467197
3.2	2.6	31	54J	549177	6467197
3.1	2.4	29.6	54J	549177	6467197
2.8	2.9	28.6	54J	549177	6467197
3.4	2.3	28.5	54J	549177	6467197
3.2	2.4	30	54J	549131	6467186
3	2.4	26.7	54J	549131	6467186
3.4	3.2	35.4	54J	549119	6467226
3.7	3.9	44	54J	549119	6467226
2.6	2.6	33.8	54J	549119	6467226
3.4	2.2	39.6	54J	549119	6467226
2.9	2.4	31.7	54J	549119	6467226
2.9	2.9	33.9	54J	549129	6467312
3	2.2	32.5	54J	549129	6467312
3.1	2.8	31.6	54J	549129	6467312

3.5	2.9	41.6	54J	549129	6467312
2.6	2.3	32.3	54J	549167	6467320
3.4	2.5	32.9	54J	549167	6467320
3.3	2.7	36.7	54J	549167	6467320
3.5	2.6	39.1	54J	549167	6467320
3.2	2.5	30.4	54J	549167	6467320
3.3	2.8	31.2	54J	549167	6467320
4	2.9	32.4	54J	549167	6467320
3.5	1.8	34.6	54J	549195	6467309
3	2.2	33.3	54J	549195	6467309
3	2.3	23.8	54J	549195	6467309
3.1	2.4	30	54J	549195	6467309
3	3.5	33.1	54J	549081	6467291
3.2	2.4	37.1	54J	549081	6467291
4	2.7	37.7	54J	549081	6467291
3.1	3.6	34.2	54J	549081	6467291
2.5	2.2	29.5	54J	549081	6467291
3	3.0	34	54J	549081	6467291
3	2.6	32.2	54J	549081	6467291
4	3.7	41	54J	549081	6467291
4.9	4.3	45	54J	549081	6467291
3.2	3.4	34.8	54J	549081	6467291
3.2	3.4	38.2	54J	549044	6467295
4.1	2.3	44.9	54J	549044	6467295
3.2	2.7	30.8	54J	549044	6467295
3.2	2.4	34.6	54J	549044	6467295
3.2	2.4	34.9	54J	549044	6467295
3.4	3.0	36.1	54J	549044	6467295
3.7	2.8	38.5	54J	549044	6467295
3.9	3.3	38.5	54J	549044	6467295
3.7	2.3	35.9	54J	549044	6467295
3.6	2.7	35.8	54J	549044	6467295
4	4.2	42.1	54J	549044	6467295
3.5	3.8	41.1	54J	549044	6467295
3.4	3.0	31.2	54J	549044	6467295
3.5	2.1	32	54J	549044	6467295
3.8	2.7	25.6	54J	549044	6467295
3.3	2.8	32.5	54J	549099	6467352
2.9	2.8	35.5	54J	549099	6467352
2	2.4	32.7	54J	549099	6467352
2.9	2.3	30.9	54J	549099	6467352
3.4	2.7	43.4	54J	549099	6467352
2.9	2.4	34	54J	549099	6467352
2.9	2.6	35.4	54J	549099	6467352
2.8	3.8	39.7	54J	549099	6467352
3.1	2.2	37.6	54J	549099	6467352
3	2.8	39	54J	549099	6467352
2.8	2.4	28.6	54J	549099	6467352
3.2	3.3	35.3	54J	549150	6467552
3.8	2.5	28.2	54J	549150	6467552

3.9	2.7	30.9	54J	549150	6467552
4.3	3.0	33.2	54J	549150	6467552
3.3	3.2	37.4	54J	549150	6467552
3	3.2	31.3	54J	549150	6467552
3.5	3.0	32.4	54J	549150	6467552
3.4	2.1	26.8	54J	555462	6469364
4.1	3.3	34.1	54J	555462	6469364
4.2	2.3	31.6	54J	555462	6469364
3.2	2.2	26	54J	555516	6469400
4	2.3	26.7	54J	555516	6469400
3.6	2.7	23.3	54J	555516	6469400
3.8	2.4	24	54J	555516	6469400
3.6	2.3	27	54J	555516	6469400
5	3.1	36.6	54J	555516	6469400
4.6	2.9	27.3	54J	555547	6469076
5.8	3.6	38.6	54J	555547	6469076
4.1	1.8	29.5	54J	555610	6469248
4.2	2.1	28.4	54J	555610	6469248
4.5	2.3	29.2	54J	555610	6469248
4.9	2.6	33.8	54J	555610	6469248
4.3	2.8	29.1	54J	555610	6469248
4.6	2.3	33.9	54J	555610	6469248
4.2	3.1	31.4	54J	555610	6469248
4.7	2.9	5.2	54J	555610	6469248
3.6	2.1	24.9	54J	555610	6469248
4.2	3.4	33.4	54J	555593	6469216
4.7	4.1	45.5	54J	555593	6469216
3.2	2.6	27.7	54J	555593	6469216
1.6	1.7	24.3	54J	555593	6469216
4	2.6	36.4	54J	555593	6469216
3.1	2.9	39.6	54J	555625	6469175
5.4	2.2	37.2	54J	555625	6469175
4.6	1.8	28.6	54J	555625	6469175
3.4	2.5	26	54J	555625	6469175
3.8	2.2	26.7	54J	555625	6469175
4.6	2.6	25.2	54J	555625	6469175
6.1	3.7	37.2	54J	555625	6469175
4.2	2.9	27.85	54J	555625	6469175
4	2.8	26.6	54J	555625	6469175
4.2	2.7	32.5	54J	549308	6467198
4.4	2.5	34	54J	549308	6467198
3.4	2.0	35	54J	549287	6467238
3.8	2.2	29.9	54J	549287	6467238
3.1	2.4	27.7	54J	549258	6467245
4.8	2.4	25.3	54J	549258	6467245
3.6	2.7	30.5	54J	549177	6467197
2.7	2.4	25.1	54J	549177	6467197
3.8	2.2	35	54J	549177	6467197
5.4	2.7	28.7	54J	549177	6467197
3.5	2.6	33.4	54J	549131	6467186

3.5	2.2	28.4	54J	549131	6467186
3.1	2.6	29.8	54J	549119	6467226
3.1	2.3	34.4	54J	549119	6467226
2.9	2.2	33.4	54J	549119	6467226
2.8	2.1	30	54J	549119	6467226
2.5	0.9	8	54J	549129	6467312
2.6	2.1	32.4	54J	549129	6467312
2.8	2.4	29.5	54J	549129	6467312
2.9	2.9	33.4	54J	549129	6467312
2.8	2.2	36.5	54J	549167	6467320
3.4	2.1	41	54J	549167	6467320
2.7	1.7	36.5	54J	549167	6467320
2.7	1.8	32.1	54J	549167	6467320
2.8	2.4	32.6	54J	549167	6467320
3.1	2.6	33.9	54J	549167	6467320
3.2	2.9	38.6	54J	549167	6467320
3.1	2.4	32.2	54J	549167	6467320
3.6	2.5	36.3	54J	549195	6467309
3.3	2.3	34.9	54J	549195	6467309
3.3	2.7	37.1	54J	549195	6467309
3.2	2.5	32.8	54J	549081	6467291
2.7	2.9	37.2	54J	549081	6467291
3.4	3.0	35.4	54J	549081	6467291
2.9	2.4	28	54J	549081	6467291
2.9	2.4	40.2	54J	549081	6467291
3.5	2.8	36	54J	549081	6467291
2.8	2.4	34.9	54J	549081	6467291
3.2	2.5	35	54J	549081	6467291
3	2.8	40.8	54J	549081	6467291
3.2	2.4	32.3	54J	549044	6467295
2.8	2.7	37.7	54J	549044	6467295
3.4	2.5	34.6	54J	549044	6467295
3.3	1.5	40.8	54J	549044	6467295
3.5	3.0	32.4	54J	549044	6467295
3.4	2.9	38.9	54J	549044	6467295
3.1	2.7	38.7	54J	549044	6467295
3.2	2.5	34.5	54J	549044	6467295
3.1	2.6	32	54J	549044	6467295
2.8	1.8	31.3	54J	549044	6467295
3.5	2.1	38.7	54J	549044	6467295
3	2.0	37.5	54J	549044	6467295
3.4	2.4	37.6	54J	549044	6467295
3.5	2.8	33.7	54J	549044	6467295
3.4	2.9	40.1	54J	549044	6467295
3.4	2.9	35.7	54J	549044	6467295
2.6	3.1	31	54J	549099	6467352
3.3	2.1	37	54J	549099	6467352
3.1	2.7	38	54J	549099	6467352
2.9	2.6	36.6	54J	549099	6467352
2.8	2.5	35.3	54J	549099	6467352

2.8	2.7	36.3	54J	549099	6467352
2.8	2.2	35.5	54J	549099	6467352
2.7	2.6	36.3	54J	549099	6467352
3	2.5	31.6	54J	549099	6467352
3.1	2.0	39.8	54J	549099	6467352
2.9	1.8	34.7	54J	549099	6467352
3.4	2.9	45.7	54J	549150	6467552
1.8	2.1	25.3	54J	549150	6467552
3.5	2.3	34.4	54J	549150	6467552
3.3	2.3	28.5	54J	549150	6467552
3.6	2.5	32.5	54J	549150	6467552
3.5	2.1	34.7	54J	549150	6467552
3.3	2.0	33	54J	549150	6467552
3.5	2.4	33.1	54J	549150	6467552
2.9	4.6	49.9	54J	549150	6467552
3.4	2.0	27	54J	555462	6469364
3.2	1.7	30.6	54J	555462	6469364
3	2.6	29.9	54J	555462	6469364
3.1	2.4	22.4	54J	555516	6469400
3.3	2.4	24.4	54J	555516	6469400
2.9	1.6	18.2	54J	555516	6469400
4	2.3	29.7	54J	555516	6469400
4.9	2.3	36.9	54J	555516	6469400
4.7	2.0	38.2	54J	555516	6469400
4.5	1.9	32.3	54J	555516	6469400
4.2	1.9	38.6	54J	555516	6469400
3.9	2.5	36.4	54J	555516	6469400
4	2.3	30.3	54J	555547	6469076
4.6	2.2	37.8	54J	555610	6469248
4.5	2.0	31.8	54J	555610	6469248
5.4	2.1	33.5	54J	555610	6469248
4.8	2.0	27.1	54J	555610	6469248
4.2	1.8	28.8	54J	555610	6469248
3.4	1.8	29.1	54J	555610	6469248
4.5	1.8	35.2	54J	555610	6469248
4.9	2.5	32.7	54J	555610	6469248
3.1	2.1	25.7	54J	555593	6469216
3.8	2.6	32.3	54J	555593	6469216
3.7	1.8	33.3	54J	555593	6469216
1.9	1.9	32.3	54J	555593	6469216
1.4	1.4	27.8	54J	555593	6469216
2.1	1.5	24.5	54J	555593	6469216
2.8	3.0	32.5	54J	555593	6469216
4.7	2.8	37	54J	555593	6469216
2.6	1.9	26.4	54J	555593	6469216
2.5	1.6	25.5	54J	555625	6469175
4.5	1.3	28.2	54J	555625	6469175
4.1	2.5	29.2	54J	555625	6469175
4.4	2.4	34.2	54J	555625	6469175
3.5	2.3	29	54J	555625	6469175

4.4	2.6	29.5	54J	555625	6469175
3.5	3.0	32.2	54J	555625	6469175
5.2	2.6	34.2	54J	555625	6469175
4	1.6	19.5	54J	555625	6469175
4.2	2.0	26.1	54J	555625	6469175
3.8	2.3	24.2	54J	555625	6469175
4.6	2.2	28	54J	555625	6469175
4.2	2.2	30.7	54J	555625	6469175
4.8	2.8	29.3	54J	555625	6469175
4.5	2.0	29.6	54J	555625	6469175
5.3	2.3	35.5	54J	555625	6469175
3.8	2.4	25.3	54J	555625	6469175
4.9	1.9	32.1	54J	555625	6469175
3.9	2.9	28	54J	555625	6469175
4.05	2.3	33.2	54J	549308	6467198
4.8	1.9	38.4	54J	549311	6467221
4.35	2.3	35.5	54J	549287	6467238
2.69	1.5	34	54J	549287	6467238
4.22	0.0	34.1	54J	549258	6467245
3.72	2.1	29.6	54J	549258	6467245
3.9	2.6	32.8	54J	549177	6467197
3.92	2.0	36.7	54J	549177	6467197
3.91	1.5	36.7	54J	549177	6467197
3.63	1.9	39.9	54J	549177	6467197
3.66	3.2	34.8	54J	549131	6467186
3.55	2.2	36.2	54J	549131	6467186
3.23	2.5	39.2	54J	549119	6467226
3.41	1.4	38.4	54J	549119	6467226
3.73	4.8	41.6	54J	549119	6467226
3.51	3.9	42.9	54J	549119	6467226
3.33	3.0	38.6	54J	549129	6467312
2.71	3.0	37.2	54J	549129	6467312
3.02	3.8	37.6	54J	549129	6467312
3.4	0.0	33	54J	549167	6467320
3.26	1.7	40.4	54J	549167	6467320
3.33	2.6	45.5	54J	549167	6467320
3.71	2.1	42.1	54J	549167	6467320
3.28	2.4	41	54J	549167	6467320
3.82	2.2	41.7	54J	549167	6467320
3.54	1.6	38.9	54J	549195	6467309
2.94	2.6	36.3	54J	549195	6467309
3.6	1.8	37.3	54J	549195	6467309
2.86	2.5	38.6	54J	549081	6467291
3.13	2.4	41.3	54J	549081	6467291
3.73	2.7	48.8	54J	549081	6467291
3.22	2.1	44.2	54J	549081	6467291
3.02	3.1	35.6	54J	549081	6467291
4.78	1.5	56.6	54J	549081	6467291
3.37	2.1	44.7	54J	549081	6467291
3.25	2.5	45.8	54J	549081	6467291

3.05	3.0	40.1	54J	549044	6467295
3.24	3.4	35.1	54J	549044	6467295
3.18	3.1	37.2	54J	549044	6467295
3.37	2.9	36.6	54J	549044	6467295
3.1	1.3	31.5	54J	549044	6467295
3.12	1.8	36.5	54J	549044	6467295
2.8	2.1	37.7	54J	549044	6467295
3.77	1.3	40.9	54J	549044	6467295
4.12	2.6	44.5	54J	549044	6467295
3.43	1.1	38.8	54J	549044	6467295
3.28	3.1	38.8	54J	549044	6467295
3.69	2.2	43.1	54J	549044	6467295
4.15	2.1	39.3	54J	549044	6467295
3.63	3.1	39.7	54J	549044	6467295
2.98	2.0	40.5	54J	549099	6467352
3.08	2.8	39.9	54J	549099	6467352
3.31	2.9	45.5	54J	549099	6467352
3.41	1.0	35.9	54J	549099	6467352
3.48	4.0	36.7	54J	549099	6467352
3.51	3.0	40.7	54J	549099	6467352
3.12	2.6	36.7	54J	549099	6467352
2.5	1.7	29.7	54J	549150	6467552
3.45	3.6	36.6	54J	549150	6467552
4.44	3.7	44.5	54J	549150	6467552
3.67	3.1	38.2	54J	549150	6467552
3.82	2.7	36.3	54J	549150	6467552
3.5	2.9	39.4	54J	549150	6467552
4.37	3.3	41.4	54J	549150	6467552
3.12	2.5	42.6	54J	549150	6467552
3.12	2.5	42.6	54J	549150	6467552
3.47	3.2	41.9	54J	549150	6467552
3.8	5.4	65.8	54J	549150	6467552
3.69	4.0	51.5	54J	549150	6467552
4.12	0.0	36.6	54J	555462	6469364
3.74	1.4	33.9	54J	555462	6469364
2.86	0.0	28.9	54J	555462	6469364
3.74	0.0	32.9	54J	555462	6469364
3.23	2.6	40.6	54J	555516	6469400
3.57	1.6	30.3	54J	555516	6469400
4.6	2.0	33.9	54J	555516	6469400
3.45	0.0	28.19	54J	555516	6469400
3.82	1.5	30.8	54J	555516	6469400
5.52	3.3	39	54J	555547	6469076
4.6	2.5	38.1	54J	555547	6469076
4.54	1.1	39.2	54J	555547	6469076
4.62	2.5	33.8	54J	555610	6469248
4.79	1.9	38.5	54J	555610	6469248
4.43	1.8	36.6	54J	555610	6469248
4.92	2.4	33.7	54J	555610	6469248
4.22	2.5	36.9	54J	555610	6469248

4.33	2.0	37	54J	555610	6469248
5.21	5.4	41.4	54J	555610	6469248
4.25	2.0	33.5	54J	555610	6469248
4	1.2	36.6	54J	555593	6469216
4.34	4.0	31	54J	555593	6469216
3.5	1.8	34.3	54J	555593	6469216
4.3	4.0	40.6	54J	555593	6469216
5.31	2.8	48.8	54J	555593	6469216
4.2	1.1	33.7	54J	555625	6469175
3.74	2.4	29.9	54J	555625	6469175
2.71	1.4	26.5	54J	555625	6469175
4.57	2.7	32.7	54J	555625	6469175
4.61	2.2	34.1	54J	555625	6469175
4.4	2.6	33.3	54J	555625	6469175
4.77	1.1	30.7	54J	555625	6469175
3.98	3.0	33.4	54J	555625	6469175
5.02	2.9	32.2	54J	555625	6469175
3.69	3.1	27.7	54J	555701	6469044
3.88	2.7	29.1	54J	555701	6469044
4.33	1.1	29.7	54J	555701	6469044
4.96	2.0	33.1	54J	555701	6469044
3.53	1.7	26.2	54J	555701	6469044
4.25	1.1	31.1	54J	555701	6469044
5.08	1.4	31.8	54J	555701	6469044
4.63	1.3	30.3	54J	555701	6469044
4.82	1.7	32.3	54J	555701	6469044
5.51	1.7	36.5	54J	555701	6469044
3.19	1.0	18.58	54J	549308	6467198
4.61	1.0	21.83	54J	549308	6467198
3.75	0.7	25.02	54J	549287	6467238
5.02	1.1	29.1	54J	549287	6467238
4.73	1.7	31.76	54J	549287	6467238
5.34	2.7	33.04	54J	549258	6467245
5.33	1.6	32.62	54J	549258	6467245
4.97	1.6	30.83	54J	549258	6467245
4.64	1.4	30.86	54J	549177	6467197
5.28	2.0	33.19	54J	549177	6467197
4.79	1.7	29.29	54J	549177	6467197
4.68	1.5	27.7	54J	549131	6467186
4.99	1.5	28.35	54J	549131	6467186
3.76	0.9	21.01	54J	549119	6467226
5.46	1.8	28.35	54J	549129	6467312
5.14	2.0	36.91	54J	549129	6467312
4.45	1.7	26.38	54J	549167	6467320
4.79	2.0	29.18	54J	549167	6467320
4.88	1.9	32.34	54J	549195	6467309
4.7	1.1	29.74	54J	549195	6467309
5.4	2.3	41.43	54J	549195	6467309
4.55	1.6	34.2	54J	549081	6467291
4.21	1.1	31.46	54J	549081	6467291

4.61	1.5	34.39	54J	549081	6467291
5.56	1.8	37.37	54J	549081	6467291
5.24	2.0	36.84	54J	549044	6467295
5.08	2.0	36.5	54J	549044	6467295
4.7	1.5	32.44	54J	549044	6467295
4.28	1.6	28.46	54J	549044	6467295
5.8	2.0	38.03	54J	549099	6467352
4.47	1.5	27.61	54J	549099	6467352
4.58	1.7	26.75	54J	549099	6467352
4.58	1.5	29.68	54J	549099	6467352
4.8	1.5	31.8	54J	549099	6467352
5.1	1.6	30.42	54J	549099	6467352
5.37	2.0	34.27	54J	549099	6467352
5.16	1.9	30.82	54J	549099	6467352
3.36	1.1	21.06	54J	549150	6467552
4.61	1.4	29.78	54J	549150	6467552

Ivrea GRS Data

K (wt%)	U (ppm)	Th (ppm)	UTM Zone	Easting	Northing
3.6	1.9	18.3	32T	452335	5082612
3.5	2.7	19.5	32T	452335	5082612
3.8	2.3	22.5	32T	452335	5082612
3.5	2.5	19.2	32T	452335	5082612
3.9	2.5	24.8	32T	452335	5082612
4	2.7	23.5	32T	452335	5082612
4.4	2.4	24.7	32T	452335	5082612
3.9	2.7	21.6	32T	452335	5082612
4.2	2.5	23.5	32T	452335	5082612
4.2	3.0	23.4	32T	452335	5082612
2.1	1.2	13.2	32T	452284	5082700
3.6	1.7	9.4	32T	452284	5082700
5	2.3	15.7	32T	452284	5082700
2.9	1.3	9.8	32T	452284	5082700
4	2.0	9.2	32T	452253	5082727
4	3.0	19	32T	452253	5082727
3	2.2	17.8	32T	452253	5082727
3.1	2.4	15.9	32T	452253	5082727
4.1	2.8	18.3	32T	452253	5082727
4.1	2.8	19.2	32T	452253	5082727
2.8	2.5	17.4	32T	452253	5082727
1.8	3.0	19	32T	449390	5084067
1.9	1.8	17.9	32T	449390	5084067
2.4	2.6	25.7	32T	449390	5084067
2.8	3.0	25.2	32T	449390	5084067
3.5	2.2	23.5	32T	449390	5084067
2.9	2.8	21.6	32T	449812	5083630
4.3	3.3	28.1	32T	449812	5083630
4.3	4.9	27.3	32T	449812	5083630
3.3	3.7	28.9	32T	449812	5083630
4.2	3.3	25.1	32T	449812	5083630
4.3	2.9	31.4	32T	449812	5083630
2.4	3.2	25.8	32T	449812	5083630
4.1	2.6	20.4	32T	450095	5083631
3.1	1.9	23.9	32T	450113	5083627
3.7	2.4	21.6	32T	450804	5083388
3.8	2.3	16.3	32T	450804	5083388
4.4	2.4	24	32T	450804	5083388
2.5	2.5	16.1	32T	450804	5083388
3.5	1.9	22.7	32T	450804	5083388
3.6	2.4	21.2	32T	450804	5083388
3.8	2.3	20.6	32T	450804	5083388
3.5	2.5	19.6	32T	450804	5083388
3.3	2.6	19.6	32T	450804	5083388
3.9	2.7	22.1	32T	450804	5083388
3.2	2.6	21.2	32T	450804	5083388
4.2	2.3	16.2	32T	450804	5083388
2.7	2.0	18.6	32T	450804	5083388

3	2.6	1.76	32T	451834	5083247
4.2	2.8	14.8	32T	451834	5083247
3.6	1.9	15.7	32T	451834	5083247
3.4	3.2	23.9	32T	451834	5083247
3	2.0	13.3	32T	451834	5083247
2.5	2.5	17.6	32T	451834	5083247
3.3	2.3	22.6	32T	451834	5083247
3.1	2.4	19.1	32T	451834	5083247
3.9	1.9	22.5	32T	452131	5082826
3.3	2.0	20.5	32T	452131	5082826
2.9	2.5	17.4	32T	452131	5082826
3.5	2.4	15.3	32T	452131	5082826
3.8	3.2	17.4	32T	452131	5082826
3.4	3.2	17.3	32T	452131	5082826
3.1	2.3	16	32T	452131	5082826
4.3	2.6	18.4	32T	452131	5082826
4.2	2.1	18.5	32T	452131	5082826
3.7	2.9	20.4	32T	452131	5082826
3.1	2.4	13.7	32T	452167	5082799
3.6	1.9	19	32T	452167	5082799
3	1.8	15.4	32T	452167	5082799
3.2	1.9	19.3	32T	452167	5082799
3.4	2.1	20.4	32T	452167	5082799
3.3	1.8	21.9	32T	452167	5082799
3.1	2.3	17.4	32T	452152	5082820
3.1	2.6	17.2	32T	452152	5082820
3.4	2.9	15.6	32T	452152	5082820
3.6	2.8	18.2	32T	452152	5082820
4.3	3.6	20.4	32T	452152	5082820
3.5	2.6	22.7	32T	452152	5082820
4	2.7	18.2	32T	452152	5082820
3.5	2.3	19.1	32T	452144	5082841
3.1	2.2	20.6	32T	452144	5082841
3	2.1	18.7	32T	452144	5082841
3.2	2.2	19	32T	452144	5082841
3.9	2.4	19.3	32T	452144	5082841
2.6	2.4	17.6	32T	452122	5082924
2.5	2.0	14.9	32T	452122	5082924
4.5	3.0	21.9	32T	451959	5083053
4.6	3.1	26.2	32T	451959	5083053
3.8	2.6	22.9	32T	451959	5083053
5.3	2.5	28	32T	451959	5083053
3.3	2.8	21.9	32T	451959	5083053
4.1	2.4	17.5	32T	451922	5083058
3.7	2.4	20.8	32T	451922	5083058
3	2.0	17.4	32T	451922	5083058
3.1	2.0	14.2	32T	451388	5083107
3.2	2.5	16.6	32T	451388	5083107
4.1	2.0	19.5	32T	451388	5083107
4.1	2.0	19	32T	451388	5083107

3.6	2.4	22	32T	451388	5083107
4	2.4	20.5	32T	451388	5083107
3.9	2.5	24.8	32T	451307	5083783
4	2.7	23.5	32T	451307	5083783
4.4	2.4	24.7	32T	451307	5083783
3.9	2.7	21.6	32T	451307	5083783
4.2	2.5	23.5	32T	451307	5083783
4.2	3.0	23.4	32T	451307	5083783
2.3	1.3	28.3	32T	445036	5086767
2	1.5	20.5	32T	445036	5086767
2.4	1.5	30.5	32T	445036	5086767
1.9	1.2	26.2	32T	445036	5086767
1.7	1.3	22.8	32T	445036	5086767
2.9	1.9	32.7	32T	445036	5086767
2.5	1.2	25.5	32T	445036	5086767
2.6	1.6	27.3	32T	445036	5086767
2.2	1.4	22.5	32T	445036	5086767
3.2	2.1	25.4	32T	445036	5086767
2.4	1.6	21	32T	445036	5086767
3.1	1.1	20.1	32T	445036	5086767
2.5	1.1	18	32T	445036	5086767
3.5	1.5	21	32T	445036	5086767
2.9	2.3	21.9	32T	445036	5086767
2.6	2.2	20.5	32T	445036	5086767
1.8	1.0	8.6	32T	445036	5086767
3.3	1.8	21.3	32T	445208	5086040
2.8	1.6	25.6	32T	445208	5086040
3	1.7	18.6	32T	445208	5086040
2.7	1.4	22.5	32T	445264	5085802
3.4	1.1	17.2	32T	445264	5085802
3.8	1.3	15.7	32T	445264	5085802
2.8	1.3	24.2	32T	445264	5085802
2.8	1.8	21.9	32T	445264	5085802
2.8	2.0	24.5	32T	445264	5085802
2.4	1.8	24.5	32T	445264	5085802
3.4	1.3	27.1	32T	445264	5085802
1.9	1.2	16.4	32T	445294	5085638
1.8	1.7	15.5	32T	445294	5085638
2.4	1.7	19.6	32T	445294	5085638
2.7	1.8	23.2	32T	445294	5085638
2.6	2.2	27.2	32T	445294	5085638
2.7	1.7	24.3	32T	445294	5085638
3.1	1.6	18.4	32T	445294	5085638
2.8	1.6	18.2	32T	445294	5085638
2.2	1.6	14.6	32T	445294	5085638
2.8	1.4	17	32T	445294	5085638
3.3	1.9	25.4	32T	445294	5085638
3.5	2.0	27	32T	445294	5085638
3.7	1.7	25.5	32T	445294	5085638
4.2	1.8	24.1	32T	445294	5085638

3.2	1.7	29.9	32T	445294	5085638
2.9	2.1	24.7	32T	445487	5085282
3.4	2.1	21.3	32T	445487	5085282
4.2	2.0	26.9	32T	445487	5085282
3	1.4	21.9	32T	445743	5085064
3.1	1.4	19.5	32T	445743	5085064
3.2	1.5	22.8	32T	445743	5085064
3.1	1.4	21.5	32T	445743	5085064
1.7	1.4	38.8	32T	445065	5086884
1.6	1.0	22.1	32T	445065	5086884
2.5	1.2	19.6	32T	445065	5086884
2	0.8	20	32T	445065	5086884
3.4	1.1	27.1	32T	445065	5086884
2.5	1.8	26.4	32T	443395	5087136
3.6	1.3	30.2	32T	443395	5087136
4.3	1.8	31.9	32T	443395	5087136
2.3	1.7	26.4	32T	443395	5087136
3	1.6	28.4	32T	443395	5087136
3.6	1.5	29.1	32T	443395	5087136
2.2	1.2	13	32T	443395	5087136
3.7	1.5	24.3	32T	443395	5087136
3.8	1.2	25.7	32T	443395	5087136
3.5	1.7	30.3	32T	443395	5087136
2.6	1.0	22.1	32T	443395	5087136
1.6	1.5	17.5	32T	443345	5087067
2.6	1.3	22.7	32T	443345	5087067
3.1	1.8	22.9	32T	443345	5087067
1.9	0.9	19.9	32T	443345	5087067
3.4	1.8	27.2	32T	443345	5087067
3.6	1.7	22.7	32T	443345	5087067
2.2	0.9	16.1	32T	443345	5087067
3.1	1.2	26.8	32T	443345	5087067
4.2	1.6	29.5	32T	443345	5087067
4	2.2	20.4	32T	450652	5083484
3.2	2.4	14.1	32T	450652	5083484
4.3	2.3	19.3	32T	450652	5083484
4.1	2.4	21.9	32T	450591	5083495
2.5	1.7	14.6	32T	450591	5083495
3.5	2.0	18.9	32T	450591	5083495
3.1	2.2	16.3	32T	450591	5083495
3.1	1.7	15.9	32T	450543	5083503
3.2	2.4	18.2	32T	450543	5083503
3.7	2.0	24.8	32T	450543	5083503
2.6	2.3	14.9	32T	450412	5083524
3.1	2.4	20.5	32T	450303	5083527
3.2	2.3	16	32T	450303	5083527
3.2	2.6	17.5	32T	450303	5083527
3.6	2.9	20.2	32T	450303	5083527
3.1	2.5	20.1	32T	450303	5083527
4	2.9	23.2	32T	450225	5083554

3.2	2.5	19.8	32T	450225	5083554
5.1	2.6	14.8	32T	450187	5083601
4.1	2.6	20.9	32T	450128	5083635
4	2.8	18.7	32T	450128	5083635
3.1	3.2	14.7	32T	450128	5083635
4.3	2.3	23.1	32T	450128	5083635
3.5	2.4	18.4	32T	450054	5083660
3.3	2.6	21.6	32T	450054	5083660
3.1	2.7	21.6	32T	450054	5083660
4.4	2.2	23.5	32T	450054	5083660
2.6	2.7	28.4	32T	449829	5083635
3.4	3.4	33.7	32T	449829	5083635
3.8	3.5	29.1	32T	449829	5083635
2.9	2.2	15	32T	449580	5083805
3.8	2.6	23.8	32T	449542	5083916
4.1	3.1	23.3	32T	449542	5083916
3.7	3.1	26.5	32T	449469	5084029
2.4	2.6	24	32T	449469	5084029
3.4	3.1	29.1	32T	449469	5084029
4.7	2.7	28.3	32T	449469	5084029
3.5	3.0	38.8	32T	448637	5083926
2.9	3.0	34	32T	448637	5083926
3.2	3.3	38.2	32T	448637	5083926
3.1	2.9	31.2	32T	448637	5083926
4	2.7	25.7	32T	448574	5083941
3.6	2.7	22.9	32T	448574	5083941
3.5	2.2	18.8	32T	448574	5083941
4.5	2.5	29.6	32T	448499	5083980
3.5	2.5	20.6	32T	448499	5083980
4.2	2.1	25.2	32T	448499	5083980
4	2.4	29.1	32T	448499	5083980
4.1	2.5	24.7	32T	448499	5083980
3.9	2.7	26.6	32T	448466	5084020
3.3	2.3	25.5	32T	448466	5084020
3.5	3.0	26	32T	448241	5084013
1.9	2.3	25.3	32T	448241	5084013
2.6	2.8	27.1	32T	448241	5084013
3.4	1.9	23.7	32T	448150	5083963
3.5	2.2	18.7	32T	448150	5083963
3.8	2.4	21.8	32T	448150	5083963
3.8	1.7	20.4	32T	448028	5083926
3.6	2.5	21.9	32T	448028	5083926
3.3	2.5	17.6	32T	448028	5083926
4	2.4	22.8	32T	448028	5083926
4.3	2.9	22.5	32T	448028	5083926
3.8	1.9	21.7	32T	447978	5083877
3	2.6	17.6	32T	447978	5083877
3.7	2.8	18.7	32T	447936	5083869
2.7	1.6	18.6	32T	447936	5083869
3.1	2.4	22.2	32T	447936	5083869

4.7	2.6	26.1	32T	447878	5083878
4.6	2.8	22.9	32T	447878	5083878
4.4	2.5	24.1	32T	447878	5083878
3.8	2.8	22.1	32T	447838	5083895
3.9	2.8	20.3	32T	447838	5083895
4	2.1	23.8	32T	447838	5083895
4.1	2.0	24	32T	447838	5083874
4.1	2.4	22.8	32T	447838	5083874
3.8	3.1	17.6	32T	447641	5083965
3.8	2.7	19.9	32T	447641	5083965
3.4	2.7	19.4	32T	447641	5083965
4.4	3.4	20.8	32T	447568	5084006
3.8	2.6	18.7	32T	447568	5084006
3	1.9	15.8	32T	447568	5084006
4.6	2.4	24.3	32T	447501	5084127
4.4	2.1	24.4	32T	447342	5084214
5	2.7	18.2	32T	447342	5084214
5.7	2.0	17.7	32T	447342	5084214
3.3	1.8	11.9	32T	447342	5084214
4.4	2.4	21.6	32T	447229	5084268
4.1	1.9	21.4	32T	447229	5084268
4.2	2.2	22.7	32T	447229	5084268
4.3	2.6	25.4	32T	447229	5084268
2.8	1.8	18.6	32T	446870	5084260
3.5	2.1	22.7	32T	446841	5084355
2.8	1.9	21.5	32T	446841	5084355
3.6	2.6	21.5	32T	446841	5084355
3.4	2.4	20.1	32T	446841	5084355
3.1	1.8	19	32T	446841	5084355
3.2	2.0	22.5	32T	446542	5084484
2.9	1.8	20.6	32T	446542	5084484
3.3	2.2	21.4	32T	446542	5084484
4.1	2.4	30.2	32T	446582	5084540
3.9	2.4	23.8	32T	446582	5084540
3.8	2.9	26.3	32T	446582	5084540
4	2.1	20.6	32T	446519	5084754
3.4	2.0	19.3	32T	446506	5084816
3.6	2.4	22.9	32T	446506	5084816
3	2.8	18.7	32T	446506	5084816
3.5	2.5	23.5	32T	446477	5084847
4.2	2.6	22.6	32T	446477	5084847
3.4	2.4	22.7	32T	446477	5084847
4.6	2.1	28.6	32T	446460	5084935
3.3	3.0	29.6	32T	446460	5084935
4.4	2.5	26.7	32T	446460	5084935
4	2.6	23.4	32T	446460	5084935
2.1	4.8	14.9	32T	446378	5084903
3.2	3.7	19.7	32T	446378	5084903
3.4	2.3	28.1	32T	446328	5084922
3.1	2.4	22.1	32T	446328	5084922

3.4	1.6	15.7	32T	446328	5084922
3.2	2.2	18.7	32T	446263	5084915
3.5	2.1	20.3	32T	446263	5084915
4.5	2.2	25	32T	446152	5084968
3.2	2.4	18.8	32T	446152	5084968
3.5	2.1	17.6	32T	446109	5084946
3.3	2.2	18.7	32T	446055	5084943
5.7	3.2	29.5	32T	446055	5084943
3.4	1.8	17.6	32T	446055	5084943
4.1	2.6	30.2	32T	446018	5084948
3.8	1.8	25.5	32T	446018	5084948
3	2.7	17.5	32T	446018	5084948
3.5	2.8	26.8	32T	445971	5084968
3.7	2.5	22.6	32T	445971	5084968
3.6	2.5	25.8	32T	445971	5084968
3.7	2.6	29.2	32T	445971	5084968
1.9	1.8	29.4	32T	445095	5086859
1.6	1.5	16.2	32T	445095	5086859
1.9	1.8	25.9	32T	445095	5086859
1.8	1.9	35.6	32T	445095	5086859
1.5	1.0	11.8	32T	444661	5087241
0.5	0.9	5.5	32T	444661	5087241
1.3	1.1	8.7	32T	444608	5087269
2.6	1.6	22.8	32T	444608	5087269
2.9	1.2	23.8	32T	444608	5087269
0.8	1.5	9.4	32T	444608	5087269
1.5	1.2	16.8	32T	444576	5087278
1.2	1.3	14.3	32T	444576	5087278
2.4	1.2	16.5	32T	444530	5087302
2.3	1.2	18.5	32T	444530	5087302
1.3	1.2	14.1	32T	444530	5087302
1.3	0.9	11.5	32T	444530	5087302
1.6	1.0	18.3	32T	444530	5087302
1.6	1.0	14.5	32T	444530	5087302
1.3	1.2	14.9	32T	444530	5087302
1.7	1.2	20.1	32T	444530	5087302
2.3	1.0	19.1	32T	444343	5087452
2.7	0.7	27.9	32T	444343	5087452
1.7	1.0	14.6	32T	444343	5087452
1.5	0.9	18.7	32T	444343	5087452
2.4	1.2	12	32T	444343	5087452
3.8	0.9	20.7	32T	444343	5087452
1.3	1.1	16	32T	444343	5087452
3.1	1.3	16.5	32T	444343	5087452
1.3	1.5	22.5	32T	444308	5087486
2	2.4	47.5	32T	444308	5087486
1.3	1.2	18.6	32T	444308	5087486
1.7	1.7	30.6	32T	444308	5087486
2	1.2	18.8	32T	443718	5087424
2	1.3	13	32T	443718	5087424

2	1.0	16	32T	443718	5087424
2.2	1.1	18.8	32T	443718	5087424
1.8	1.2	14.2	32T	443718	5087424
2.2	1.2	17.4	32T	443718	5087424
2.2	1.1	20.1	32T	443718	5087424
2	1.2	15.3	32T	443718	5087424
2.7	1.1	17.3	32T	443666	5087369
3.4	1.0	22.1	32T	443666	5087369
3.4	1.5	19.5	32T	443666	5087369
2.8	1.0	14.9	32T	443666	5087369
3.9	2.1	30.6	32T	443395	5087136
3.3	1.3	26.2	32T	443395	5087136
3.9	1.7	33	32T	443395	5087136
3	1.5	32	32T	443395	5087136
3.8	1.8	29.9	32T	443395	5087136
3.9	1.4	25.5	32T	443395	5087136
3.1	1.5	26.7	32T	443357	5087085
2.8	1.7	17.7	32T	443357	5087085
2.6	1.4	23.8	32T	443357	5087085
2.6	1.7	28.6	32T	443357	5087085
3.4	1.8	23.2	32T	443247	5087000
2.9	1.8	25.4	32T	443247	5087000
3	2.1	28.2	32T	443193	5087004
2.5	1.1	19.1	32T	443193	5087004
2.8	1.4	25.3	32T	443193	5087004
2.8	1.2	25.6	32T	443193	5087004
2.2	1.8	29.8	32T	443193	5087004
2.7	1.7	24.8	32T	443193	5087004
4.2	2.5	25.9	32T	445772	5085044
3.7	1.6	26.5	32T	445772	5085044
1.9	1.6	13	32T	445772	5085044
3.8	2.2	21	32T	445772	5085044
2.8	1.7	23.6	32T	445135	5086576
2.5	1.9	21.1	32T	445135	5086576
2.4	2.0	23.2	32T	445135	5086576
2	1.6	20.4	32T	445135	5086576
2.7	1.9	22.3	32T	445135	5086576
2.7	1.6	24.7	32T	445135	5086576
3.2	1.6	24.8	32T	445135	5086576
4	1.9	19.1	32T	445135	5086576
4.6	1.9	24.2	32T	445135	5086576
3.7	1.2	31	32T	445135	5086576
3.6	2.0	30.4	32T	445135	5086576
2.4	1.3	20.2	32T	445135	5086576
3.3	1.4	20.8	32T	445420	5085449
3.2	1.4	17.1	32T	445420	5085449
2.8	1.8	16.2	32T	445420	5085449
3.1	1.8	21.7	32T	445420	5085449
3.5	1.5	20.7	32T	445420	5085449
4.9	1.3	24.7	32T	445420	5085449

3	1.3	15.4	32T	444335	5087460
1.3	1.7	26.7	32T	444335	5087460
3.5	2.8	19.2	32T	447613	5083964
3.7	2.9	15.2	32T	447613	5083964
3.1	2.7	20.6	32T	447613	5083964
3.9	3.2	20.6	32T	447613	5083964
4.1	3.4	28.1	32T	446706	5084125
3.4	2.8	24.1	32T	446706	5084125
3.1	2.9	19.7	32T	446706	5084125
4.1	3.4	27.7	32T	446559	5084449
4.7	2.7	23.4	32T	446559	5084449
2.4	2.8	21.6	32T	446472	5084856
3.3	3.0	22.4	32T	446472	5084856
4.1	2.5	22	32T	446472	5084856
4.3	2.5	23	32T	446472	5084856
2.7	3.3	18.9	32T	446472	5084856
2.7	2.4	17.9	32T	446472	5084856
2.2	2.9	17.9	32T	446472	5084856
3.2	1.3	23.5	32T	442972	5087044
2.7	1.4	16.1	32T	442972	5087044
2.6	1.7	27.9	32T	442972	5087044
1.8	1.4	17	32T	442972	5087044
2.6	1.4	22.1	32T	442972	5087044
2.8	1.6	22.9	32T	442972	5087044
2.7	1.4	25	32T	442972	5087044
2.9	1.8	19.6	32T	442972	5087044
3	1.7	22.7	32T	442972	5087044
3.1	1.0	27.1	32T	442943	5087030
2.6	1.2	25.3	32T	442943	5087030
3.1	1.5	22.5	32T	442943	5087030
2.2	1.4	22.1	32T	442943	5087030
2.6	1.1	24	32T	442943	5087030
2.4	0.8	22.5	32T	442943	5087030
1.2	1.1	14.3	32T	442894	5087059
2.7	1.9	26.7	32T	443248	5086983
1.9	1.3	19.1	32T	443171	5086996
3	1.8	23.6	32T	443171	5086996
1.7	1.4	16.8	32T	444315	5087488
1.9	1.1	15.4	32T	444315	5087488
2.4	1.4	19.5	32T	444315	5087488
1.9	1.9	22.1	32T	444315	5087488
2	1.5	19.8	32T	444315	5087488
2.8	0.9	22.2	32T	444315	5087488
3.4	1.8	29.5	32T	442203	5087338
3.1	1.8	21.9	32T	442203	5087338
2.7	1.7	17.7	32T	442203	5087338
3.1	1.5	22.9	32T	442203	5087338
2.5	1.5	17.2	32T	442203	5087338
2.5	1.8	18.1	32T	442203	5087338
3.1	2.2	18.3	32T	444484	5087489

3.8	1.7	26.5	32T	444484	5087489
3.6	2.3	24.8	32T	444484	5087489
3	2.2	19.6	32T	444484	5087489
2.9	2.1	19.1	32T	444484	5087489
3.1	2.0	23.2	32T	444484	5087489
3.4	2.3	22.1	32T	444484	5087489
3	2.2	21.7	32T	444484	5087489
3.2	2.3	21.8	32T	444484	5087489
3.3	2.6	19.1	32T	444484	5087489
3.2	2.2	21.1	32T	444484	5087489
3.5	2.0	24.8	32T	444484	5087489
3.5	2.0	24.2	32T	444484	5087489

Mt Stafford GRS Data

K (wt%)	U (ppm)	Th (ppm)	UTM Zone	Easting	Northing
3	1.7	20.5	53K	241351	7567787
4.2	2.2	19.5	53K	241351	7567787
3.9	2.6	22.6	53K	241351	7567787
4	1.0	20.3	53K	241351	7567787
4.2	1.1	20.3	53K	241351	7567787
4.2	1.2	19.2	53K	241351	7567787
3.7	1.2	20	53K	241351	7567787
4.3	1.2	19.4	53K	241351	7567787
4	1.6	20.4	53K	241351	7567787
2.4	1.6	19	53K	241351	7567787
2.4	1.4	20.5	53K	241351	7567787
2.5	2.1	22.3	53K	241351	7567787
2.2	1.2	20.5	53K	241351	7567787
2.4	1.6	20.4	53K	241351	7567787
2.8	1.9	17.5	53K	241351	7567787
4.9	2.0	21	53K	241351	7567787
4.2	1.8	21.5	53K	241351	7567787
4.3	1.9	22.6	53K	241351	7567787
4.2	1.8	20.5	53K	241351	7567787
3.9	1.8	21.5	53K	241351	7567787
3.9	1.2	21.2	53K	241351	7567787
3.7	1.6	20.6	53K	241351	7567787
3.9	1.6	21.7	53K	241351	7567787
3.9	1.9	22.3	53K	241351	7567787
3.7	2.4	22.8	53K	241351	7567787
3.4	2.0	21.2	53K	241351	7567787
3.9	2.2	23.2	53K	241351	7567787
4	2.6	21.1	53K	241351	7567787
4.4	1.4	23.8	53K	241351	7567787
4	1.5	21.8	53K	241351	7567787
3.7	1.6	22.3	53K	241351	7567787
3.9	2.4	20.7	53K	241351	7567787
4.6	2.5	19.9	53K	241351	7567787
2.8	1.9	23.7	53K	241351	7567787
3.6	2.7	23.6	53K	241351	7567787
2.5	1.9	19.3	53K	241351	7567787
4.5	2.2	19.2	53K	241351	7567787
4.9	1.5	22.1	53K	241351	7567787
3.9	2.7	21.5	53K	241351	7567787
5.2	1.7	22.8	53K	241351	7567787
4.8	2.1	24.8	53K	241351	7567787
4.5	1.8	22.7	53K	241351	7567787
4.6	2.6	21.3	53K	241351	7567787
4.3	1.8	20.5	53K	241351	7567787
4.4	1.8	21.6	53K	241351	7567787
4.3	2.0	20.5	53K	241351	7567787
4.3	2.1	21.7	53K	241351	7567787
4.4	2.3	20.9	53K	241351	7567787

4	1.8	22.8	53K	241351	7567787
4.7	2.1	24.2	53K	241351	7567787
4.5	2.0	22	53K	241351	7567787
4.2	2.4	22	53K	241351	7567787
4.3	1.9	23	53K	241351	7567787
4.5	1.8	24.2	53K	241379	7567828
4.1	1.7	21.1	53K	241379	7567828
4.6	1.7	22.9	53K	241379	7567828
4.9	2.1	21.9	53K	241379	7567828
4.6	2.0	22.1	53K	241336	7567840
4.2	1.5	23.1	53K	241336	7567840
4.3	2.5	20.9	53K	241315	7567870
4	2.0	22.3	53K	241315	7567870
4.7	2.2	23	53K	241303	7567841
4.6	2.2	21.5	53K	241303	7567841
2.8	2.1	23.1	53K	241351	7567787
3.5	1.7	22.9	53K	241351	7567787
3.9	1.5	20	53K	241351	7567787
3.7	1.6	20.4	53K	241351	7567787
4.9	1.6	22.3	53K	241351	7567787
2.3	1.7	22.2	53K	241351	7567787
2.4	1.9	20.2	53K	241351	7567787
3.3	1.6	22.4	53K	241351	7567787
4.1	2.1	24.7	53K	241351	7567787
4.6	2.3	21.7	53K	241351	7567787
4.3	1.8	24.7	53K	241351	7567787
4.3	1.8	24.1	53K	241351	7567787
4.2	1.8	23.8	53K	241351	7567787
4.2	1.9	22.7	53K	241351	7567787
4	2.3	24.4	53K	241351	7567787
4	1.7	23	53K	241351	7567787
4.3	2.1	24.7	53K	241351	7567787
4.7	1.6	24.8	53K	241351	7567787
2.12	0.9	15.74	53K	246943	7562149
1.2	0.6	14.32	53K	246947	7562135
2.92	0.7	23.02	53K	247184	7562331
4.69	1.5	23.32	53K	247226	7562362
1.6	1.0	19.39	53K	248127	7562484
3.38	1.6	21.54	53K	248704	7562833
5	1.7	26.47	53K	250367	7561480
4.92	1.7	24.98	53K	250329	7561484
3.41	1.4	22.7	53K	250426	7561507
2.12	0.9	15.74	53K	246943	7562149
1.2	0.6	14.32	53K	246947	7562135
2.92	0.7	23.02	53K	247184	7562331
4.69	1.5	23.32	53K	247226	7562362
1.6	1.0	19.39	53K	248127	7562484
3.38	1.6	21.54	53K	248704	7562833
5	1.7	26.47	53K	250367	7561480
4.92	1.7	24.98	53K	250329	7561484

3.41	1.4	22.7	53K	250426	7561507
3.59	1.2	20.93	53K	250688	7561805
4.99	1.9	25.18	53K	251159	7562260
5.63	1.8	25.74	53K	251144	7562275
4.13	1.2	25.68	53K	251174	7562305
5.6	2.3	27.02	53K	251195	7562285
5.17	2.0	27.19	53K	251251	7562300
5.43	1.7	23.1	53K	251294	7562342
5.21	2.2	28.44	53K	251344	7562399
4.02	1.9	25.8	53K	251355	7562416
2.42	1.3	22.66	53K	251363	7562433
3.9	1.6	24.61	53K	251365	7562451
4.99	2.1	25.76	53K	251374	7562488
5.61	2.7	28.15	53K	251435	7562528
4.4	1.5	24.42	53K	251448	7562545
5.02	2.1	26.44	53K	251477	7562573
4.51	1.7	25.57	53K	251507	7562616
4.96	2.2	27.03	53K	251537	7562641
5.66	2.6	27.09	53K	251553	7562651
4.05	1.7	24.78	53K	251847	7562700
4.86	2.1	26.04	53K	251886	7562769
5.38	2.6	26.94	53K	251910	7562821
4.8	2.1	26.01	53K	251967	7562885
5.67	2.0	27.49	53K	252002	7562913
3.82	1.5	23.22	53K	252078	7562935
2.02	1.3	22.16	53K	252147	7562949
4.06	1.8	25.44	53K	251912	7563398
3.2	1.4	23.25	53K	251963	7563443
3.04	1.4	24.26	53K	252028	7563482
4.45	1.8	25.63	53K	252091	7563531
3.25	1.5	22.28	53K	252103	7563599
4.17	2.2	23.73	53K	252153	7563759
3.17	1.4	25.22	53K	252235	7563901
2.58	1.3	22.09	53K	252277	7563982
2.43	1.4	19.8	53K	252317	7563962
3.35	1.2	21.09	53K	252343	7563950
3.9	1.3	21.44	53K	252341	7564072
2.68	1.0	24.06	53K	252395	7564125
4.52	1.4	22.86	53K	252455	7564172
4.2	1.3	22.22	53K	252568	7564194
2.87	1.2	22.67	53K	252694	7564226
2.49	1.3	22.97	53K	252826	7564191
2.95	1.4	23.84	53K	253033	7564136
3.12	1.9	22.33	53K	253107	7564162
2.66	0.9	23.17	53K	253223	7564180
2.57	1.6	24.57	53K	253564	7564365
4.18	2.0	26.16	53K	253610	7564431
4.18	1.7	23.42	53K	253715	7564384
2.4	1.1	23.09	53K	253835	7564385
2.17	1.2	22.93	53K	253916	7564451

3.93	1.7	23.49	53K	253972	7564466
3.22	1.6	21.67	53K	254022	7564515
2.33	1.4	22.36	53K	254088	7564514
1.81	1.6	24.18	53K	254190	7564503
3.59	1.2	20.93	53K	250688	7561805
5.63	1.8	25.74	53K	251144	7562275
4.99	1.9	25.18	53K	251159	7562260
4.13	1.2	25.68	53K	251174	7562305
5.6	2.3	27.02	53K	251195	7562285
5.17	2.0	27.19	53K	251251	7562300
5.43	1.7	23.1	53K	251294	7562342
5.21	2.2	28.44	53K	251344	7562399
4.02	1.9	25.8	53K	251355	7562416
2.42	1.3	22.66	53K	251363	7562433
3.9	1.6	24.61	53K	251365	7562451
4.99	2.1	25.76	53K	251374	7562488
5.61	2.7	28.15	53K	251435	7562528
4.4	1.5	24.42	53K	251448	7562545
3.1	2.2	19.2	53K	251469	7562340
2.9	2.0	23	53K	251469	7562340
4.9	2.5	20.4	53K	251470	7562325
4.6	2.4	24.3	53K	251470	7562325
2.8	2.1	20.8	53K	251472	7562338
3	2.2	19.8	53K	251472	7562338
5.02	2.1	26.44	53K	251477	7562573
3	1.9	20.8	53K	251478	7562241
3.2	1.8	21.3	53K	251478	7562241
2.7	1.7	21.2	53K	251478	7562241
2.8	1.8	20.2	53K	251478	7562241
4.8	2.9	26.3	53K	251478	7562241
4.9	2.6	25.4	53K	251478	7562241
3.8	2.3	23.3	53K	251478	7562241
4.6	2.8	25.9	53K	251478	7562241
3.7	2.9	25.3	53K	251478	7562241
3.3	2.2	25.5	53K	251478	7562241
4.1	2.7	25.7	53K	251478	7562241
3.3	2.1	23.1	53K	251478	7562241
4.6	2.8	24.2	53K	251478	7562241
3.6	2.3	26.4	53K	251478	7562241
5.6	3.2	25.2	53K	251478	7562241
5.3	2.3	25	53K	251478	7562241
3.1	2.4	24.6	53K	251478	7562241
4.2	1.8	21.6	53K	251478	7562241
4.5	2.6	23.7	53K	251478	7562241
2.7	2.3	22.2	53K	251478	7562241
2.7	1.6	20.4	53K	251478	7562241
3.8	1.6	23.7	53K	251478	7562241
2.9	1.8	23.5	53K	251478	7562241
4.5	2.8	23.5	53K	251478	7562241
3.6	2.2	19.5	53K	251478	7562241

4.4	2.4	23.7	53K	251478	7562241
3.5	2.2	21.1	53K	251478	7562241
3.4	2.0	22.4	53K	251478	7562241
3.5	2.1	22.7	53K	251478	7562241
4	1.8	23.3	53K	251478	7562241
3.8	2.5	24.7	53K	251478	7562241
4.4	2.6	24.3	53K	251478	7562241
3.8	2.4	21.7	53K	251478	7562241
3.7	2.0	22.5	53K	251478	7562241
4.4	2.4	20.7	53K	251478	7562241
2.4	1.9	21.7	53K	251478	7562241
3.7	2.3	22.4	53K	251478	7562241
4.6	2.7	24.5	53K	251489	7562370
4.4	2.3	23.6	53K	251489	7562370
3	2.1	19.4	53K	251491	7562241
3.1	2.0	20.6	53K	251491	7562241
3.2	1.8	18.9	53K	251491	7562241
4.51	1.7	25.57	53K	251507	7562616
2.8	2.3	16.8	53K	251529	7562393
2.9	2.0	19.2	53K	251529	7562393
4.3	2.6	21.7	53K	251532	7562406
3.8	2.4	22.7	53K	251532	7562406
4.96	2.2	27.03	53K	251537	7562641
3.7	2.2	18.2	53K	251544	7562424
3.6	2.4	22.3	53K	251544	7562424
5.66	2.6	27.09	53K	251553	7562651
3.7	2.4	24.2	53K	251560	7562466
3.2	2.0	22	53K	251560	7562466
4.1	3.0	22.5	53K	251571	7562491
4.7	2.7	24.5	53K	251571	7562491
4.6	1.9	23.4	53K	251598	7562523
4.2	2.1	19	53K	251598	7562523
3.1	1.8	22	53K	251618	7562551
2.7	2.4	20.4	53K	251618	7562551
2.9	2.9	25.9	53K	251638	7562555
2.6	2.7	30.1	53K	251638	7562555
4.05	1.7	24.78	53K	251847	7562700
4.86	2.1	26.04	53K	251886	7562769
5.38	2.6	26.94	53K	251910	7562821
4.06	1.8	25.44	53K	251912	7563398
3.2	1.4	23.25	53K	251963	7563443
4.8	2.1	26.01	53K	251967	7562885
5	3.3	26.6	53K	252002	7562935
5.67	2.0	27.49	53K	252002	7562913
5	3.0	24.1	53K	252003	7562884
3.9	2.7	22.8	53K	252003	7562884
4.8	2.9	23.3	53K	252003	7562884
5.3	3.4	23.1	53K	252003	7562884
5.5	3.0	23.1	53K	252003	7562884
4.9	2.9	23.4	53K	252003	7562884

5.2	3.4	22.9	53K	252003	7562884
5.6	3.5	26.1	53K	252003	7562884
5.4	3.0	23.4	53K	252003	7562884
4.1	2.6	23.6	53K	252003	7562884
5.6	3.5	22.8	53K	252003	7562884
3.2	2.4	23.6	53K	252003	7562884
2.3	1.7	19.8	53K	252003	7562884
4.7	2.6	25.4	53K	252003	7562884
3.8	1.9	23.1	53K	252003	7562884
3.6	1.7	23.8	53K	252003	7562884
4.1	2.2	26.8	53K	252003	7562884
4.9	2.6	25.8	53K	252003	7562884
4.9	2.4	22.7	53K	252003	7562884
4.3	2.7	22.7	53K	252003	7562884
4.6	2.4	22.5	53K	252003	7562884
4.6	2.0	25.3	53K	252003	7562884
4.9	3.5	25.8	53K	252003	7562884
4.1	2.6	25.9	53K	252003	7562884
4.8	3.1	27	53K	252003	7562884
4.6	2.3	25.2	53K	252003	7562884
4.9	2.5	28.7	53K	252003	7562884
5.4	3.0	25.1	53K	252003	7562884
5.1	2.4	28	53K	252003	7562884
4.8	3.2	26.5	53K	252003	7562884
4.5	2.9	25.1	53K	252003	7562884
4.5	2.2	25.7	53K	252003	7562884
4.6	2.8	24.7	53K	252003	7562884
4.7	2.4	25.7	53K	252004	7562905
3.2	2.4	21.8	53K	252004	7562905
3.04	1.4	24.26	53K	252028	7563482
3.82	1.5	23.22	53K	252078	7562935
4.45	1.8	25.63	53K	252091	7563531
3.25	1.5	22.28	53K	252103	7563599
2.02	1.3	22.16	53K	252147	7562949
4.17	2.2	23.73	53K	252153	7563759
3.17	1.4	25.22	53K	252235	7563901
2.58	1.3	22.09	53K	252277	7563982
2.43	1.4	19.8	53K	252317	7563962
4.3	2.7	23.1	53K	252340	7564026
5.2	3.2	28.7	53K	252340	7564026
4	3.6	26.5	53K	252340	7564026
4.4	2.9	22.5	53K	252340	7564026
4.3	2.4	25.1	53K	252340	7564026
3.1	2.5	20.6	53K	252340	7564026
3.7	2.6	27.7	53K	252340	7564026
4.6	2.3	26.4	53K	252340	7564026
5	1.9	21	53K	252340	7564026
4.1	1.9	22.7	53K	252340	7564026
4.1	2.7	22.8	53K	252340	7564026
4	1.8	21	53K	252340	7564026

3.8	1.4	19.8	53K	252340	7564026
2.4	1.3	21.6	53K	252340	7564026
4.9	2.5	23.8	53K	252340	7564026
3.6	2.4	20	53K	252340	7564026
4.6	2.6	26.7	53K	252340	7564026
3.1	2.3	19.9	53K	252340	7564026
3.5	1.9	21.8	53K	252340	7564026
4.8	2.4	23.2	53K	252340	7564026
4.3	2.0	24.4	53K	252340	7564026
4.2	1.8	22.6	53K	252340	7564026
2.7	1.8	23	53K	252340	7564026
4.8	1.4	23.2	53K	252340	7564026
4.8	2.8	25.1	53K	252340	7564026
3.2	2.0	21.5	53K	252340	7564026
5	2.3	47.5	53K	252340	7564026
4.2	2.3	21.1	53K	252340	7564026
4.4	2.4	23.4	53K	252340	7564026
3.7	2.0	19.5	53K	252340	7564026
3.2	2.0	23.5	53K	252340	7564026
3.1	2.1	21.6	53K	252340	7564026
4.7	3.1	26.3	53K	252340	7564026
5.8	2.6	29.7	53K	252340	7564026
4.9	2.3	21.7	53K	252340	7564026
4.5	2.6	22.2	53K	252340	7564026
4.3	2.0	18.5	53K	252340	7564026
2.8	1.8	21.4	53K	252340	7564026
4.3	2.8	21.5	53K	252340	7564026
4.3	2.3	20.9	53K	252340	7564026
3.9	1.3	21.44	53K	252341	7564072
3.35	1.2	21.09	53K	252343	7563950
2.68	1.0	24.06	53K	252395	7564125
4.52	1.4	22.86	53K	252455	7564172
4.2	1.3	22.22	53K	252568	7564194
2.87	1.2	22.67	53K	252694	7564226
2.49	1.3	22.97	53K	252826	7564191
3.1	2.3	24	53K	252919	7564197
3.4	2.7	23	53K	252919	7564197
5.1	2.1	20.1	53K	252919	7564197
3.9	1.7	19.5	53K	252919	7564197
3.1	1.9	24.1	53K	252919	7564197
3.7	2.0	23.6	53K	252919	7564197
3.6	1.8	22.1	53K	252919	7564197
4.2	2.1	23.3	53K	252919	7564197
4.7	2.3	21.7	53K	252919	7564197
4.9	2.4	26.2	53K	252919	7564197
4.5	2.0	27.3	53K	252919	7564197
4.1	2.2	24.3	53K	252919	7564197
1.9	2.0	20.4	53K	252919	7564197
1.2	1.2	25.3	53K	252919	7564197
3.6	2.0	23.2	53K	252919	7564197

2.6	2.3	20.9	53K	252919	7564197
5.3	3.4	43.9	53K	252919	7564197
4.2	3.4	38.6	53K	252919	7564197
2.8	2.2	17.7	53K	252919	7564197
3.4	2.5	23	53K	252919	7564197
5.1	2.4	23.7	53K	252919	7564197
2.6	2.1	23.1	53K	252919	7564197
3.6	2.2	23.7	53K	252919	7564197
3	2.4	23.8	53K	252919	7564197
5.4	2.6	26.1	53K	252919	7564197
3.9	2.5	24.2	53K	252919	7564197
4.8	2.7	22.8	53K	252919	7564197
2.1	2.2	27.8	53K	252919	7564197
1.3	1.4	21.7	53K	252919	7564197
3.9	2.4	21.8	53K	252919	7564197
2.8	2.1	20.5	53K	252919	7564197
4.5	3.8	35.1	53K	252919	7564197
4.9	3.9	35	53K	252919	7564197
4.2	2.0	20.9	53K	252919	7564197
2.4	2.1	22.9	53K	252919	7564197
2.7	2.4	19.5	53K	252919	7564197
2.9	2.0	22.2	53K	252919	7564197
3.4	2.3	22.2	53K	252919	7564197
3.4	2.3	21.3	53K	252919	7564197
4.3	2.1	22.1	53K	252919	7564197
1.9	1.5	22.9	53K	252919	7564197
3.9	1.9	28	53K	252919	7564197
3.3	1.7	27.9	53K	252919	7564197
1.7	2.1	31.9	53K	252919	7564197
1.4	1.0	20.3	53K	252919	7564197
2.1	1.9	21.5	53K	252919	7564197
1.7	1.5	20.4	53K	252919	7564197
4.3	2.9	23.7	53K	252919	7564197
3.2	2.6	19.7	53K	252919	7564197
3.9	2.5	22.4	53K	252919	7564197
4.9	2.8	22.9	53K	252919	7564197
3.9	2.5	24.9	53K	252919	7564197
3.1	2.2	21.8	53K	252919	7564197
4.8	2.0	21.3	53K	252919	7564214
3.5	2.1	21.1	53K	252924	7564221
2.4	2.0	24.3	53K	252946	7564246
1.4	2.3	21	53K	252946	7564246
3.8	2.8	23.3	53K	252969	7564251
2.8	1.8	24.3	53K	252990	7564256
3.5	2.3	23.6	53K	253001	7564249
3.2	2.0	23.1	53K	253017	7564247
2.95	1.4	23.84	53K	253033	7564136
3	1.8	21.1	53K	253060	7564223
4.5	3.1	21.5	53K	253106	7564178
3.12	1.9	22.33	53K	253107	7564162

2.66	0.9	23.17	53K	253223	7564180
4	2.8	20.2	53K	255286	7560353
5.2	2.4	27	53K	255286	7560353
4.9	3.4	27	53K	255286	7560353
3	1.6	22.5	53K	255286	7560353
4.8	2.5	22.7	53K	255286	7560353
3.8	2.4	22.9	53K	255286	7560353
3.7	2.4	22.3	53K	255286	7560353
4.2	2.4	23.6	53K	255286	7560353
2.7	1.8	28.9	53K	255286	7560353
4.8	2.9	25.1	53K	255286	7560353
3.5	2.6	20.1	53K	255286	7560353
3.3	2.6	20.4	53K	255286	7560353
4.9	2.8	25	53K	255286	7560353
4.4	2.4	24	53K	255286	7560353
4	2.3	20.6	53K	255286	7560353
4.2	2.1	22.7	53K	255286	7560353
4.4	2.9	25	53K	255286	7560353
4.7	2.5	25.2	53K	255286	7560353
4.1	2.6	20.2	53K	255286	7560353
3	2.0	21.5	53K	255286	7560353
5.4	2.2	24.3	53K	255286	7560353
3.5	1.9	22.4	53K	255286	7560353
5	3.0	23.5	53K	255286	7560353
4.5	2.5	23.3	53K	255286	7560353
4.8	2.4	20.9	53K	255286	7560353
5	3.2	24.4	53K	255286	7560353
3.4	2.0	23.5	53K	255286	7560353
3.1	1.5	22.1	53K	255286	7560353
4.4	2.6	22.6	53K	255286	7560353
4.1	2.4	22.4	53K	255286	7560353
2.7	2.2	22.1	53K	255286	7560353
5.3	2.6	23.9	53K	255286	7560353
3.4	2.4	25.1	53K	258519	7566070
4.1	5.2	39.9	53K	258519	7566070
4.2	3.2	37.2	53K	258519	7566070
3.9	3.0	25.3	53K	258519	7566070
2.8	2.4	22.9	53K	258519	7566070
2.6	2.5	23	53K	258519	7566070
3.5	2.9	20.9	53K	258519	7566070
1.8	2.2	19.3	53K	258519	7566070
2.1	2.7	17.3	53K	258519	7566070
3.5	3.5	25.8	53K	258519	7566070
2.4	2.0	21.2	53K	258519	7566070
3.5	3.3	23.7	53K	258519	7566070
3.1	2.2	21.3	53K	258519	7566070
3.2	2.7	21.9	53K	258519	7566070
3.2	2.7	27.6	53K	258519	7566070
4.1	2.7	27.2	53K	258519	7566070
2.3	2.6	25	53K	258519	7566070

2.8	2.9	25.2	53K	258519	7566070
2.9	2.6	26.7	53K	258519	7566070
3.8	2.7	26.8	53K	258519	7566070
3.4	3.0	23.3	53K	258519	7566070
3.1	2.3	23.8	53K	258519	7566070
2.8	2.6	22.5	53K	258519	7566070
3.5	2.4	28.1	53K	258519	7566070
4.1	3.2	26.5	53K	258519	7566070
2.4	2.3	25.2	53K	258519	7566070
4.3	2.9	29.9	53K	258519	7566070
2.7	2.6	21.1	53K	258519	7566070
4.1	2.9	25.8	53K	258519	7566070
2.8	2.4	18.5	53K	258519	7566070
3.8	3.1	26.9	53K	258519	7566070
3.8	2.9	24.5	53K	258519	7566070
2.8	3.1	20.6	53K	258519	7566070
4.4	3.0	27.5	53K	258519	7566070
3.6	2.8	26	53K	258519	7566070
3.4	2.4	25.5	53K	258519	7566070
4.5	3.1	27.2	53K	258519	7566070
3.1	2.4	23.1	53K	258519	7566070
4.1	3.3	28.7	53K	258519	7566070
4	3.8	28.1	53K	258519	7566070
4.6	3.7	29.1	53K	258519	7566070
4.7	4.1	25.4	53K	258519	7566070
3.7	3.2	34.8	53K	258831	7566466
3.7	2.8	38.1	53K	258831	7566466
3.6	3.0	32.7	53K	258831	7566466
4.1	3.0	36.4	53K	258831	7566466
3.7	3.0	36.8	53K	258831	7566466
3.9	4.1	35	53K	258831	7566466
3.4	2.8	35	53K	258831	7566466
3.6	2.7	32.5	53K	258831	7566466
3.1	2.9	32.6	53K	258831	7566466
3.8	3.1	42.2	53K	258831	7566466
3.7	3.2	33	53K	259078	7566925
4.8	2.9	46.5	53K	259078	7566925
5.8	3.0	16.1	53K	259078	7566925
4.7	2.5	44.6	53K	259078	7566925
4.4	2.6	44.9	53K	259078	7566925
3.1	1.8	26.7	53K	259976	7564102
3.3	2.0	21.9	53K	259976	7564102
4	2.7	29.8	53K	259976	7564102
3.2	1.8	24.8	53K	259976	7564102
3.5	2.0	29.5	53K	259976	7564102
5.4	3.0	31.7	53K	259976	7564102
3	1.8	26.6	53K	259976	7564102
2.7	2.1	27.9	53K	259976	7564102
3.2	2.2	23.3	53K	259976	7564102
2.8	2.7	29.4	53K	259976	7564102

3.8	3.0	35.7	53K	259976	7564102
4.4	2.5	28.8	53K	259976	7564102
4.1	2.2	29.5	53K	259318	7563216
3.6	2.2	32.9	53K	251251	7562300
2.5	2.3	24.7	53K	251251	7562300
2.8	1.7	26.3	53K	251251	7562300
4.1	2.3	33.6	53K	251251	7562300
2.6	1.8	27.5	53K	251251	7562300
4.3	2.6	32.4	53K	251251	7562300
3.3	2.0	24	53K	251251	7562300
1.9	1.6	21.8	53K	251251	7562300
2.9	1.9	25	53K	251251	7562300
3.2	2.1	29.1	53K	251251	7562300
1.7	1.8	21.6	53K	251251	7562300
2	2.0	25.4	53K	251251	7562300
3.1	3.0	29.6	53K	251251	7562300
5.3	2.7	35.6	53K	251251	7562300
5.4	3.2	34.1	53K	251251	7562300
5.2	3.2	31.2	53K	251251	7562300
1.7	1.7	25.3	53K	258861	7562864
5.8	2.7	37.5	53K	258861	7562864
6	2.5	35.3	53K	258861	7562864
6.6	3.0	40.7	53K	258861	7562864
5.4	2.9	35.3	53K	258861	7562864
5.7	2.8	34.6	53K	258861	7562864
4.8	3.2	34.3	53K	258861	7562864
4.9	2.5	37.2	53K	258861	7562864
1.9	1.5	22.2	53K	258861	7562864
2.1	1.5	19	53K	258861	7562864
4	2.4	28.9	53K	258861	7562864
3.2	2.3	28.7	53K	258861	7562864
4	2.5	33.1	53K	258861	7562864
4.5	2.4	33	53K	258861	7562864
3.4	2.7	32.1	53K	258861	7562864
1.6	2.7	29.3	53K	258861	7562864
5.1	3.3	34.5	53K	258861	7562864
2.7	2.5	24.8	53K	258861	7562864
2.4	2.1	22.4	53K	258861	7562864
5.2	2.4	32.6	53K	258861	7562864
6.1	3.1	37.9	53K	258861	7562864
5.9	3.0	33.9	53K	258861	7562864
5.6	2.4	35	53K	258861	7562864
2.3	1.7	24.4	53K	258861	7562894
2.9	2.4	23.8	53K	258861	7562944
4.5	2.5	33	53K	258861	7562944
3	2.3	30.6	53K	258861	7562944
7.1	3.2	41.7	53K	258861	7562944
3.8	2.2	30.6	53K	258861	7562944
2.4	1.6	24.1	53K	258861	7562944
2.6	2.4	25.6	53K	259320	7563275

4.4	2.6	35.4	53K	259320	7563275
1.7	2.4	26.1	53K	259320	7563275
2.8	2.4	28.8	53K	259320	7563275
3.7	2.5	29.1	53K	259320	7563275
4.7	2.2	28.5	53K	259320	7563275
4.5	3.1	27.4	53K	259320	7563275
2.8	2.2	22.5	53K	259320	7563275
3.5	2.6	25.4	53K	259320	7563275
6.3	3.2	36.7	53K	259320	7563275
6.5	3.1	40.3	53K	259320	7563275
3.49	1.8	26.79	53K	259330	7563364
4.04	1.6	30.97	53K	259431	7563405
4.44	2.0	28.3	53K	259581	7563384
4.62	1.6	29.77	53K	259707	7563360
4.51	1.9	30.98	53K	259858	7563357
5.38	2.2	32.84	53K	259985	7563369
4.29	1.7	29.12	53K	260143	7563419
4.15	0.9	26.76	53K	260253	7563409
4.44	1.9	23.88	53K	254277	7564508
3.13	1.4	26.64	53K	254358	7564485
2.25	1.8	25.04	53K	254463	7564485
2.77	1.6	25.13	53K	254563	7564493
2.49	1.3	24.72	53K	254662	7564478
2.53	0.9	22.81	53K	254750	7564483
2.75	1.6	23.3	53K	254825	7564488
4.06	2.3	25.95	53K	254944	7564495
3.18	1.5	26.26	53K	255020	7564496
4.56	1.3	43.09	53K	255069	7564523
4.11	2.0	28.23	53K	254326	7565012
3.49	1.8	26.79	53K	259330	7563364
4.04	1.6	30.97	53K	259431	7563405
4.44	2.0	28.3	53K	259581	7563384
4.62	1.6	29.77	53K	259707	7563360
4.51	1.9	30.98	53K	259858	7563357
5.38	2.2	32.84	53K	259985	7563369
4.29	1.7	29.12	53K	260143	7563419
4.15	0.9	26.76	53K	260253	7563409
5.2	3.1	23.6	53K	255286	7560353
3.5	2.6	25.4	53K	255286	7560353
3.2	2.5	20.6	53K	255286	7560353
4.2	2.3	22.1	53K	255286	7560353
3.8	2.0	24	53K	255286	7560353
4.4	2.8	22.9	53K	255286	7560353
2.7	1.9	23.2	53K	255286	7560353
4	3.0	21.6	53K	255286	7560353
4.2	3.1	24.9	53K	255286	7560353
3	2.4	21.1	53K	255286	7560353
3.2	2.5	19.4	53K	255286	7560353
2.6	2.2	19.2	53K	255286	7560353
2.7	2.4	20.6	53K	255286	7560353

2.5	2.0	23.4	53K	255286	7560353
1.8	2.4	23.2	53K	255286	7560353
2.5	2.6	23.9	53K	255286	7560353
2.7	2.2	19.2	53K	255286	7560353
2.9	2.3	21.5	53K	255286	7560353
2.7	2.2	21.7	53K	255286	7560353
3.1	2.1	23.9	53K	255286	7560353
2.3	1.6	18.9	53K	255286	7560353
4.5	3.0	25.5	53K	255286	7560353
4.3	2.9	21.1	53K	255286	7560353
3.1	1.9	23.9	53K	255286	7560353
3	1.5	23.8	53K	255286	7560353
1.7	2.1	33.1	53K	255286	7560353
3.1	1.8	26.3	53K	255286	7560353
2.8	1.6	21.5	53K	255286	7560353
4.2	2.7	20.8	53K	255286	7560353
4.1	2.2	23.4	53K	255286	7560353
3.7	3.2	23.1	53K	255286	7560353
3.5	2.0	20.5	53K	255286	7560353
2.7	2.1	21.8	53K	255286	7560353
2.7	2.0	21.3	53K	255286	7560353
3.6	1.8	21.7	53K	255286	7560353
2.5	1.7	23.5	53K	255286	7560353
2.8	1.7	24.4	53K	255286	7560353
3.8	2.1	21.8	53K	255286	7560353
1.8	1.4	19.4	53K	255286	7560353
2.2	2.2	28.1	53K	255286	7560353
2.6	2.1	21.5	53K	255286	7560353
2.2	2.0	23.8	53K	255286	7560353
2.4	1.9	22	53K	255286	7560353
2.5	1.9	20.4	53K	255286	7560353
2.3	1.8	22.3	53K	255286	7560353
2.7	2.3	23.7	53K	255286	7560353
2.4	2.0	23.4	53K	255286	7560353
2.7	2.3	22.3	53K	255286	7560353
4.2	2.9	29.8	53K	255286	7560353
3	2.2	22.8	53K	255286	7560353
2.7	2.0	23.6	53K	255286	7560353
4.1	2.8	22.9	53K	255286	7560353
4	2.4	22.4	53K	255286	7560353
4.4	2.4	21	53K	255286	7560353
3.3	1.9	22	53K	255286	7560353
3.1	1.9	27.1	53K	255286	7560353
2.2	2.1	21.9	53K	255286	7560353
4.6	2.7	23.3	53K	255286	7560353
3.6	2.0	22.4	53K	255286	7560353
2.9	1.9	23.9	53K	255286	7560353
2.8	2.3	21.8	53K	255342	7560376
2.2	2.2	25.5	53K	255342	7560376
2.5	2.3	24.1	53K	255367	7560386

2.5	2.0	21.7	53K	255381	7560390
3.1	2.0	21.6	53K	255402	7560404
2.6	1.8	23.1	53K	255413	7560417
4.4	2.6	22.8	53K	255413	7560417
2.8	2.0	23.6	53K	255430	7560450
4.1	2.6	22.1	53K	255432	7560458
5	2.4	29.7	53K	255398	7560529
2.9	1.8	26.4	53K	255392	7560547
3.5	2.3	24.9	53K	255392	7560547
2.4	2.0	25.8	53K	255390	7560556
4.7	2.7	19.4	53K	255463	7560556
4.1	2.2	22.9	53K	255463	7560556
4.9	3.2	20.8	53K	255463	7560556
4.9	2.1	21.4	53K	255463	7560556
4.6	2.6	20.8	53K	255463	7560556
2.4	2.4	21.8	53K	255463	7560556
4.6	2.1	22.6	53K	255463	7560556
3.7	2.5	20.8	53K	255469	7560566
3	2.3	28.4	53K	255398	7560570
2.5	2.1	24.1	53K	255487	7560571
3.4	2.3	23.9	53K	255546	7560607
4.4	3.0	28.1	53K	255553	7560611
2.57	1.6	24.57	53K	253564	7564365
4.18	1.7	23.42	53K	253715	7564384
2.4	1.1	23.09	53K	253835	7564385
4.6	2.1	22.5	53K	253521	7564398
5.1	3.0	27.9	53K	253538	7564411
4	3.0	22.6	53K	253538	7564411
4.1	2.9	23.3	53K	253538	7564411
4.6	3.0	24.8	53K	253538	7564411
4	2.6	25.6	53K	253538	7564411
3.7	2.4	23.7	53K	253538	7564411
5	2.7	22.8	53K	253538	7564411
4.8	2.8	28.6	53K	253538	7564411
4.5	2.6	21.3	53K	253538	7564411
4	3.0	24.6	53K	253538	7564411
4.1	3.1	23.4	53K	253538	7564411
4.3	2.9	23.8	53K	253538	7564411
4.3	2.3	21.8	53K	253538	7564411
3.8	3.0	24.7	53K	253538	7564411
4.2	2.7	19.6	53K	253538	7564411
4.2	3.0	21.6	53K	253538	7564411
4	2.5	21.5	53K	253538	7564411
5.4	2.8	20.8	53K	253538	7564411
5.5	3.1	21.2	53K	253538	7564411
3.6	2.3	19.8	53K	253538	7564411
3.9	3.2	21.2	53K	253538	7564411
5	3.4	24.8	53K	253538	7564411
5	2.3	23.5	53K	253538	7564411
4.2	3.0	21.4	53K	253538	7564411

4.5	3.3	23.4	53K	253538	7564411
4.1	3.0	20.1	53K	253538	7564411
4.5	3.5	20.4	53K	253538	7564411
4.7	3.0	23.3	53K	253538	7564411
4.6	3.1	21.1	53K	253538	7564411
3.3	2.1	19.8	53K	253538	7564411
5	2.9	23.8	53K	253538	7564411
4	2.6	19.4	53K	253538	7564411
4.5	2.7	20.2	53K	253538	7564411
4.2	2.5	21	53K	253538	7564411
2.8	2.2	22.4	53K	253538	7564411
4.4	2.9	21.4	53K	253538	7564411
3.8	2.2	21	53K	253538	7564411
5.1	2.4	19.2	53K	253538	7564411
4.18	2.0	26.16	53K	253610	7564431
3.4	2.9	26	53K	253523	7564436
3.3	2.1	23.4	53K	253523	7564436
2.17	1.2	22.93	53K	253916	7564451
3.93	1.7	23.49	53K	253972	7564466
2.49	1.3	24.72	53K	254662	7564478
2.53	0.9	22.81	53K	254750	7564483
3.13	1.4	26.64	53K	254358	7564485
2.25	1.8	25.04	53K	254463	7564485
2.75	1.6	23.3	53K	254825	7564488
2.77	1.6	25.13	53K	254563	7564493
4.06	2.3	25.95	53K	254944	7564495
3.18	1.5	26.26	53K	255020	7564496
1.81	1.6	24.18	53K	254190	7564503
4.44	1.9	23.88	53K	254277	7564508
2.33	1.4	22.36	53K	254088	7564514
3.22	1.6	21.67	53K	254022	7564515
4.56	1.3	43.09	53K	259976	7564102
4.1	2.6	25.5	53K	259976	7564102
4.2	2.8	34.2	53K	259976	7564102
3.7	1.9	25.9	53K	259976	7564102
2.7	2.2	21.6	53K	259362	7563665
3.7	1.8	24.3	53K	259362	7563665
2.1	1.4	20.4	53K	259362	7563665
3.4	1.9	26.4	53K	259383	7563427
3.6	1.7	31.1	53K	259383	7563427
2.7	1.8	25.9	53K	259383	7563427
4.7	2.9	37	53K	259383	7563427
2.2	2.1	23.8	53K	259383	7563427
4.8	2.7	38.4	53K	259383	7563427
5.6	3.1	31.1	53K	259383	7563427
5.4	2.4	37.7	53K	259383	7563427
2.8	1.7	25.3	53K	259383	7563427
1.9	1.3	20.8	53K	259383	7563427
2.4	1.9	23.1	53K	259383	7563427
3	1.8	30.5	53K	259383	7563427

3.4	2.5	32.3	53K	259383	7563427
5	2.1	34.9	53K	259383	7563427
4.6	2.8	31.5	53K	259383	7563427
2.3	1.8	27.6	53K	259383	7563427
4.5	2.8	28.6	53K	259383	7563427
5.6	2.7	36.9	53K	259383	7563427
7.3	3.8	41.8	53K	259383	7563427
5.3	3.1	35.4	53K	259383	7563427
2	1.8	21.9	53K	259383	7563427
3.6	2.8	30.5	53K	259383	7563427
5	3.0	35.4	53K	259383	7563427
4.9	2.5	31.7	53K	259383	7563427
4.4	2.1	32.9	53K	259383	7563427
4.4	2.4	35.1	53K	259383	7563427
2.5	1.6	21.7	53K	259383	7563427
2.1	1.8	21.8	53K	259383	7563427
2.9	2.2	27.7	53K	259383	7563427
4.7	3.0	39.3	53K	259383	7563427
2.2	2.3	28	53K	259383	7563427
1.6	2.2	21.8	53K	259383	7563427
3.5	2.5	33.8	53K	259383	7563427
4	2.4	32.6	53K	259383	7563427
4.5	2.4	33.1	53K	259383	7563427
1.6	2.4	21.2	53K	259383	7563427
3.9	2.4	27	53K	259383	7563427
2.8	1.8	25.2	53K	259383	7563427
4.8	2.3	31.7	53K	259383	7563427
1.4	1.8	25.3	53K	259383	7563427
5.2	2.8	32.8	53K	259383	7563427
4.8	3.1	35.9	53K	259383	7563427
2.5	2.5	26.1	53K	259383	7563427
2.9	1.8	24.4	53K	259383	7563427
5.5	3.4	39.3	53K	259383	7563427
4.7	2.8	37.3	53K	259383	7563427
3.7	2.3	29.8	53K	259383	7563427
5.3	2.5	43.4	53K	259383	7563427
1.8	1.1	21.3	53K	259383	7563427
4.1	2.1	28.4	53K	259383	7563427
3.8	2.0	27.3	53K	259383	7563427
5.4	2.6	36.6	53K	259383	7563427
4.4	2.4	35.4	53K	259383	7563427
6.2	3.0	43	53K	259383	7563427
3.2	2.0	21.8	53K	259383	7563427
5	2.8	34.4	53K	259383	7563427
2.8	2.0	28.7	53K	259383	7563427

Reynolds Range GRS Data

K (wt%)	U (ppm)	Th (ppm)	UTM Zone	Easting	Northing
4.35	1.8	17.22	53K	265475	7541650
1.76	1.7	6.41	53K	265450	7541640
4.89	1.8	19.05	53K	265446	7541637
4.67	1.9	16.56	53K	265435	7541623
5.85	2.2	19.86	53K	265431	7541601
5.92	2.0	20.97	53K	265414	7541589
4.73	1.2	19.37	53K	265395	7541557
5.27	1.0	18.23	53K	265368	7541551
5.32	1.6	18.04	53K	265368	7541528
6.01	1.7	19.05	53K	265307	7541408
6.41	1.6	20.89	53K	265282	7541371
5.98	1.4	19.26	53K	265278	7541366
5.55	1.3	17.94	53K	265265	7541351
5.77	1.8	18.32	53K	265256	7541339
5.79	1.5	18.53	53K	265249	7541314
5.9	1.9	17.9	53K	265243	7541315
6.1	1.6	18.75	53K	265237	7541293
6.07	1.5	19.83	53K	265244	7541283
6.69	1.9	22.46	53K	265244	7541277
4.89	1.7	16.19	53K	265226	7541256
5.17	1.5	17.61	53K	265218	7541242
5.25	1.8	18.61	53K	265219	7541227
6.33	2.3	21.87	53K	265197	7541223
6.32	1.6	21.03	53K	265184	7541221
6.09	1.6	18.42	53K	265186	7541203
5.92	1.8	18.08	53K	265173	7541191
5.64	1.6	18.64	53K	265155	7541162
5.85	1.7	19.74	53K	265144	7541157
5.37	1.8	18.5	53K	265130	7541138
5.73	1.9	20	53K	265117	7541124
5.98	1.8	20.01	53K	265097	7541119
6.18	1.8	18.59	53K	265087	7541103
5.93	1.6	18.05	53K	265068	7541092
6.07	1.7	21.43	53K	265057	7541080
6.3	1.9	20.98	53K	265047	7541056
6.65	1.6	22.15	53K	265047	7541048
5.78	1.6	18.78	53K	265012	7541033
4.74	1.6	14.26	53K	264997	7541011
5.91	1.6	18.8	53K	264985	7541005
4.79	1.7	14.14	53K	264979	7540987
4.94	1.3	16.79	53K	264961	7540974
5.15	1.8	18.38	53K	264944	7540962
5.17	1.9	19.5	53K	264925	7540949
4.61	1.9	15.82	53K	264912	7540924
7.02	2.3	26.21	53K	265030	7540867
3.7	1.8	14.48	53K	265068	7540888
5.76	2.1	22.47	53K	265080	7540900
6.03	2.1	20.58	53K	265091	7540922

6.84	2.1	22.51	53K	265121	7540947
6.64	1.8	21.3	53K	265158	7541014
6.42	2.1	21.38	53K	265154	7541091
5.3	3.7	31.4	53K	291256	7517509
6.9	4.0	33	53K	291256	7517509
6.7	4.2	33.4	53K	291256	7517509
4.5	3.3	28.8	53K	291256	7517509
5.3	3.9	33.5	53K	291256	7517509
5.5	3.9	32.8	53K	291256	7517509
5.8	5.3	31.8	53K	291256	7517509
6.5	4.1	35	53K	291256	7517509
5.2	3.4	28.4	53K	291256	7517509
4.9	3.8	23.9	53K	291256	7517509
5.4	3.4	29.1	53K	291256	7517509
4.8	3.3	23.4	53K	291256	7517509
4.4	2.4	24	53K	291256	7517509
4.9	2.3	24.4	53K	291256	7517509
4.5	2.7	24.2	53K	291256	7517509
5	2.8	23.1	53K	291256	7517509
4.7	2.4	25.2	53K	291256	7517509
4.4	2.4	25.4	53K	291256	7517509
3.9	2.8	25.3	53K	291251	7517592
5.1	2.2	27.5	53K	291251	7517592
5.4	2.4	25.5	53K	291251	7517592
4.8	2.5	24.1	53K	291251	7517592
4.5	2.6	20.9	53K	291251	7517592
6.5	3.8	27.5	53K	291251	7517592
5.1	4.3	23.5	53K	291251	7517592
6.9	5.7	32.6	53K	291251	7517592
5.8	4.9	36.6	53K	291251	7517592
6	7.6	32.6	53K	291251	7517592
6.7	6.8	32.5	53K	291251	7517592
5.1	4.7	28.3	53K	291251	7517592
6.5	6.6	30.7	53K	291248	7517648
5.8	4.9	30.5	53K	291248	7517648
4.3	3.0	35.9	53K	291248	7517648
8.1	3.4	31.8	53K	291248	7517648
6.3	2.5	23.8	53K	291248	7517648
6.6	2.7	26.9	53K	291248	7517648
4.7	2.5	23.6	53K	291248	7517648
4.7	2.5	26.6	53K	291248	7517648
5.1	3.3	22.7	53K	291248	7517648
5.7	2.5	26.5	53K	291248	7517648
4.3	2.8	24	53K	291248	7517648
5.6	2.7	23.3	53K	291248	7517648
5.8	2.6	24.8	53K	291248	7517648
4.6	2.5	22.1	53K	291247	7517709
4.7	3.0	24.8	53K	291247	7517709
4	3.1	22.7	53K	291247	7517709
5.5	3.9	31.4	53K	291247	7517709

6	4.3	32	53K	291247	7517709
7	6.6	42.2	53K	291247	7517709
6.8	5.4	36.2	53K	291247	7517709
5	4.9	30.4	53K	291247	7517709
3.8	4.1	25.7	53K	291247	7517709
5.8	4.8	31.9	53K	291247	7517709
5.7	4.2	34.4	53K	291247	7517709
5.7	3.6	31.4	53K	291247	7517709
3.7	2.5	24	53K	291247	7517709
5	2.4	24.5	53K	291245	7517795
5.4	2.3	27.5	53K	291245	7517795
5.1	2.8	28.3	53K	291245	7517795
6.6	3.0	24.2	53K	291245	7517795
4.8	3.2	26.5	53K	291245	7517795
5.8	2.6	30.1	53K	291245	7517795
3.9	1.9	25.4	53K	291245	7517795
5	2.6	29.2	53K	291245	7517795
5	2.5	26.4	53K	291245	7517795
4.5	2.2	22.7	53K	291245	7517795
5.2	3.0	26.8	53K	291245	7517795
5.9	2.5	26.8	53K	282331	7522567
4.2	1.7	23.1	53K	282331	7522567
5.1	2.4	20.3	53K	282331	7522567
5.8	2.5	25.1	53K	282331	7522567
3.4	2.2	20.2	53K	282331	7522567
3.5	2.2	22.2	53K	282331	7522567
4.6	2.3	23.9	53K	282331	7522567
4.8	2.1	25.3	53K	282331	7522567
5.3	2.4	23	53K	282331	7522567
3.6	2.3	17.2	53K	282331	7522567
4.3	2.4	19.9	53K	282331	7522567
5.2	2.1	26.9	53K	282331	7522567
4.3	2.3	23.9	53K	282331	7522567
4	2.2	17.6	53K	282331	7522567
4	2.3	23.7	53K	282331	7522567
4.7	2.4	23.6	53K	282331	7522567
4.4	2.1	22.6	53K	282331	7522567
4.6	2.2	21	53K	282331	7522567
5	2.0	19.5	53K	282331	7522567
3.6	1.8	20.3	53K	282331	7522567
4	2.3	21.9	53K	282331	7522567
3.3	2.4	19.3	53K	282331	7522567
4.3	1.7	22.8	53K	282331	7522567
4.6	2.4	19.9	53K	282331	7522567
4.3	1.9	21.4	53K	282371	7522592
4.4	1.9	23.4	53K	282371	7522592
4.6	2.3	19.2	53K	282371	7522592
5.1	2.6	20.9	53K	282371	7522592
4.4	2.1	19.3	53K	282371	7522592
4.9	2.6	20.7	53K	282371	7522592

5.5	2.7	24.7	53K	282371	7522592
5	2.3	23.8	53K	282371	7522592
5.1	2.2	23.5	53K	282371	7522592
4.5	2.4	18.7	53K	282371	7522592
4.8	2.3	25.4	53K	282371	7522592
4.4	2.4	23	53K	282371	7522592
5.1	2.3	25.3	53K	282371	7522592
3.2	1.8	20.2	53K	282371	7522592
3.6	2.2	19.2	53K	282371	7522592
3.7	1.8	20	53K	282371	7522592
4.2	2.9	21.1	53K	282371	7522592
6	2.6	27.4	53K	282371	7522592
4.5	2.2	20.3	53K	282371	7522592
4.2	1.8	21.2	53K	282371	7522592
5.3	2.0	24.8	53K	282371	7522592
4.3	2.3	23.9	53K	282371	7522592
4.1	1.6	24.3	53K	282371	7522592
4.3	2.2	23.3	53K	282371	7522592
4.3	1.8	22.1	53K	282371	7522592
2.9	1.8	18.7	53K	282371	7522592
4.3	2.2	24.8	53K	282371	7522592
3.1	1.6	15.7	53K	282371	7522592
3.7	1.3	20.5	53K	282371	7522592
3.6	2.0	18.5	53K	282371	7522592
5.3	1.9	23.4	53K	282371	7522592
5.2	2.0	22.4	53K	282371	7522592
3.4	1.9	17.1	53K	277437	7528253
3.6	1.8	14	53K	277437	7528253
3.2	2.1	15.4	53K	277437	7528253
3.5	1.5	14.3	53K	277437	7528253
3.9	1.6	16.9	53K	277437	7528253
3.8	1.6	17.3	53K	277437	7528253
4.1	2.4	14.5	53K	277437	7528253
2.8	2.1	16.5	53K	277437	7528253
3.9	1.9	18.6	53K	277437	7528253
2.9	2.4	16.3	53K	277437	7528253
2.9	2.3	18.5	53K	277437	7528253
3.7	2.2	14.9	53K	277437	7528253
3.4	1.8	17	53K	277437	7528253
2.1	1.6	16.1	53K	277437	7528253
5.4	2.5	20.1	53K	277437	7528253
4.2	2.4	19.2	53K	277437	7528253
2.4	1.3	13.7	53K	277437	7528253
1.2	1.6	14.3	53K	277509	7528305
3	1.2	14.3	53K	277509	7528305
4.7	2.9	25.1	53K	277509	7528305
4.7	2.0	20.9	53K	277509	7528305
4.7	2.6	22.6	53K	277509	7528305
5.5	2.3	24.5	53K	277509	7528305
3.1	1.9	18.5	53K	277509	7528305

3.5	1.8	19.3	53K	277509	7528305
3.2	2.0	18.6	53K	277509	7528305
3.3	2.4	23.3	53K	277509	7528305
3.6	3.0	20.5	53K	277509	7528305
3.1	2.8	18.8	53K	277509	7528305
3.5	1.9	17.1	53K	277509	7528305
2.2	1.7	12.2	53K	277509	7528305
5.3	2.3	23.5	53K	277509	7528305
5.6	2.2	23.7	53K	277509	7528305
4.1	2.8	19.6	53K	277509	7528305
4.9	3.0	19.2	53K	277509	7528305
4.2	3.0	19.7	53K	277509	7528305
4.1	2.5	20.9	53K	277509	7528305
4.9	2.4	21.2	53K	277509	7528305
3.9	2.8	20.1	53K	277509	7528305
3.5	2.3	19	53K	277509	7528305
3.8	2.1	15.1	53K	277509	7528305
4.5	2.4	16.9	53K	277509	7528305
3.9	2.2	17.9	53K	277509	7528305
3.5	2.1	14.1	53K	277509	7528305
3.2	1.7	17.5	53K	277509	7528305
4.1	1.4	16.7	53K	277509	7528305
3.7	1.4	17.3	53K	277509	7528305
4.5	2.2	17.3	53K	277509	7528305
2.9	1.8	14.8	53K	277509	7528305
5	3.1	20.6	53K	277509	7528305
4.1	3.6	20.7	53K	277509	7528305
2.2	2.2	17.3	53K	277509	7528305
3.6	2.1	15.7	53K	277509	7528305
4.1	2.8	18.3	53K	277509	7528305
7.1	1.9	23.6	53K	277509	7528305
4.8	1.7	17.3	53K	277509	7528305
7	2.2	23.6	53K	277509	7528305
4.9	1.9	17.2	53K	277509	7528305
4	2.0	20.2	53K	277509	7528305
3.8	1.6	16.8	53K	277509	7528305
4.1	1.7	16.6	53K	277672	7528335
3.8	2.1	19.1	53K	277672	7528335
5.7	2.0	21.5	53K	277672	7528335
7.3	3.0	27.2	53K	277672	7528335
7	2.9	25.8	53K	277672	7528335
7.2	3.6	28.2	53K	277672	7528335
4.1	2.4	21.8	53K	277672	7528335
3.3	2.1	20.2	53K	277672	7528335
4	2.3	21	53K	277672	7528335
3.5	3.3	18.8	53K	277672	7528335
4.4	3.6	22.3	53K	277672	7528335
4.9	2.7	20.3	53K	277672	7528335
3.6	3.0	20.7	53K	277672	7528335
3.8	2.0	18.3	53K	277672	7528335

3.4	2.3	20.2	53K	277672	7528335
6.7	2.9	25.1	53K	277740	7528392
6.1	3.2	23.2	53K	277740	7528392
5.2	2.6	22.1	53K	277740	7528392
5.1	2.4	21.4	53K	277740	7528392
5.2	2.5	22.7	53K	277740	7528392
5	2.7	20.5	53K	277740	7528392
5.5	3.0	25.5	53K	277740	7528392
5.2	3.3	24.7	53K	277740	7528392
5.5	3.1	22.7	53K	277740	7528392
3.6	2.3	18.7	53K	277740	7528392
4.7	1.9	21.6	53K	277740	7528392
3.2	2.1	15.7	53K	277740	7528392
2.7	1.8	16.1	53K	277740	7528392
3.4	1.7	15.9	53K	277740	7528392
4	1.6	17.8	53K	277740	7528392
4.3	2.4	18.2	53K	277740	7528392
2.5	2.2	15.1	53K	277740	7528392
3.6	1.9	19.8	53K	277740	7528392
3.4	2.3	18.2	53K	277740	7528392
3.3	2.0	18	53K	277740	7528392
3	2.4	17.4	53K	277740	7528392
4	2.3	19.4	53K	277740	7528392
2.9	2.5	23.6	53K	277740	7528392
4.4	1.8	19.7	53K	277740	7528392
4.4	2.0	20.1	53K	277740	7528392
3.6	1.6	17.5	53K	277740	7528392
2	1.9	14.4	53K	277810	7528464
3.5	1.4	20.6	53K	277810	7528464
5	2.6	24.7	53K	277810	7528464
5.6	2.6	23.7	53K	277810	7528464
5.1	2.0	23.6	53K	277810	7528464
6.4	2.7	28.2	53K	277810	7528464
3	2.5	22.4	53K	277810	7528464
3.5	2.0	21.5	53K	277810	7528464
2.9	2.1	19.3	53K	277810	7528464
2.7	2.0	20.4	53K	277810	7528464
2.5	3.0	19.8	53K	277810	7528464
2.3	1.8	19.5	53K	277810	7528464
4.4	3.2	22.7	53K	277850	7528523
3.6	2.5	22.3	53K	277850	7528523
6	3.0	23.9	53K	277850	7528523
5	2.4	21.3	53K	277850	7528523
4.7	1.9	23.9	53K	277850	7528523
4.4	1.9	20.9	53K	277850	7528523
4.2	3.0	21.8	53K	277850	7528523
5.3	2.6	25.1	53K	277850	7528523
5.2	2.5	23.8	53K	277850	7528523
4	2.5	24	53K	277850	7528523
3.4	2.3	24.9	53K	277850	7528523

5.24	1.3	29.93	53K	304528	7508062
5.86	1.3	30.96	53K	304533	7508073
6.34	1.6	34.69	53K	304543	7508077
3	1.1	20.29	53K	304547	7508096
4.94	1.1	27.11	53K	304556	7508140
4.88	1.6	29.92	53K	304562	7508156
4.28	1.4	23.65	53K	304550	7508162
5.49	1.3	31.27	53K	304570	7508156
3.84	0.8	20.71	53K	304550	7508165
5.9	1.0	31.66	53K	304560	7508177
5.3	1.3	30.4	53K	304567	7508177
6.75	1.1	34.42	53K	304566	7508178
5.06	1.3	28.11	53K	304571	7508189
5.15	1.7	36.82	53K	304572	7508191
5.92	1.4	31.95	53K	304575	7508199
6.47	1.4	30.99	53K	304575	7508197
4.28	1.4	30.98	53K	304572	7508201
4.33	1.0	26.82	53K	304581	7508202
5.53	1.1	28.12	53K	304578	7508210
3.83	1.0	22.86	53K	304575	7508215
3.48	1.1	22.81	53K	304586	7508218
4.94	1.2	28.51	53K	304536	7508220
5.1	1.2	25.87	53K	304592	7508236
4.56	1.2	30.59	53K	304603	7508246
4.58	1.5	27.4	53K	304600	7508256
5.13	1.1	24.9	53K	304602	7508276
5.04	1.2	25.91	53K	304600	7508270
4.44	1.3	20.29	53K	303693	7507963
7.08	1.3	27.73	53K	303894	7508170
6.63	1.1	30.2	53K	303900	7508208
5.46	1.4	28.18	53K	303902	7508213
3.78	1.2	23.4	53K	303933	7508575
4.98	1.6	28.89	53K	303935	7508582
5.16	1.7	29.42	53K	303950	7508608
4.97	1.2	25.83	53K	303975	7508621
5.79	1.3	28.98	53K	303935	7508628
4.04	1.4	28.1	53K	304011	7508644
4.57	1.4	27.46	53K	304014	7508652
5.2	1.5	30	53K	304031	7508650
4.56	2.2	42.65	53K	304039	7508656
4.75	1.3	30.88	53K	304045	7508666
4.93	1.5	26.46	53K	304060	7508679
4.66	1.7	30.17	53K	304073	7508682
3.76	1.5	25.8	53K	304084	7508688
4.9	2.2	24.1	53K	279626	7525845
3.8	2.1	21.3	53K	279626	7525845
4.1	1.8	21.6	53K	279626	7525845
4.4	1.9	18.1	53K	279626	7525845
5.2	2.3	22.6	53K	279626	7525845
4.6	1.9	20.8	53K	279626	7525845

4.1	1.8	22.3	53K	279626	7525845
4.6	1.8	22.7	53K	279626	7525845
3.2	1.7	20.5	53K	279626	7525845
2.8	1.2	18.3	53K	279626	7525845
5	1.8	28.3	53K	284769	7522022
4.5	1.6	22.3	53K	284769	7522022
5.1	1.8	30.2	53K	284769	7522022
4.4	1.5	23.5	53K	284769	7522022
4.4	2.5	23.5	53K	284769	7522022
2.3	1.6	18.8	53K	284769	7522022
2.1	1.1	14.5	53K	284769	7522022
4.8	1.6	21.6	53K	284769	7522022
3.9	1.5	24.6	53K	284769	7522022
4.8	1.8	23.3	53K	284769	7522022
4.8	2.3	22.2	53K	284769	7522022
5	1.6	20.3	53K	284769	7522022
4.2	1.9	19.3	53K	284769	7522022
5.9	2.2	24.7	53K	284769	7522022
4	1.9	22	53K	284769	7522022
3.2	1.6	22.3	53K	284769	7522022
3.1	1.6	17.4	53K	284769	7522022
4.7	1.8	24	53K	284769	7522022
4.2	1.6	22.5	53K	288687	7519263
4.4	1.6	21.7	53K	288687	7519263
3.9	1.8	22.2	53K	288687	7519263
3.3	1.6	20.7	53K	288687	7519263
5.4	1.7	22.7	53K	288687	7519263
4.6	1.4	20	53K	288687	7519263
5.7	2.0	15.7	53K	288687	7519263
5.3	2.2	19.8	53K	288687	7519263
4.6	1.8	18.9	53K	288687	7519263
6.2	2.2	20.2	53K	288687	7519263
4.1	1.9	23	53K	288687	7519263
4.3	1.9	21.4	53K	288687	7519263
3.7	1.4	25.8	53K	288687	7519263
3.7	0.9	22	53K	288687	7519263
3.4	1.9	19	53K	288687	7519263
4.2	1.8	20.5	53K	288687	7519263
3.6	2.1	23.3	53K	295396	7515652
4.1	1.5	23.8	53K	295396	7515652
3.4	1.7	22.9	53K	295396	7515652
5.1	2.0	24.9	53K	295396	7515652
5	1.8	24.5	53K	295396	7515652
4.1	1.7	20.8	53K	295396	7515652
3	1.7	18.9	53K	295396	7515652
4.5	2.0	19.3	53K	295396	7515652
3.6	1.8	20.2	53K	295396	7515652
3.6	1.7	23.1	53K	295396	7515652
5.2	1.9	26.2	53K	295396	7515652
2.9	1.6	19.1	53K	295396	7515652

3.6	1.7	19.2	53K	295396	7515652
4.7	1.6	26.9	53K	295396	7515652
5.2	1.4	24.8	53K	295396	7515652
3.8	1.8	23.4	53K	300758	7512715
4.1	1.4	24.2	53K	300758	7512715
3.8	1.2	23.9	53K	300758	7512715
2.1	1.1	20.9	53K	300758	7512715
3.9	1.3	23.3	53K	300758	7512715
3.6	1.3	22.5	53K	300758	7512715
3.2	2.0	23.1	53K	300758	7512715
4	1.8	24.7	53K	300758	7512715
5.1	2.1	19.5	53K	300758	7512715
4	1.6	19.4	53K	300758	7512715
4.2	1.7	21.4	53K	300758	7512715
2.2	1.2	17.4	53K	300758	7512715
3.9	1.0	22.9	53K	305217	7508546
3.2	1.9	21.4	53K	305217	7508546
3.1	1.5	22.5	53K	305217	7508546
3.3	1.5	24.4	53K	305217	7508546
3.6	1.3	20.2	53K	305217	7508546
3.6	1.2	26.8	53K	305217	7508546
3.6	1.5	23.3	53K	305217	7508546
3.7	2.0	26.7	53K	305217	7508546
3.4	1.6	24.1	53K	305217	7508546

Sierra De Quilmes GRS Data

K (wt%)	U (ppm)	Th (ppm)	UTM Zone	Easting	Northing
3	1.5	16.1	20J	200717	7097754
3.2	1.7	16.8	20J	200717	7097754
4.2	2.1	23.1	20J	200717	7097754
3.9	1.9	17.6	20J	200717	7097754
2.9	1.8	15.4	20J	200717	7097754
3.1	1.5	17.2	20J	200717	7097754
3.8	1.8	21.8	20J	200717	7097754
4.3	2.2	19.9	20J	200717	7097754
3.2	1.7	19.1	20J	200717	7097754
2.9	1.5	16.1	20J	200717	7097754
3.1	1.8	20	20J	200717	7097754
3.1	1.5	14	20J	200717	7097754
4.1	2.0	17.7	20J	200717	7097754
4.3	2.1	24	20J	200717	7097754
3.6	1.3	21.8	20J	200717	7097754
3.3	1.6	15.8	20J	200717	7097754
3.6	1.8	16.3	20J	200717	7097754
3.4	1.7	15.5	20J	200717	7097754
3.6	1.9	18.1	20J	200717	7097754
3.5	2.1	18.9	20J	201457	7097766
2.7	1.7	16.3	20J	201457	7097766
2.6	1.4	15.6	20J	201457	7097766
2.9	1.7	15.2	20J	201457	7097766
2.8	2.0	20.2	20J	201457	7097766
2.9	1.1	17	20J	201457	7097766
3.8	1.7	24.2	20J	201457	7097766
3.4	2.6	20.2	20J	201457	7097766
3.6	1.3	21.5	20J	201457	7097766
4.1	2.1	28.6	20J	201457	7097766
3.7	2.8	22.6	20J	201457	7097766
4.9	1.3	29.6	20J	201457	7097766
4.7	2.3	26.7	20J	201457	7097766
3.7	2.6	26.8	20J	201457	7097766
3.5	2.3	20.9	20J	201457	7097766
4.7	2.1	27.4	20J	201457	7097766
3	2.4	19.6	20J	201457	7097766
5.6	2.9	26.1	20J	201457	7097766
2.6	2.2	14.3	20J	201717	7105930
3.1	2.5	21	20J	201717	7105930
4.1	3.2	18.6	20J	201717	7105930
3.4	2.6	18.3	20J	201717	7105930
4.3	2.7	20.6	20J	201717	7105930
3.7	2.3	17.9	20J	201717	7105930
2.8	1.9	17.2	20J	201717	7105930
2.8	2.5	16.8	20J	201717	7105930
2.9	1.5	14	20J	201792	7106304
4.2	2.1	19.8	20J	201792	7106304
3	1.8	15.8	20J	201792	7106304

3.1	1.6	17	20J	201792	7106304
3.5	2.4	16	20J	201792	7106304
3.9	1.8	17.8	20J	201792	7106304
3.1	3.2	26.6	20J	201948	7106562
2.1	5.1	14.7	20J	201948	7106562
3.2	4.2	38.4	20J	201948	7106562
1.6	5.1	13.3	20J	201948	7106562
1.4	3.2	13.1	20J	201948	7106562
4.5	2.8	18.4	20J	201948	7106562
4.1	2.5	16.3	20J	201948	7106562
3.9	2.4	15.6	20J	201948	7106562
3.1	2.3	14.1	20J	201948	7106562
2.5	3.3	26.8	20J	201948	7106562
2.5	2.4	16.6	20J	201948	7106562
2.8	2.0	17.9	20J	201948	7106562
2.9	2.3	15.4	20J	201948	7106562
1.5	1.3	7.8	20J	204059	7105244
2.9	2.0	14	20J	204059	7105244
0.9	1.2	8	20J	204059	7105244
2.5	2.3	14.6	20J	204059	7105244
2.3	1.8	12.2	20J	204059	7105244
2.1	1.5	10.6	20J	204059	7105244
2.5	1.8	15	20J	204059	7105244
3	2.1	15.4	20J	204059	7105244
2.5	2.0	13.9	20J	204059	7105244
2.3	2.0	11.9	20J	204059	7105244
3	2.2	13.6	20J	204883	7096382
3.5	2.2	15.3	20J	204883	7096382
3.2	1.9	15.9	20J	204883	7096382
3.5	2.0	19.4	20J	204883	7096382
3.1	2.0	16.7	20J	204883	7096382
3.2	2.2	14.8	20J	204883	7096382
3.9	2.3	13.4	20J	204883	7096382
2.6	2.4	12.8	20J	204883	7096382
1.9	2.0	12.3	20J	204883	7096382
3.3	2.2	14.1	20J	204883	7096382
1.7	2.3	14.4	20J	204883	7096382
3.6	1.9	15.7	20J	204883	7096382
3.5	2.4	18.4	20J	204883	7096382
2.9	2.2	14.4	20J	204883	7096382
3.3	2.4	16.8	20J	204883	7096382
4.1	2.1	19.6	19J	796077	7120675
4.7	2.5	22.7	19J	796077	7120675
4.4	2.3	25.2	19J	796077	7120675
3.5	2.0	22.6	19J	796077	7120675
4.7	2.1	23.4	19J	796077	7120675
4.7	2.6	22.7	19J	796077	7120675
5	3.0	23.3	19J	796077	7120675
5.7	2.4	25.1	19J	796077	7120675
5.7	2.4	25.1	19J	796077	7120675

3.1	2.5	18.1	19J	796351	7108014
3.4	2.2	17.3	19J	796351	7108014
3.4	1.9	20.5	19J	796351	7108014
2.6	1.6	14.1	19J	796351	7108014
3.1	2.2	17.3	19J	796351	7108014
2.9	1.5	15.2	19J	796351	7108014
3.2	2.2	19.6	19J	796351	7108014
2.8	2.0	15.6	19J	796351	7108014
3.4	2.3	18.3	19J	796351	7108014
2.1	1.7	12.9	19J	796351	7108014
4.7	2.0	19.5	19J	796781	7135574
4.9	2.3	19.5	19J	796781	7135574
4.2	2.4	17.5	19J	796781	7135574
5	2.1	19.6	19J	796781	7135574
5.3	2.6	23.3	19J	796781	7135574
4.9	1.6	19.1	19J	796781	7135574
3.9	1.6	15.7	19J	796781	7135574
4.4	2.2	19.9	19J	796781	7135574
3.4	2.1	19.9	19J	796883	7108420
3.1	2.0	18.8	19J	796883	7108420
3.3	2.5	18.2	19J	796883	7108420
3.4	2.6	18.9	19J	796883	7108420
3.4	2.0	18.4	19J	796883	7108420
3.2	2.2	17.4	19J	796883	7108420
3.1	2.2	17.2	19J	796883	7108420
3.7	2.2	17.9	19J	796883	7108420
3	2.0	15.1	19J	796883	7108420
3.3	1.8	19	19J	796883	7108420
4.4	1.2	17.3	19J	796959	7086394
2.8	1.3	9.7	19J	796959	7086394
3.7	1.5	44.4	19J	796959	7086394
4.2	1.4	33.4	19J	796959	7086394
3.8	1.7	18	19J	796959	7086394
2.1	1.9	29.8	19J	796959	7086394
3.8	1.5	20.9	19J	796959	7086394
4.1	2.4	31.1	19J	796959	7086394
3.7	1.2	17.5	19J	796959	7086394
4.2	1.0	40.6	19J	796959	7086394
4	0.6	27.3	19J	796997	7087473
3.4	1.4	26.9	19J	796997	7087473
3.8	1.2	24.4	19J	796997	7087473
3.1	1.2	29	19J	796997	7087473
3.5	1.5	24.5	19J	796997	7087473
3.9	1.3	22.2	19J	796997	7087473
3.6	1.4	21.1	19J	796997	7087473
3.2	1.0	16.6	19J	796997	7087473
3.7	1.5	25.7	19J	796997	7087473
3.7	0.7	18.5	19J	796997	7087473
3.8	1.3	33.1	19J	796997	7087473
4	1.2	24.6	19J	796997	7087473

3.4	2.3	27.7	19J	796997	7087473
4.3	2.1	27.5	19J	796997	7087473
2.9	1.8	28.7	19J	796997	7087473
3.5	1.0	20.7	19J	796997	7087473
3.8	1.3	30.2	19J	797044	7087739
3.3	1.7	33.5	19J	797044	7087739
4.6	1.0	26	19J	797044	7087739
4.3	1.5	20	19J	797044	7087739
3.4	1.5	26.9	19J	797044	7087739
3.7	1.7	22.5	19J	797044	7087739
4.2	1.6	23.8	19J	797044	7087739
3	1.1	26.1	19J	797044	7087739
2.9	1.1	27	19J	797044	7087739
3.2	0.9	20.5	19J	797044	7087739
2.4	1.2	16.8	19J	797044	7087739
3.4	1.4	28.3	19J	797044	7087739
2.4	1.5	19.7	19J	797118	7087870
3.3	1.6	21.9	19J	797118	7087870
2.7	1.1	18.9	19J	797118	7087870
2.4	1.5	20.8	19J	797118	7087870
1.8	1.2	18.2	19J	797118	7087870
3.5	1.6	24.5	19J	797118	7087870
2	1.6	18	19J	797118	7087870
2.1	1.3	20.1	19J	797118	7087870
2.2	0.8	16.2	19J	797118	7087870
2.6	1.1	17.7	19J	797118	7087870
2.8	1.3	19.8	19J	797415	7085799
2.6	1.5	20.1	19J	797415	7085799
3.9	1.2	24.5	19J	797415	7085799
2.1	1.0	19.6	19J	797415	7085799
2.9	1.2	20.5	19J	797415	7085799
2.8	1.1	21.1	19J	797415	7085799
3.3	1.6	21.7	19J	797415	7085799
2.7	2.1	13.4	19J	797518	7122686
3.5	1.9	17.4	19J	797518	7122686
2.8	2.0	18.2	19J	797518	7122686
4	1.9	18.3	19J	797518	7122686
3.6	2.2	16.8	19J	797518	7122686
3	1.8	16.4	19J	797518	7122686
3.4	2.2	15.8	19J	797518	7122686
3	1.7	14.3	19J	797518	7122686
3.4	1.4	16.2	19J	797622	7122756
4.1	1.7	18.3	19J	797622	7122756
3.4	2.2	16.4	19J	797622	7122756
3.2	1.9	14	19J	797622	7122756
2.7	1.2	14.6	19J	797622	7122756
2.7	1.7	11.3	19J	797622	7122756
2.7	1.6	14.1	19J	797622	7122756
1.5	0.9	9.6	19J	797861	7122846
3	1.6	12.8	19J	797861	7122846

1.3	1.0	8.8	19J	797861	7122846
2.8	1.5	12.1	19J	797861	7122846
3.9	1.9	17.2	19J	797861	7122846
3	1.6	13.8	19J	797861	7122846
3	1.3	15.2	19J	798002	7122989
4	1.7	18.1	19J	798002	7122989
3.3	1.4	15.7	19J	798002	7122989
4	2.0	17.5	19J	798002	7122989
4.5	1.7	20.7	19J	798002	7122989
3.9	1.8	18.1	19J	798002	7122989
3.1	1.7	14.3	19J	798002	7122989
4	1.9	18.1	19J	798002	7122989
2.3	1.6	14.5	19J	798434	7123338
2.4	1.5	15.2	19J	798434	7123338
2.6	2.0	15.4	19J	798434	7123338
2.5	1.2	16.1	19J	798434	7123338
2.8	1.7	15.2	19J	798434	7123338
2.6	2.0	14.9	19J	798434	7123338
5.1	1.8	21.6	19J	798565	7123522
3.9	1.4	18.6	19J	798565	7123522
3.4	1.6	19.2	19J	798565	7123522
3.5	1.6	17.6	19J	798565	7123522
4.4	2.3	21.4	19J	798565	7123522
3.8	1.9	15.8	19J	798565	7123522
2.2	1.1	19.1	19J	798565	7123522
3.1	1.7	17.8	19J	798565	7123522

Appendix 3

Supplementary material for: Thermal modelling of very long-lived (>140 Myr) high thermal gradient metamorphism as a result of radiogenic heating in the Reynolds Range, central Australia

Appendix 3A: Microprobe analyses
Greenschist-facies

RR2014-5

Mineral	bi	bi	bi	bi	bi	bi	bi	bi	bi	bi
SiO2	36.37	34.24	35.83	36.96	34.04	33.87	52.51	43.60	45.11	44.55
TiO2	1.51	1.59	1.85	1.29	1.56	1.88	0.35	0.41	0.43	0.40
Al2O3	21.10	16.33	16.84	22.53	17.35	16.51	26.72	32.67	33.11	34.65
Cr2O3	0.02	0.01	0.02	0.02	0.01	0.03	0.02	0.02	0.02	0.02
FeO	16.06	20.23	19.95	14.94	21.44	21.49	3.09	4.18	4.02	2.78
MnO	0.03	0.00	0.01	0.00	0.04	0.03	0.00	0.00	0.00	0.00
MgO	6.33	9.25	7.97	5.41	9.57	8.89	0.99	1.08	1.19	0.76
ZnO	0.04	0.00	0.04	0.00	0.00	0.04	0.00	0.00	0.02	0.02
CaO	0.07	0.10	0.03	0.05	0.07	0.05	0.03	0.03	0.03	0.04
Na2O	0.13	0.08	0.06	0.11	0.04	0.05	0.27	0.34	0.33	0.45
K2O	9.55	8.22	8.91	9.49	8.29	9.22	9.20	10.34	10.48	10.41
Cl	0.05	0.05	0.04	0.04	0.04	0.03	0.01	0.03	0.01	0.01
F	0.33	0.44	0.46	0.31	0.40	0.39	0.03	0.00	0.05	0.00
H2O	3.70	3.50	3.57	3.74	3.60	3.56	4.43	4.29	4.38	4.40

Mineral	bi	bi	bi	bi	bi	bi	**Ave**
SiO2	45.43	51.56	44.89	47.11	45.38	45.06	**42.28**
TiO2	0.41	0.41	0.39	0.40	0.47	0.40	**0.86**
Al2O3	32.76	28.61	34.30	30.49	33.17	32.94	**26.88**
Cr2O3	0.00	0.01	0.00	0.00	0.00	0.00	**0.01**
FeO	3.26	3.65	3.03	4.38	3.81	4.56	**9.43**
MnO	0.00	0.01	0.00	0.01	0.00	0.00	**0.01**
MgO	1.29	1.37	0.80	1.24	1.28	1.27	**3.67**
ZnO	0.00	0.00	0.00	0.00	0.00	0.00	**0.01**
CaO	0.02	0.01	0.01	0.02	0.01	0.03	**0.04**
Na2O	0.29	0.29	0.39	0.29	0.33	0.34	**0.24**
K2O	10.55	9.58	10.62	9.93	10.42	10.58	**9.74**
Cl	0.02	0.02	0.01	0.03	0.02	0.04	**0.03**
F	0.03	0.00	0.00	0.17	0.01	0.09	**0.17**
H2O	4.37	4.52	4.41	4.30	4.41	4.36	**4.10**

Mineral	ru	ru	ru	ru	ru	ru	ru	ru	ru	ru	**Ave**
SiO2	0.65	1.96	0.60	62.83	84.21	10.20	36.21	61.16	16.66	**30.50**
TiO2	67.42	64.66	66.60	28.55	5.34	49.72	0.05	26.20	53.28	**40.20**
Al2O3	1.35	4.28	1.24	1.57	2.73	7.93	7.32	1.13	7.09	**3.85**
Cr2O3	0.00	0.02	0.01	0.00	0.00	0.00	0.00	0.00	0.03	**0.01**
FeO	19.75	18.61	20.67	4.09	2.28	18.42	1.14	7.73	9.74	**11.38**
MnO	0.53	0.44	0.55	0.05	0.00	0.36	0.00	0.21	0.13	**0.25**
MgO	0.05	0.08	0.06	0.05	0.09	0.52	0.19	0.12	0.59	**0.19**
ZnO	0.22	0.27	0.21	0.00	0.02	0.15	0.00	0.06	0.04	**0.11**
CaO	0.08	0.07	0.08	0.05	0.06	0.13	0.06	0.07	0.12	**0.08**
Na2O	0.10	0.11	0.08	0.03	0.04	0.12	0.00	0.06	0.11	**0.07**
K2O	0.13	0.44	0.12	0.62	1.00	2.46	2.77	0.41	2.53	**1.16**
Cl	0.03	0.02	0.03	0.00	0.01	0.03	0.01	0.02	0.03	**0.02**
F	0.00	0.00	0.00	0.00	0.00	0.08	0.00	0.00	0.05	**0.01**
H2O	0.00	0.00	0.00	0.00	0.00	0.00	0.00	0.00	0.00	**0.00**

Mineral	mu	mu	mu	mu	mu	mu	mu	**Ave**
SiO2	43.45	40.82	39.06	45.42	34.64	43.19	40.78	**41.05**
TiO2	0.37	6.47	1.10	0.32	1.88	0.36	0.74	**1.60**
Al2O3	33.90	18.35	23.94	30.93	16.16	33.91	28.08	**26.47**
Cr2O3	0.00	0.03	0.01	0.00	0.01	0.02	0.02	**0.01**
FeO	3.07	15.37	12.71	3.05	20.97	2.97	8.16	**9.47**
MnO	0.01	0.00	0.02	0.01	0.04	0.00	0.02	**0.01**
MgO	1.03	3.29	4.73	1.56	8.84	0.72	2.79	**3.28**
ZnO	0.00	0.02	0.05	0.00	0.01	0.00	0.00	**0.01**
CaO	0.01	0.07	0.03	0.01	0.03	0.04	0.04	**0.03**
Na2O	0.36	0.12	0.14	0.30	0.03	0.48	0.20	**0.23**
K2O	10.46	7.44	9.56	10.52	8.45	10.21	9.90	**9.51**
Cl	0.01	0.03	0.04	0.01	0.05	0.00	0.05	**0.03**
F	0.05	0.17	0.21	0.05	0.43	0.00	0.15	**0.15**
H2O	0.00	0.00	0.00	0.00	0.00	0.00	0.00	**0.00**

Amphibolite-facies

RR2015 3-13

Mineral	bi	bi	bi	bi	bi	bi	**Ave**
SiO2	33.39	33.19	33.46	37.65	33.33	33.38	**34.07**
TiO2	2.36	2.36	2.41	1.79	2.25	2.43	**2.27**
Al2O3	18.69	18.59	18.89	26.16	18.38	18.96	**19.94**
Cr2O3	0.02	0.02	0.03	0.00	0.02	0.00	**0.02**
FeO	19.72	18.16	19.93	14.36	19.71	19.08	**18.49**
MnO	0.09	0.03	0.04	0.05	0.07	0.08	**0.06**
MgO	8.11	8.21	8.38	4.56	7.48	8.22	**7.49**
ZnO	0.02	0.00	0.06	0.01	0.00	0.01	**0.02**
CaO	0.02	0.03	0.01	0.02	0.03	0.01	**0.02**
Na2O	0.15	0.16	0.15	0.18	0.14	0.15	**0.16**
K2O	9.30	9.12	9.46	8.77	9.11	9.35	**9.18**
Cl	0.00	0.03	0.00	0.02	0.01	0.00	**0.01**
F	0.31	0.37	0.34	0.15	0.32	0.35	**0.31**
H2O	3.63	3.55	3.65	3.99	3.57	3.62	**3.67**

Mineral	mu	mu	mu	mu	mu	mu	**Ave**
SiO2	42.32	43.57	47.66	43.42	77.36	44.14	**49.74**
TiO2	0.51	0.39	0.43	0.55	0.24	0.29	**0.40**
Al2O3	33.75	35.12	23.20	34.32	7.81	36.13	**28.39**
Cr2O3	0.00	0.01	0.00	0.00	0.00	0.00	**0.00**
FeO	3.03	2.62	2.32	2.95	1.44	1.94	**2.38**
MnO	0.00	0.00	0.00	0.00	0.00	0.00	**0.00**
MgO	0.52	0.47	0.35	0.60	0.10	0.33	**0.39**
ZnO	0.00	0.00	0.00	0.00	0.00	0.00	**0.00**
CaO	0.02	0.02	0.03	0.00	0.01	0.05	**0.02**
Na2O	0.29	0.28	0.29	0.37	0.17	0.22	**0.27**
K2O	9.12	8.35	6.84	9.90	2.64	5.41	**7.04**
Cl	0.03	0.03	0.13	0.00	0.04	0.07	**0.05**
F	0.00	0.00	0.00	0.00	0.00	0.00	**0.00**
H2O	4.20	4.31	3.90	4.32	4.68	4.30	**4.29**

Garnet granulite-facies

RR2014-12A

Mineral	bi	bi	
SiO2	33.23	33.43	**33.33**
TiO2	4.14	3.91	**4.02**
Al2O3	17.24	17.77	**17.50**
Cr2O3	0.14	0.10	**0.12**
FeO	22.76	22.56	**22.66**
MnO	0.01	0.03	**0.02**
MgO	6.56	6.61	**6.58**
ZnO	0.02	0.00	**0.01**
CaO	0.02	0.01	**0.01**
Na2O	0.11	0.12	**0.11**
K2O	9.40	9.51	**9.45**
Cl	0.04	0.05	**0.04**
F	0.25	0.29	**0.27**
H2O	3.65	3.66	**3.66**
Total	**97.55**	**98.05**	

Mineral	ksp	ksp	ksp	ksp	ksp	ksp	**Ave**
SiO2	61.73	60.64	60.53	62.55	62.84	62.96	**61.88**
TiO2	0.00	0.06	0.04	0.02	0.01	0.01	**0.02**
Al2O3	18.47	18.22	19.43	18.74	18.98	19.19	**18.84**
Cr2O3	0.00	0.00	0.00	0.00	0.02	0.00	**0.00**
FeO	0.09	0.27	0.00	0.10	0.04	0.01	**0.08**
MnO	0.00	0.00	0.00	0.00	0.01	0.01	**0.00**
MgO	0.01	0.02	0.00	0.02	0.00	0.01	**0.01**
ZnO	0.01	0.00	0.05	0.03	0.00	0.00	**0.01**
CaO	0.01	0.02	0.03	0.04	0.11	0.06	**0.04**
Na2O	0.66	0.86	0.77	0.97	1.10	0.96	**0.89**
K2O	15.83	15.28	15.26	15.34	14.84	15.38	**15.32**
Cl	0.00	0.00	0.01	0.01	0.01	0.01	**0.01**
F	0.00	0.00	0.02	0.00	0.00	0.00	**0.00**
H2O	0.00	0.00	0.00	0.00	0.00	0.00	**0.00**
Total	**96.81**	**95.36**	**96.16**	**97.81**	**97.95**	**98.60**	

Mineral	gt	gt	gt	gt	gt	**Ave**
SiO2	46.85	47.65	47.05	47.04	47.16	**47.15**
TiO2	0.03	0.00	0.01	0.04	0.00	**0.02**
Al2O3	33.35	33.23	32.81	32.82	32.98	**33.03**
Cr2O3	0.00	0.00	0.00	0.00	0.00	**0.00**
FeO	10.42	9.61	9.32	9.40	9.23	**9.60**
MnO	0.10	0.11	0.04	0.10	0.08	**0.08**
MgO	7.29	7.49	7.64	7.53	7.87	**7.57**
ZnO	0.00	0.01	0.03	0.00	0.00	**0.01**
CaO	0.00	0.00	0.01	0.01	0.00	**0.00**
Na2O	0.06	0.04	0.04	0.04	0.05	**0.05**
K2O	0.00	0.00	0.00	0.01	0.00	**0.00**
Cl	0.00	0.00	0.00	0.02	0.01	**0.01**
F	0.00	0.00	0.00	0.00	0.00	**0.00**
H2O	0.00	0.00	0.00	0.00	0.00	**0.00**
Total	**98.10**	**98.15**	**96.95**	**97.00**	**97.39**	

Mineral	ilm	ilm	ilm	ilm	**Ave**

Al2O3	9.26	51.99	15.42	23.31	**24.99**
Cr2O3	0.09	0.03	0.03	0.05	**0.05**
FeO	25.27	7.96	24.79	19.50	**19.38**
MnO	0.29	0.09	0.19	0.17	**0.18**
MgO	0.89	0.05	0.11	2.39	**0.86**
ZnO	0.02	0.00	0.00	0.00	**0.01**
CaO	0.04	0.01	0.03	0.14	**0.05**
Na2O	0.06	0.02	0.05	0.20	**0.08**
K2O	1.34	0.03	0.20	2.30	**0.97**
Cl	0.08	0.01	0.01	0.10	**0.05**
F	0.21	0.00	0.01	0.40	**0.15**
H2O	0.00	0.00	0.00	0.00	**0.00**
Total	**95.76**	**98.73**	**94.72**	**85.95**	

Mineral	cd	cd	cd	cd	cd	**Ave**
SiO2	49.33	48.51	48.71	49.32	49.53	**49.08**
TiO2	0.02	0.00	0.00	0.00	0.00	**0.00**
Al2O3	32.71	32.36	31.98	32.58	32.17	**32.36**
Cr2O3	0.00	0.00	0.01	0.00	0.01	**0.00**
FeO	9.60	10.04	10.24	10.32	10.34	**10.11**
MnO	0.07	0.04	0.03	0.07	0.06	**0.05**
MgO	7.07	7.17	6.99	6.63	7.01	**6.97**
ZnO	0.04	0.00	0.00	0.02	0.00	**0.01**
CaO	0.08	0.00	0.00	0.00	0.00	**0.02**
Na2O	0.09	0.04	0.04	0.07	0.05	**0.06**
K2O	0.06	0.00	0.01	0.02	0.01	**0.02**
Cl	0.01	0.00	0.00	0.00	0.00	**0.00**
F	0.00	0.00	0.00	0.00	0.00	**0.00**
H2O	0.00	0.00	0.00	0.00	0.00	**0.00**
Total	**99.07**	**98.16**	**98.01**	**99.03**	**99.17**	

Cordierite granulite-facies

RR2014-9

Mineral	ilm	ilm	ilm	ilm	ilm	ilm	ilm
SiO2	0.05	0.00	0.17	0.01	0.01	0.06	0.04
TiO2	47.09	46.48	46.59	46.09	47.14	32.59	28.50
Al2O3	0.07	0.02	0.47	0.06	0.07	0.17	0.14
Cr2O3	0.06	0.06	0.05	0.06	0.06	0.14	0.26
FeO	48.89	49.44	48.94	50.01	49.39	61.39	64.39
MnO	0.06	0.04	0.04	0.06	0.08	0.04	0.00
MgO	0.57	0.59	0.67	0.62	0.69	0.59	0.36
ZnO	0.03	0.00	0.00	0.00	0.00	0.00	0.00
CaO	0.02	0.00	0.02	0.02	0.03	0.02	0.04
Na2O	0.01	0.00	0.01	0.00	0.00	0.00	0.00
K2O	0.00	0.00	0.00	0.01	0.01	0.01	0.01
Cl	0.00	0.00	0.00	0.00	0.01	0.00	0.00
F	0.07	0.08	0.09	0.12	0.16	0.21	0.18
H2O	3.63	3.55	3.65	3.99	3.90	4.20	4.68
Total	**100.55**	**100.27**	**100.70**	**101.03**	**101.55**	**99.41**	**98.61**

Mineral	ilm	ilm	ilm	**Ave**
SiO2	0.00	0.03	0.02	**0.04**
TiO2	45.98	44.82	47.41	**43.27**
Al2O3	0.04	0.06	0.06	**0.12**
Cr2O3	0.09	0.06	0.06	**0.09**
FeO	50.36	51.05	48.84	**52.27**
MnO	0.03	0.04	0.03	**0.04**
MgO	0.48	0.45	0.49	**0.55**
ZnO	0.00	0.00	0.00	**0.00**
CaO	0.03	0.02	0.02	**0.02**
Na2O	0.00	0.00	0.00	**0.00**
K2O	0.00	0.00	0.00	**0.00**
Cl	0.01	0.00	0.00	**0.00**
F	0.11	0.15	0.10	**0.13**
H2O	4.30	0.00	0.00	**3.19**
Total	**101.43**	**96.68**	**97.02**	

Mineral	mt	mt	mt	mt	mt	**Ave**
SiO2	0.09	0.01	0.34	0.23	1.41	**0.42**
TiO2	1.15	0.71	8.60	0.44	17.51	**5.68**
Al2O3	0.38	0.26	0.57	0.63	7.45	**1.86**
Cr2O3	0.58	0.60	0.28	0.25	0.51	**0.44**
FeO	87.92	88.03	80.65	88.23	62.27	**81.42**
MnO	0.00	0.00	0.01	0.00	0.07	**0.02**
MgO	0.03	0.03	0.15	0.06	0.34	**0.12**
ZnO	0.00	0.00	0.00	0.00	0.00	**0.00**
CaO	0.02	0.01	0.03	0.04	0.21	**0.06**
Na2O	0.00	0.00	0.05	0.03	0.19	**0.05**
K2O	0.00	0.00	0.00	0.01	0.06	**0.02**
Cl	0.00	0.00	0.01	0.00	0.08	**0.02**
F	0.26	0.24	0.21	0.27	0.21	**0.24**
H2O	3.57	3.62	4.31	4.32	0.00	**3.16**
Total	**93.99**	**93.50**	**95.22**	**94.50**	**90.29**	

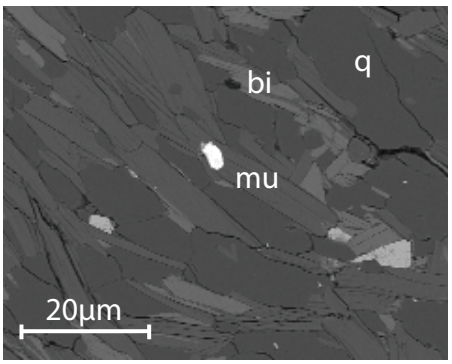
Mineral	bi	bi	bi	bi	bi	bi	bi	bi
SiO2	35.35	37.60	35.60	35.51	35.89	35.77	35.92	44.20
TiO2	3.11	3.26	3.37	3.39	3.43	3.33	2.56	2.06
Al2O3	17.68	19.21	17.65	17.46	17.06	17.19	16.13	14.03
Cr2O3	0.06	0.08	0.08	0.05	0.11	0.07	0.05	0.05
FeO	14.63	15.25	15.44	15.58	15.75	15.82	14.73	10.90
MnO	0.01	0.01	0.01	0.00	0.00	0.01	0.00	0.00
MgO	12.00	13.07	11.97	11.80	12.28	12.22	14.96	12.93
ZnO	0.01	0.03	0.00	0.01	0.00	0.01	0.01	0.00
CaO	0.13	0.03	0.03	0.03	0.01	0.00	0.01	0.04
Na2O	0.05	0.01	0.03	0.02	0.01	0.01	0.02	0.03
K2O	9.85	9.90	10.09	10.01	9.95	10.10	10.13	8.64
Cl	0.02	0.01	0.01	0.00	0.01	0.01	0.01	0.01
F	0.38	0.31	0.52	0.45	0.43	0.43	0.70	0.69
H2O	0.00	0.00	0.00	3.65	3.66	0.00	0.00	0.00
Total	**93.27**	**98.78**	**94.81**	**97.97**	**98.60**	**94.99**	**95.23**	**93.57**

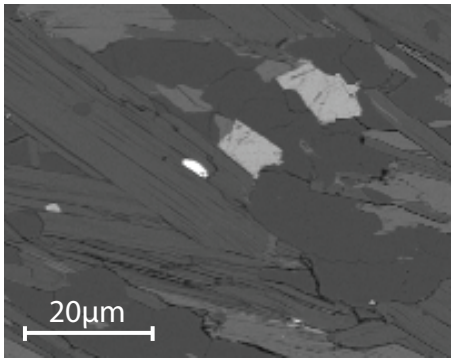
Mineral	bi	bi	bi	bi	bi	bi	bi	**Ave**

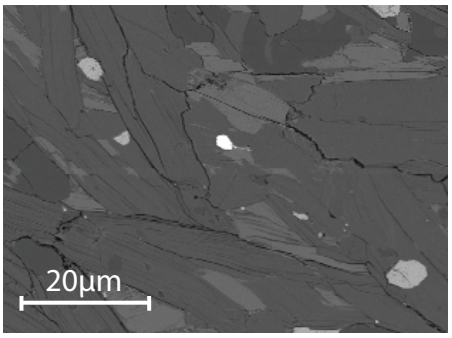
TiO2	2.38	2.75	2.42	1.21	2.07	2.30	2.36	**2.67**
Al2O3	17.75	17.25	17.78	19.94	18.04	17.78	17.16	**17.47**
Cr2O3	0.06	0.05	0.03	0.00	0.01	0.04	0.03	**0.05**
FeO	11.70	12.06	10.64	12.60	11.76	12.07	12.37	**13.42**
MnO	0.01	0.00	0.01	0.01	0.01	0.00	0.02	**0.01**
MgO	16.12	16.15	16.90	15.54	16.06	15.81	16.36	**14.28**
ZnO	0.02	0.02	0.01	0.00	0.00	0.01	0.00	**0.01**
CaO	0.00	0.05	0.02	0.02	0.03	0.06	0.02	**0.03**
Na2O	0.03	0.05	0.04	0.04	0.03	0.06	0.06	**0.03**
K2O	10.12	9.89	10.23	10.15	9.84	9.74	10.06	**9.91**
Cl	0.01	0.01	0.00	0.00	0.01	0.01	0.01	**0.01**
F	0.67	0.68	0.73	0.57	0.68	0.70	0.80	**0.58**
H2O	0.00	0.00	0.00	0.00	0.00	0.00	0.00	**0.49**
Total	95.46	95.30	95.58	94.87	95.09	95.07	95.84	
Mineral	cd	cd	cd	cd	cd	cd	cd	**Ave**
SiO2	48.41	47.90	43.89	48.32	44.49	48.49	48.44	**47.14**
TiO2	0.00	0.00	0.02	0.00	0.03	0.01	0.00	**0.01**
Al2O3	33.10	34.64	39.43	33.44	33.96	33.39	33.43	**34.48**
Cr2O3	0.00	0.00	0.01	0.00	0.00	0.00	0.00	**0.00**
FeO	6.10	5.97	9.73	6.03	5.75	6.31	6.15	**6.58**
MnO	0.00	0.00	0.00	0.01	0.01	0.00	0.02	**0.01**
MgO	10.11	9.52	6.19	10.21	9.12	10.10	10.04	**9.33**
ZnO	0.00	0.06	0.00	0.01	0.00	0.00	0.05	**0.02**
CaO	0.00	0.01	0.00	0.00	0.10	0.01	0.01	**0.02**
Na2O	0.03	0.02	0.00	0.01	0.08	0.01	0.02	**0.03**
K2O	0.00	0.00	0.01	0.01	0.07	0.00	0.02	**0.02**
Cl	0.00	0.00	0.00	0.00	0.04	0.00	0.00	**0.01**
F	0.00	0.00	0.00	0.00	0.00	0.00	0.00	**0.00**
H2O	0.00	0.00	0.00	0.00	0.00	0.00	0.00	**0.00**
Total	**97.74**	**98.13**	**99.29**	**98.04**	**93.67**	**98.33**	**98.18**	
Mineral	ksp	ksp	ksp	ksp	ksp	ksp	ksp	**Ave**
SiO2	63.38	63.30	63.92	63.37	63.32	63.23	63.74	**63.47**
TiO2	0.01	0.00	0.01	0.01	0.01	0.02	0.01	**0.01**
Al2O3	18.35	18.44	18.38	18.26	18.60	18.40	18.33	**18.39**
Cr2O3	0.02	0.01	0.00	0.00	0.02	0.01	0.02	**0.01**
FeO	0.01	0.04	0.00	0.14	0.16	0.03	0.08	**0.07**
MnO	0.00	0.00	0.01	0.01	0.00	0.00	0.00	**0.00**
MgO	0.00	0.00	0.00	0.04	0.14	0.00	0.00	**0.03**
ZnO	0.00	0.03	0.00	0.00	0.03	0.02	0.01	**0.01**
CaO	0.02	0.03	0.01	0.04	0.03	0.01	0.01	**0.02**
Na2O	0.24	0.21	0.18	0.25	0.20	0.15	0.16	**0.20**
K2O	16.60	16.56	16.75	16.46	16.39	16.95	16.84	**16.65**
Cl	0.00	0.00	0.00	0.01	0.01	0.00	0.00	**0.00**
F	0.00	0.00	0.00	0.00	0.00	0.00	0.00	**0.00**
H2O	0.00	0.00	0.00	0.00	3.70	3.50	3.57	**1.54**
Total	**98.64**	**98.64**	**99.26**	**98.60**	**102.61**	**102.31**	**102.76**	

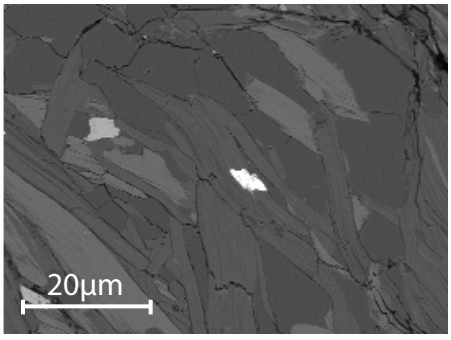
Appendix B. Representitive BSE monazite images and textural relationships.

RR2015 3-13

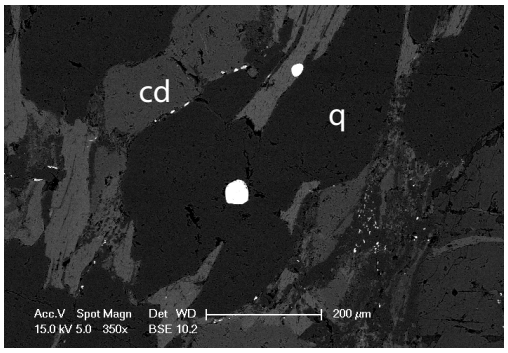


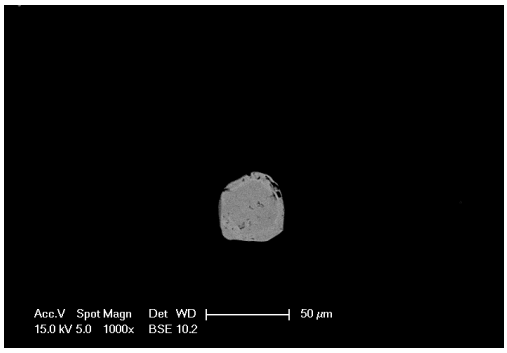


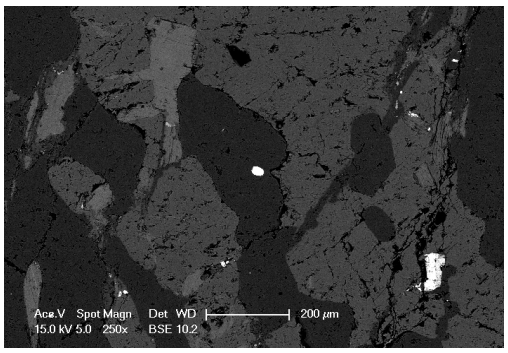


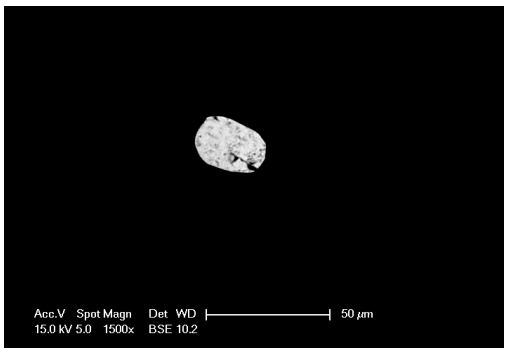


RR2014-9

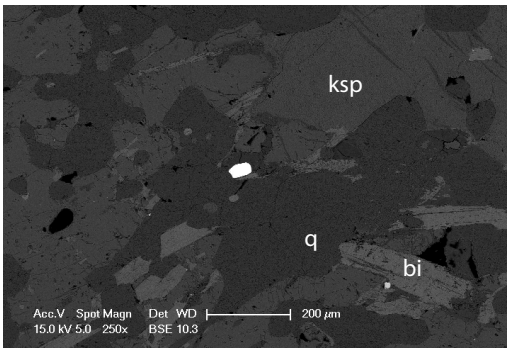


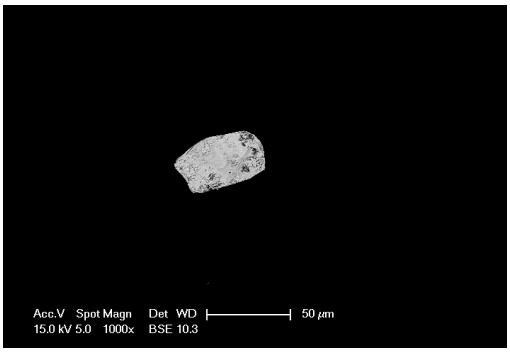


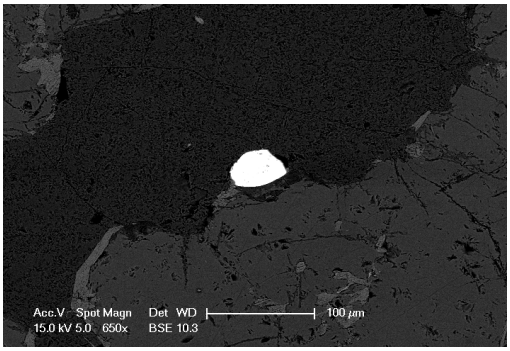


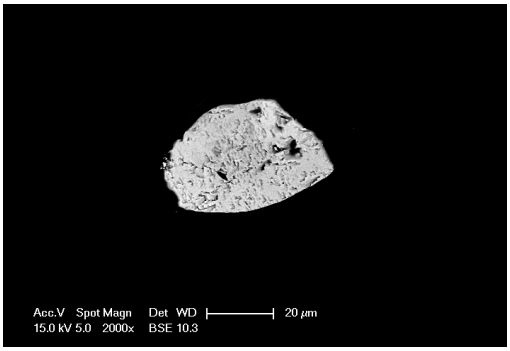


RR2014-12A


ksp
q
bi
Acc.V Spot Magn Det WD 200 µm
15.0 kV 5.0 250x BSE 10.3


Acc.V Spot Magn Det WD 50 µm
15.0 kV 5.0 1000x BSE 10.3


Acc.V Spot Magn Det WD 100 µm
15.0 kV 5.0 650x BSE 10.3


Acc.V Spot Magn Det WD 20 µm
15.0 kV 5.0 2000x BSE 10.3

Appendix 3C

T–X and TCInvestigator plots

Greenschist–facies

For the greenschist–facies sample RR2014-5, a T–M_O section was calculated to determine the oxidation state for *P–T* modelling. As the sample was deemed too fine grained to be able to calculate accurate mineral modal proportions, the composition at the centre of the peak field was taken as the most representative oxidation state for this sample (Figure 1).

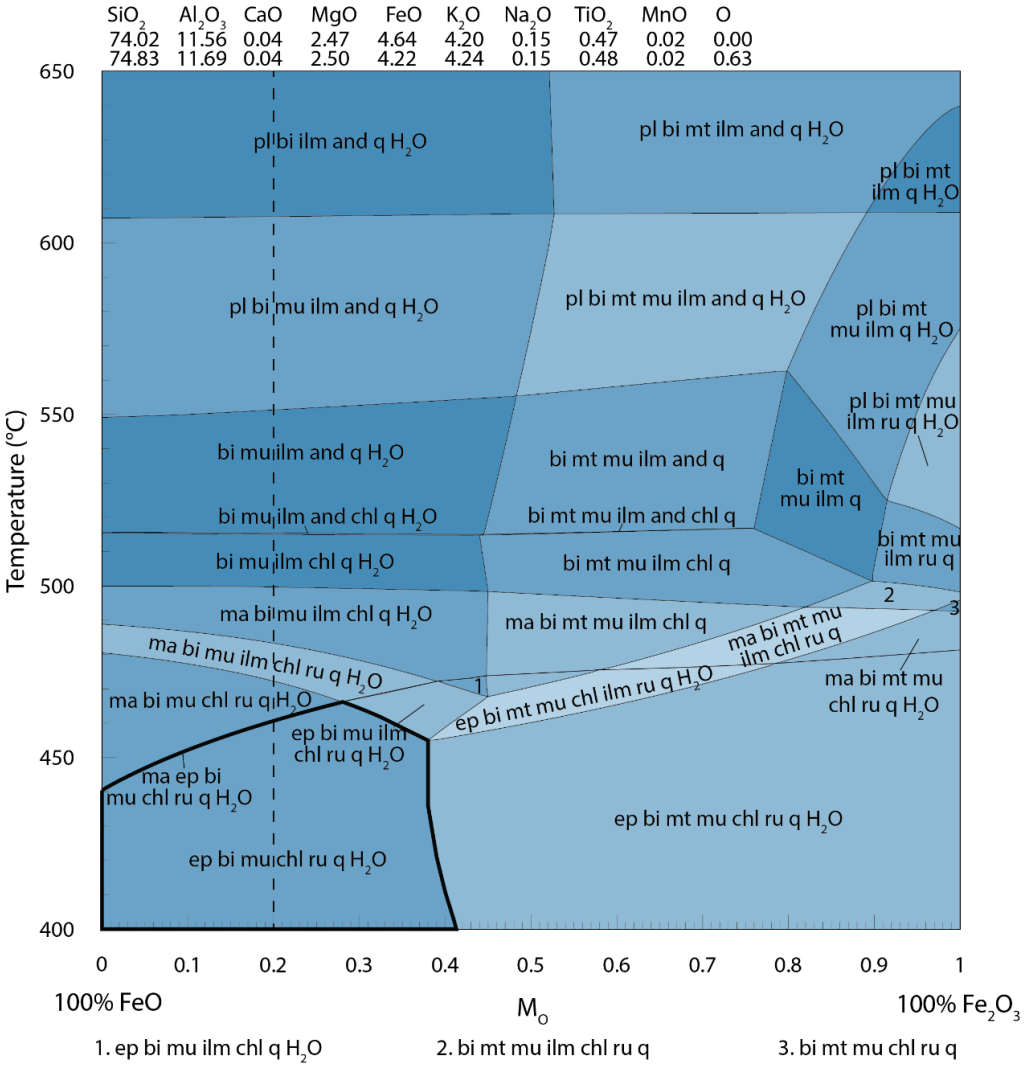
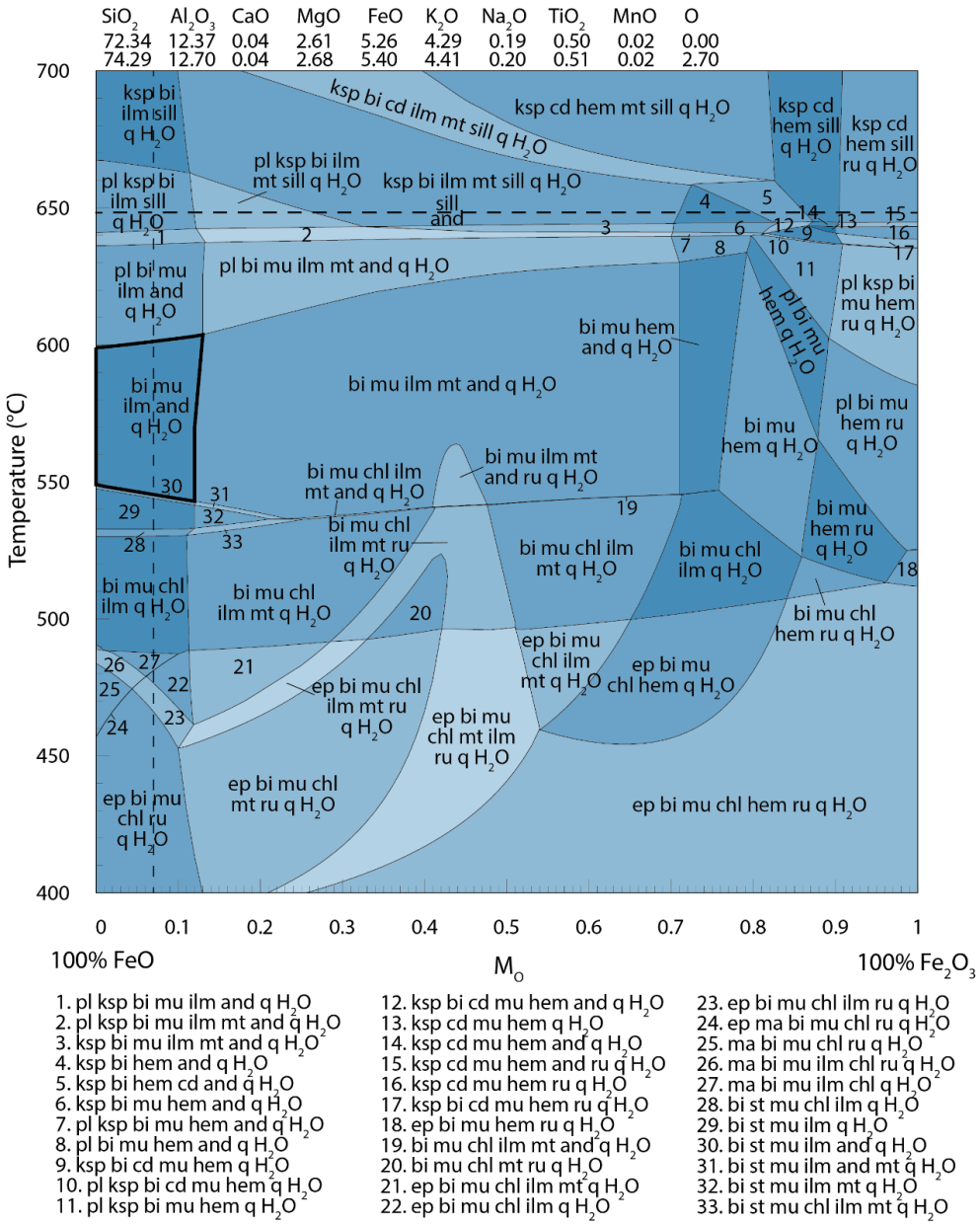


Figure 1. Calculated T–M_O section for the greenschist–facies sample RR2014-5 of the Pine Hill Formation. The bulk compositions (in mol%) are given above the pseudosection. The top composition represents the left composition of the diagram and the bottom composition represents the right side of the diagram. The field outlined in bold is the interpreted peak assemblage and the thin dashed line represents the composition that was chosen for *P–T* modelling.

Amphibolite–facies

For the amphibolite–facies sample RR2015 3-13, a T–M_O section was calculated to determine the oxidation state for *P–T* modelling. The true peak assemblage, as observed in the rock, was not able to be achieved in the T–M_O section (Figure 2). In reality, the sample does not contain ilmenite. However, a peak field with ilmenite was chosen, as it likely best represents the oxidation state of the sample. The peak field only covered a narrow compositional range, and so the composition in the middle of the field was chosen for further *P–T* modelling.



1. pl ksp bi mu ilm and q H_2O
2. pl ksp bi mu ilm mt and q H_2O
3. ksp bi mu ilm mt and q H_2O
4. ksp bi hem and q H_2O
5. ksp bi hem cd and q H_2O
6. ksp bi mu hem and q H_2O
7. pl ksp bi mu hem and q H_2O
8. pl bi mu hem and q H_2O
9. ksp bi cd mu hem q H_2O
10. pl ksp bi cd mu hem q H_2O
11. pl ksp bi mu hem q H_2O
12. ksp bi cd mu hem and q H_2O
13. ksp cd mu hem q H_2O
14. ksp cd mu hem and q H_2O
15. ksp cd mu hem and ru q H_2O
16. ksp cd mu hem ru q H_2O
17. ksp bi cd mu hem ru q H_2O
18. ep bi mu hem ru q H_2O
19. bi mu chl ilm mt and q H_2O
20. bi mu chl mt ru q H_2O
21. ep bi mu chl ilm mt q H_2O
22. ep bi mu chl ilm q H_2O
23. ep bi mu chl ilm ru q H_2O
24. ep ma bi mu chl ru q H_2O
25. ma bi mu chl ru q H_2O
26. ma bi mu ilm chl ru q H_2O
27. ma bi mu ilm chl q H_2O
28. bi st mu chl ilm q H_2O
29. bi st mu ilm q H_2O
30. bi st mu ilm and q H_2O
31. bi st mu ilm and mt q H_2O
32. bi st mu ilm mt q H_2O
33. bi st mu chl ilm mt q H_2O

Figure 2. Calculated T–M_O section for the amphibolite–facies sample RR2015 3-13 of the Pine Hill Formation. The bulk compositions (in mol%) are given above the pseudosection. The top composition represents the left composition of the diagram and the bottom composition represents the right side of the diagram. The field outlined in bold is the

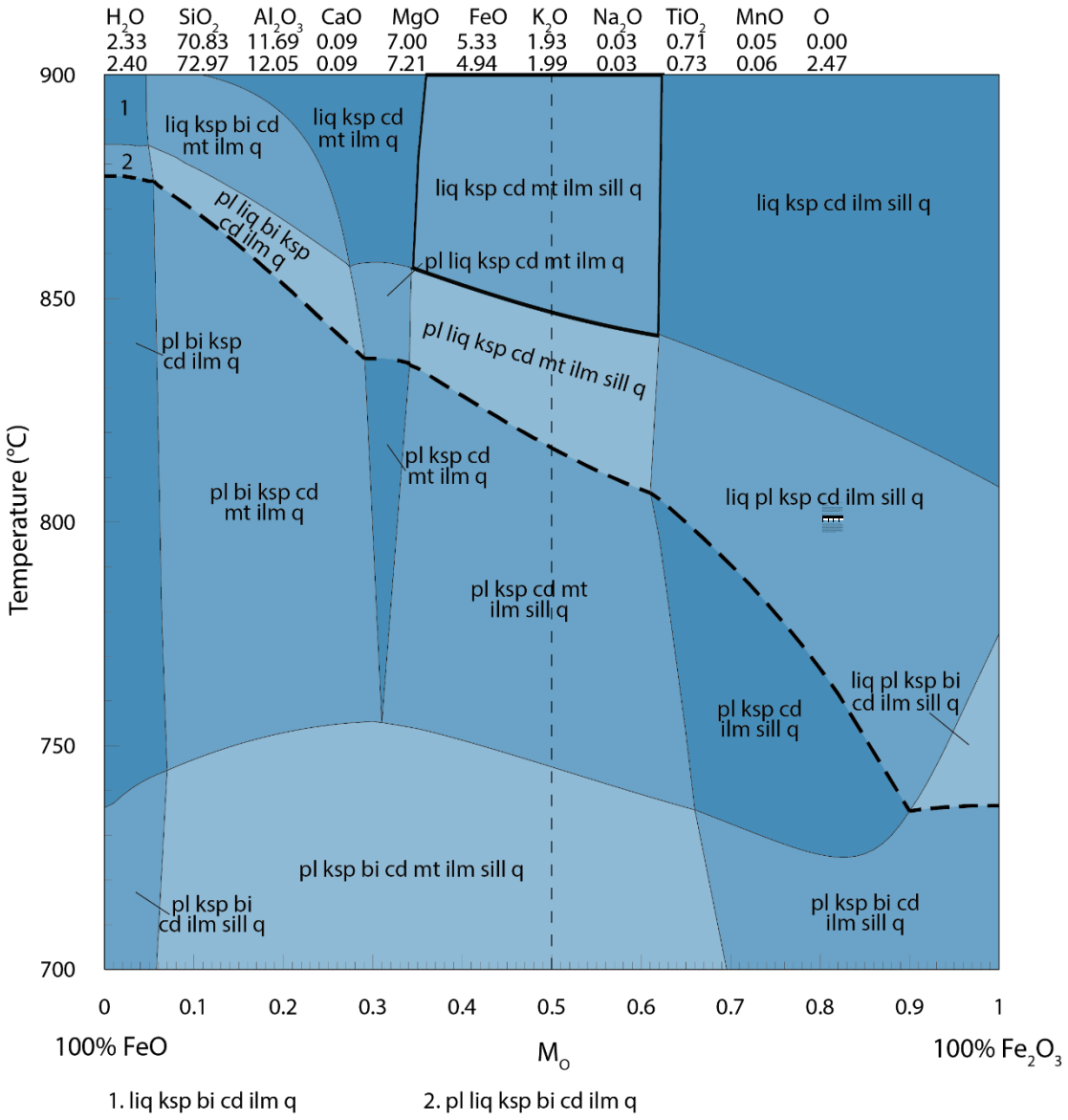


Figure 3. Calculated T–M_O section for the cordierite granulite–facies sample RR2014-9 of the Pine Hill Formation. The bulk compositions (in mol%) are given above the pseudosection. The top composition represents the left composition of the diagram and the bottom composition represents the right side of the diagram. The field outlined in bold is the interpreted peak assemblage and the thin dashed line represents the composition that was chosen for *P–T* modelling. The solidus is represented by the bold dashed line.

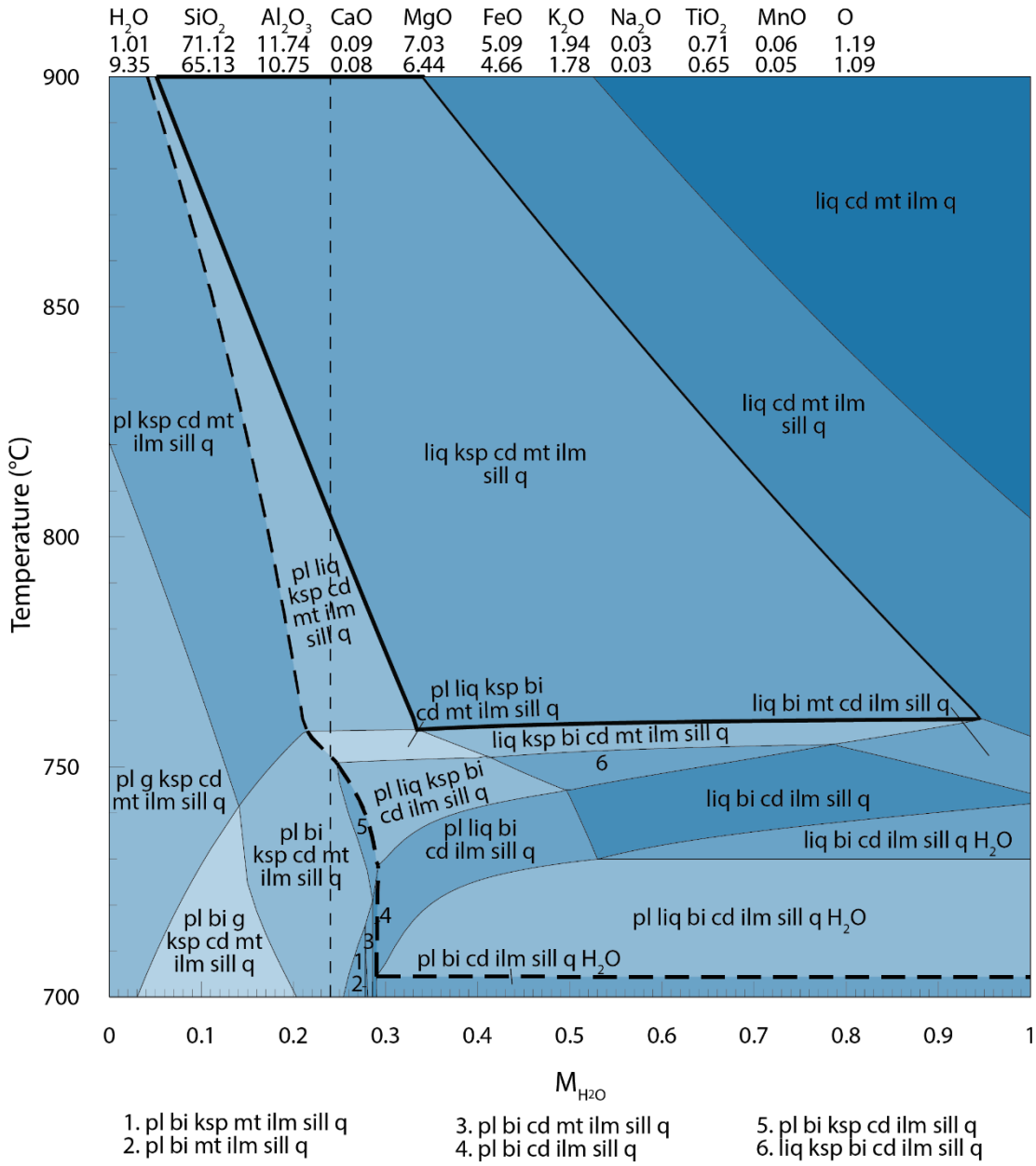


Figure 4. Calculated T–M_{H2O} section for the cordierite granulite–facies sample RR2014-9 of the Pine Hill Formation. The bulk compositions (in mol%) are given above the pseudosection. The top composition represents the left composition of the diagram and the bottom composition represents the right side of the diagram. The field outlined in bold is the interpreted peak assemblage and the thin dashed line represents the composition that was chosen for *P–T* modelling. The solidus is represented by the bold dashed line.

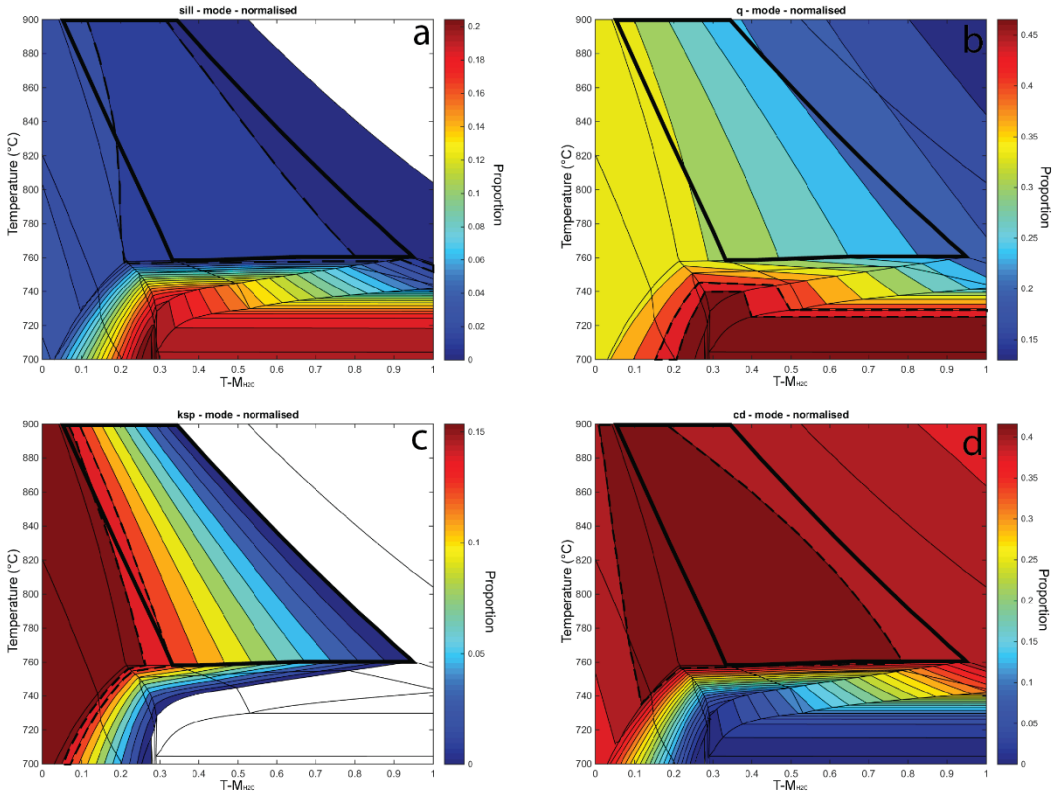


Figure 5. Modal proportion contours of (a) sillimanite, (b) quartz, (c) K-feldspar and (d) cordierite in the T–M_{H2O} section (Figure 5) from sample RR2014-9, produced by TCInverstigator (Pearce et al. 2015). In all diagrams the peak field is outlined in bold and the contour that best matches the modal abundance of each mineral has a dashed outline.

Garnet granulite-facies

For the garnet granulite–facies sample RR2014 12-A, a T–M_O section was calculated to determine the oxidation state for *P–T* modelling. As the peak field covered a very small compositional range the composition at the centre of the peak field was taken as the most representative oxidation state for this sample (Figure 6). A T–M_{H2O} section was also calculated for sample RR2014 12-A to determine the H_2O content (Figure 7) of the sample. The composition chosen was to the left of the peak field which best matched the modal proportions of most of the minerals observed in the sample. Modal contours of the T-M_{H2O} section are shown in Figure 8s. The proportion of quartz, sillimanite and garnet in Table 1 was not able to be reached within the peak field, so the highest attainable value was used. Cordierite was not used as a constraint because its abundance remained the same across the entire peak field.

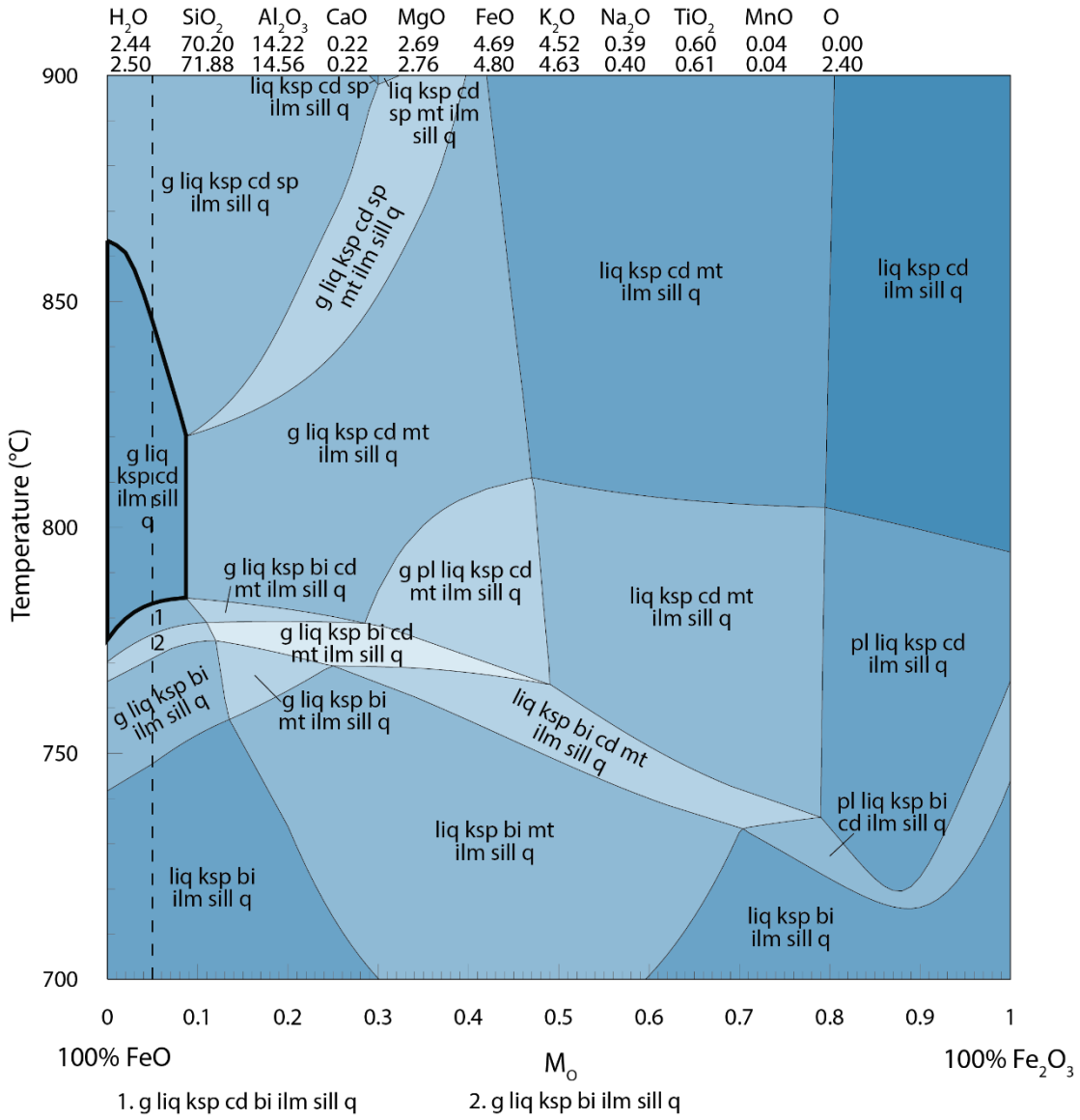


Figure 6. Calculated T–M_O section for the garnet granulite–facies sample RR2014 12-A of the Pine Hill Formation. The bulk compositions (in mol%) are given above the pseudosection. The top composition represents the left composition of the diagram and the bottom composition represents the right side of the diagram. The field outlined in bold is the interpreted peak assemblage and the thin dashed line represents the composition that was chosen for *P–T* modelling.

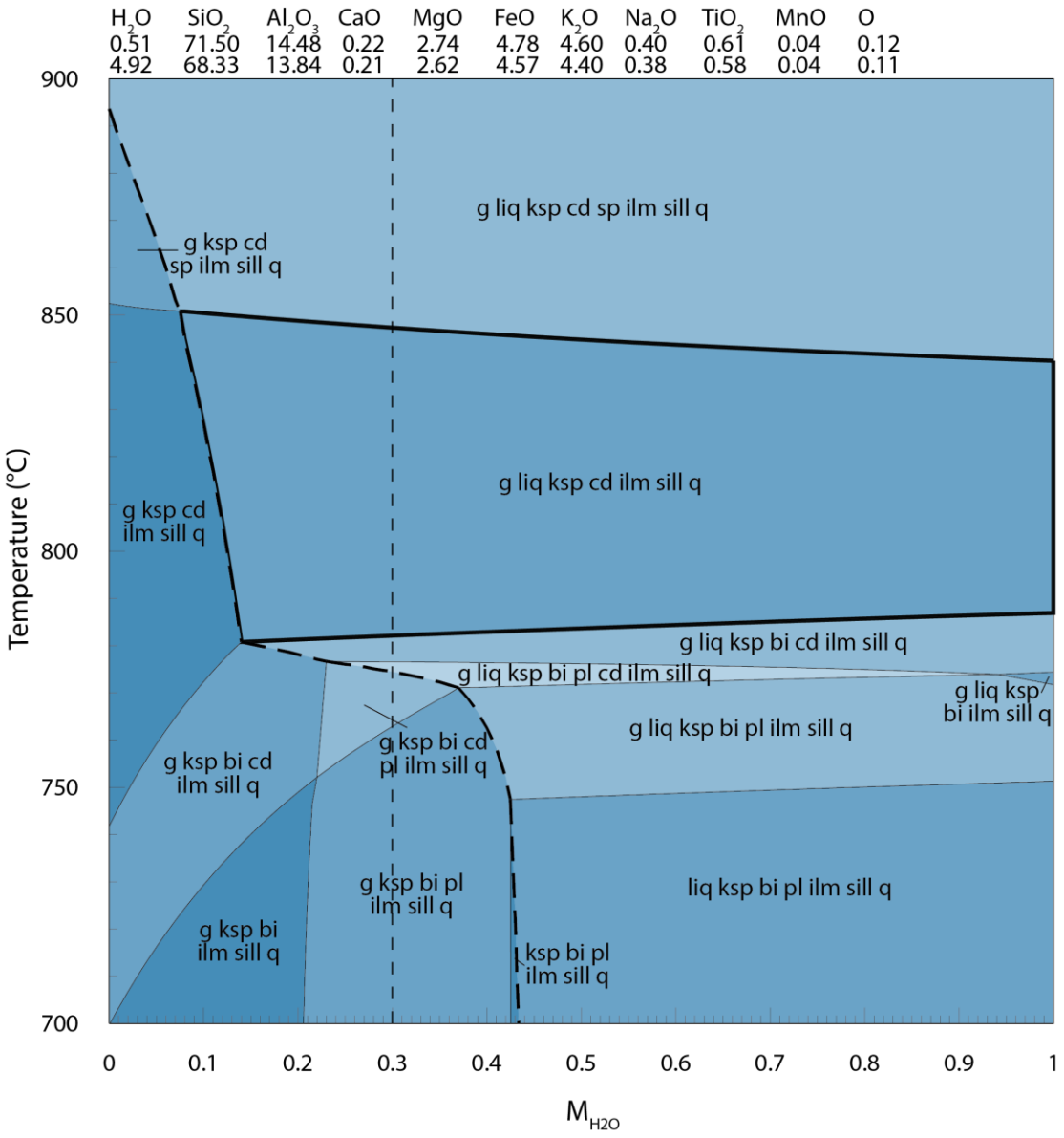


Figure 7. Calculated T–M_{H2O} section for the garnet granulite–facies sample RR2014 12-A of the Pine Hill Formation. The bulk compositions (in mol%) are given above the pseudosection. The top composition represents the left composition of the diagram and the bottom composition represents the right side of the diagram. The field outlined in bold is the interpreted peak assemblage and the thin dashed line represents the composition that was chosen for *P–T* modelling. The solidus is represented by the bold dashed line.

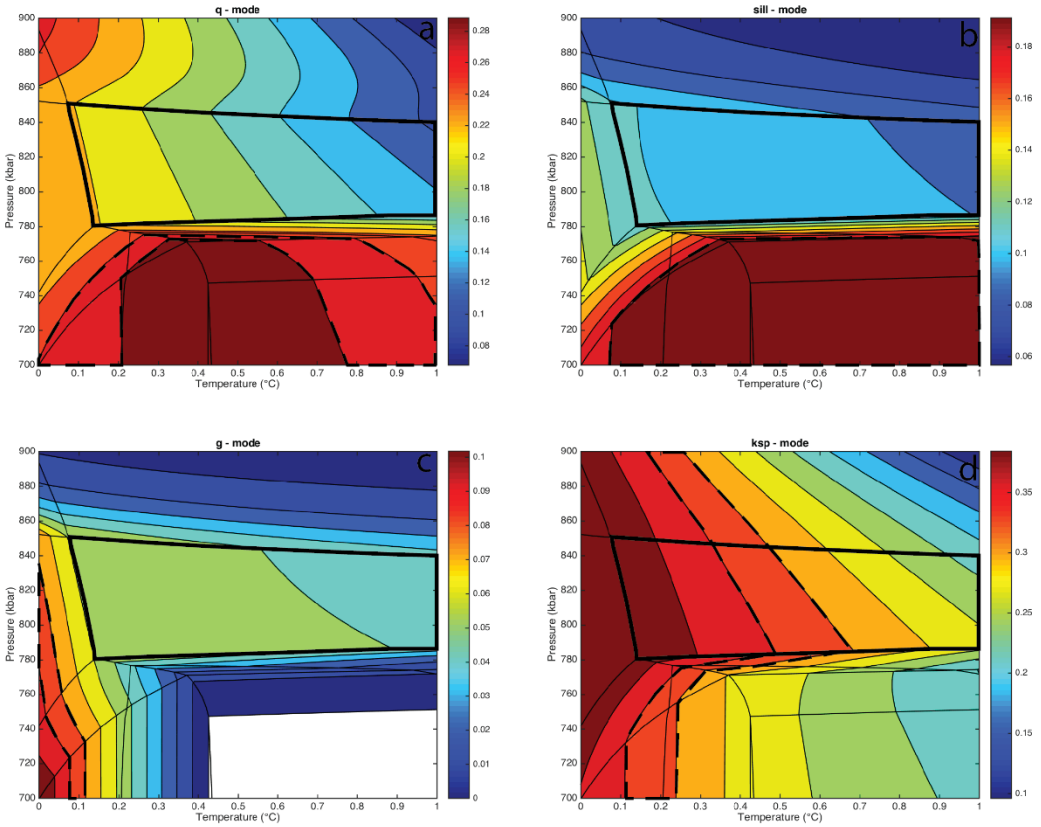


Figure 8. Modal proportion contours of (a) quartz, (b) sillimanite, (c) garnet and (d) K-feldspar in the T–M_{H2O} section (Figure 8) from sample RR2014 12-A, produced by TCInverstigator (Pearce et al. 2015). In all diagrams the peak field is outlined in bold and the contour that best matches the modal abundance of each mineral has a dashed outline.

Appendix 3D

RR2015 3-13

	Final207_235	Final207_235_Prop2	Final206_238	Final206_238_Prop2	ErrorCorrelation_6_3	FinalAge207_235	FinalAge207_235_Pr	FinalAge206_238	FinalAge206_238_Pr	FinalAge207_206	FinalAge
RR20153131A_5	3.757	0.093	0.2822	0.0056	0.81921	1583	20	1602	28	1559	
RR20153131A_2	3.663	0.094	0.2737	0.0055	0.64574	1562	21	1563	30	1569	
RR20153131A_11	3.777	0.1	0.2826	0.0059	0.68314	1587	21	1608	29	1572	
RR2015313C1_8	3.953	0.09	0.2916	0.0053	0.68178	1623.5	18	1652	28	1576	
RR2015313B2_1	3.897	0.085	0.2877	0.005	0.61079	1612.2	18	1630	25	1584	
RR2015313C1_7	3.869	0.091	0.2844	0.0054	0.80297	1606	19	1613	27	1590	
RR2015313C1_6	3.997	0.1	0.2939	0.0061	0.66892	1632	20	1661	30	1590	
RR20153131A_6	3.877	0.088	0.2865	0.0051	0.70925	1608	18	1624	26	1592	
RR2015313B1_4	3.861	0.1	0.2845	0.006	0.59084	1604	21	1614	30	1593	
RR2015313B1_3	3.821	0.093	0.2813	0.0058	0.65772	1596	20	1597	29	1598	
RR2015313C1_2	3.691	0.086	0.271	0.0051	0.60834	1568	19	1545	26	1602	
RR20153131A_4	3.778	0.089	0.2769	0.0053	0.74135	1587	19	1575	27	1608	
RR2015313B1_2	3.972	0.1	0.2898	0.0066	0.76719	1627	21	1640	33	1614	
RR20153131A_8	3.901	0.09	0.2814	0.0051	0.69062	1612.8	18	1598	26	1620	
RR2015313A2_2	3.876	0.1	0.2817	0.006	0.48541	1608	22	1599	30	1622	
RR20153131A_1	3.907	0.094	0.2836	0.0055	0.5463	1614	19	1609	27	1622	
RR20153131A_10	3.818	0.093	0.2766	0.0052	0.60238	1596	19	1574	26	1625	
RR2015313B1_1	4.182	0.11	0.3034	0.0067	0.50754	1669	22	1707	33	1635	
RR2015313C1_5	4.218	0.1	0.3036	0.0061	0.65133	1676	20	1708	30	1637	
RR2015313C1_4	3.937	0.088	0.2833	0.0053	0.69404	1620.2	18	1607	27	1638	
RR20153131A_12	4.083	0.12	0.2926	0.0062	0.71471	1648	24	1654	31	1641	
RR2015313B2_2	4.049	0.1	0.289	0.0058	0.60633	1643	21	1636	29	1648	
RR20153131A_3	3.907	0.098	0.2795	0.0056	0.63914	1614	20	1589	28	1649	
RR20153131A_13	4.095	0.089	0.2918	0.005	0.52983	1652.3	18	1650	25	1651	
RR2015313C1_9	4.06	0.11	0.2873	0.0061	0.44323	1644	23	1632	29	1663	
RR2015313B2_3	3.975	0.12	0.2818	0.0068	0.79588	1627	25	1600	34	1664	
RR2015313A2_3	4.37	0.15	0.3058	0.0083	0.801	1706	27	1718	40	1682	
RR2015313C1_3	4.054	0.11	0.2844	0.006	0.52049	1644	22	1613	30	1684	
RR2015313A2_4	4.03	0.1	0.2812	0.006	0.54464	1639	20	1597	30	1695	
RR2015313C1_1	4.08	0.13	0.2714	0.0059	0.68914	1649	25	1548	30	1766	
RR20153131A_7	4.069	0.091	0.2982	0.0056	0.56461	1647	18	1682	28	1600	
RR2015313A2_1	3.652	0.095	0.2648	0.0059	0.60938	1560	21	1514	30	1623	
RR2015313B2_4	3.795	0.096	0.2737	0.0056	0.80822	1594	22	1559	28	1633	
RR20153131A_9	3.958	0.094	0.2784	0.0053	0.57117	1625	19	1583	27	1679	

Discordant analyses

RR2014-9

	Final207_235	Final207_235_Prop2	Final206_238	Final206_238_Prop2	ErrorCorrelation_6_	FinalAge207_235	FinalAge207_235_P	FinalAge206_238	FinalAge206_238_P	FinalAge207_206	FinalAge207_
cd_gran_7	3.586	0.052	0.2743	0.0029	0.41276	1545.7	11	1562	15	1525	
cd_gran_1	3.444	0.041	0.2632	0.0025	0.58857	1514.3	9.4	1506.2	13	1526	
cd_gran_3	3.44	0.054	0.2626	0.0031	0.24265	1512.5	12	1503	16	1528	
cd_gran_13	3.563	0.05	0.2699	0.0028	0.24788	1540.6	11	1540.2	14	1539	
cd_gran_6	3.596	0.044	0.2716	0.0028	0.37753	1548.2	9.7	1548.8	14	1540	
cd_gran_4	3.557	0.054	0.2697	0.0035	0.52577	1539.1	12	1539	18	1542	
cd_gran_0	3.467	0.051	0.2626	0.0027	0.49701	1519	12	1503	14	1544	
cd_gran_14	3.671	0.062	0.2767	0.0033	0.58047	1564	14	1574	17	1547	
cd_gran_2	3.647	0.057	0.2748	0.0029	0.35841	1558.9	13	1565	15	1549	
cd_gran_10	3.574	0.048	0.2691	0.0028	0.46173	1543.1	11	1536.2	14	1549	
cd_gran_9	3.583	0.048	0.2695	0.0029	0.59628	1545.1	11	1538	15	1557	
cd_gran_5	3.579	0.043	0.2689	0.0026	0.58723	1544.6	9.4	1535	13	1561	
cd_gran_11	3.659	0.05	0.2729	0.0032	0.63978	1561.9	11	1555	16	1573	
cd_gran_12	3.537	0.04	0.2649	0.0025	0.56851	1535.4	8.9	1514.7	13	1559	
cd_gran_8	3.406	0.043	0.2542	0.0026	0.54375	1505.4	9.8	1460.2	13	1569	

Discordant analyses

RR2014 12-A

	Final207_235	Final207_235_P	Final206_238	Final206_238_P	ErrorCorrelation	FinalAge207_23	FinalAge207_23	FinalAge206_23	FinalAge206_23	FinalAge207_20	FinalAge207
gtgranulite_21	3.542	0.06	0.2685	0.005	0.45093	1536.3	12	1533.1	25	1543	
gtgranulite_8	3.559	0.028	0.2689	0.0031	0.439	1540	6.2	1535	16	1544	
gtgranulite_24	3.609	0.026	0.2723	0.0029	0.40552	1551.1	5.6	1552.5	15	1544	
gtgranulite_26	3.633	0.031	0.2727	0.0029	0.43101	1556.2	6.9	1554.4	15	1548	
gtgranulite_23	3.586	0.026	0.27	0.0028	0.35287	1546.1	5.7	1540.9	14	1549	
gtgranulite_16	3.576	0.023	0.272	0.0029	0.5366	1544	5.1	1550.9	15	1549	
gtgranulite_7	3.622	0.024	0.2725	0.0028	0.53147	1554.2	5.3	1553.3	14	1553	
gtgranulite_22	3.543	0.025	0.2661	0.0029	0.4302	1536.5	5.6	1520.8	15	1555	
gtgranulite_17	3.582	0.024	0.271	0.0028	0.63012	1545.2	5.3	1545.6	14	1555	
gtgranulite_15	3.551	0.029	0.2695	0.0028	0.48961	1538.3	6.6	1538	14	1556	
gtgranulite_27	3.661	0.026	0.2728	0.003	0.42598	1562.6	5.6	1554.7	15	1562	
gtgranulite_19	3.588	0.021	0.2695	0.003	0.51476	1546.5	4.7	1538.3	15	1567	
gtgranulite_13	3.614	0.022	0.2707	0.0028	0.36498	1552.3	4.8	1544.4	14	1567	
gtgranulite_9	3.867	0.036	0.2862	0.0032	0.59994	1606.3	7.6	1622	16	1589	
gtgranulite_10	3.759	0.087	0.2746	0.0046	0.67316	1583.3	17	1564	23	1612	
gtgranulite_2	3.54	0.022	0.2644	0.0027	0.63005	1535.9	4.9	1512.5	14	1557	
gtgranulite_5	3.516	0.026	0.2634	0.003	0.56168	1530.6	5.8	1506.9	15	1558	
gtgranulite_14	3.435	0.035	0.2574	0.0033	0.60517	1512	8	1477	17	1562	
gtgranulite_25	3.488	0.027	0.2612	0.0029	0.58539	1524.3	6	1495.9	15	1552	
gtgranulite_0	3.572	0.025	0.2649	0.003	0.7065	1543	5.6	1514.6	15	1570	
gtgranulite_1	3.952	0.04	0.2927	0.0037	0.5249	1623.8	8.3	1655	19	1573	

Discordant analyses

Appendix 3E

Upper Crust	**Heat production @ 1650 Ma(µWm-3)**	**Density (kg m-3)**	**Specific Heat Capacity (J kg-1 K-1)**	**Thermal Conductivity (W m-1 K-1)**
Shale	1.68	2720	740	1.5
Sandstone	0.81	2650	775	2.05
Average	**1.245**	**2685**	**757.5**	**1.775**
	Hasterok et al. 2017		Waples and Waples 2004	

Mid crust

Map Unit	**Proportion of area**	**Heat production @ 1650 Ma(µWm-**	**Contribution to heat production (µ**	**Primary Rock Type(s)**
Boothby Orthogneiss	0.075	4.70	0.4	granite
Napperby Gneiss	0.159	5.98	0.9	granite
Conniston Schist	0.016	4.72	0.1	granite
Mt Airy Orthogneiss	0.124	4.86	0.6	granite
Anmatjira Orthogneiss	0.112	6.86	0.8	granite
Tyson Creek Granulite	0.005	3.78	0.0	mafic and felsic granulites
Weldon Metamorphics	0.017	5.15	0.1	pelite, granofels, granulite
Central Mount Stewart Formation	0.003	3.69	0.0	arenite, siltstone dolostone
Vaughan Springs Quartzite	0.005	1.99	0.0	quartzite
Possum Creek Charnokite	0.002	7.19	0.0	charnockite
Mt Dunkin Schist	0.003	3.33	0.0	schist
Lander Rock Formation	0.131	3.71	0.5	pelitic schist and psammite
Ennugan Granites	0.198	5.16	1.0	granite
Mount Stafford Member	0.034	3.71	0.1	metapelitic and metapsammitic hornfels
Reynolds Range Group	0.055	3.08	0.2	Quartzite, orthoquartzite, shale
Aileron Metamorphics	0.007	4.93	0.0	granulite, amphibolite, gneiss
Mt Freeling Schist	0.014	4.14	0.1	schist
Wickstead Creek Beds	0.040	4.32	0.2	Calc-silicate, marble, gneiss
Final Value			**4.97**	
		Radiometrics		Stewart 1981

Map Unit	**Density (kg m-3)**	**Specific Heat Capacity (J kg-1 K-1)**	**Thermal Conductivity (W m-1 K-1)**
Boothby Orthogneiss	2660	720	3.01
Napperby Gneiss	2660	720	3.01
Conniston Schist	2660	720	3.01
Mt Airy Orthogneiss	2660	720	3.01
Anmatjira Orthogneiss	2660	720	3.01
Tyson Creek Granulite	2906	795	2.04
Weldon Metamorphics	2787	775	2.52
Central Mount Stewart Formation	2767	759	2.83
Vaughan Springs Quartzite	2679	730	4.56
Possum Creek Charnokite	2660	720	3.01
Mt Dunkin Schist	2682	731	2.79
Lander Rock Formation	2670	725	2.98
Ennugan Granites	2660	720	3.01
Mount Stafford Member	2787	775	2.52
Reynolds Range Group	2710	750	2.79
Aileron Metamorphics	2787	775	2.52
Mt Freeling Schist	2682	731	2.79
Wickstead Creek Beds	2739	752	3.05
Final Value	**2712**	**741**	**2.91**
		Waples and Waples 2004	

Lower Crust

Unit	**Heat production @ 1650 Ma (µWm-3)**	**Rock Type**	**Density (kg m-3)**
Mount Hay Block	1.34	mafic (some felsic) intrusive granulit	2906
Mount Chapple Hills	1.83	Mafic and intermedite intrusive garr	2906
Average Value	**1.59**		**2906**
			Waples and Waples 2004

Lower Crust	**Specific Heat Capacity (J kg-1 K-1)**	**Thermal Conductivity (W m-1 K-1)**
Unit	795	2.04
Mount Hay Block	795	2.04
Mount Chapple Hills	**795**	**2.04**
Average Value	Waples and Waples 2004	

References

Hasterok D., Gard M. & Webb J. 2017 On the radiogenic heat production of metamorphic, igneous, and sedimentary rocks.

Stewart A. 1981 Reynolds Range Region, Northern Territory, 1: 100 000 Geological Map Commentary, Bureau of Mineral Resources, Geology and Geophysics, Canberra, ACT.

Waples D. W. & Waples J. S. 2004 A Review and Evaluation of Specific Heat Capacities of Rocks, Minerals, and Subsurface Fluids. Part 1: Minerals and Nonporous Rocks, Natural Resources Research, vol. 13, no. 2, pp. 97-122.

Appendix 3F

Documentation of MATLAB App hp_burial

K.L. Alessio, M. Hand, D. Hasterok, L. Morrissey, D.E. Kelsey, and T. Raimondo

June 3, 2019

1 Introduction

This document describes the thermal modelling code `hp_burial\verb`, an App programmed in MATLAB. The purpose of this code is to produce hypothesis testing scenarios for metamorphic conditions as a result of vertical heat production distributions coupled with erosion and sedimentation effects. The code solves the one-dimensional, transient heat flow equation with sources using a finite difference approximation. The solver uses a tridiagonal algorithm to the Crank-Nicholson formulation. At present, the code starts from a steady-state thermal regime with a user defined lithologic profile that sets the thermal properties and then evolves by simulating erosion or deposition of sediment. Customized rock types may be defined or a user may simply choose to modify the heat production of an individual rock type.

2 Model Formulation

The program `hp_burial` solves the one-dimensional, transient heat flow equation with sources, i.e.,

$$\rho C_P \frac{\partial T}{\partial t} = k \frac{\partial^2 T}{\partial z^2} + A,$$

where ρ, C_P, k, and A are the physical properties, density, specific heat capacity, thermal conductivity, and heat production, respectively. We use a Crank-Nicholson finite-difference formulation with a node spacing of 1 km. Sediment is added by using a Lagrangian specification and the bedrock beneath is using and Eulerian specified grid. This choice simplifies the formulation by keeping the basement nodes fixed while moving sediment nodes as material is added. Erosion is simply handled by removing cells and interpolating the position of the surface cell during each time step.

The upper surface boundary condition is held fixed (Dirichlet-type) at a surface temperature, generally 15°C, and the lower boundary condition is set as a fixed flux (Neumann-type) condition to a prescribed mantle heat flow. The initial condition is simply assumed to be a steady-state conductive geotherm, using a layered-Earth with the prescribed physical properties.

To compute the steady-state geotherms, we use the one-dimensional, conductive, layered-Earth solutions similar to (Chapman, 1986). Temperature at the base of the i-th layer, is given by

$$T_i = T_{i-1} + \frac{q_{i-1}}{k_i}\Delta z - \frac{A_i}{2k_i}\Delta z^2.$$

where T_{i-1} and q_{i-1} are the temperature and heat flow at the top of layer i, A_i is the heat produc-

tion and k_i is the thermal conductivity within layer i. The heat flow at the top of layer i is

$$q_{i-1} = q_0 - \sum_{j=1}^{i-1} A_j \Delta z.$$

Since we use a temperature and pressure dependent thermal conductivity, the thermal conductivity of layer i is unknown, but can be solved along with temperature using an iterative Newton's method approach.

To compute the temporal changes to the temperature field, we use a tridiagonal solver. Because we are assuming temperature-dependent thermal properties, the temperature solution at each time step must be solved iteratively. To handle this, we compute the temperature solution using physical properties derived from temperatures at the previous time-step and then recompute the physical properties using the average of the previous and current time-step's temperature estimates (McKenzie et al., 2005). This step is performed twice as physical property changes are not dramatic between time steps.

3 Physical Properties

The standard temperature and pressure estimates of physical properties needed to estimate temperature are supplied to the program by a specified set of rock types. The advantage of such a choice is that the physical properties co-vary in a way that represents the average behavior of rocks as a function of composition. Though variants of specific rock types can be included as user-specified rock types with custom physical properties more appropriate when known. While the global median heat production is supplied for a set of common rock types, this parameter can be easily changed to reflect measured values while keeping the other parameters the same.

Because the physical properties in question are dependent on temperature (and possibly pressure) we have included mathematical approximations as described below.

4 Rock properties

4.0.1 Thermal conductivity

To estimate thermal conductivity, we have devised a general model that is meant to incorporate several desirable features of existing models including P–T dependence and compositional variations consistent with common rock types. It has not been optimized because of the disparate nature of the models used to construct the one here, but the model provides a reasonable approximation for the compositional, thermal and barometric variations in thermal conductivity. The model incorporates estimates of P–T variations of thermal conductivity for several broad rock types (Zoth and Hänel, 1988). However, these coarse compositions of these P-T models are much too general for most rocks. More recent estimates of thermal conductivity (Jennings et al., in review) are based on a more continuous compositional variation, but the measurements upon which this model is founded are only made for at room temperature. Thus a hybrid model is necessary. The

conductivity model developed below is

$$k_1 = \frac{k_0(n-1)}{n}(1+\beta P)$$
$$k_2 = \frac{k_0}{n}\exp\left(\frac{-(T-25)}{300}\right)(1+\beta P)$$
$$k_{\text{eff}} = k_1 + k_2,$$

where T is in celsius and P is in GPa. The parameter n is an empirical factor that is dependent on composition as expressed in the reference thermal conductivity, $n = 6.4 - 2.3 \log k_0$. The pressure coefficient, β, is set to 0.1 GPa^{-1} estimated after (Chapman, 1986). Values for k_0 are given in Table 1.

Thermal diffusivity is computed by $\kappa = k(\rho C_P)^{-1}$, where ρ is the density and C_P is the specific heat capacity as defined below.

4.0.2 Specific heat capacity

The specific heat capacity at standard temperature and pressure (STP) was taken directly from Waples and Waples (2004), or is approximated by a fit to C_P data in Waples and Waples (2004). Because the temperature behavior of most rocks are very similar, the temperature–dependent specific heat capacity can be estimated as

$$C_P(T) = C_{P,0}\frac{C_{Pn}(T)}{C_{Pn,0}}$$

where C_{Pn} and $C_{Pn,0}$ are a normalized heat capacity and a reference normalized heat capacity given by

$$C_{Pn,0} = 8.95 \times 10^{-10} 298^3 - 2.13 \times 10^{-6} 298^2 + 1.72 \times 10^{-3} 298 + 0.716$$
$$C_{Pn}(T) = 8.95 \times 10^{-10} T^3 - 2.13 \times 10^{-6} T^2 + 1.72 \times 10^{-3} T + 0.716$$

where T is in kelvins (Waples and Waples, 2004).

4.0.3 Density

Density is computed by

$$\rho(T) = \rho_0(1 - \alpha T),$$

where T is in celsius and α is the expansivity, which we assume to be 3×10^{-5} K^{-1}. The reference density at 25°C is estimated for a number of rock types (Table 1). No pressure effect on density is presently included in the analysis.

4.0.4 Heat production

Heat production may be directly specified by for each rock layer, or chosen from a look-up table associated with individual rock types (Table 1). Estimated heat productions for various rock types are derived from a global geochemical dataset (Hasterok et al., 2018).

4.1 Sediment properties

The physical properties are handled a little differently than the rocks below because it is assumed the rocks have negligible porosity. To compute the physical properties of sediments we compute

first the matrix property using the surface values in Table 2. The properties are then adjusted for temperature and or pressure as above for rocks. Finally, the physical properties of the sediments are adjusted for porosity using the appropriate mixing relationship with water as the assumed pore fluid,

$$
\begin{aligned}
k &= k_m^{(1-\phi)} k_w^{\phi} \\
C_P &= (1-\phi) C_{P,m} + \phi C_{P,w} \\
\rho &= (1-\phi)\rho + \phi\rho_w \\
A &= (1-\phi) A
\end{aligned}
$$

where the subscripts m refer to the matrix and w refer to water filling the pore spaces. At present compaction is not included as an influence on the physical properties.

References:

Chapman, D., 1986. Thermal gradients in the continental crust, in: Dawson, J., Carswell, D., Hall, J., Wedepohl, K. (Eds.), The Nature of the Lower Continental Crust. Geol. Soc. Spec. Pub., Denver. 24, pp. 63–70. doi:10.1144/GSL.SP.1986.024.01.07.

Hasterok, D., Gard, M., Webb, J., 2018. On the radiogenic heat production of metamorphic, igneous, and sedimentary rocks. Geoscience Frontiers 9, 1777–1794. doi:10.1016/j.gsf.2017.10.012.

Jennings, S., Hasterok, D., Payne, J., in review. A new compositionally-based thermal conductivity model for plutonic rocks. Physics of the Earth and Planetary Interiors .

McKenzie, D., Jackson, J., Priestley, K., 2005. Thermal structure of oceanic and continental lithosphere. Earth Planet. Sci. Lett. 233, 337–349.

Waples, D.W., Waples, J.S., 2004. A review and evaluation of specific heat capacities of rocks, minerals, and subsurface fluids. part 1: minerals and nonporous rocks. Natural Resources Research 13, 97–122. doi:10.1023/B:NARR.0000032647.41046.e7.

Zoth, G., Hänel, R., 1988. Appendix, in: Hänel, R., Rybach, L., Stegena, I. (Eds.), Terrestrial Handbook of Heat-Flow Density Determination. Kluwer Academic Publishers, Dordrecht, pp. 449–466.

Table 1: Physical properties of default rock types. Values for density and heat production from Hasterok et al. (2018). Specific heat capacity estimates estimated from Waples and Waples (2004). Thermal conductivity estimated from the global geochemical dataset for various rock types defined by Hasterok et al. (2018) using the compositional model derived by Jennings et al. (in review).

rock type	ρ	C_P	k	A
	kg m^{-3}	J kg^{-1} K^{-1}	W m^{-1} K^{-1}	μW m^{-3}
quartzolite	2700	739	4.65	2.403
granite	2660	720	3.01	3.461
granodiorite	2718	752	2.77	1.838
diorite	2787	775	2.52	1.221
gabbroic diorite	2897	794	2.38	0.725
subalkalic gabbro	2969	807	2.3	0.498
peridotgabbro	3245	844	2.19	0.466
cumulate peridotite	3160	834	1.97	3.229
mantle peridotite	3364	855	2.02	0.02
syenite	2664	723	2.12	3.513
quartz monzonite	2690	735	2.54	2.872
monzonite	2762	743	2.27	2.196
monzodiorite	2838	781	2.14	1.521
monzogabbro	2906	795	2.04	1.482
alkalic gabbro	2954	804	2.11	0.743
foid gabbro	3001	812	1.83	4.047
foid monzodiorite	2831	779	1.86	3.693
foid monzosyenite	2757	759	1.95	3.892
foid syenite	2631	705	1.76	4.986
ultra-high alkali plutonic	2598	682	3.31	3.204
intermediate foidolite	2760	760	1.55	2.653
mafic foidolite	2944	803	1.64	3.436
ultramafic foidolite	3081	824	1.76	5.212
carbonatite	2825	778	1.75	6.021
dolomite	2784	767	1.93	2.066
limestone	2726	804	1.8	2.513
iron-rich shale	2755	758	2.66	2.725
shale	2682	731	2.79	5.933
arkose	2637	709	3.17	2.774
iron-rich sand	2731	750	2.66	3.822
litharenite	2687	734	3.77	3.463
quartz arenite	2835	780	3.76	1.726
subarkose	2731	750	3.92	2.948
sublitharenite	2743	754	3.77	2.196
wacke	2668	725	3.13	3.799
quartzite	2679	730	4.56	2.041

Table 2: Estimated physical properties for the sedimentary matrix. Values after Waples and Waples (2004). Heat production from Hasterok et al. (2018).

sediment type	ρ	C_P	k	A
	kg m^{-3}	J kg^{-1} K^{-1}	W m^{-1} K^{-1}	μW m^{-3}
carbonate ooze	2700	815	2.24	0.52
pelagic clay	2500	860	2.3	1.68
sandstone	2650	775	2.05	0.81
shale	2720	740	1.5	1.68

Appendix 4

Supplementary material for: Contrasting temperature–time records in interlayered granulites

Appendix 4A: Microprobe analyses

MB2017-1

Mineral	Hbl	Hbl	Hbl	Hbl	Cpx	Cpx	Cpx	Cpx	Cpx
SiO2	45.21	44.98	44.04	44.31	50.97	52.89	51.44	52.25	51.64
TiO2	1.70	1.71	1.80	1.81	0.22	0.23	0.23	0.21	0.21
Al2O3	10.63	10.36	10.43	10.66	1.80	1.71	1.75	1.78	1.76
Cr2O3	0.03	0.05	0.05	0.05	0.01	0.02	0.02	0.01	0.02
FeO	15.62	16.36	16.45	15.99	11.66	11.00	11.07	11.05	11.32
MnO	0.22	0.29	0.34	0.28	0.44	0.48	0.44	0.47	0.46
MgO	10.59	10.05	10.03	10.19	11.55	11.41	11.69	11.86	11.70
ZnO	0.01	0.02	0.00	0.04	0.04	0.02	0.03	0.00	0.00
CaO	10.44	10.93	10.84	10.94	21.53	21.27	21.46	21.48	21.59
Na2O	1.81	1.54	1.54	1.62	0.37	0.36	0.39	0.36	0.37
K2O	0.55	0.57	0.61	0.61	0.00	0.00	0.00	0.00	0.00
Cl	0.00	0.00	0.00	0.01	0.01	0.00	0.00	0.00	0.00
F	0.00	0.00	0.00	0.00	0.00	0.00	0.00	0.00	0.00
H2O	2.01	2.00	1.98	1.99	0.00	0.00	0.00	0.00	0.00
OH = Cl ("Cl factor")	0.00	0.00	0.00	0.00	0.00	0.00	0.00	0.00	0.00
OH = F ("F factor")	0.00	0.00	0.00	0.00	0.00	0.00	0.00	0.00	0.00
Total	96.83	96.87	96.12	96.50	98.59	99.39	98.53	99.47	99.07
No. Oxygens	23.00	23.00	23.00	23.00	6.00	6.00	6.00	6.00	6.00
Si	6.99	7.00	6.90	6.90	1.95	2.01	1.97	1.98	1.97
Ti	0.20	0.20	0.21	0.21	0.01	0.01	0.01	0.01	0.01
Al	1.94	1.90	1.93	1.96	0.08	0.08	0.08	0.08	0.08
Cr	0.00	0.01	0.01	0.01	0.00	0.00	0.00	0.00	0.00
Fe3+	0.00	0.00	0.00	0.00	0.03	0.00	0.00	0.00	0.00
Fe2+	2.02	2.13	2.16	2.08	0.35	0.35	0.35	0.35	0.36
Mn2+	0.03	0.04	0.04	0.04	0.01	0.02	0.01	0.02	0.01
Mg	2.44	2.33	2.34	2.37	0.66	0.65	0.67	0.67	0.66
Zn	0.00	0.00	0.00	0.00	0.00	0.00	0.00	0.00	0.00
Ca	1.73	1.82	1.82	1.83	0.88	0.87	0.88	0.87	0.88
Na	0.54	0.46	0.47	0.49	0.03	0.03	0.03	0.03	0.03
K	0.11	0.11	0.12	0.12	0.00	0.00	0.00	0.00	0.00
Cl	0.00	0.00	0.00	0.00	0.00	0.00	0.00	0.00	0.00
F	0.00	0.00	0.00	0.00	0.00	0.00	0.00	0.00	0.00
OH-	2.00	2.00	2.00	2.00	0.00	0.00	0.00	0.00	0.00
Total cations (S)	16	16	16	16	4	4	4	4	4

Mineral	Cpx	Cpx	Cpx	Cpx	Cpx	Cpx	Cpx	Ilm	Ilm	Ilm	Ilm
SiO2	53.19	52.38	51.46	52.59	52.49	52.98	51.69	0.04	0.03	0.02	0.11
TiO2	0.21	0.21	0.21	0.21	0.21	0.19	0.19	53.19	53.45	53.72	53.34
Al2O3	1.76	1.72	1.80	1.74	1.65	1.61	1.59	0.06	0.06	0.05	0.15
Cr2O3	0.02	0.03	0.03	0.02	0.00	0.02	0.01	0.02	0.03	0.02	0.01
FeO	10.88	10.73	11.34	10.93	11.04	11.28	11.17	43.68	44.76	42.22	43.54
MnO	0.45	0.46	0.45	0.48	0.44	0.46	0.45	1.19	1.16	1.16	1.20
MgO	12.12	11.64	11.75	11.88	11.61	11.99	11.65	0.81	0.91	0.77	0.71
ZnO	0.01	0.05	0.05	0.01	0.02	0.00	0.00	0.02	0.04	0.02	0.07
CaO	21.43	21.77	21.68	21.67	21.56	21.06	21.45	0.01	0.00	0.00	0.04
Na2O	0.41	0.36	0.37	0.40	0.35	0.38	0.37	0.00	0.00	0.01	0.01
K2O	0.00	0.00	0.00	0.01	0.00	0.02	0.01	0.00	0.00	0.00	0.00
Cl	0.00	0.00	0.01	0.00	0.00	0.01	0.00	0.00	0.00	0.00	0.00
F	0.00	0.00	0.00	0.00	0.00	0.00	0.00	0.00	0.00	0.00	0.00
H2O	0.00	0.00	0.00	0.00	0.00	0.00	0.00	0.00	0.00	0.00	0.00
OH = Cl ("Cl factor")	0.00	0.00	0.00	0.00	0.00	0.00	0.00	0.00	0.00	0.00	0.00
OH = F ("F factor")	0.00	0.00	0.00	0.00	0.00	0.00	0.00	0.00	0.00	0.00	0.00
Total	100.48	99.37	99.13	99.95	99.38	100.00	98.59	99.02	100.43	97.99	99.17
No. Oxygens	6.00	6.00	6.00	6.00	6.00	6.00	6.00	3.00	3.00	3.00	3.00
Si	1.99	1.99	1.96	1.98	1.99	2.00	1.98	0.00	0.00	0.00	0.00
Ti	0.01	0.01	0.01	0.01	0.01	0.01	0.01	1.01	1.00	1.04	1.02
Al	0.08	0.08	0.08	0.08	0.07	0.07	0.07	0.00	0.00	0.00	0.00
Cr	0.00	0.00	0.00	0.00	0.00	0.00	0.00	0.00	0.00	0.00	0.00
Fe3+	0.00	0.00	0.02	0.00	0.00	0.00	0.00	0.00	0.00	0.00	0.00
Fe2+	0.34	0.34	0.34	0.34	0.35	0.36	0.36	0.93	0.93	0.91	0.92
Mn2+	0.01	0.01	0.01	0.02	0.01	0.01	0.01	0.03	0.02	0.03	0.03
Mg	0.68	0.66	0.67	0.67	0.66	0.67	0.66	0.03	0.03	0.03	0.03
Zn	0.00	0.00	0.00	0.00	0.00	0.00	0.00	0.00	0.00	0.00	0.00
Ca	0.86	0.89	0.88	0.88	0.88	0.85	0.88	0.00	0.00	0.00	0.00
Na	0.03	0.03	0.03	0.03	0.03	0.03	0.03	0.00	0.00	0.00	0.00
K	0.00	0.00	0.00	0.00	0.00	0.00	0.00	0.00	0.00	0.00	0.00

Cl	0.00	0.00	0.00	0.00	0.00	0.00	0.00	0.00	0.00	0.00	0.00
F	0.00	0.00	0.00	0.00	0.00	0.00	0.00	0.00	0.00	0.00	0.00
OH-	0.00	0.00	0.00	0.00	0.00	0.00	0.00	0.00	0.00	0.00	0.00
Total cations (S)	4	4	4	4	4	4	4	2	2	2	2

Mineral	**Pl**	**Pl**	**Pl**	**Pl**	**Ttn**	**Gt**	**Gt**	**Gt**	**Gt**	**Gt**	**Gt**
SiO2	56.75	57.16	57.04	56.71	29.67	37.03	38.35	36.83	37.41	36.43	37.20
TiO2	0.00	0.00	0.02	0.01	38.49	0.15	0.18	0.16	0.17	0.19	0.17
Al2O3	26.22	26.24	26.28	26.25	1.12	21.36	21.63	21.75	21.29	20.93	21.47
Cr2O3	0.00	0.01	0.01	0.00	0.01	0.02	0.03	0.04	0.05	0.03	0.04
FeO	0.04	0.06	0.05	0.01	0.35	24.88	24.70	24.73	24.75	24.83	24.89
MnO	0.00	0.00	0.00	0.01	0.06	2.49	2.34	2.35	2.41	2.30	2.31
MgO	0.00	0.00	0.01	0.01	0.02	4.50	4.63	4.81	4.69	4.58	4.73
ZnO	0.00	0.00	0.00	0.00	0.04	-0.02	0.01	-0.02	-0.01	-0.02	-0.03
CaO	8.74	8.66	8.67	8.63	27.08	8.57	8.23	8.52	8.57	8.59	8.62
Na2O	6.62	6.51	6.34	6.59	0.03	0.00	0.05	0.03	0.02	0.01	0.01
K2O	0.21	0.18	0.18	0.17	0.00	0.00	0.02	0.01	0.00	0.01	0.00
Cl	0.00	0.01	0.00	0.00	0.01	0.00	0.00	0.01	0.01	-0.01	-0.01
F	0.00	0.00	0.00	0.00	0.11	0.06	-0.01	0.01	0.05	0.07	0.04
H2O	0.00	0.00	0.00	0.00	0.00	0.00	0.00	0.00	0.00	0.00	0.00
OH = Cl ("Cl factor")	0.00	0.00	0.00	0.00	0.00	0.00	0.00	0.00	0.00	0.00	0.00
OH = F ("F factor")	0.00	0.00	0.00	0.00	0.05	0.02	0.00	0.01	0.02	0.03	0.02
Total	98.58	98.83	98.60	98.38	96.94	99.01	100.17	99.21	99.38	97.92	99.43
No. Oxygens	8.00	8.00	8.00	8.00	5.00	12.00	12.00	12.00	12.00	12.00	12.00
Si	2.58	2.59	2.59	2.58	1.00	2.93	2.99	2.90	2.95	2.91	2.93
Ti	0.00	0.00	0.00	0.00	0.97	0.01	0.01	0.01	0.01	0.01	0.01
Al	1.40	1.40	1.41	1.41	0.04	1.99	1.99	2.02	1.98	1.97	1.99
Cr	0.00	0.00	0.00	0.00	0.00	0.00	0.00	0.00	0.00	0.00	0.00
Fe3+	0.00	0.00	0.00	0.00	0.00	0.12	0.01	0.17	0.10	0.16	0.13
Fe2+	0.00	0.00	0.00	0.00	0.01	1.53	1.60	1.46	1.53	1.50	1.51
Mn2+	0.00	0.00	0.00	0.00	0.00	0.17	0.15	0.16	0.16	0.16	0.15
Mg	0.00	0.00	0.00	0.00	0.00	0.53	0.54	0.56	0.55	0.55	0.55
Zn	0.00	0.00	0.00	0.00	0.00	0.00	0.00	0.00	0.00	0.00	0.00
Ca	0.42	0.42	0.42	0.42	0.97	0.73	0.69	0.72	0.72	0.74	0.73
Na	0.58	0.57	0.56	0.58	0.00	0.00	0.01	0.01	0.00	0.00	0.00
K	0.01	0.01	0.01	0.01	0.00	0.00	0.00	0.00	0.00	0.00	0.00
Cl	0.00	0.00	0.00	0.00	0.00	0.00	0.00	0.00	0.00	0.00	0.00
F	0.00	0.00	0.00	0.00	0.01	0.01	0.00	0.00	0.01	0.02	0.01
OH-	0.00	0.00	0.00	0.00	0.00	0.00	0.00	0.00	0.00	0.00	0.00
Total cations (S)	5	5	5	5	3	8	8	8	8	8	8

MB2017-7

Mineral	Bi	Bi	Bi	Bi	Ru	Ru	Ru	Ru	Ru
SiO2	37.25	37.05	37.46	37.89	0.08	0.01	0.05	0.33	0.06
TiO2	2.55	2.42	2.67	2.84	99.02	99.30	98.36	98.06	98.20
Al2O3	17.29	17.40	17.37	17.30	0.10	0.04	0.07	0.23	0.07
Cr2O3	0.06	0.07	0.09	0.07	0.10	0.12	0.14	0.09	0.10
FeO	12.32	12.34	12.13	12.94	0.34	0.30	0.29	0.69	0.58
MnO	0.02	0.01	0.02	0.00	0.00	0.00	0.00	0.00	0.00
MgO	15.58	15.47	15.94	15.46	0.02	0.00	0.00	0.05	0.00
ZnO	0.06	0.06	0.07	0.05	0.03	0.03	0.00	0.00	0.02
CaO	0.07	0.06	0.10	0.05	0.01	0.00	0.07	0.04	0.08
Na2O	0.30	0.32	0.28	0.34	0.00	0.00	0.00	0.00	0.00
K2O	8.60	8.61	8.21	8.43	0.02	0.03	0.02	0.03	0.02
Cl	0.09	0.07	0.06	0.08	0.00	0.00	0.00	0.00	0.00
F	0.39	0.40	0.26	0.33	0.08	0.04	0.11	0.06	0.04
H2O	3.86	3.84	3.94	3.94	0.00	0.00	0.00	0.00	0.00
OH = Cl ("Cl factor")	0.02	0.02	0.01	0.02	0.00	0.00	0.00	0.00	0.00
OH = F ("F factor")	0.17	0.17	0.11	0.14	0.03	0.02	0.04	0.03	0.02
Total	94.42	94.10	94.54	95.62	99.77	99.85	99.05	99.54	99.17
No. Oxygens	11.00	11.00	11.00	11.00	2.00	2.00	2.00	2.00	2.00
Si	2.74	2.74	2.74	2.76	0.00	0.00	0.00	0.00	0.00
Ti	0.14	0.13	0.15	0.16	0.99	0.99	0.99	0.98	0.99
Al	1.50	1.52	1.50	1.48	0.00	0.00	0.00	0.00	0.00
Cr	0.00	0.00	0.01	0.00	0.00	0.00	0.00	0.00	0.00
Fe3+	0.04	0.04	0.07	0.04	0.00	0.00	0.00	0.00	0.00
Fe2+	0.72	0.72	0.67	0.75	0.00	0.00	0.00	0.01	0.01
Mn2+	0.00	0.00	0.00	0.00	0.00	0.00	0.00	0.00	0.00
Mg	1.71	1.70	1.74	1.68	0.00	0.00	0.00	0.00	0.00
Zn	0.00	0.00	0.00	0.00	0.00	0.00	0.00	0.00	0.00
Ca	0.01	0.00	0.01	0.00	0.00	0.00	0.00	0.00	0.00
Na	0.04	0.05	0.04	0.05	0.00	0.00	0.00	0.00	0.00
K	0.81	0.81	0.77	0.78	0.00	0.00	0.00	0.00	0.00
Cl	0.01	0.01	0.01	0.01	0.00	0.00	0.00	0.00	0.00
F	0.09	0.09	0.06	0.08	0.00	0.00	0.00	0.00	0.00
OH-	1.90	1.90	1.93	1.91	0.00	0.00	0.00	0.00	0.00
Total cations (S)	7.72	7.73	7.69	7.70	1.00	1.00	1.00	1.00	1.00

Mineral	Pl	Pl	Pl	Pl	Pl	Pl	Pl	Pl	Pl	Pl	Pl
SiO2	62.35	58.99	63.39	59.34	62.00	61.51	60.51	61.04	59.45	60.58	61.15
TiO2	0.00	0.00	0.00	0.00	0.03	0.01	0.00	0.01	-0.01	0.00	0.01
Al2O3	25.44	24.72	23.96	24.35	24.70	24.89	24.55	24.40	24.88	24.68	24.54
Cr2O3	0.00	0.00	0.00	0.00	-0.01	0.01	-0.01	0.02	0.00	-0.01	-0.01
FeO	0.01	0.00	0.03	0.00	0.00	0.01	-0.01	0.02	0.03	-0.02	0.02
MnO	0.00	0.00	0.00	0.00	0.00	0.00	0.00	0.00	0.01	0.00	-0.02
MgO	0.00	0.00	0.04	0.00	0.01	0.05	0.00	0.01	0.03	-0.01	0.00
ZnO	0.00	0.00	0.00	0.00	0.01	-0.02	0.02	-0.04	0.02	0.00	-0.01
CaO	5.28	5.79	3.57	5.30	5.49	5.61	5.76	5.68	6.11	5.38	5.39
Na2O	9.13	8.66	10.87	8.51	8.95	8.90	8.40	8.65	8.27	8.96	8.81
K2O	0.10	0.08	0.10	0.06	0.04	0.04	0.05	0.07	0.08	0.09	0.10
Cl	0.01	0.01	0.01	0.01	0.00	-0.01	-0.01	0.00	0.00	0.00	0.00
F	0.00	0.00	0.00	0.00	0.00	0.00	0.02	0.01	-0.01	0.03	-0.01
H2O	0.00	0.00	0.00	0.00	0.00	0.00	0.00	0.00	0.00	0.00	0.00
OH = Cl ("Cl factor")	0.00	0.00	0.00	0.00	0.00	0.00	0.00	0.00	0.00	0.00	0.00
OH = F ("F factor")	0.00	0.00	0.00	0.00	0.00	0.00	0.01	0.01	0.00	0.01	0.00
Total	102.32	98.25	101.96	97.56	101.22	101.00	99.28	99.85	98.86	99.66	99.97
No. Oxygens	8.00	8.00	8.00	8.00	8.00	8.00	8.00	8.00	8.00	8.00	8.00
Si	2.69	2.65	2.72	2.69	2.71	2.69	2.70	2.71	2.67	2.68	2.70
Ti	0.00	0.00	0.00	0.00	0.00	0.00	0.00	0.00	0.00	0.00	0.00

Al	1.29	1.31	1.21	1.30	1.27	1.28	1.29	1.28	1.31	1.29	1.28
Cr	0.00	0.00	0.00	0.00	0.00	0.00	0.00	0.00	0.00	0.00	0.00
Fe3+	0.00	0.00	0.00	0.00	0.00	0.00	0.00	0.00	0.00	0.00	0.00
Fe2+	0.00	0.00	0.00	0.00	0.00	0.00	0.00	0.00	0.00	0.00	0.00
Mn2+	0.00	0.00	0.00	0.00	0.00	0.00	0.00	0.00	0.00	0.00	0.00
Mg	0.00	0.00	0.00	0.00	0.00	0.00	0.00	0.00	0.00	0.00	0.00
Zn	0.00	0.00	0.00	0.00	0.00	0.00	0.00	0.00	0.00	0.00	0.00
Ca	0.24	0.28	0.16	0.26	0.26	0.26	0.28	0.27	0.29	0.26	0.26
Na	0.76	0.75	0.90	0.75	0.76	0.76	0.73	0.74	0.72	0.77	0.76
K	0.01	0.00	0.01	0.00	0.00	0.00	0.00	0.00	0.00	0.01	0.01
Cl	0.00	0.00	0.00	0.00	0.00	0.00	0.00	0.00	0.00	0.00	0.00
F	0.00	0.00	0.00	0.00	0.00	0.00	0.00	0.00	0.00	0.00	0.00
OH-	0.00	0.00	0.00	0.00	0.00	0.00	0.00	0.00	0.00	0.00	0.00
Total cations (S)	5.00	5.00	5.00	5.00	5.00	5.00	5.00	5.00	5.00	5.00	5.00

Mineral	**Gt**	**Gt**	**Gt**	**Gt**	**Gt**	**Gt**	**Gt**	**Gt**	**Gt**
SiO2	37.68	37.68	37.47	37.86	39.21	39.03	39.32	37.96	38.21
TiO2	0.01	0.02	0.02	0.01	0.01	0.00	0.00	0.00	0.00
Al2O3	21.68	21.79	21.56	21.49	22.16	21.78	22.96	21.43	21.76
Cr2O3	0.02	0.02	0.03	0.01	0.02	0.01	0.02	0.02	0.03
FeO	28.24	27.69	28.22	28.29	28.07	28.38	27.38	28.68	28.30
MnO	0.80	0.76	0.77	0.82	0.79	0.75	0.82	0.79	0.80
MgO	9.51	9.38	9.12	9.31	9.66	9.61	10.09	9.39	9.47
ZnO	0.00	0.00	0.00	0.00	0.02	0.00	0.00	0.00	0.05
CaO	1.20	1.20	1.25	1.26	1.25	1.22	1.23	1.27	1.28
Na2O	0.01	0.07	0.03	0.01	0.01	0.01	0.05	0.00	0.01
K2O	0.00	0.01	0.01	0.02	0.00	0.00	0.00	0.01	0.00
Cl	0.00	0.00	0.00	0.00	0.00	0.00	0.00	0.00	0.00
F	0.00	0.00	0.00	0.00	0.00	0.00	0.00	0.00	0.00
H2O	0.00	0.00	0.00	0.00	0.00	0.00	0.00	0.00	0.00
OH = Cl ("Cl factor")	0.00	0.00	0.00	0.00	0.00	0.00	0.00	0.00	0.00
OH = F ("F factor")	0.00	0.00	0.00	0.00	0.00	0.00	0.00	0.00	0.00
Total	99.15	98.62	98.48	99.07	101.20	100.78	101.88	99.56	99.90
No. Oxygens	12.00	12.00	12.00	12.00	12.00	12.00	12.00	12.00	12.00
Si	2.93	2.94	2.93	2.95	2.98	2.98	2.95	2.94	2.95
Ti	0.00	0.00	0.00	0.00	0.00	0.00	0.00	0.00	0.00
Al	1.98	2.00	1.99	1.97	1.99	1.96	2.03	1.96	1.98
Cr	0.00	0.00	0.00	0.00	0.00	0.00	0.00	0.00	0.00
Fe3+	0.16	0.13	0.15	0.14	0.05	0.07	0.06	0.16	0.13
Fe2+	1.67	1.67	1.70	1.70	1.73	1.74	1.66	1.70	1.69
Mn2+	0.05	0.05	0.05	0.05	0.05	0.05	0.05	0.05	0.05
Mg	1.10	1.09	1.06	1.08	1.09	1.09	1.13	1.08	1.09
Zn	0.00	0.00	0.00	0.00	0.00	0.00	0.00	0.00	0.00
Ca	0.10	0.10	0.11	0.10	0.10	0.10	0.10	0.11	0.11
Na	0.00	0.01	0.00	0.00	0.00	0.00	0.01	0.00	0.00
K	0.00	0.00	0.00	0.00	0.00	0.00	0.00	0.00	0.00
Cl	0.00	0.00	0.00	0.00	0.00	0.00	0.00	0.00	0.00
F	0.00	0.00	0.00	0.00	0.00	0.00	0.00	0.00	0.00
OH-	0.00	0.00	0.00	0.00	0.00	0.00	0.00	0.00	0.00
Total cations (S)	8.00	8.00	8.00	8.00	8.00	8.00	8.00	8.00	8.00

Appendix 4B: Geochronology and REEs

MB2017-1 zircon

	Source file	Final207_235	Final207 235 P	Final206_238	Final206 238 P	ErrorCorrelation	FinalAge207 23	FinalAge207 23	FinalAge206 23	FinalAge206 23	FinalAge207 20	FinalAge207_206_Prop25E
MB2017_1_4	MB2017-1 zr - 6	0.548	0.022	0.06828	0.0013	0.1969	442	14	425.7	7.8	540	86
MB2017_1_7	MB2017-1 zr - 1	0.539	0.096	0.0715	0.0039	0.021524	440	64	444	24	360	370
MB2017_1_3	MB2017-1 zr - 4	0.551	0.024	0.0718	0.0014	0.01	447	15	446.9	8.4	423	90
MB2017_1_5	MB2017-1 zr - 7	0.572	0.016	0.07205	0.0012	0.14662	462	10	448.5	7.1	499	66
Output_1_4	MB2017-1BZrTi	0.565	0.021	0.0731	0.0014	0.16364	454	14	454.5	8.3	449	80
MB2017_1_2	MB2017-1 zr - 3	0.568	0.025	0.07427	0.0012	0.01	456	17	461.8	7	390	110
Output_1_2	MB2017-1BZrTi	0.58	0.019	0.07468	0.0011	0.11413	466	12	464.3	6.3	440	58
Output_1_7	MB2017-1BZrTi	0.593	0.017	0.07537	0.0011	0.18462	475	11	468.4	6.8	492	49
MB2017_1_6	MB2017-1 zr - 8	0.578	0.03	0.0755	0.0016	0.22016	463	20	469	9.4	420	120
Output_1_10	MB2017-1BZrTi	0.64	0.19	0.0763	0.005	0.01	460	120	473	30	280	550
MB2017_1_1	MB2017-1 zr - 1	0.588	0.025	0.0778	0.0014	0.33572	467	16	482.8	8.5	390	97
Output_1_8	MB2017-1BZrTi	0.6	0.11	0.0779	0.0051	0.01	486	63	487	30	320	360
Output_1_3	MB2017-1BZrTi	0.64	0.13	0.0812	0.0042	0.091348	480	86	502	25	240	390
Output_1_3	MB2017-1B - 3	0.6	0.099	0.0736	0.0043	0.020624	428	67	456	26	200	330
Output_1_7	MB2017-1B - 7	0.5839	0.0074	0.0747	0.0011	0.16431	466.6	4.7	464.4	6.9	464	29
Output_1_2	MB2017-1B - 2	0.596	0.014	0.07481	0.0012	0.016736	473.6	9	465.1	7.2	485	55
Output_1_1	MB2017-1B - 1	0.57	0.092	0.0746	0.0042	0.013614	413	62	466	26	70	310
Output_1_4	MB2017-1B - 4	0.59	0.015	0.07527	0.0013	0.018659	469.8	9.6	467.8	7.7	453	61
Output_1_8	MB2017-1B - 8	0.68	0.12	0.0759	0.004	0.07764	469	74	470	24	310	350
Output_1_5	MB2017-1B - 5	0.77	0.1	0.0813	0.0038	0.093663	536	60	506	24	530	270
Output_1_10	MB2017-1B - 10	0.66	0.12	0.0911	0.0055	0.15342	452	79	560	32	-10	340
Output_1_9	MB2017-1B - 9	0.752	0.056	0.0933	0.0029	0.3936	565	34	575	17	450	150
Output_1_6	MB2017-1B - 6	0.97	0.18	0.076	0.0052	0.10187	585	96	471	32	830	390
Discordant or detrital analyses												

	Source file	Si_ppm_m29	La_ppm_m139	Ce_ppm_m140	Pr_ppm_m141	Nd_ppm_m146	Sm_ppm_m147	Eu_ppm_m153	Gd_ppm_m157	Tb_ppm_m159	Dy_ppm_m163	Ho_ppm_m165	Er_ppm_m	Tm_ppm_r	Yb_ppm_r	Lu_ppm_r	Th_ppm_r	U_ppm_m238
MB2017_1_4	MB2017-1 zr - 6	1.41E+05	0.027	0.68	0.022	Below LOD	0.09	0	0.69	0.258	4.44	1.87	9.71	2.19	21.9	5.49	27.6	190.2
MB2017_1_7	MB2017-1 zr - 1	1.52E+05	Below LOD	0.09	Below LOD	Below LOD	0.39	0.237	2.43	0.879	13.32	6.37	38.4	9.09	103.1	28.68	1.595	10.22
MB2017_1_3	MB2017-1 zr - 4	1.43E+05	0.006	0.9	0.016	0.38	0.029	0.288	2.13	0.7	9.52	3.83	20.4	4.05	41.9	9.68	36.01	232.5
MB2017_1_5	MB2017-1 zr - 7	1.53E+05	Below LOD	0.76	0	0	Below LOD	0.073	0.97	0.333	5.72	2.13	11.53	2.7	27.05	6.43	44.11	375.1
Output_1_4	MB2017-1BZrTi	1.52E+05	Below LOD	0.66	0	0	0.13	0.127	1.3	0.478	6.74	2.81	13.89	2.65	27.9	6.01	43.58	250.3
MB2017_1_2	MB2017-1 zr - 3	1.44E+05	0	0.68	0	0	0	0.118	1.74	0.604	7.89	3.61	18.8	3.95	40.1	9.2	34.9	201.3
Output_1_2	MB2017-1BZrTi	1.55E+05	0	0.8	Below LOD	0	0.2	0.061	1.1	0.337	5.84	2.46	12.54	2.96	28.5	6.57	42.55	320
Output_1_7	MB2017-1BZrTi	1.53E+05	0	0.91	0	0 Below LOD	Below LOD	0.128	2.44	0.97	14.76	6.23	36.5	7.92	78	18.51	72.5	421.4
MB2017_1_6	MB2017-1 zr - 8	1.49E+05	0	0.212	0 Below LOD	Below LOD	0	Below LOD	0.48	0.209	4.22	1.81	10.72	2.6	30.1	7.97	13.33	107.7
Output_1_10	MB2017-1BZrTi	1.52E+05	0	0.076	0	0 Below LOD	0	0.101	1.1	0.486	7.46	4.13	25.9	6.29	76.6	19.6	0.884	6.31
MB2017_1_1	MB2017-1 zr - 1	1.48E+05	Below LOD	0.338	Below LOD	Below LOD	0.125	0.058	0.98	0.443	6.9	3.24	18.82	4.75	55.2	14.75	9.73	82.2
Output_1_8	MB2017-1BZrTi	1.53E+05	0	0.109	Below LOD	Below LOD	Below LOD	0	0.39	0.271	3.45	2.02	12.66	3.35	38.9	11.1	1.068	10.66
Output_1_3	MB2017-1BZrTi	1.53E+05	Below LOD	0.078	Below LOD	Below LOD	0	Below LOD	0.45	0.248	4.52	2.53	15.73	3.98	47.6	12.79	1.02	7.39
Output_1_5	MB2017-1BZrTi	1.54E+05	0	0.119	0	0	0 Below LOD	0	0.4	0.175	3.88	1.95	13.12	3.67	42.2	12.16	1.36	8.21
Output_1_9	MB2017-1BZrTi	1.55E+05	0	0.097	Below LOD	Below LOD	0	Below LOD	0.5	0.22	4.76	2.4	14.9	4.23	51.2	14.54	0.734	11.24
Output_1_6	MB2017-1BZrTi	1.53E+05	0	0.115	Below LOD	Below LOD	Below LOD	0	0.4	0.296	4.07	2.19	12.83	3.7	41.1	11.69	1.707	5.39
Output_1_1	MB2017-1BZrTi	1.54E+05	Below LOD	0.143	Below LOD	Below LOD	0	Below LOD	0.59	0.282	4.66	2.66	16.7	4.4	56.6	16.83	1.214	8.01
Discordant or detrital analyses																		

MB2017-7 zircon

	Source file	Final207_235	Final207_235_	Final206_238	Final206_238_	ErrorCorrelatio	FinalAge207_2	FinalAge207_2	FinalAge206_2	FinalAge206_2	FinalAge207_2	FinalAge207_2(
MB2017_7_21	MB2017-7 zr -	0.566	0.016	0.07093	0.0012	0.11134	457	11	441.8	7.2	527	75
Output_4_20	MB2017-7A Zr	0.558	0.021	0.07309	0.0012	0.25834	451	14	454.7	7.2	402	76
MB2017_7_13	MB2017-7 zr -	0.578	0.013	0.07331	0.0011	0.01	462.5	8.7	456	6.3	467	62
MB2017_7_7	MB2017-7 - 7	0.576	0.026	0.07345	0.0016	0.22142	461.6	17	456.9	9.5	494	130
MB2017_7_10	MB2017-7 zr -	0.579	0.015	0.07347	0.0011	0.056666	463.2	9.5	457	6.6	480	63
Output_4_13	MB2017-7A Zr	0.5714	0.013	0.07398	0.00094	0.077601	458.7	8.5	460.1	5.6	434	41
MB2017_7_27	MB2017-7 - 37	0.593	0.028	0.07406	0.0017	0.1562	472	18	460.5	10	502	140
Output_4_4	MB2017-7A - 4	0.587	0.0099	0.07432	0.0012	0.040868	468.4	6.3	462.1	7.1	473	40
Output_4_6	MB2017-7A Zr	0.607	0.018	0.07443	0.00099	0.041302	481.5	11	462.8	5.9	559	57
Output_4_22	MB2017-7A - 2	0.6	0.085	0.0746	0.0042	0.2221	440	52	463	25	210	250
MB2017_7_16	MB2017-7 zr -	0.58	0.015	0.0745	0.0011	0.2463	463.9	9.4	463.2	6.4	461	61
Output_4_14	MB2017-7A - 1	0.5842	0.0068	0.07484	0.0011	0.16854	466.9	4.4	465.3	6.8	456	27
Output_4_6	MB2017-7A - 6	0.5764	0.0065	0.07501	0.0011	0.24556	461.9	4.2	466.3	6.8	421	25
Output_4_21	MB2017-7A - 2	0.577	0.015	0.07511	0.0012	0.10914	462.3	9.8	466.9	7.4	406	58
Output_4_23	MB2017-7A Zr	0.589	0.017	0.07522	0.0011	0.21858	469.3	11	467.5	6.6	453	54
MB2017_7_11	MB2017-7 zr -	0.5909	0.0097	0.07527	0.0011	0.11574	471.3	6.2	467.8	6.5	484	54
Output_4_4	MB2017-7A Zr	0.601	0.018	0.07537	0.0011	0.01	477.1	11	468.4	6.4	507	65
Output_4_9	MB2017-7A - 9	0.5808	0.009	0.07536	0.0012	0.11935	464.5	5.8	468.4	7	423	36
Output_4_11	MB2017-7A - 1	0.5917	0.0091	0.07545	0.0012	0.20191	471.5	5.8	468.9	7.1	458	34
MB2017_7_6	MB2017-7 - 6	0.5827	0.024	0.07545	0.0016	0.28995	466.1	16	468.9	9.8	460	130
Output_4_1	MB2017-7A Zr	0.591	0.014	0.07551	0.00094	0.11835	471.1	9	469.3	5.6	466	42
Output_4_9	MB2017-7A Zr	0.5902	0.014	0.0757	0.0009	0.01	470.7	8.6	470.4	5.4	457	42
MB2017_7_2	MB2017-7 - 2	0.5864	0.025	0.07577	0.0015	0.0052347	468.3	16	470.8	9.3	461	130
MB2017_7_8	MB2017-7 zr -	0.608	0.015	0.07593	0.0012	0.23121	481.9	9.7	471.8	7.2	504	60
MB2017_7_17	MB2017-7 zr -	0.593	0.0076	0.07594	0.0011	0.23437	473.3	4.9	471.9	6.7	472	42
MB2017_7_20	MB2017-7 - 29	0.6081	0.025	0.07603	0.0016	0.28607	482.1	16	472.4	9.3	504	130
MB2017_7_5	MB2017-7 - 5	0.5968	0.025	0.07606	0.0016	0.12569	474.9	16	472.5	9.4	470	130
MB2017_7_4	MB2017-7 - 4	0.5935	0.025	0.07615	0.0016	0.20466	472.8	16	473.1	9.4	458	130
MB2017_7_25	MB2017-7 - 35	0.612	0.027	0.07622	0.0018	0.21012	484.6	17	473.5	11	525	130
MB2017_7_12	MB2017-7 - 16	0.601	0.028	0.07637	0.0017	0.001	480	20	474.4	10	510	140
MB2017_7_9	MB2017-7 - 9	0.5932	0.024	0.0764	0.0016	0.15317	472.6	16	474.6	9.5	447	130
Output_4_1	MB2017-7A - 1	0.594	0.01	0.07645	0.0012	0.2298	473	6.4	474.9	7.3	438	38
MB2017_7_11	MB2017-7 - 15	0.615	0.027	0.07655	0.0016	0.32372	485.9	17	475.5	9.7	513	130
MB2017_7_14	MB2017-7 - 19	0.597	0.027	0.07695	0.0016	0.001	475	17	477.9	9.7	462	140
Output_4_24	MB2017-7A - 2	0.592	0.011	0.07717	0.0013	0.093269	471.6	7.3	479.2	7.5	411	45
MB2017_7_3	MB2017-7 - 3	0.613	0.027	0.07745	0.0016	0.001	484.9	17	480.9	9.8	513	130
MB2017_7_10	MB2017-7 - 14	0.62	0.028	0.07762	0.0017	0.34617	489.2	17	481.9	9.9	511	140
MB2017_7_5	MB2017-7 zr -	0.61	0.023	0.0787	0.0014	0.01	483	14	488.2	8.4	430	110
Output_4_18	MB2017-7A Zr	0.637	0.025	0.079	0.0012	0.1761	500	16	490.1	7	516	80
MB2017_7_22	MB2017-7 zr -	0.627	0.046	0.0792	0.0022	0.24142	492	29	492	13	550	160
MB2017_7_26	MB2017-7 zr -	0.64	0.012	0.07966	0.0011	0.10948	502	7.5	494.1	6.8	504	48
MB2017_7_26	MB2017-7 - 36	0.632	0.036	0.07494	0.0017	0.57916	496	22	465.8	10	622	140
MB2017_7_6	MB2017-7 zr -	0.648	0.022	0.07661	0.0014	0.01	506	14	475.8	8.1	602	88
MB2017_7_19	MB2017-7 - 25	1.029	0.044	0.07701	0.0017	0.14253	718	22	478.2	10	1544	110
Output_4_26	MB2017-7A - 2	0.663	0.013	0.0821	0.0016	0.16538	515	8.3	508.5	9.6	521	43
MB2017_7_34	MB2017-7 - 46	0.691	0.031	0.0823	0.0019	0.20615	532.4	19	510	11	606	130
MB2017_7_30	MB2017-7 - 40	0.688	0.035	0.0838	0.0019	0.064235	530	21	518.6	12	572	140
MB2017_7_29	MB2017-7 - 39	0.732	0.041	0.0865	0.0023	0.26674	557	24	535	13	650	150
Output_4_21	MB2017-7A Zr	0.687	0.055	0.0871	0.0032	0.32613	527	33	538	19	430	160
MB2017_7_12	MB2017-7 zr -	0.745	0.024	0.0914	0.0018	0.01	564	14	563.5	10	530	93
Output_4_5	MB2017-7A - 5	0.815	0.018	0.0914	0.0015	0.22112	606	10	563.8	9.1	740	48
Output_4_5	MB2017-7A Zr	0.766	0.028	0.0922	0.0014	0.10528	576	16	568.5	8.1	579	75
Output_4_10	MB2017-7A - 1	0.761	0.015	0.09336	0.0016	0.044356	573.5	8.8	575.3	9.2	545	46
Output_4_10	MB2017-7A Zr	0.758	0.024	0.09346	0.0013	0.15239	572	14	575.9	7.6	545	58
MB2017_7_17	MB2017-7 - 23	0.891	0.052	0.0995	0.0027	0.39603	644	28	611	16	747	150
Output_4_19	MB2017-7A - 1	0.943	0.012	0.09968	0.0017	0.30627	673.8	6.4	612.5	9.7	871	25
Output_4_15	MB2017-7A Zr	0.864	0.021	0.10184	0.0013	0.23873	631.8	11	625.2	7.7	637	41
Output_4_2	MB2017-7A Zr	0.843	0.035	0.1026	0.002	0.01	623	21	629.3	12	570	100
Output_4_16	MB2017-7A - 1	0.852	0.016	0.10364	0.0018	0.090748	624.7	8.8	636.4	11	568	39
Output_4_16	MB2017-7A Zr	0.91	0.03	0.1054	0.0016	0.01	655	16	645.7	9.6	662	71
Output_4_2	MB2017-7A - 2	0.912	0.023	0.1061	0.0018	0.0091135	656	12	649.9	11	651	57
Output_4_17	MB2017-7A Zr	0.982	0.046	0.1061	0.0024	0.051869	692	24	650	14	805	100
Output_4_17	MB2017-7A - 1	0.895	0.022	0.10626	0.0017	0.06844	647	12	650.9	10	605	57
Output_4_3	MB2017-7A Zr	1.021	0.028	0.1066	0.0015	0.28601	714	14	653.1	8.7	898	49
MB2017_7_15	MB2017-7 zr -	0.909	0.019	0.1069	0.0016	0.01	656	10	654.7	9.2	663	55
Output_4_13	MB2017-7A - 1	1.159	0.03	0.1187	0.0024	0.01	780	15	723	14	930	47
MB2017_7_33	MB2017-7 - 45	1.152	0.053	0.1225	0.0028	0.10311	777	25	744.9	16	862	130
Output_4_3	MB2017-7A - 3	1.201	0.022	0.123	0.0025	0.3001	800.4	10	747.7	14	940	26
MB2017_7_18	MB2017-7 - 24	1.239	0.078	0.1231	0.0034	0.036004	816	35	749	20	1000	160
Output_4_8	MB2017-7A - 8	1.29	0.023	0.1279	0.0023	0.12389	841	9.8	776	13	1003	29
MB2017_7_23	MB2017-7 - 33	1.524	0.068	0.1391	0.003	0.3359	939	27	839.4	17	1169	120
MB2017_7_18	MB2017-7 zr -	1.46	0.028	0.1438	0.0023	0.33067	914	12	865.8	13	999	49
Output_4_12	MB2017-7A Zr	1.405	0.048	0.1455	0.0021	0.039414	889	20	875.8	12	900	67
MB2017_7_19	MB2017-7 zr -	1.428	0.026	0.1457	0.0023	0.25542	900	11	876.6	13	950	45
MB2017_7_23	MB2017-7 zr -	1.591	0.04	0.148	0.0024	0.23806	966	16	889.5	14	1155	52
Output_4_18	MB2017-7A - 1	1.395	0.049	0.1496	0.0041	0.01	882	22	898	23	810	67
MB2017_7_24	MB2017-7 zr -	1.499	0.049	0.15	0.0027	0.12124	929	20	901	15	994	73
Output_4_24	MB2017-7A Zr	1.478	0.046	0.1512	0.0024	0.44733	920	19	908	13	930	47
MB2017_7_32	MB2017-7 - 44	1.523	0.063	0.1524	0.0033	0.41983	939.4	25	914.4	19	978	110
MB2017_7_21	MB2017-7 - 31	1.628	0.077	0.153	0.0037	0.001	980	30	917	21	1125	120
Output_4_7	MB2017-7A - 7	1.416	0.03	0.1532	0.0026	0.053265	893	12	918.7	14	812	46
Output_4_7	MB2017-7A Zr	1.519	0.057	0.1534	0.0028	0.16109	938	22	919	16	963	69
Output_4_25	MB2017-7A - 2	1.558	0.024	0.1586	0.0025	0.23555	952.4	9.6	949.2	14	944	32
MB2017_7_7	MB2017-7 zr -	1.637	0.03	0.1591	0.0026	0.33465	984	11	951.8	14	1059	46
MB2017_7_31	MB2017-7 - 43	1.585	0.068	0.16	0.0033	0.18792	963	27	956.7	18	973	120
Output_4_19	MB2017-7A Zr	1.666	0.054	0.1627	0.0023	0.0038681	994	20	971.8	12	1023	60
MB2017_7_22	MB2017-7 - 32	1.795	0.078	0.1646	0.0036	0.21917	1043	28	982	20	1150	120
MB2017_7_25	MB2017-7 zr -	1.756	0.034	0.1646	0.0027	0.29056	1029	12	982.3	15	1108	42
MB2017_7_20	MB2017-7 zr -	1.973	0.021	0.17656	0.0023	0.18717	1106.1	7.2	1048.2	13	1206	33
MB2017_7_4	MB2017-7 zr -	1.873	0.035	0.1798	0.0027	0.16299	1071	12	1065.8	15	1054	44

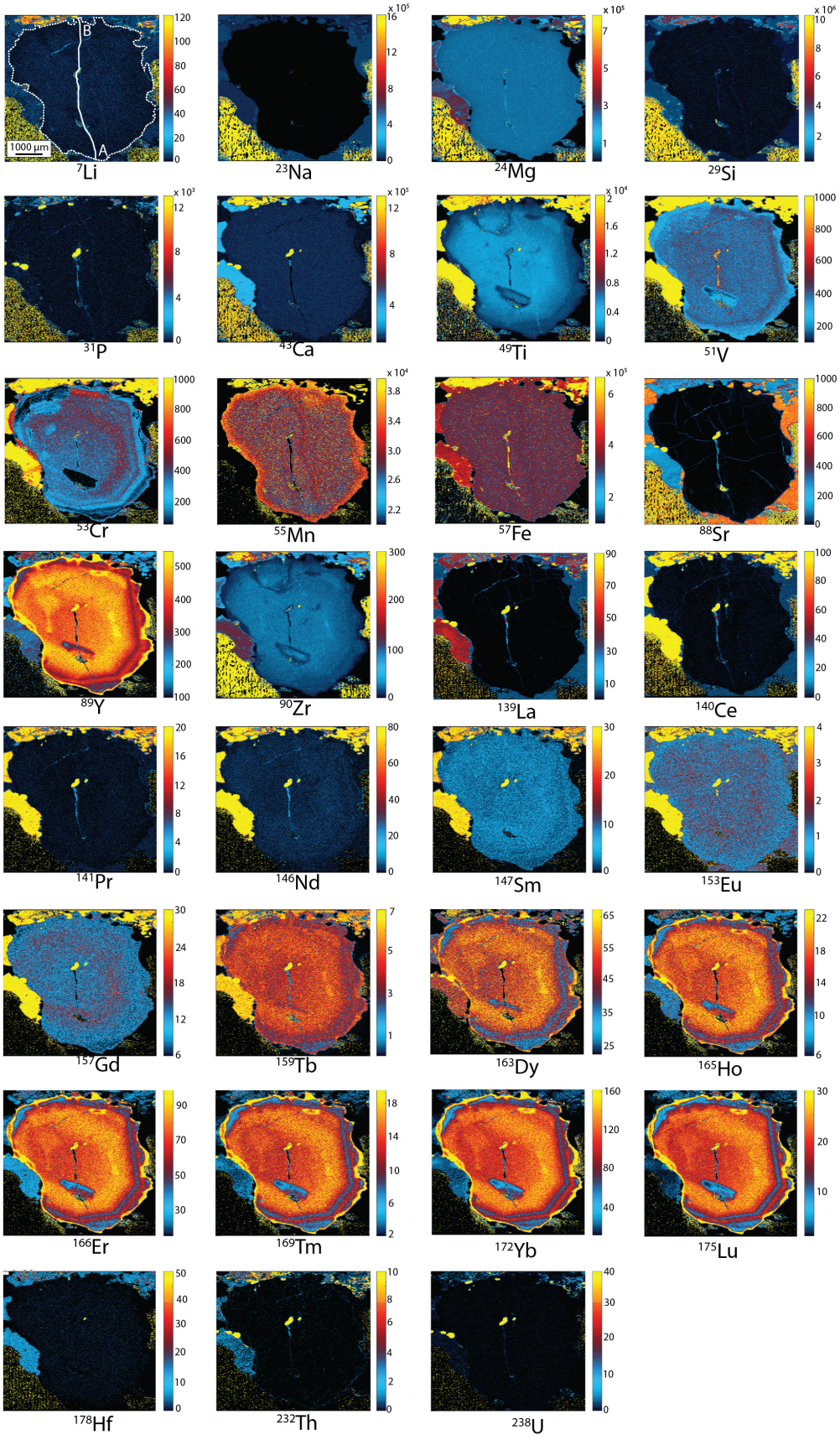
	Source file	Si_ppm_m29	La_ppm_m13	Ce_ppm_m14	Pr_ppm_m14	Nd_ppm_m14	Sm_ppm_m14	Eu_ppm_m15	Gd_ppm_m15	Tb_ppm_m15	Dy_ppm_m16	Ho_ppm_m16	Er_ppm_m	Tm_ppm_m	Yb_ppm_m	Lu_ppm_m	Th_ppm_m	U_ppm_m2
MB2017_7_21	MB2017-7 zr -	145700	0	0.83	0.03	0.34	0.34	0.294	2.56	0.855	12.17	4.74	21.83	4.57	42.4	9.42	58.63	298.4
Output_4_20	MB2017-7A Zr	156800	0.029	0.51	0	0	0	0	0	0.25	4.43	2.05	12.3	3.4	36.4	9.87	8.35	65.3
MB2017_7_13	MB2017-7 zr -	149900	0	0.648	0	0.24	1.78	0.193	14.74	4.22	22.35	2.71	5.35	0.532	3.19	0.503	25.68	437.4
MB2017_7_7	MB2017-7 - 7	144100	1.07	4.46	1.31	7.7	5.45	1.94	22.1	8.21	74.8	14.48	32.4	3.68	23.8	3.4	12.76	1011.2
MB2017_7_10	MB2017-7 zr -	154500	0	0.263	0.0035	0.24	1.36	0.259	13.3	7.38	79	14.29	29.2	2.94	15.93	2.43	5.88	448.7
Output_4_13	MB2017-7A Zr	151800	0	0.71	0	0.18	2.53	0.7	24	9.27	70.3	13.47	37.8	5.58	38	6.27	11.24	1188
MB2017_7_27	MB2017-7 - 37	142500	0.0028	0.315	0	0.18	1.32	0.283	12.06	5.81	63	16.82	62.1	10.07	78.1	13.45	4.45	320.5
Output_4_6	MB2017-7A Zr	157000	10.4	23.8	8	60	29.7	17.1	75	17.1	149	30.9	76.9	7.93	45.3	5.9	14.92	1365
MB2017_7_16	MB2017-7 zr -	146400	0	0.434	0.015	0.48	2	0.358	17.2	8.46	86.1	22.74	78.9	12.98	97.4	16.65	7.9	585
MB2017_7_26	MB2017-7 - 36	142000	0.018	0.6	0	0.57	1.38	0.47	18.3	7.54	66.1	13.04	38.7	5.99	46.3	8.66	10.55	534.7
Output_4_23	MB2017-7A Zr	149100	0	16.66	0.168	3.62	6.6	0.25	37.2	12.17	143.4	52.63	241.1	46.5	402.4	78.4	557.3	462.6
MB2017_7_11	MB2017-7 zr -	143700	2.79	4.71	2.02	11.1	6.24	3.52	27.2	9.15	79.3	16.14	41.2	5.96	38.6	6.41	11.67	676.2
Output_4_4	MB2017-7A Zr	149800	0	0.102	0	0	0.44	0.144	9.44	5.65	67.2	12.82	23.66	2.08	11.21	1.76	4.36	516
MB2017_7_6	MB2017-7 - 6	140300	0	0.52	0.017	0.073	1.81	0.37	16.7	7.38	73.8	15.2	33.5	3.17	17.2	2.25	13.86	1116.9
Output_4_1	MB2017-7A Zr	152000	0.397	3.28	0.78	5.92	3.69	1.17	17.6	9.04	131.3	36.3	95.4	10.65	59.9	7.88	8.42	761
Output_4_9	MB2017-7A Zr	151600	0.045	0.36	0.117	0.39	1.82	0.31	13.3	6.55	94	28	88.1	11.35	66.8	9.14	6.53	872.8
MB2017_7_2	MB2017-7 - 2	145800	0.03	0.58	0.044	0.63	1.21	0.48	13.2	6.61	72.5	15.35	34.5	3.32	19.22	2.39	12.46	1190
MB2017_7_8	MB2017-7 zr -	161400	0.34	1.56	0.286	1.78	2.29	0.99	13	5.98	65.3	17.75	60.4	9.34	69.8	11.81	8.91	1396
MB2017_7_17	MB2017-7 zr -	151500	2.24	14.2	3.28	21.8	11	4.3	17.9	5.73	87.9	34.37	166.1	35.09	286.5	47.67	6.87	1338
MB2017_7_20	MB2017-7 - 29	143000	0.4	3.5	0.3	1.09	2.35	1.11	18.8	8.57	93.9	24.54	84.8	13.73	96.3	15.44	11.04	1424
MB2017_7_5	MB2017-7 - 5	141700	0.017	0.481	0.027	0.47	2.41	0.48	22.2	10.36	107.1	21.6	46.9	4.9	28.44	3.6	13.97	1212
MB2017_7_4	MB2017-7 - 4	140900	0.051	0.76	0.039	0.99	1.98	0.61	19.5	9.41	98.2	20.29	43.1	4.63	23.8	2.9	15.05	1194
MB2017_7_25	MB2017-7 - 35	139300	3.16	9.5	3.22	19.7	13	7.2	36.7	10.78	116.4	34.5	135.7	24.89	186.6	30.7	6.61	713.6
MB2017_7_12	MB2017-7 - 16	146700	0	0.098	0	0	0.25	0.082	4.09	2.74	49.5	18.71	78.8	13.15	99.6	14.37	3.93	483
MB2017_7_9	MB2017-7 - 9	140700	0.144	1.05	0.12	0.81	1.99	0.93	18	9.32	124.9	33.95	94.6	11.58	66.1	9.11	6.18	943.4
MB2017_7_11	MB2017-7 - 15	139800	0.079	0.93	0.094	0.43	0.88	0.413	6.36	3.36	51.7	17.13	71.2	13.45	114.6	19.66	9.18	585.8
MB2017_7_14	MB2017-7 - 19	144200	0	0.189	0	0.13	0.92	0.211	11.71	7.02	101.2	28.66	74.8	8.42	46.5	6.34	5.75	638.8
MB2017_7_19	MB2017-7 - 25	146700	45.2	285	49.8	305	145	116.7	176.5	32	245.9	69.4	313.7	68	642	127	80.8	1382
MB2017_7_3	MB2017-7 - 3	146300	10.34	20.65	6.25	43.4	22.1	12.86	72.3	16.94	138.5	28.2	63.3	6.58	33.7	4.43	13.47	1095.3
MB2017_7_10	MB2017-7 - 14	139300	0.026	9.62	0.099	1.02	1.69	0.427	9.22	4.53	75.5	28.62	130.5	24.91	202.4	32.92	92.8	696.2
MB2017_7_5	MB2017-7 zr -	152300	0	0.184	0	0	0.44	0.119	6.9	3.47	40.5	7.58	18.5	2.2	14.4	2.4	6.21	288.4
Output_4_18	MB2017-7A Zr	152100	0	2.57	0.069	0.97	4.47	0.118	36.7	16.47	237.3	94.9	482.1	98.7	875	165.9	136	478.9
MB2017_7_22	MB2017-7 zr -	146700	0	0.43	0	0	0	0	0.95	0.474	6.13	2.3	14.2	3.15	37.6	9.25	18.09	110.5
MB2017_7_26	MB2017-7 zr -	154700	0.06	0.325	0.014	0.17	0.41	0.082	3.83	2.36	43.3	18.04	90	18.85	173.6	29.6	7.52	835
MB2017_7_34	MB2017-7 - 46	1.42E+05	0.8	6.2	1.28	7.6	3.37	2.38	8.66	4.2	57.1	17.05	59.9	10.09	79.6	13.35	11.51	414.9
MB2017_7_30	MB2017-7 - 40	1.45E+05	0.93	20	0.91	6.6	5.35	2.48	17.8	5.39	58.8	19.4	88.9	18.41	165.8	31.27	173.4	366.7
MB2017_7_29	MB2017-7 - 39	1.44E+05	2.03	24.5	2.09	12.1	7.7	3.65	18.5	4.4	47.6	16.04	74.3	15.62	147.3	29.7	192	388
Output_4_21	MB2017-7A Zr	1.50E+05	0	9.54	0.057	0.65	1.66	0.255	11.11	4.13	54.7	21.24	105.9	21.68	200.5	40.7	70.4	110.1
MB2017_7_12	MB2017-7 zr -	1.58E+05	4.63	23.63	3.31	25.7	14.4	7.64	51.8	13.25	150.2	50.03	221.5	41.5	349.6	65.9	207.6	188.1
Output_4_5	MB2017-7A Zr	1.49E+05	0	0.73	0	0	0.25	0.224	4.72	2.99	65.2	35.41	207.6	45.04	408.8	74.3	5.81	302
Output_4_10	MB2017-7A Zr	1.52E+05	0	32.59	0.069	1.04	2.92	0.73	12	3.79	43.2	15.23	70.7	14.68	132.4	25.79	329.6	328.6
MB2017_7_17	MB2017-7 - 23	1.45E+05	0.05	14.08	0.077	1.11	2.15	0.33	14.3	5.09	68.2	26.54	130.4	28.46	273.6	59.8	66.48	169.7
Output_4_15	MB2017-7A Zr	1.54E+05	0	1.65	0.024	0.56	1.6	0.1	9.85	3.73	49.1	18.12	84.7	17.46	160.4	31.66	68.59	174.7
Output_4_2	MB2017-7A Zr	1.48E+05	0.038	8.56	0.456	9.9	17.3	0.84	93.3	26.7	287	94.1	394	70.2	560	102	232.9	194.5
Output_4_16	MB2017-7A Zr	1.53E+05	0	13.6	0.017	0.52	1.34	0.138	9.27	3.54	45.9	18.59	95.1	20.83	196.9	42.09	50.61	126
Output_4_17	MB2017-7A Zr	1.45E+05	1.74	4.92	1.71	10.5	5.87	3.05	19	5.3	65	20.78	84.4	13.57	99	15.93	7.36	475.9
Output_4_3	MB2017-7A Zr	1.46E+05	7.59	43.9	10.55	60.6	25.8	18.3	33.7	7.87	81.9	23.81	110.8	25.27	278	56.1	19.51	880
MB2017_7_15	MB2017-7 zr -	1.57E+05	0	0.405	0	0.2	2.14	0	17.6	9.28	143.1	55.98	273.2	55.6	493.7	94.4	51.51	547.2
MB2017_7_33	MB2017-7 - 45	1.37E+05	0.296	13.28	0.303	3.71	4.37	0.71	22.8	7.51	82.8	28.06	125.3	24.56	207.8	39.7	173.4	350.3
MB2017_7_18	MB2017-7 - 24	1.40E+05	0.76	15.2	0.35	2.61	2.44	0.359	12.3	3.9	49	18.9	95.3	20.09	195.7	40	45.3	85.2
MB2017_7_23	MB2017-7 - 33	1.42E+05	0.077	26.13	0.086	1.04	1.72	0.297	8.55	3.2	42.1	16.83	86.3	19.44	190.5	39.78	260.1	351.9
MB2017_7_18	MB2017-7 zr -	1.50E+05	0.52	2.66	0.431	3.14	5.61	0.25	42.4	15.27	177.9	58.6	266.9	52.5	453	90	91.6	604
Output_4_12	MB2017-7A Zr	1.55E+05	0.047	6.7	0.34	4.24	6	0.35	28.4	7.61	79.6	26.5	117.3	22.24	187.9	35.6	116.5	161.7
MB2017_7_19	MB2017-7 zr -	1.64E+05	2.17	25.5	2.91	17.9	10.5	5.21	18.5	5.9	78.1	29.77	150.2	34.2	321.4	62.1	176.3	819.4
MB2017_7_23	MB2017-7 zr -	1.43E+05	0	7.36	0.056	1.13	2.64	0.29	17.3	7.21	85.5	27.3	123.2	24.5	218.9	41.5	126.6	408.8
MB2017_7_24	MB2017-7 zr -	1.39E+05	0.6	16.7	0.22	2.27	4.4	0.11	26.3	8.2	107.1	38.2	181.6	34.69	314.6	62.7	93.2	223.1
Output_4_24	MB2017-7A Zr	1.62E+05	54.8	314.6	56.2	345	147.5	117.6	201.4	31.6	228.2	57.3	218.7	42.8	378.2	75.9	1312	921
MB2017_7_32	MB2017-7 - 44	1.41E+05	0.187	23.8	0.358	4.66	6.77	0.59	35.3	11.58	140	49.7	229.4	43.4	371.6	69	527	549.9
MB2017_7_21	MB2017-7 - 31	1.49E+05	0.65	21.17	0.5	5.1	3.24	1.3	14.3	4.58	52.5	19.08	90	18.86	171.6	34.4	117.2	202.3
Output_4_7	MB2017-7A Zr	1.43E+05	0.31	10.71	0.6	8.52	11.7	0.85	45.1	12.44	127.8	41.5	176.2	30.2	267	49.9	126.5	104.2
MB2017_7_7	MB2017-7 zr -	1.59E+05	0.204	8.04	0.09	0.85	4.38	0.41	25.9	9.75	139.2	55	279.7	58.5	542	108.8	169.7	564.7
MB2017_7_31	MB2017-7 - 43	1.45E+05	0	21.18	0.126	3.38	5.46	0.163	32.5	11.06	133.9	48.46	218.5	42.26	356.4	69.9	512.7	500
Output_4_19	MB2017-7A Zr	1.51E+05	0.08	0.64	0.03	0	0	0.033	0.39	0.3	5.26	2.27	13.72	3.57	38.9	10.09	25.7	224.9
MB2017_7_22	MB2017-7 - 32	1.40E+05	0.51	18.01	0.323	2.57	2.35	0.84	9.5	3.38	44.4	16.42	76.9	16.09	149.1	30.91	143.4	291.4
MB2017_7_25	MB2017-7 zr -	1.46E+05	0	19.1	0	0.13	0.79	0.3	5.4	2.09	31.4	12.21	68.8	16.95	188.4	45.5	160.3	493
MB2017_7_20	MB2017-7 zr -	1.54E+05	0.306	6.88	0.44	2.44	1.45	1	4.18	1.36	19.58	9.18	61.5	17.84	218.1	57.8	70.2	1104
MB2017_7_4	MB2017-7 zr -	1.54E+05	0	9.72	0.056	0.6	1.76	0.054	8.2	2.82	35.7	13.59	67.6	14.14	130.9	25.22	153.7	359.5
MB2017_7_16	MB2017-7 - 21	1.51E+05	0	7.18	0.055	0.64	2.27	0.32	16.8	6	74.3	25.95	118.2	23	201.4	39.6	67.7	359.5
MB2017_7_24	MB2017-7 - 34	1.46E+05	1.2	29.15	0.67	4.64	4.63	1.97	16.3	4.68	54.6	19.3	95.9	19.78	183	36.1	170.7	174.4
MB2017_7_8	MB2017-7 - 8	1.35E+05	4.11	34.9	3.7	23.9	19.5	9.7	57	15.7	168.7	55.9	231.3	43	367	65.7	478.2	1139
Output_4_8	MB2017-7A Zr	1.48E+05	0.092	15.17	0.185	1.29	2.36	0.5	10.54	4.06	46.7	17.04	80.6	16.77	147.9	29.01	197.8	237
MB2017_7_14	MB2017-7 zr -	1.46E+05	0.038	22.96	0.044	1.23	2.25	0.41	15.4	4.58	52.9	16.87	79.2	15.48	130.1	25.01	159.7	265.1
MB2017_7_9	MB2017-7 zr -	1.46E+05	0.189	10.32	0.376	3.85	6.5	0.55	33.5	11.19	137.2	51.6	239.9	47.2	411.7	78.7	183.8	408.7
Output_4_22	MB2017-7A Zr	1.51E+05	0	0.134	0	0	0.85	0.242	13.35	8.07	95.8	17.66	28.94	2.52	12.26	1.78	3.949	458.5
MB2017_7_2	MB2017-7 zr -	1.47E+05	0	0.64	0.016	0.24	0.8	0.43	6.46	2.02	27.3	11.39	58.7	13.37	136.8	31.05	19.84	54.21
MB2017_7_13	MB2017-7 - 17	1.37E+05	0	26.43	0.029	0.83	2.38	0.33	15.5	5.34	71.9	28.35	139.7	29.94	286.5	54.7	148.9	177.6
Output_4_11	MB2017-7A Zr	1.39E+05	0	28.9	0.032	0.6	2.46	0.45	14.5	5.64	78.9	29.15	154.5	32.4	309.8	62.7	165.5	207.6
MB2017_7_28	MB2017-7 - 38	1.47E+05	0	6.94	0.199	3.39	5.4	0.44	28.7	8.96	104.4	33.4	148.3	29.2	247.3	49.5	206	498.9
MB2017_7_1	MB2017-7 zr -	1.53E+05	0.041	2.16	0	0	0	0.055	0.87	0.405	7.52	3.15	17.55	4.19	50.8	13.06	29.92	98.9
MB2017_7_3	MB2017-7 zr -	1.51E+05	0	14.44	0.036	0.36	1.74	0.128	11.1	3.82	50.5	20.06	102.9	21.95	211	41.9	191.5	351.5
MB2017_7_1	MB2017-7 - 1	1.36E+05	0.089	19.56	0.652	7.94	11	0.91	45.4	12.83	134.2	45.7	197.9	37	321	57	231.2	201.9
MB2017_7_15	MB2017-7 - 20	1.47E+05	0.023	22.9	0.281	4.4	8.9	0.48	53.9	17.61	227.6	83.8	378.1	71.1	581	109.1	232.6	445.4
Output_4_14	MB2017-7A Zr	1.47E+05	0	30.79	0.164	3.33	7.26	0.258	50	16.21	202.9	72.7	327.6	61.7	517.3	94.7	316.2	539.5

MB2017-7 monazite

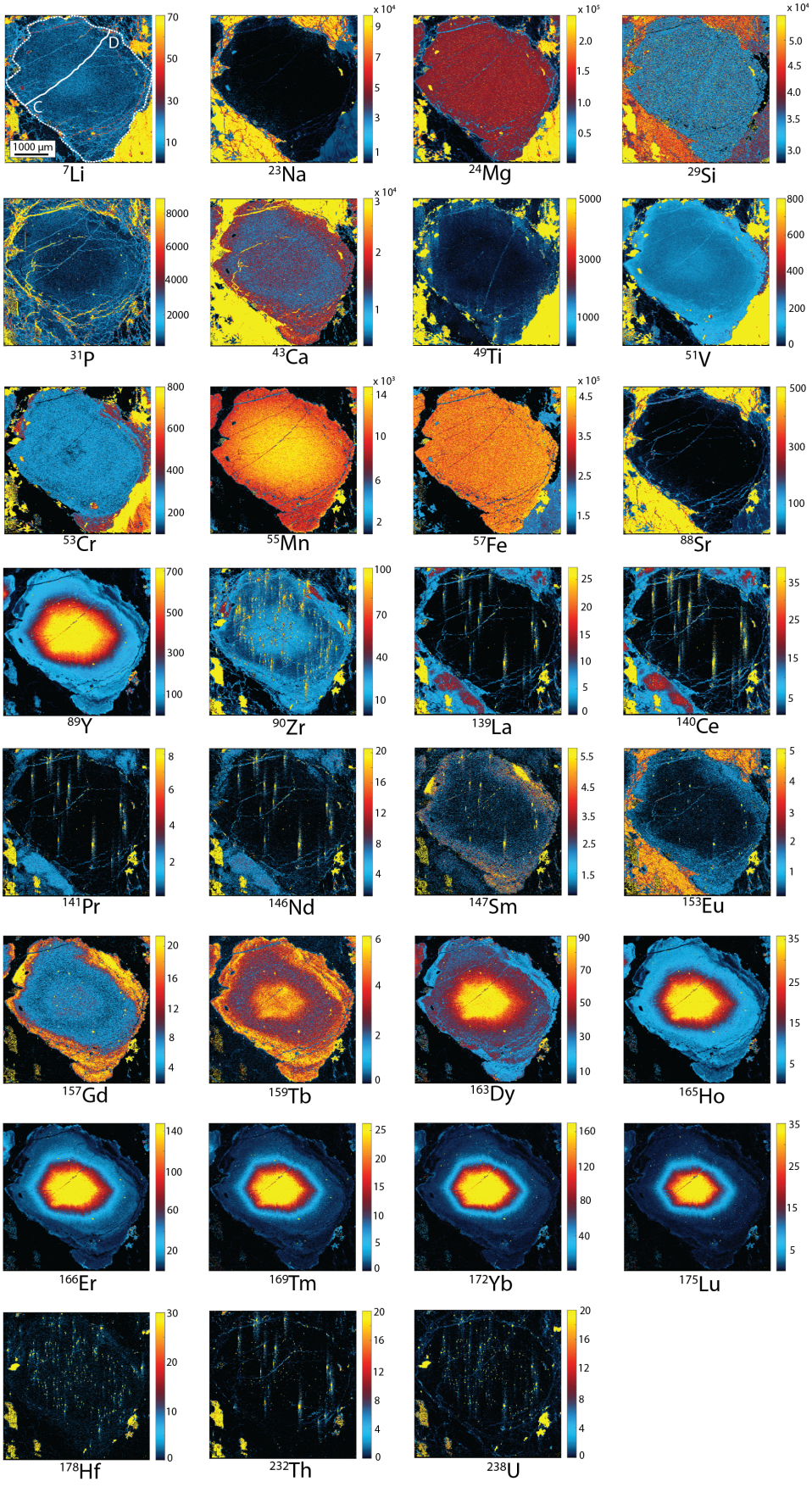
	Source file	Final207_235	Final207_235_Pr	Final206_238	Final206_238_Pr	ErrorCorrelation	FinalAge207_235	FinalAge207_231	FinalAge206_238	FinalAge206_231	FinalAge207_206	FinalAge207_206_Prop2SE
Mb20177_7	Mb2017-7 mnz -	0.5441	0.0088	0.0713	0.00099	0.48794	440.9	5.8	444	6	425	35
Mb20177_6	Mb2017-7 mnz -	0.5478	0.0076	0.07161	0.00088	0.60844	443.4	5	445.9	5.3	429	25
Mb20177_2	Mb2017-7 mnz -	0.5537	0.0067	0.07174	0.00082	0.26481	447.2	4.4	446.6	5	449	27
Mb20177_11	Mb2017-7 mnz -	0.5475	0.0077	0.07195	0.00087	0.22699	443.2	5	447.9	5.2	417	32
Mb20177_4	Mb2017-7 mnz -	0.5485	0.007	0.07202	0.00089	0.52803	443.9	4.6	448.3	5.4	420	25
MB20177Amon	MB2017-7A mor	0.5553	0.022	0.07221	0.0024	0.59319	448.3	14	449.4	14	433	37
MB20177Amon	MB2017-7A mor	0.5569	0.021	0.07246	0.0024	0.30843	449.4	14	451	14	441	38
MB20177Amon	MB2017-7A mor	0.56	0.024	0.07265	0.0024	0.19137	452.3	16	452.1	15	440	58
Mb20177_10	Mb2017-7 mnz -	0.5617	0.0061	0.07274	0.00081	0.42726	452.5	3.9	452.6	4.8	455	21
MB20177Amon	MB2017-7A mor	0.5632	0.021	0.07281	0.0024	0.38733	453.4	14	453	14	444	36
Mb20177_8	Mb2017-7 mnz -	0.565	0.01	0.07297	0.001	0.17885	454.7	6.6	454	6.1	457	43
MB20177Amon	MB2017-7A mor	0.551	0.023	0.07307	0.0025	0.36274	445.4	15	454.6	15	402	52
Mb20177_5	Mb2017-7 mnz -	0.5634	0.0078	0.07309	0.00096	0.28346	453.6	5.1	454.7	5.8	448	33
Mb20177_9	Mb2017-7 mnz -	0.563	0.011	0.07325	0.0011	0.47416	453.3	6.9	455.7	6.4	440	37
MB20177Amon	MB2017-7A mor	0.5716	0.021	0.07326	0.0024	0.31668	459	14	455.8	14	461	37
MB20177Amon	MB2017-7A mor	0.556	0.023	0.0733	0.0026	0.45199	448.6	15	455.9	16	432	48
MB20177Amon	MB2017-7A mor	0.5613	0.021	0.07328	0.0024	0.44838	452.2	14	455.9	14	433	34
MB20177Amon	MB2017-7A mor	0.57	0.024	0.07332	0.0024	0.61004	457.4	16	456.1	15	451	47
MB20177Amon	MB2017-7A mor	0.5605	0.021	0.07353	0.0024	0.54142	451.7	14	457.4	14	432	35
Mb20177_3	Mb2017-7 mnz -	0.5615	0.0064	0.07353	0.00081	0.28224	452.3	4.1	457.4	4.9	426	26
MB20177Amon	MB2017-7A mor	0.5634	0.021	0.07367	0.0024	0.32491	453.6	14	458.2	14	437	37
MB20177Amon	MB2017-7A mor	0.581	0.025	0.07379	0.0024	0.26356	464.3	16	458.9	15	488	56
Mb20177_1	Mb2017-7 mnz -	0.576	0.0091	0.0738	0.00089	0.49134	461.7	5.9	459	5.3	469	31

	Source file	Si ppm m29	P ppm m31	Ca ppm m43	Y ppm m89	Zr ppm m90	La ppm m139	Pr ppm m141	Nd ppm m146	Sm ppm m147	Eu ppm m153	Gd ppm m157	Tb ppm m159	Dy ppm m163	Ho ppm m165	Er ppm m166	Tm ppm m169	Yb ppm m172	Lu ppm m175	Th ppm m232	U ppm m238
MB20177Amon	MB2017-7A mor	3530	102800	6580	138	0.183	101900	23130	86800	13190	420	4691	162.5	178	6.19	4.48	0.187	0.58	0.041	59640	587
MB20177Amon	MB2017-7A mor	1490	102600	8130	1321	0.064	100200	23340	89300	16210	775	10000	659	1166	54.4	38.4	1.41	3.96	0.211	52900	2289
MB20177Amon	MB2017-7A mor	750	111700	7870	2440	0.187	103900	22520	82500	14820	839	10390	867	1940	96	57.3	2.04	4.14	0.289	42790	4260
MB20177Amon	MB2017-7A mor	820	111600	9690	4429	0.16	103200	22430	82990	14880	1005	10980	1118	3119	171.8	106.2	3.74	7.3	0.424	50580	5598
MB20177Amon	MB2017-7A mor	1340	106300	6830	933	0.087	101500	22720	84960	14340	724	7984	456.1	775	39	31.4	1.38	3.66	0.245	43380	1170
MB20177Amon	MB2017-7A mor	910	106100	7680	1464	0.165	97600	22830	84650	15510	977	9240	621	1156	60.2	45.7	1.97	4.36	0.326	37500	3260
MB20177Amon	MB2017-7A mor	800	107700	8690	3340	0.22	100300	22250	83100	15480	913	10540	863	2041	136.1	134.6	7.29	18.6	1.34	47480	6020
MB20177Amon	MB2017-7A mor	530	108500	7580	5577	0.302	96900	23420	90290	18120	854.8	13980	1240	3194	229.5	252.2	13.59	40.4	3.27	35850	2767
MB20177Amon	MB2017-7A mor	580	98700	7240	988	0.082	99300	22530	84700	15310	874	9540	610	1013	40.04	21.07	0.7	1.51	0.158	40990	2055
MB20177Amon	MB2017-7A mor	700	103100	7800	4376	0.154	103900	22620	83400	15320	906	11700	1185	3277	166.9	91.1	2.55	5.11	0.342	40440	5756
MB20177Amon	MB2017-7A mor	970	107900	8540	3104	0.092	100200	22400	84270	15200	749.7	10640	871.2	2049	127.3	114.8	5.57	15.01	1.07	47260	4580
MB20177Amon	MB2017-7A mor	930	106200	8070	3080	0.186	101900	22140	82020	14520	726.7	10070	849	1999	126	116.2	5.55	15.2	1.15	42880	4507
Mb20177_1	Mb2017-7 mnz -	540	86500	7110	2736	0.33	105000	22840	83800	14940	819	11070	933	2089	111.1	80	3.09	7.76	0.547	38510	2770
Mb20177_2	Mb2017-7 mnz -	690	92500	8930	2945	0.41	101900	22730	82900	14890	959	10900	1000	2432	116.3	63.9	1.99	3.61	0.29	46300	5098
Mb20177_3	Mb2017-7 mnz -	560	93300	9260	3336	0.165	103100	22730	82170	14550	965	10860	1040	2657	131.1	70.5	2.11	4.56	0.311	48800	4928
Mb20177_4	Mb2017-7 mnz -	740	92000	8940	3650	2.61	100450	22590	82560	14880	998	11170	1087	2845	143.9	79.8	2.42	4.6	0.334	50270	5191
Mb20177_5	Mb2017-7 mnz -	460	89400	8250	4691	0.55	105600	22770	83300	14550	876	11290	1160	3297	179.9	110.5	3.38	7.19	0.51	43700	5349
Mb20177_6	Mb2017-7 mnz -	490	94800	10170	3810	0.22	98700	22910	84090	15800	912	11100	908	2209	153.6	159	8.22	22.7	1.72	51500	6901
Mb20177_7	Mb2017-7 mnz -	770	87700	8740	1997	0.39	100400	22840	85000	16090	1104	10080	714	1439	82.3	71	3.35	8.07	0.59	42100	7160
Mb20177_8	Mb2017-7 mnz -	430	90200	6570	989	0.18	102000	22920	85600	15240	860	9550	615	1011	39.6	22	0.641	1.62	0.177	41010	2044
Mb20177_9	Mb2017-7 mnz -	830	88200	9400	3380	1.06	101000	22800	84000	15020	836	10540	882	2170	135	119	5.85	15.6	0.98	52900	4160
Mb20177_10	Mb2017-7 mnz -	780	96100	9610	4144	0.117	99550	22890	85800	15750	827.4	11500	1012	2529	172.2	171.2	9.21	24.9	1.85	52020	5566
Mb20177_11	Mb2017-7 mnz -	720	96800	8800	7300	0.2	98700	22470	83500	15160	783	11300	1088	3471	279.5	250.9	10.21	22.6	1.62	47960	4490

Appendix 4C
MB2017-1 Garnet LA-ICP-MS maps



MB2017-7 Garnet LA-ICP-MS maps



Appendix 4D
MB2017-1 garnet LA-ICP-MS analyses

	Li ppm	n Na ppm	r Mg ppm	Si ppm	r P ppm	m Ca ppm	r Ti ppm	m Cr ppm	r Mn ppm	Fe ppm	n Y ppm	m Zr ppm	r La ppm	n Ce ppm	r Pr ppm	r Nd ppm	i Sm ppm	Eu ppm	a Gd ppm	r Tb ppm	r Dy ppm	r Ho ppm	i Er ppm	r Tm ppm	Yb ppm	r Lu ppm	n Hf_ppm_m178
MB2017_1	3.72	68	8.38E-04	1.64E-05	423	1.58E-04	252.4	92.6	10610	3.99E-05	86.2	12.12	0	0	0	0	0.38	2.33	0.5785	19.4	5.24	27.38	3.14	4.8	0.484	2.66	0.325	0.216
MB2017_2	4.53	105	8.78E-04	1.66E-05	508	1.48E-04	231.2	126.8	10270	3.96E-05	60.54	13.06	0	0	0.032	0	0.48	2.72	0.4675	17.47	4.72	22.94	2.19	3.08	0.475	1.23	0.13	0.216
MB2017_3	3.82	93	8.88E-04	1.62E-05	604	1.52E-04	214.7	146	10170	3.91E-05	62.7	13.86	0.021	0.056	0.027	0.021	0.62	3.14	0.4755	17.1	4.72	22.84	1.9	2.81	0.261	1.64	0.175	0.3
MB2017_4	4.06	93	9.12E-04	1.58E-05	404	1.51E-04	222.4	153.7	10490	3.94E-05	62.7	13.98	0	0	0	0	0.62	3.14	0.4795	17.1	4.77	22.84	1.9	2.81	0.261	1.64	0.175	0.3
MB2017_5	5.88	87	8.50E-04	1.51E-05	452	1.49E-04	183	75.3	9860	3.69E-05	120.5	9.69	0.0138	0	0	0	0.32	2.12	0.4511	15.42	5.25	34	4.37	7.39	0.785	3.85	0.533	0.218
MB2017_6	4.56	86	9.01E-04	1.62E-05	423	1.69E-04	181.7	96.9	9650	3.54E-05	130	11.31	0	0	0	0	0.32	2.55	0.498	17.33	5.7	37.5	4.91	8.08	0.742	3.83	0.552	0.31
MB2017_7	5.52	86	8.20E-04	1.39E-05	464	1.46E-04	172.2	59.4	9580	3.49E-05	94.9	11.25	0	0	0.023	0	0.29	1.94	0.421	14.43	4.75	29.3	3.42	4.94	0.41	2.26	0.307	0.3
MB2017_8	5.31	92	8.04E-04	1.56E-05	420	1.52E-04	168.8	68.8	9650	3.46E-05	98.4	14.32	0.024	0.077	0.021	0.077	0.37	1.73	0.4045	13.73	4.45	29.4	3.5	5.28	0.468	2.09	0.286	0.37
MB2017_9	4.63	90	8.98E-04	1.46E-05	448	1.51E-04	168.7	99.8	10830	3.80E-05	100.3	16.6	6.3	0.025	0.024	0	0.36	1.8	0.51	16.8	4.72	32.4	3.28	4.99	0.439	2.56	0.263	0.43
MB2017_10	4.92	72	7.22E-04	3.16E-05	440	1.41E-04	184.5	46.7	8900	3.06E-05	105	6.3	0.0125	0.024	0	0.167	0.37	1.4	0.349	10.29	3.94	26.98	3.73	5.66	0.525	2.53	0.311	0.084
MB2017_11	5.71	112	9.05E-04	1.61E-05	545	1.35E-04	184.9	98.9	11310	3.87E-05	155.9	6.65	0	0	0.0144	0	0.36	1.55	0.3555	18.95	5.83	36.17	3.47	5.55	0.843	4.11	0.537	0.178
MB2017_12	5.15	107	9.02E-04	1.59E-05	562	1.46E-04	184.9	108.4	11520	3.86E-05	169.9	6.76	0	0	0	0.328	1.32	3.0165	7.77	3.47	36.17	5.83	9.91	0.852	4.74	0.572	0.107
MB2017_13	5.7	101	9.04E-04	1.55E-05	559	1.28E-04	188.5	95.1	11600	3.84E-05	169.8	5.74	0	0.014	0	0	0.3	1.2	0.268	6.75	3.22	34.8	5.72	9.38	0.828	4.25	0.467	0.14
MB2017_14	5.11	125	9.13E-04	1.61E-05	581	1.34E-04	193.6	85.1	12130	3.84E-05	212.3	4.83	0	0.082	0	0	0.68	1.81	0.5	4.95	2.33	35	6.84	12.45	1.075	5.23	0.669	0.179
MB2017_15	4.49	114	9.16E-04	1.61E-05	560	1.23E-04	74.7	195.6	12270	3.82E-05	238.9	4.6	0	0	0.0136	0.026	0.33	0.87	0.166	4.71	2.77	37.1	7.82	14.64	1.221	6.17	0.784	0.108
MB2017_16	4.59	123	9.08E-04	1.59E-05	508	1.24E-04	70.2	196	12530	3.83E-05	261.4	4.55	0	0	0.019	0.134	0.55	0.3305	4.53	2.74	30.3	5.66	8.59	16.46	1.407	6.81	0.916	0.141
MB2017_17	4.51	97	9.17E-04	1.57E-05	447	1.23E-04	64.5	193.7	12530	3.83E-05	285.7	4.67	0	0	0	0.145	0.33	0.1485	4.27	2.8	30.3	5.73	9.16	19.02	1.69	7.51	0.976	0.15
MB2017_18	3.99	108	9.26E-04	1.60E-05	447	1.23E-04	200.1	63.3	12680	3.84E-05	321.6	4.29	0	0	0	0.17	0.37	0.1795	4.54	2.75	40.3	10.27	23.2	2.15	10.5	1.273	0.144
MB2017_19	4.23	103	9.27E-04	1.58E-05	415	1.18E-04	202.2	52.6	12870	3.87E-05	376.5	4.36	0	0	0	0.206	0.5	0.1615	4.31	2.78	40.3	11.91	31.05	3.26	15.31	1.86	0.128
MB2017_20	4.62	101	9.38E-04	1.57E-05	430	1.44E-04	209.5	50	13080	3.84E-05	418.5	5.43	0	0.016	0	0.2	0.52	0.15	4.27	3.04	44.7	13.41	38.3	4.1	22.7	2.48	0.11
MB2017_21	4.06	130	9.13E-04	1.57E-05	371	1.21E-04	203.5	47	12960	3.78E-05	439	5.3	0	0.029	0.014	0.151	0.37	0.1485	3.88	2.64	44.7	14.44	43.9	5.3	28.4	3.48	0.17
MB2017_22	4.2	106	9.11E-04	3.76E-05	381	1.27E-04	215.6	48.4	13190	3.82E-05	492.6	8.54	0	0.0009	0	0	0.56	0.133	3.98	2.79	48.6	15.5	52.3	6.74	37.7	4.25	0.22
MB2017_23	4.71	127	9.11E-04	3.65E-05	436	1.38E-04	207.8	42.4	13270	3.85E-05	492.6	8.54	0	0.0009	0	0	0.39	0.1075	3.79	2.77	49.6	16.83	57.9	7.57	41.1	5.04	0.195
MB2017_24	4.62	113	9.23E-04	3.72E-05	422	1.26E-04	202.7	42.3	13540	3.85E-05	513.9	9.65	0	0	0	0	0.28	0.118	3.83	2.83	49.9	17.59	62.5	8.27	49.2	5.92	0.185
MB2017_25	4.81	114	9.17E-04	1.62E-05	424	1.37E-04	202.2	38.8	13540	3.83E-05	535	8.32	0	0	0	0	0.39	0.1425	3.9	2.77	51.6	18.24	68.9	9.63	58.5	7.22	0.13
MB2017_26	5.03	143	9.09E-04	1.60E-05	405	1.32E-04	197.6	40.3	13600	3.78E-05	547.2	9.83	0	0	0	0.161	0.41	0.087	3.77	2.87	53.1	20.1	75.1	10.97	69.3	8.99	0.26
MB2017_27	5.32	142	9.06E-04	1.61E-05	386	1.38E-04	209.3	44.5	13840	3.83E-05	599.7	13.8	0	0.013	0	0.106	0.35	0.132	5.46	3.16	60.8	23.61	91	14.13	91	12.38	0.34
MB2017_28	5.03	148	9.28E-04	1.68E-05	402	1.37E-04	203.6	44.5	13950	3.84E-05	660.2	12.95	0	0	0	0.128	0.42	0.1815	4.52	3.52	66.6	27.13	104.6	15.95	101.9	14.59	0.43
MB2017_29	5.35	149	9.07E-04	1.64E-05	382	1.35E-04	196	48.7	14050	3.81E-05	655.8	13.57	0	0.098	0	0.188	0.46	0.113	3.63	2.68	68.3	27.28	106.3	15.87	105.3	15.03	0.193
MB2017_30	5.67	137	9.11E-04	1.58E-05	319	1.40E-04	208.1	53.7	14140	3.77E-05	703.2	13.93	0	0	0	0.073	0.5	0.1495	5.62	3.79	72.8	29.37	114.9	17.76	118.2	16.5	0.27
MB2017_31	5.37	162	9.07E-04	1.66E-05	410	1.30E-04	211.2	53.9	14170	3.85E-05	742	13.49	0	0	0	0.113	0.45	0.1535	6.06	4.09	76.7	31.1	123.8	19.07	128.8	18.35	0.35
MB2017_32	6.07	144	9.30E-04	1.59E-05	327	1.37E-04	214.2	55.3	14360	3.85E-05	763.7	13.6	0	0	0	0.053	0.4	0.1522	6.05	4.15	80.8	32.63	131.1	20.14	140.2	19.79	0.26
MB2017_33	5.61	155	9.04E-04	1.59E-05	391	1.36E-04	206.7	60.1	14280	3.86E-05	772	13.47	0	0	0	0.46	0.7125	5.69	4.41	80.6	33.51	137	21.84	148.1	20.94	20.25	0.25
MB2017_34	6.54	163	9.23E-04	1.55E-05	335	1.33E-04	219.3	60.6	14640	3.92E-05	843.4	15.07	0	0	0	0.179	0.54	0.194	6.86	4.7	89.9	38	160.7	25.47	178.8	25.93	0.22
MB2017_35	6.98	177	9.12E-04	1.54E-05	329	1.34E-04	213.6	51.2	14420	3.85E-05	828.1	11.12	0	0	0	0	0.4	0.1055	6.06	4.33	86.4	37.75	166.2	26.93	186	27.61	0.2
MB2017_36	7.43	174	9.20E-04	1.66E-05	366	1.43E-04	209.9	55.7	14720	3.94E-05	878	12.68	0	0	0	0.09	0.2	0.1635	6.87	4.57	90.2	40.1	176.5	28.83	201.1	30.87	0.27
MB2017_37	6.06	166	9.02E-04	1.51E-05	382	1.24E-04	212.2	67.4	14560	3.85E-05	921	14.53	0	0	0	0.182	0.54	0.188	7.25	5.02	99.1	43.04	185.9	30.31	210.5	31.37	0.32
MB2017_38	6.73	166	9.11E-04	1.64E-05	383	1.29E-04	62	67.4	14740	3.97E-05	926	15.85	0	0	0	0.093	0.48	0.151	7.06	5.02	101.4	44.14	192.2	30.96	216.2	32.12	0.29
MB2017_39	6.7	175	9.16E-04	3.57E-05	400	1.32E-04	60.6	205.7	14670	3.89E-05	916	15.39	0	0	0.015	0.097	0.49	0.1695	7.07	5.27	98.6	43.94	192.8	30.99	217.4	32.16	0.169
MB2017_40	6.46	173	8.98E-04	3.59E-05	397	1.27E-04	62.8	216.4	14680	3.90E-05	925	16.97	0	0	0	0	0.51	0.17	7.52	5.14	101.8	44.84	195	31.77	223.8	33.86	0.39
MB2017_41	6.68	176	9.05E-04	3.55E-05	383	1.23E-04	61	186.5	14570	3.84E-05	913	16	0	0	0	0.112	0.42	0.185	7.19	5.08	99.5	44.47	193.3	31.62	224.8	33.54	0.38
MB2017_42	6.64	190	9.17E-04	3.57E-05	357	1.34E-04	56	197.1	14460	3.87E-05	909	18.5	0	0	0	0.112	0.41	0.172	7.47	5.05	100.9	44.38	197.8	32.48	228.4	34.42	0.4
MB2017_43	6.64	176	9.30E-04	3.62E-05	365	1.39E-04	201.4	60.4	14690	3.90E-05	922	22.4	0	0	0	0.067	0.41	0.1795	7.28	4.92	96.3	43.11	189.2	31.4	218.5	33.28	0.252
MB2017_44	6.44	178	9.03E-04	3.57E-05	374	1.33E-04	203.7	49.9	14640	3.86E-05	871.3	17.1	0	0	0	0.192	0.4	0.1795	7.28	4.92	96.3	43.11	189.2	31.4	218.5	33.28	0.252
MB2017_45	6.87	168	9.15E-04	3.61E-05	354	1.45E-04	197.4	54.4	14440	3.89E-05	853	16.63	0	0	0	0	0.54	0.1665	7.15	4.96	93.9	41.98	185	30.35	211.6	31.65	0.28
MB2017_46	6.3	164	8.95E-04	3.64E-05	408	1.38E-04	213.4	59.1	14470	3.83E-05	829	16.17	0	0	0	0.197	0.46	0.1505	6.49	4.74	90.2	38.68	165.8	26.68	182.7	27.04	0.126
MB2017_47	6.31	157	8.93E-04	3.47E-05	348	1.37E-04	214.4	57.1	14160	3.75E-05	799	15.83	0	0	0	0.168	0.48	0.151	7.02	4.5	87.4	37.07	154.7	24.25	167.8	24.31	0.31
MB2017_48	5.47	150	9.14E-04	1.65E-05	359	1.38E-04	214.7	55.2	14350	3.83E-05	771	14.8	0	0.01	0.129	0.53	0.168	5.52	4.43	80.8	34.18	139.6	21.86	148.5	21.23	0.31
MB2017_49	5.53	150	9.01E-04	1.55E-05	308	1.33E-04	216	54.3	14240	3.83E-05	723	13.16	0	0.0052	0	0.219	0.44	0.1725	5.81	4.07	75.8	30.22	121.4	18.81	127.5	18.3	0.29
MB2017_50	5.16	154	9.17E-04	1.66E-05	348	1.33E-04	213.5	60.6	14380	3.88E-05	708.5	13.49	0	0	0	0.183	0.47	0.1655	4.97	3.86	72.7	28.27	113.2	17.42	118.2	16.66	0.34
MB2017_51	5.19	135	9.05E-04	1.58E-05	334	1.49E-04	203.6	55.6	14090	3.80E-05	654	11.85	0	0	0	0.37	0.39	0.1645	5.25	3.72	65.7	26.09	101.6	15.42	102.2	14.42	0.23
MB2017_52	4.97	130	9.08E-04	1.62E-05	411	1.39E-04	194.4	51.4	14080	3.82E-05	615.7	11.66	0	0.011	0	0.25	0.54	0.114	5.09	3.3	61.4	23.71	93.5	14.17	94.3	13.15	0.23
MB2017_53	5.18	144	9.02E-04	1.62E-05	380	1.43E-04	194.7	50.4	13970	3.80E-05	598.5	11.85	0	0	0	0.23	0.63	0.14	4.49	3.1	59.6	23.25	88.4	13.37	88.7	12.52	0.24
MB2017_54	5.07	123	9.25E-04	1.60E-05	440	1.32E-04	192.8	48.9	13870	3.84E-05	587.7	11.09	0	0.015	0	0.119	0.5	0.138	4	2.87	58.5	22.29	85	12.7	83.6	11.32	0.28
MB2017_55	4.8	132	9.28E-04	1.56E-05	419	1.32E-04	192.7	49	14020	3.86E-05	573.1	10.91	0	0.013	0	0.23	0.42	0.144	4.19	3.04	55.4	21.36	79.6	11.97	76	10.68	0.141
MB2017_56	5.1	127	9.09E-04	3.44E-05	330	1.36E-04	185.5	46.4	13770	3.81E-05	545	10.2	0	0	0	0.28	0.51	0.1025	4.44	2.8	53.9	19.87	75.4	11.07	70.6	9.97	0.25
MB2017_57	5.15	108	9.25E-04	3.54E-05	344	1.45E-04	195	53.2	13560	3.85E-05	530.2	8.55	0	0.017	0	0.136	0.53	0.2035	3.92	2.82	52	18.67	67	9.49	58.6	7.23	0.26
MB2017_58	5.36	129	9.18E-04	1.62E-05	388	1.30E-04	197.9	49.9	13560	3.90E-05	509	8.23	0.0039	0	0	0.28	0.34	0.1325	3.33	2.83	49	17.54	63.8	8.47	50.7	6.1	0.19
MB2017_59	4.54	117	9.10E-04	1.60E-05	394	1.28E-04	192	49.3	13410	3.81E-05	489.3	7.1	0	0.013	0	0.152	0.48	0.1385	3.48	2.67	46.9	16.73	57.5	7.5	42.5	5.26	0.28
MB2017_60	4.85	119	9.21E-04	1.61E-05	364	1.29E-04	199.8	57.2	13470	3.92E-05	490.1	0.2	0.036	0.063	0.25	0.063	0.2	0.1385	4.25	2.77	48.5	16.1	53.3	7.02	38.6	4.96	75
MB2017_61	4.85	101	9.21E-04	1.61E-05	388	1.28E-04	198	53.7	13300	3.85E-05	438.4	5.9	0.0109	0	0.205	0.65	0.1765	4.25	3.73	2.55	44.8	14.35	45.4	5.35	29.4	3.48	0.157
MB2017_62	4.93	117	9.13E-04	3.51E-05	332	1.21E-04	65.2	198	13260	3.85E-05	340.5	4.5	0.017	0	0.197	0.54	0.197	4.26	2.69	2.62	32	12.28	32	4.65	23.6	2.98	0.083
MB2017_63	4.79	120	9.18E-04	1.61E-05	430	1.22E-04	61.2	199.8	12980	3.90E-05	350	5.3	0.0128	0.021	0.1735	0.71	0.3	4.33	2.59	2.59	40	10.62	25.26	2.47	18.6	2.79	1.41	0.157	9.9
MB2017_64	4.58	117	9.15E-04	1.64E-05	480	1.25E-04	72	197	12740	3.88E-05	328.2	4.95	0	0.01	0.207	1.08	0.203	4.65	2.74	2.67	39.5	9.91	32	4.65	26.2	2.24	1.77	0.083
MB2017_65	5.47	99	9.14E-04	3.54E-05	475	1.22E-04	75.9	206.4	12540	3.82E-05	284.7	5.93	0	0	0.016	0.16	0.96	4.74	2.74	2.74	37.6	9.01	29.1	4.65	24.2	2.47	1.58	7.48	0.929	0.127
MB2017_66	5.74	109	9.01E-04	3.60E-05	620	1.25E-04	86.3	191	12250	3.88E-05	248.1	5.02	0.013	0	0.207	0.16	0.94	5.26	3.04	3.45	38.5	7.97	19.15	2.99	15	1.35	0.8	0.27
MB2017_67	4.67	104	9.07E-04	3.54E-05	438	1.30E-04	90.9	167	11530	3.82E-05	210.8	5.72	0	0	0.2415	0.28	0.43	6.86	3.45	3.84	38.4	7.21	12.5	1.25	7.05	1.022	0.162
MB2017_68	4.51	81	9.18E-04	3.59E-05	400	1.38E-04	154.8	96	11600	3.87E-05	204	5.5	0	0	0.374	0.32	0.222	9.26	4.16	4.24	42	7.11	12.5	1.204	6.57	0.935	0.154
MB2017_69	4.51	87	9.16E-04	3.49E-05	386	1.29E-04	169.1	93	11930	3.85E-05	229.9	5.25	0	0	0.017	0.42	1.43	6.62	3.2	3.7	39.7	7.57	14.35	1.43	7.7	1.042	0
MB2017_70	4.75	120	9.15E-04	3.60E-05	499	1.48E-04	160.7	107.7	11410	3.87E-05	142.9	7.22	0	0	0.031	0.45	1.44	10.77	4.24	4.84	36.4	7.3	3.35	0.599	3.01	0.4	0.075
MB2017_71	5.08	96	9.13E-04	3.58E-05	492	1.53E-04	170	118.8	11310	3.91E-05	124.4	8.99	0	0.014	0.018	0.47	2.06	12.67	4.52	4.47	34.7	6.2	0.488	2.57	0.376	0.33	
MB2017_72	4.69	75	7.96E-04	3.36E-05	430	1.39E-04	172.8	101.7	9840	3.44E-05	122.7	8.79	0	0	0.016	0.28	1.7	13.27	4.68	5.3	35.1	8.29	0.79	4	0.559	0.24	
MB2017_73	4.52	78	9.06E-04	3.55E-05	447	1.54E-04	234.3	139.4	10960	3.94E-05	91.9	14.88	0	0	0	0.66	3.04	0.5515	18.6	4.79	27.8	4.76	0.454	2.71	0.293	0.36	
MB2017_74	3.27	66	9.03E-04	3.58E-05	277	1.51E-04	236.6	177	10600	4.02E-05	70.7	15.22	0	0	0.012	0.92	5.39	0.725	25.9	5.3	24.7	2.68	0.377	0.212	0.32		
MB2017_75	3.23	60	8.91E-04	3.58E-05	210	1.65E-04	244	244	10390	3.93E-05	15.14	50.7	0	0	0.034	1.31	8.44	1.085	35.5	3.44	7.71	0.356	0.023	0.29	0.01	0.74	
MB2017_76	3.29	47	8.97E-04	3.50E-05	195	1.59E-04	448	300	10250	3.95E-05	11.08	55.3	0	0.03	0.06	1.47	10.31	1.24	38.1	4.09	8	0.397	0.268	0.025	0	1.12	
MB2017_77	2.42	43	8.93E-04	3.62E-05	238	1.60E-04	417	319	10230	3.99E-05	13.91	45.7	0	0.051	0.073	1.99	8.67	1.045	37.6	4.5	10.23	0.513	0.37	0.018	0.131	0.63	
MB2017_78	2.99	62	8.28E-04	3.50E-05	181	1.62E-04	379	170.6	9360	3.81E-05	23.35	31.4	0	0.029	0.066	1.27	6.41	0.825	29.3	4.01	12.68	0.803	0.92	0.075	0.43	0.054	0.51
MB2017_79	2.73	76	8.59E-04	3.44E-05	252	1.78E-04	162	162	10130	4.08E-05	12.14	0	0	0.032	0.024	0.81	3.12	0.65	20.8	4.39	21.19	2.33	3.67	0.382	2.12	0.235	0.23
MB2017_80	4.05	92	8.43E-04	3.63E-05	428	1.73E-04	471	139	10350	4.16E-05	61.4	11.49	0	0	0.023	0.36	2.21	0.683	15.88	4.11	19.92	2.23	3.47	0.302	1.38	0.174	0.34
MB2017_81	3.59	76	8.13E-04	3.55E-05	516	1.83E-04	437	122.7	10700	4.07E-05	60.1	10.83	0	0.021	0.019	0.194	2.52	0.555	16.58	4.53	26.12	3.31	3.23	0.294	4.15	0.122	0.28
MB2017_82	3.27	72	8.12E-04	3.51E-05	371	1.67E-04	305.6	95.7	11440	4.15E-05	91.2	6.82	0	0.026	0.0118	0.44	1.9	0.639	16.58	4.53	26.12	3.31	6.44	0.743	4.15	0.509	0

MB2017-7 garnet LA-ICP-MS analyses

	Li_ppm_m	Na_ppm_m	Mg_ppm_n	Si_ppm_m	P_ppm_m3	Ca_ppm_m	Ti_ppm_m	Cr_ppm_m	Mn_ppm_r	Fe_ppm_m	Y_ppm_m3	Zr_ppm_m	La_ppm_n	Ce_ppm_r	Pr_ppm_r	Nd_ppm_r	Sm_ppm_r	Eu_ppm_a	Gd_ppm_r	Tb_ppm_a	Dy_ppm_r	Ho_ppm_r	Er_ppm_m	Tm_ppm_a	Yb_ppm_r	Lu_ppm_n	Hf_ppm_m178
MB2017i_1	1.71	87	44280	3.67E+05	187	1.00E+05	476	461	36120	3.49E+05	614.3	4.99	0	0.127	0.072	1.21	2.28	0.879	13.08	4.65	58.9	22.24	106.8	21.12	187.3	37.3	0.059
MB2017i_2	1.71	100	44950	3.63E+05	243	1.06E+05	835	59.4	34660	3.50E+05	335	13.03	0	0.156	0.078	1.15	1.86	0.8595	8.95	3	35.2	11.4	49.1	8.64	72	12.28	0.223
MB2017i_3	1.38	83	45780	3.68E+05	170	1.11E+05	836	108.8	33320	3.48E+05	296.4	12.89	0.013	0.169	0.083	0.97	1.72	0.9045	7.82	2.68	31.78	10.47	43.26	7.68	63.2	10.61	0.276
MB2017i_4	1.26	100	44890	3.71E+05	220	1.11E+05	771	134.1	31070	3.54E+05	282.1	11.3	0.0135	0.166	0.101	1.31	1.39	0.9325	8.01	2.602	29.1	9.4	38.04	6.63	53.5	9.07	0.191
MB2017i_5	1.63	107	44890	3.85E+05	258	1.10E+05	820	121.7	31300	3.57E+05	298.7	11.62	0	0.227	0.103	1.1	1.87	0.935	8.55	2.69	31.8	10.57	42.5	7.4	59.7	10.11	0.203
MB2017i_6	1.62	119	44860	3.68E+05	199	1.13E+05	944	87	30350	3.47E+05	341.1	14.09	0.0127	0.247	0.121	1.42	2.05	0.96	8.93	3.09	35.3	12.28	52.7	9.43	77.5	14.01	0.199
MB2017i_7	1.51	105	47140	3.54E+05	234	1.09E+05	970	130.1	33010	3.38E+05	370.2	13.82	0.013	0.26	0.106	1.67	2.26	1.17	9.59	3.28	38.9	13.42	58.9	10.75	91	16.43	0.162
MB2017i_8	1.55	117	46540	3.70E+05	203	1.09E+05	941	216	31010	3.43E+05	371	13.19	0.012	0.27	0.17	1.49	3.1	1.05	11.1	3.61	41.6	13.46	55.1	9.85	82.9	15.05	0.11
MB2017i_9	1.5	128	47960	3.58E+05	217	1.11E+05	951	240.7	30670	3.49E+05	346.5	13.78	0.019	0.33	0.15	2.01	2.94	1.195	11.44	3.7	39.1	12.59	49.3	8.54	67.7	11.84	0.34
MB2017i_10	1.31	130	48220	3.85E+05	206	1.18E+05	1064	321	32550	3.60E+05	313.8	14.49	0.0073	0.302	0.14	1.77	2.44	1.14	9.51	3.13	34.7	11.14	45.3	7.52	60.6	10.22	0.23
MB2017i_11	1.36	173	49040	3.78E+05	207	1.18E+05	1329	370	32250	3.66E+05	359.3	17.04	0	0.285	0.13	1.62	2.25	1.225	10.53	3.37	39.7	13.39	56.3	10.04	83.4	14.92	0.32
MB2017i_12	1.9	164	48740	3.81E+05	203	1.13E+05	1424	341	32510	3.52E+05	393.2	17.68	0.015	0.344	0.129	1.69	2.49	1.155	11.07	3.69	43	14.97	64.7	11.55	95	17.67	0.23
MB2017i_13	1.82	163	46760	3.74E+05	227	1.15E+05	1530	334.9	31480	3.44E+05	422.6	18.3	0.021	0.324	0.157	2.04	2.68	1.265	12.45	4.05	46.7	16.13	69.4	12.78	103	19.01	0.295
MB2017i_14	2.44	178	49480	3.73E+05	149	1.13E+05	1659	380	33540	3.63E+05	445	18.56	0.021	0.33	0.16	1.82	3.06	1.315	12.78	4.29	49.6	16.93	74.4	13.4	111.9	20.98	0.2
MB2017i_15	2.27	219	49380	3.69E+05	191	1.15E+05	1800	406	32530	3.68E+05	467	19.56	0	0.383	0.128	2.25	3.13	1.31	13.73	4.51	52.4	18.08	79.3	14.5	119.9	22.27	0.34
MB2017i_16	2.1	204	49760	3.80E+05	243	1.07E+05	1809	415	33440	3.52E+05	473	20.51	0	0.337	0.165	1.96	3.06	1.355	13.85	4.53	53.7	18.22	80.9	14.91	122.8	22.69	0.24
MB2017i_17	2.15	213	50160	3.70E+05	185	1.10E+05	1867	439	33210	3.53E+05	484	20.58	0.029	0.347	0.128	2.03	3.34	1.389	14.28	4.72	55.3	18.74	83.8	15.15	125.6	23.38	0.35
MB2017i_18	2.16	214	49240	3.60E+05	232	1.12E+05	1879	434	32810	3.50E+05	480	21.78	0.017	0.345	0.174	2.2	3.07	1.35	14.25	4.65	54.5	18.7	81.1	15.04	125	23.19	0.35
MB2017i_19	2.62	245	48880	3.74E+05	242	1.10E+05	1955	458	32950	3.62E+05	486	21.91	0.025	0.332	0.164	1.98	3.32	1.415	14.55	4.61	53.5	19.05	83	15.12	125.8	23.2	0.44
MB2017i_20	3.04	216	48770	3.70E+05	226	1.14E+05	2065	470	33490	3.45E+05	501	23.3	0.019	0.34	0.208	2.22	3.69	1.43	14.3	4.93	57	20.29	87.7	15.88	132	24.73	0.33
MB2017i_21	2.02	238	48440	3.62E+05	164	1.09E+05	2040	457	33140	3.53E+05	484.7	22.26	0.022	0.312	0.179	2.52	3.46	1.405	15.1	4.7	55.1	19.07	84.5	14.88	125.8	23.35	0.39
MB2017i_22	2.71	235	48890	3.64E+05	188	1.14E+05	2140	450	32660	3.45E+05	486	23.4	0.025	0.302	0.166	2.35	3.17	1.35	14.4	4.73	55.8	19.25	82.9	14.83	127.3	22.8	0.42
MB2017i_23	2.66	236	48980	3.62E+05	224	1.07E+05	2126	428	33110	3.46E+05	465	23.4	0.02	0.287	0.136	2.05	3.37	1.33	14.5	4.65	54.1	18.42	80	14.34	116.4	21.98	0.39
MB2017i_24	3.08	245	48840	3.71E+05	184	1.16E+05	2259	436	32170	3.52E+05	486.6	24.45	0	0.387	0.195	2.3	3.42	1.435	14.87	4.8	55.4	18.96	82.2	14.71	121.9	22.64	0.3
MB2017i_25	2.79	266	48770	3.86E+05	208	1.13E+05	2296	431	32880	3.49E+05	494	24	0.024	0.344	0.212	2.31	3.09	1.335	15.3	4.85	55.6	19.17	83.2	14.9	121.3	22.07	0.45
MB2017i_26	2.65	276	48080	3.65E+05	201	1.12E+05	2269	411	32860	3.48E+05	481.4	24.87	0.0104	0.317	0.17	2.05	3.53	1.28	14.91	4.77	54.5	18.53	79.2	14.39	117.1	21.57	0.27
MB2017i_27	2.77	253	47410	3.76E+05	180	1.13E+05	2318	394	32940	3.53E+05	473	24.76	0.0163	0.314	0.168	2.37	3.15	1.415	14.25	4.66	53.3	18.44	77.5	14.16	116	21.85	0.248
MB2017i_28	2.78	266	48860	3.91E+05	215	1.13E+05	2410	384	33610	3.40E+05	456	24.2	0.016	0.361	0.177	2.11	2.95	1.33	14	4.45	52	17.44	75.3	13.12	108.7	20.5	0.31
MB2017i_29	2.51	257	48560	3.76E+05	217	1.15E+05	2320	388	33640	3.49E+05	454	24.1	0.02	0.296	0.132	2.56	3.27	1.475	13.9	4.25	50.1	17.5	73.3	13.18	109.2	19.66	0.4
MB2017i_30	2.69	261	48250	3.76E+05	179	1.11E+05	2307	401	33610	3.58E+05	459	24.8	0	0.355	0.176	2.04	2.94	1.425	14.02	4.37	52.4	17.58	75.9	13.57	110	20.63	0.257
MB2017i_31	2.83	220	48820	3.43E+05	220	1.15E+05	2188	383	33410	3.47E+05	454	24.4	0	0.212	0.167	1.8	2.94	1.27	13.5	4.39	52.1	17.55	74.1	13.69	112.7	20.11	0.37
MB2017i_32	2.62	212	48990	3.65E+05	257	1.10E+05	2227	390	33410	3.49E+05	446.8	24.45	0.0081	0.248	0.113	1.6	2.91	1.32	13.43	4.42	50	17.56	74.9	13.3	109.3	20.12	0.37
MB2017i_33	2.6	208	47060	3.70E+05	236	1.18E+05	2224	390	33810	3.44E+05	446	23.6	0	0.196	0.123	1.87	2.54	1.225	12	4.39	51.2	17.37	74.9	13.46	110.3	20.12	0.4
MB2017i_34	2.96	228	47860	3.75E+05	223	1.12E+05	2204	405	33410	3.65E+05	456	23.9	0	0.181	0.128	1.61	2.83	1.335	13.53	4.29	51.5	17.21	74.4	13.46	110.3	20.12	0.46
MB2017i_35	2.11	201	52140	3.82E+05	270	1.11E+05	2340	409	34440	3.73E+05	461	23.5	0	0.215	0.134	1.54	2.89	1.4	13.7	4.56	51.8	17.46	75.4	13.37	111.4	19.75	0.38
MB2017i_36	2.94	199	49540	3.57E+05	173	1.06E+05	2219	398	32410	3.53E+05	444	23.9	0.011	0.178	0.085	1.62	2.67	1.205	13.6	4.46	50.3	17	74.4	13.04	110.1	19.09	0.38
MB2017i_37	2.71	195	48740	3.92E+05	236	1.18E+05	2254	408	33810	3.65E+05	454	24.2	0	0.184	0.082	1.57	3	1.41	14.16	4.44	51.8	17.37	73.6	13.18	108.1	20.02	0.42
MB2017i_38	3.28	222	49060	3.69E+05	189	1.13E+05	2224	406	34110	3.49E+05	434	24.2	0	0.196	0.108	1.73	2.83	1.285	12.74	4.28	49.2	16.75	69.6	12.09	100.4	18.85	0.42
MB2017i_39	2.81	213	50040	3.73E+05	203	1.09E+05	2214	408	33250	3.61E+05	445	23.56	0	0.191	0.078	1.54	2.72	1.335	12.99	4.25	50	16.79	71.6	12.8	105.5	19.18	0.4
MB2017i_40	2.72	207	50040	3.72E+05	210	1.16E+05	2207	411	33400	3.59E+05	446.8	22.97	0.0099	0.178	0.098	1.6	2.72	1.248	13.51	4.31	50	17.19	72.1	12.83	105.8	19.22	0.31
MB2017i_41	2.39	215	47220	3.95E+05	213	1.14E+05	2223	409	33460	3.57E+05	440	24.2	0	0.203	0.152	1.76	3.05	1.275	13.5	4.33	49.3	16.65	70.5	12.32	103.9	18.95	0.34
MB2017i_42	2.64	173	49380	3.68E+05	189	1.14E+05	2199	404	32340	3.47E+05	440.5	24.65	0.002	0.17	0.096	1.55	2.81	1.285	13.57	4.25	48.8	16.63	71.6	12.53	102.9	19	0.38
MB2017i_43	2.31	186	49640	3.79E+05	231	1.14E+05	2170	408	33280	3.53E+05	426	22.9	0.017	0.161	0.091	1.3	2.74	1.41	13	4.24	48.6	16.22	70.4	12.04	98.3	18.15	0.31
MB2017i_44	2.64	203	49880	3.97E+05	203	1.18E+05	2018	420	33440	3.60E+05	440	20.54	0	0.15	0.103	1.2	2.39	1.335	12.73	4.28	50.1	16.89	71.9	12.59	104	19.2	0.39
MB2017i_45	2.38	142	47140	3.80E+05	247	1.10E+05	1698	420	33490	3.64E+05	442.2	16.72	0.0081	0.123	0.068	1.23	2.57	1.26	12.89	4.38	49.9	16.74	71.4	12.81	104.1	19.02	0.34
MB2017i_46	1.94	169	47880	3.71E+05	233	1.10E+05	1758	424	33290	3.56E+05	444.6	18.15	0	0.124	0.09	1.19	2.62	1.225	12.53	4.23	48.9	16.68	71.2	12.71	105.4	19.68	0.25
MB2017i_47	2.54	141	47660	3.77E+05	230	1.13E+05	1922	424	33440	3.50E+05	445.8	20.09	0	0.135	0.063	1.36	2.51	1.19	12.9	4.13	48.3	17.21	70.7	12.52	101.9	19.33	0.37
MB2017i_48	3.03	205	48240	3.73E+05	201	1.10E+05	2116	412	32010	3.53E+05	436	22.57	0.013	0.156	0.092	1.65	2.63	1.255	11.25	4.34	48.6	16.6	70	12.48	102	18.62	0.29
MB2017i_49	2.56	211	50160	3.72E+05	218	1.15E+05	2219	424.2	33450	3.56E+05	438.1	24.05	0	0.246	0.132	1.57	2.66	1.173	13.04	4.3	50	17.24	71.1	12.55	103.7	18.99	0.288
MB2017i_50	3.37	221	48440	3.71E+05	221	1.15E+05	2262	433	33010	3.49E+05	429	24.6	0.012	0.26	0.125	1.73	2.57	1.26	12.62	4.23	47.1	16.44	69	12.4	100.8	18.5	0.4
MB2017i_51	3.21	217	48940	3.71E+05	211	1.15E+05	2312	416	32930	3.50E+05	439	24.62	0	0.215	0.119	1.65	2.57	1.26	12.76	4.26	49.3	16.69	70.8	12.39	103.3	18.6	0.43
MB2017i_52	3.15	215	48240	3.81E+05	267	1.11E+05	2196	455	33210	3.56E+05	455	24.7	0.011	0.234	0.107	1.43	2.95	1.32	12.47	4.28	49.7	16.51	69.5	12.51	102.5	18.37	0.24
MB2017i_53	2.85	208	49640	3.64E+05	253	1.19E+05	2312	435	33770	3.54E+05	449	25.6	0	0.181	0.125	1.53	2.8	1.34	13.6	4.35	50.2	17.5	72.6	13.15	109.1	19.59	0.27
MB2017i_54	3.14	169	49340	3.62E+05	162	1.20E+05	2281	438	32650	3.45E+05	453	24.8	0.02	0.199	0.116	1.6	2.92	1.375	13.1	4.35	50.7	17.22	74.2	13.35	110	20.04	0.37
MB2017i_55	3.15	218	47260	3.57E+05	220	1.10E+05	2196	455	32770	3.53E+05	455	23.8	0.013	0.246	0.099	1.7	2.87	1.48	14.13	4.4	52.9	17.85	74.7	13.57	112.7	20.29	0.44
MB2017i_56	3.14	246	47960	3.76E+05	219	1.12E+05	2246	436	33460	3.51E+05	468	24.24	0.0069	0.199	0.119	1.42	2.75	1.345	14.16	4.56	52	18.24	78.2	14.09	113.4	21.41	0.36
MB2017i_57	2.99	204	47960	3.76E+05	155	1.10E+05	2218	437	32410	3.45E+05	465	23.6	0.017	0.173	0.104	1.85	2.76	1.305	14.03	4.44	52.6	17.63	77	14.01	114.4	20.79	0.33
MB2017i_58	3.47	213	47560	3.72E+05	262	1.14E+05	2281	456	33180	3.59E+05	461	22.7	0	0.145	0.086	1.61	2.69	1.29	12.9	4.48	50.8	18	77.2	14.01	119.1	21.62	0.27
MB2017i_59	2.6	179	47760	3.72E+05	161	1.11E+05	2108	451	32810	3.49E+05	446	21.8	0	0.206	0.082	1.45	2.66	1.1745	12.3	4.07	49.5	17.26	75.9	13.39	113.8	21.03	0.177
MB2017i_60	2.31	158	47560	3.81E+05	267	1.11E+05	2124	466	32480	3.54E+05	479	23.24	0	0.251	0.116	1.77	3.27	1.32	12.7	4.27	52.5	17.59	77	14.08	115.7	21.5	0.27
MB2017i_61	2.57	183	46140	3.70E+05	174	1.17E+05	2131	481	33770	3.53E+05	489	23.8	0.011	0.29	0.131	1.85	3.39	1.32	15.4	4.89	55.9	19.01	83.3	15.4	126.2	23.21	0.55
MB2017i_62	2.82	193	49240	3.59E+05	214	1.14E+05	2131	481	33720	3.51E+05	495.5	22.83	0.02	0.304	0.131	2.26	3.21	1.395	14.69	4.82	55.5	19.37	82.7	15.23	124.4	23.36	0.37
MB2017i_63	2.79	193	49340	3.85E+05	220	1.12E+05	2115	491	34140	3.66E+05	495	23.56	0	0.273	0.155	2.12	3.01	1.465	15.7	4.62	56.4	19.5	83.5	15.41	129	23.44	0.37
MB2017i_64	2.55	173	49940	3.78E+05	212	1.09E+05	1960	486	33640	3.56E+05	489	22.04	0.011	0.189	0.149	1.67	3.19	1.28	14.28	4.75	55.5	18.91	81.1	15.22	124.4	23.23	0.37
MB2017i_65	2.54	160	47060	3.55E+05	222	1.13E+05	1960	475	33340	3.56E+05	482	23.56	0	0.199	0.136	2.22	3.37	1.33	14.4	4.65	54.4	18.95	82	15.3	125.4	22.55	0.38
MB2017i_66	2.91	170	48890	3.59E+05	205	1.16E+05	1863	469	33770	3.48E+05	470	21.2	0.014	0.269	0.151	1.98	2.93	1.28	14.47	4.44	53.9	18.18	81.2	14.49	121.2	22.55	0.38
MB2017i_67	2.67	160	47060	3.93E+05	270	1.13E+05	1829	466	33580	3.64E+05	473	19.6	0	0.235	0.133	1.95	3.42	1.23	13.7	4.52	53.4	18.57	80.2	14.64	121.6	22.5	0.31
MB2017i_68	2.31	156	47660	3.80E+05	178	1.14E+05	1759	462	33420	3.51E+05	466	18.9	0	0.194	0.116	1.66	3.39	1.275	13.6	4.4	50.2	17.94	78.1	14.29	119.2	22.61	0.35
MB2017i_69	3.39	163	50740	3.80E+05	221	1.12E+05	1802	471	33540	3.59E+05	480	21.3	0.021	0.18	0.134	1.98	2.85	1.35	14.3	4.39	54.3	18.96	80.2	14.91	124.7	22.92	0.59
MB2017i_70	2.78	142	47080	3.76E+05	164	1.09E+05	1715	440	33340	3.43E+05	465	18.5	0	0.228	0.097	1.77	2.82	1.31	13.5	4.49	51.2	17.87	78.5	14.3	119.1	22.23	0.32
MB2017i_71	2.46	136	47140	3.70E+05	180	1.05E+05	1677	419	32660	3.42E+05	462	19.57	0	0.22	0.106	1.46	2.9	1.295	13.36	4.45	50.8	18.03	80.3	14.3	119.2	22.23	0.44
MB2017i_72	2.69	147	46540	3.70E+05	170	1.12E+05	1604	428	32430	3.47E+05	458	18.38	0.012	0.237	0.118	1.63	2.89	1.25	13.59	4.32	50.3	18.05	77.4	13.91	117.8	21.83	0.29
MB2017i_73	2.85	136	48880	3.65E+05	196	1.07E+05	1888	456	33940	3.50E+05	463	20.2	0	0.172	0.111	2.03	3.56	1.415	12.8	4.52	52.4	18.13	80.2	14.46	119.6	22.38	0.31
MB2017i_74	2.79	154	48740	3.82E+05	225	1.11E+05	1661	444	34190	3.57E+05	463.1	20.04	0.056	0.263	0.137	1.95	2.87	1.35	13.84	4.39	52.2	17.83	78.9	14.08	115.5	21.5	0.31
MB2017i_75	2.08	116	47660	3.72E+05	217	1.09E+05	1452	422	32770	3.44E+05	441	16.98	0.026	0.197	0.11	1.65	3.01	1.3	13.05	4.2	49.8	16.8	72.4	13.48	109.7	20.46	0.202
MB2017i_76	2.09	95	47460	3.55E+05	272	1.06E+05	1404	451	33090	3.48E+05	428.4	16.79	0.0131	0.263	0.103	1.68	2.99	1.25	13.2	3.95	48.5	16.07	69	12.46	103.4	18.95	0.226
MB2017i_77	1.96	105	47460	3.71E+05	187	1.13E+05	1069	463	33130	3.43E+05	436.1	1.81	0.018	0.167	0.098	1.37	2.65	1.215	13.07	4.29	48.2	15.99	69	12.37	104	19.05	0.241
MB2017i_78	1.68	94	48260	3.83E+05	145	1.15E+05	925	548	34210	3.52E+05	447.9	6.91	0.021	0.12	0.078	1.49	3.01	1.21	14.2	4.37	47.4	15.41	64.4	11.58	96.2	17.37	0.136
MB2017i_79	1.54	96	48440	3.68E+05	165	1.02E+05	986	532	34640	3.53E+05	383.5	6.09	0.0091	0.123	0.068	1.31	2.74	1.14	13.9	4.04	44.6	14.46	58.5	10.45	84.7	14.92	0.16
MB2017i_80	2.36	114	47460	3.85E+05	264	1.08E+05	889	640	33560	3.51E+05	358.4	9.86	0.008	0.146	0.08	1.18	2.66	1.122	12.6	3.83	42.1	13.47	49.9	8.61	69.7	12.1	0.17
MB2017i_81	1.8	82	47460	3.72E+05	183	1.08E+05	819	576	33760	3.55E+05	385	7.58	0	0.096	0.063	1.13	2.7	1.1	13.57	4.17	44.1	13.58	52.9	8.99	68.3	11.36	0.133
MB2017i_82	1.53	99	47460	3.65E+05	193	1.06E+05	600	311	33610	3.62E+05	525	6.44	0.0127	0.111	0.047	1.07	2.62	0.9785	12.25	4.28	53.9	18.19	81.3	15.51	134.9	24.12	0.1
MB2017i_83	2.05	94	47460	3.65E+05	156	1.04E+05	512	2061	34030	3.58E+05	587	6.57	0	0.081	0.066	0.95	2.2	0.785	11.04	4.15	53.4	19.64	93.5	19.33	178.2	33.7	0.094
MB2017i_84	1.42	1920	46960	3.98E+05	203	1.17E+05	1330	228	40210	3.81E+05	499	3.42	2.01	5.51	0.84	4.84	2.68	0.925	10.93	4.06	50.9	18.3	79.9	14.98	129.1	22.93	0.13